Comparative Study of Surface Permanent Magnet and Interior Permanent Magnet Machines for Direct Drive Wind Power Application

Radu Ştefan Constantin

A thesis submitted for the degree of Doctor of Philosophy

Department of Electronic and Electrical Engineering
Faculty of Engineering
The University of Sheffield, UK

11 December 2017

Abstract

This thesis investigates the feasibility of interior permanent magnet (IPM) machines for direct drive wind power application.

The influence of key machine parameters, such as the number of rotor poles and the air gap length, on the average PM and reluctance torques in surface permanent magnet (SPM) and IPM machines is investigated. The design parameters of the SPM and IPM machines equipped with NdFeB and ferrite magnets are optimized for maximum torque density, torque per material cost and torque per mass, respectively. It shows that the NdFeB IPM machine is 5% more expensive than the NdFeB SPM machine designed for a 3MW megawatt direct drive wind power application.

Analytical and finite element models are used to predict the fault current in DD PM machines. The influence of the key PM machine parameters for the demagnetization withstand capability, such as the magnet thickness and the number of rotor poles, is investigated. The demagnetization performance of the machines designed for minimum cost is reported. The cost of the IPM machines is found to be 13% higher than the SPM machines when their key parameters are designed for no irreversible demagnetization during the fault transient of a symmetrical three phase to ground converter short circuit. Finally, an experiment for validating the accuracy of Cobham Opera's Vector Field's demagnetization solver is presented in order to fulfil the requirement of the industrial sponsor.

Acknowledgement

First and foremost, I would like to thank my supervisor, Professor Zi-Qiang Zhu, for the guidance and support during my postgraduate course at The University of Sheffield.

I also thank Dr Arwyn Thomas, Dr Yuan Wu, Dr Ziad Azar, and all the members of the generator team at Sheffield Siemens Wind Power Research Centre for all the advice and labor for the experimental project, and for the amazing opportunity to work in the technology group of an industry leading company.

I would like to thank Siemens Wind Power A/S for the financial support during my PhD study.

Thanks to my family and friends for their continual support.

List of symbols

Symbol	Description	Unit
a	barrier angle in V-shape IPM rotor	deg.
A	cross sectional area of copper wire	mm^2
A_g	air gap area	mm^2
A_m	magnet area	mm^2
b_d	barrier depth in V-shape IPM rotor	mm
B_g	air gap flux density	T
b_p	barrier pitch to pole pitch ratio of V-shape IPM rotor	
B_r	remanence flux density	T
C	heat capacity	J K
c	specific heat	J/kg·K
E	electromotive force	V
g	air gap length	mm
H_{avg}	average H-field along magnetization direction in PM	A/m
H_g	magnetic field strength in air gap	A/m
H_m	magnetic field strength in magnet	A/m
H_{min}	minimum H-field along magnetization direction in PM	A/m
I	current amplitude	A
I_d	d-axis current amplitude	A
I_{demag}	amplitude of demagnetization current	A
I_{fault}	current amplitude during fault	A
I_q	q-axis current amplitude	A
I_r	rated current amplitude	A
k_{leak}	ratio between IPM and SPM d-axis PM flux linkage	
k_w	winding factor of fundamental	
l	length of copper wire	m
L	phase inductance	H
L_d	d-axis average self-inductance	H
L_{eff}	axial length	m
l_{gr}	air gap length to pole pitch ratio	

Symbol	Description	Unit
L_q	q-axis average self-inductance	H
M_{dq}	d-axis average mutual inductance due to q-axis current	H
M_{qd}	q-axis average mutual inductance due to d-axis current	H
N	number of turns per coil	
N_{ph}	number of turns per phase	
N_s	number of stator slots	
p	number of rotor pole pairs	
P_{cu}	average copper loss	W
pmp	PM pitch to pole pitch ratio	
Q	heat	W
q	number of slots per pole per phase	
R	phase resistance	Ω
R_g	radius of machine air gap	m
R	reluctance over PM torque ratio for an IPM machine	
$R_{required}$	reluctance over PM torque capabilities ratio for a machines equipped with an SPM rotor and an IPM rotor to exhibit the same average torque	
s_d	stator slot depth	mm
t	time	s
T_{FE}	average torque obtained by 2D finite element analysis	Nm
T_{IPM}	average torque of IPM machine	Nm
t_m	thickness of PM	mm
T_{PM}	average PM torque	Nm
tps	tooth pitch to slot pitch ratio	
$T_{reluctance}$	average reluctance torque	Nm
T_{SPM}	average torque of SPM machine	Nm
β	current advance angle (q-axis corresponds to 0, β<0 for flux weakening operation)	elec.deg.
γ	PM PC point	
ΔH_{avg}	average delta magnetic field strength in PM (reference H_{avg} is the open circuit working point)	A/m
ΔT	temperature rise	K
θ	rotor position	elec.deg.

Symbol	Description	Unit
μ_r	relative magnetic permeability	
ρ_e	electrical resistivity	Ωm
ρ_m	mass density	kg/m^3
τ	time constant	s
Ψ_d	d-axis average flux linkage	Wb
Ψ_{PMd} or Ψ_{PM}	average d-axis PM flux linkage due to PM field	Wb
Ψ_{PMq}	average q-axis PM flux linkage due to PM field	Wb
Ψ_q	q-axis average flux linkage	Wb
ω	synchronous angular electrical frequency	rad/s

Table of contents

1. General Introduction of Permanent Magnet Machines for Direct Drive Applications

1.1 Direct drive applications

1.1.1 Geared vs direct drive

In the late 19th century, most of the wind power generator systems were based on induction machines that were operated at a fixed speed. In the fixed speed setup, the electrical machine is connected to the blade hub through a multi-stage gearbox. The most significant disadvantage of this setup is its performance at wind speeds below or above the rated wind speed for which the turbine was designed. Pitch control of the turbine blades is used to reduce the mechanical power harnessed when the wind speed is above the rated speed. For even higher wind speed, when the pitch of the blades can no longer effectively limit the mechanical power, stall control is implemented to stop the turbine operation.

Variable speed systems allow for better energy production at wind speeds below and above the rated speed. This increases the annual energy production (AEP). Furthermore, as the system speed can be increased above the rated speed when the wind speed is high, the pitch control requirement is relaxed.

Over the last 30 years, the gearless, direct drive concept has gained popularity. This is mainly due to the mechanical reliability issues associated with a multi-stage gearbox. As the mechanical failures of these gearboxes reduce the annual energy production due to long repair times especially for off-shore wind power generation, gearless, direct drive systems have been confirmed to be a more suitable solution. The torque capabilities of an electrical machine are related to its size so the direct drive generator is significantly larger, and thus, more expensive when compared to the generator in a

geared system capable of inputting the same average torque. The mechanical gearing losses are the highest in a three stage gearbox, lower in a single stage gearbox and absent for the direct drive system.

Diagrams of the geared and the direct drive wind power generator systems are presented in Fig. 1-1. The nacelle houses the electrical machine and the gearbox in Fig. 1-1(a) and the electrical machine stator for the direct drive system in Fig. 1-1(b). For the direct drive application, an outer rotor PM machine has the electromagnetic advantage of a marginally higher air gap diameter compared to an inner rotor electrical machine, and thus a wider pole pitch, a higher magnetic loading and torque density. Moreover, the rotor in the direct drive system is mounted directly in the hub, reducing the number of parts required to connect the system and further enhancing its mechanical reliability.

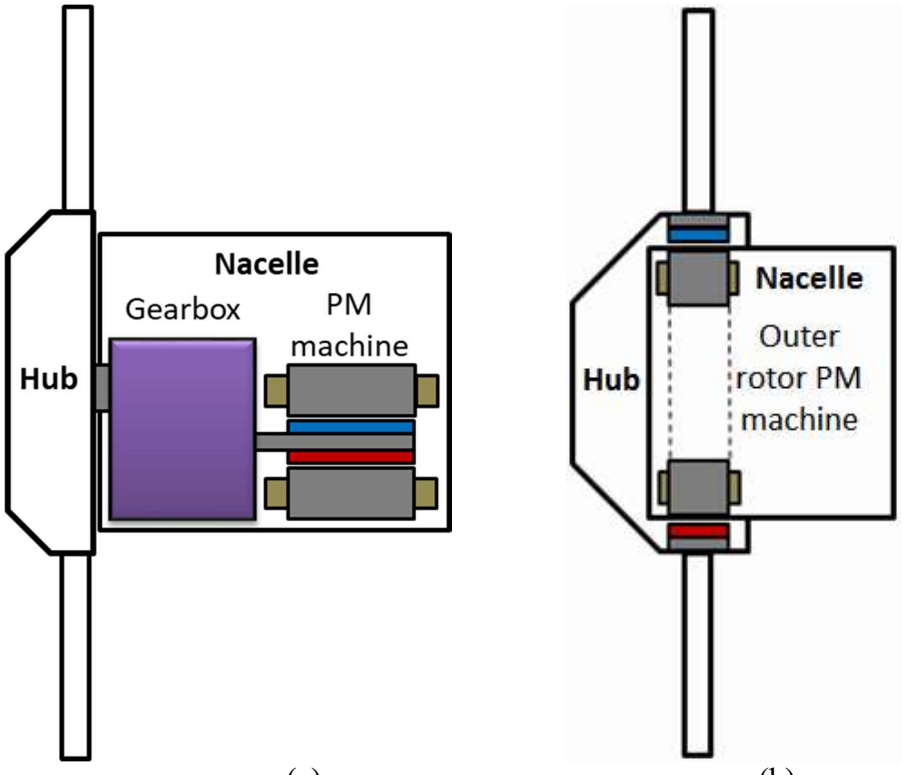

(a) (b)

Fig. 1-1 Schematic diagrams of turbine hub and nacelle for (a) geared and (b) a direct drive wind power generator systems.

In [1], the economic aspects such as the system costs and the annual energy production are compared for generators optimized for minimum total system cost. The generators

are a direct drive electrically excited synchronous generator (EESG), a direct drive PM rotor generator, a doubly-fed induction generator (DFIG) with a single stage gearbox, a PM generator with a single stage gearbox and a DFIG with a three stage gearbox. The PM generator with a single stage gearbox is the cheapest option in [1]. However, the annual energy yield of the direct drive PM generator was found to be the highest due to the good performance at low wind speed. At low wind speeds the DD PM generator has the advantages of a higher energy yields due to the absence of gearing losses and rotor losses. The authors mention the reliability of the presented systems, i.e. the downtimes associated with gearbox or other system failures, has not been included in the investigation. The geared generators in this study would generally experience, on average, a longer maintenance downtime than the direct drive solutions, and thus, the direct drive PM generator is expected to be the best candidate for off-shore wind power generation. A similar study with the generators optimized for minimum total system cost at 0.75MW, 3MW and 10 MW power rating is presented in [2]. For the same power rating, the conclusions are similar to those in [1]. For increasing power ratings, the AEP/cost of all generators in [2] is found to decrease. The reported AEP/cost is computed without accounting for the higher average maintenance downtimes of the generators equipped with gearboxes.

A qualitative comparison of fixed speed and different variable speed generator systems is presented in [3]. The advantages of a generator with a PM excited rotor field over a generator with an electrically excited rotor field are presented. These include higher efficiency and energy yield, higher reliability (no slip rings) and lower total mass. The disadvantages of the PM generators are the higher cost and the risk of irreversible demagnetization. Although characterized by a higher torque density, the axial and transversal flux PM generators have the following disadvantages: mechanical feasibility

issues with maintaining the air gap at large air gap diameters, low power factor and manufacturing issues with winding the stator.

In [4], the authors show that for a single stage gearbox PM generator system, there is an optimum gear ratio which yields the minimum total system cost. Comparison to a direct drive PM generator is not presented.

[5] presents an AEP and cost comparisons of geared and direct drive generators. The conclusions are similar to those in [1] and [2]: the direct drive PM generator has the highest AEP at low wind speeds and the single stage gearbox DFIG has the highest AEP per cost.

[6] is a review of the PM machines designed for DD applications. It highlights the advantages that the PM machines have over other AC excited rotor machines: the rotor PM flux is relatively insensitive to air gap diameter. However, compared to their geared counterparts, the direct drive generators are considerably larger, and thus, more expensive and have problems maintaining the air gap length at large diameters.

1.1.2 Direct drive application requirements and limitations

Maintaining the air gap length between the stationary and the moving part in large scale PM machines can be challenging [6]. The air gap length data of typical large scale generators is presented in Table 1-1. The optimum air gap length to pole pitch ratio has similar values for all the machines, around 0.05 at all power ratings.

The air gap length to air gap diameter ratio of the 3kW-DD prototype is 4-5 times larger than that of the other machines. For the generators optimized for industrial applications, in order to reduce the material costs, the minimum mechanically feasible air gap length

is used. The 0.1% lower limit for the air gap length to the air gap diameter ratio is due to considerations for the stator thermal expansion and for the manufacturing tolerances [1]. The copper loss is the major contributor to the total loss and to the heat generated in a PM machine optimized for a DD application. The thermal expansion is mostly due to the copper loss and partly due to the seasonal variation of temperature. Hence, the choice of air gap length will limit the allowed thermal expansion of the stator, and thus, it will limit the electrical loading of the generator. A good engineering compromise is achieved for air gap lengths around 0.1% of the air gap diameter.

Table 1-1 Air gap length data of direct drive SPM generators.

Model	Air gap diameter (mm)	Air gap length (mm)	Number of rotor poles	Pole pitch (mm)	Air gap length to pole pitch ratio	Air gap length to air gap diameter ratio
3kW-DD prototype	390.4	2	32	38.3	0.0522	0.0051
3MW-DD	4050	5	108	117.8	0.0424	0.0012
8MW-DD	6355	7	144	138.6	0.0505	0.0011
15MW-DD	10500	10.8	192	171.8	0.0629	0.001

1.2 Stator winding configurations

The PM machine can be classified into two categories according to the number of slots per pole per phase, q.

The machines in Fig. 1-2 have an integer slot per pole per phase q=1 and are equipped with an overlapping distributed winding (ISDW). They are characterized by a fundamental winding factor, k_w=1, high cogging torque [7], and a low magnetizing inductance compared to the machines with fractional slots per pole per phase and

concentrated windings (FSCW). The low average inductance in ISDW machines is mainly due to the absence of sub-harmonic orders in the magnetic field produced by the winding. For FSCW machines q should be selected between 0.25 and 0.5 for a fundamental winding factor, $k_w \geq 0.866$. The FSCW machines with $k_w \geq 0.866$ only have between a quarter and a half of the number of slots of the ISDW machines with $q=1$ for the same number of rotor poles. The second reason the ISDW machine has a lower average inductance compared to the equivalent FSCW machine is the higher number of stator slots and of coils, and thus, the lower number of turns per coil [8]. The lower average inductance and stator MMF of the ISDW are beneficial for the rated operation power factor and for the demagnetization withstand capability. Furthermore, the difference in magnetic reluctance along the *d*- and *q*- axes is considerably higher for the ISDW machines compared to the FSCW machines when equipped with a salient rotor, and hence, so are the average reluctance torque capabilities.

The machines in Fig. 1-3 are equipped with FSCW with the coils wound around alternate teeth in (a) and around all teeth in (b). They offer some manufacturing and electromagnetic performance advantages compared to the more conventional ISDW machines [9] [10] [11] [12] [13] [14]. The manufacturing and winding process of the FSCW machine stator is simpler and cheaper. The packing factor is generally higher in the FSCW machines and they have considerably shorter end-windings, and thus, a lower copper loss compared to the ISDW machines in Fig. 1-2.

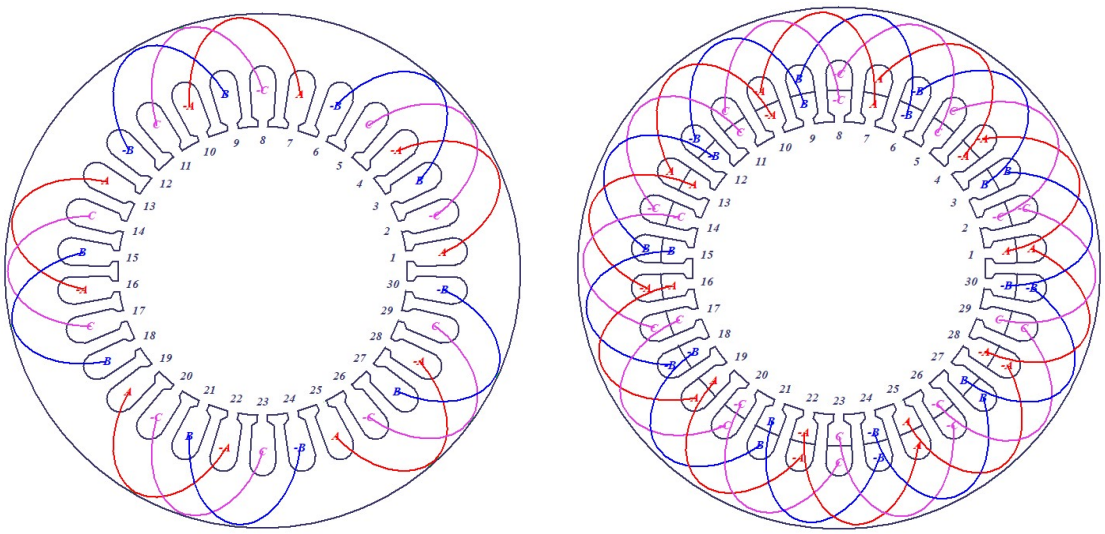

(a) (b)

Fig. 1-2 Integer slot per pole per phase, overlapping winding (ISDW) configuration with (a) end-windings grouped and (b) evenly distributed along circumference (30slots-10poles).

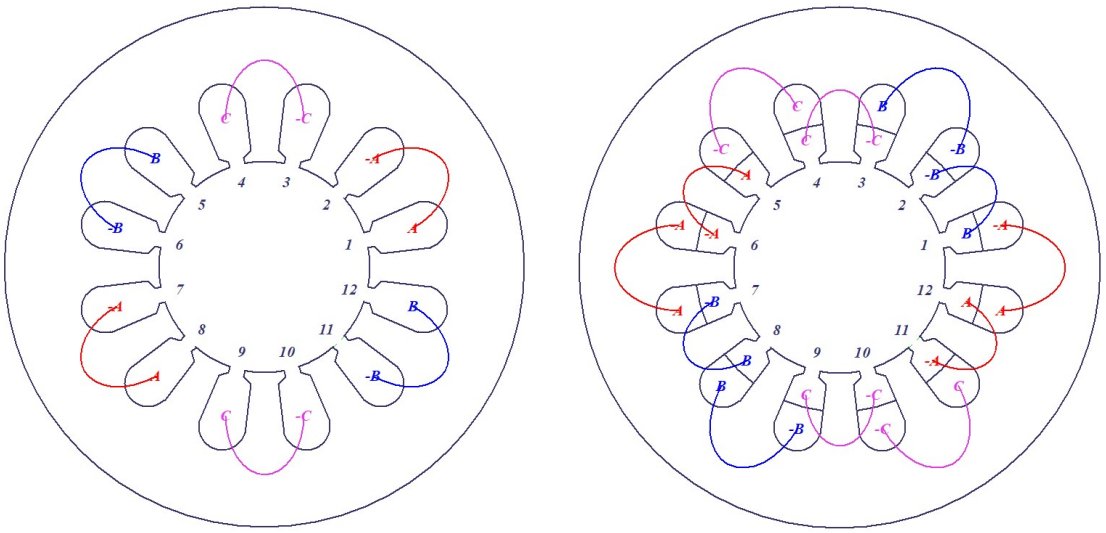

(a) (b)

Fig. 1-3 Fractional slot per pole per phase, concentrated winding (FSCW) configuration with (a) alternate teeth wound and (b) all teeth wound (12slots-10poles).

The peak to peak cogging torque is significantly lower in the FSCW machines. However, they can exhibit a high unbalanced magnetic force when the phase windings are not evenly distributed along the stator circumference of FSCW machines [15]. For the FSCW machines, the average magnetic reluctance along the *d*- and *q*- axes is similar for most slot pole combinations, and thus, they exhibit a low average reluctance torque capability. The exceptions to this are the q=0.25 and q=0.5 windings which can exhibit

significant inductance difference along the *d*- and *q*- axes, and thus, significant average reluctance torque. Hence, in FSCW machines with high fundamental winding factor (N_s=2p±1, N_s=2p±2 etc.) the average reluctance torque will be low even when equipped with a salient rotor. The FSCW machines with high average reluctance torque capabilities, and q=0.25 or q=0.5, have a low fundamental winding factor k_w=0.866 and yield a poor utilization of the PM material. Thus, q=0.25 or q=0.5 are rarely used for power generation applications. Furthermore, the armature reaction of machines equipped with FSCW stators has rich sub-harmonics which contribute to the iron and PM losses.

1.3 Rotor topologies

The rotor topologies of PM machines can be classified into two general categories: non-salient and salient. Most PM machines are equipped with a non-salient rotor with the PM mounted on the surface as shown in Fig. 1-4. As the magnets are installed directly on the rotor back iron surface, the SPM has the lowest rotor flux leakage and the highest PM flux linkage per PM volume. In a non-salient rotor topology, the effective air gap lengths along the *d*- and *q*- axes are equal, and thus, the average reluctance and the average inductance in the *d*- and *q*- axes are of similar amplitude. The effective air gap length of the SPM topology is equal to the mechanical air gap plus the PM thickness, as the relative magnetic permeability of the NdFeB (μ_r=1.05) is close to that of air. Hence, compared to the salient rotor topologies, the SPM will exhibit the lowest air gap inductance due to the highest air gap reluctance. The high PM flux linkage and low winding inductance are key advantages for a high power factor in DD applications. A high power factor helps to reduce the cost of the required converters.

The salient rotors, the second category of PM machine rotors, are shown in Fig. 1-5. PM machines equipped with salient rotors can exhibit a significant average reluctance torque, owing to the inductance (or reluctance) difference along the *d*- and *q*- axis rotor magnetic circuits. The inset surface permanent magnet rotor in Fig. 1-5(a) is an example of a salient topology with the PM not covered by the rotor laminations. It offers the advantage of a lower PM flux leakage compared to the other salient rotor topologies, but it does not shield the PM from the eddy current losses induced by the stator slotting effect and by the armature reaction field. All the interior permanent magnet topologies from Fig. 1-5(b) to Fig. 1-5(f) use rectangular magnets, which are cheaper to manufacture. The eddy current loss in the magnets of the IPM topologies is lower than that in the magnets of the SPM and the inset SPM; however the total rotor loss (PM and back iron) is significantly higher due to the shorter effective air gap length. The shielding effect of the IPM rotor laminations is still beneficial even though it yields an increase in total loss and a decrease of efficiency. The temperature rise of the NdFeB rare earth magnetic material has a detrimental effect on the coercivity and can lead to irreversible demagnetization, and hence, the PM eddy current loss cannot be neglected. PM machines equipped with salient rotors exhibit an average reluctance torque, which peaks when the current angle is between the *d*- and *q*- axes, at $90k$+45 elec.deg., where k=(0,1,2,3). The presence of the salient structure shifts the optimum current angle for maximum torque per ampere (MTPA) away from the *q*- axis at 0 elec.deg, towards -45 elec.deg. for motoring operation.

The IPM rotor topology in Fig. 1-5(b) consists of a single rectangular magnet. Compared to the other buried salient rotor structures, it has the cheapest and simplest manufacturing process. It is characterized by a low PM flux leakage and mild reluctance torque capabilities. The spoke type IPM in Fig. 1-5(c) uses the depth of the rotor

laminations to increase the magnet volume. The PM flux leakage increases when the PM is buried deeper inside the rotor structure. The spoke IPM can have a heavy rotor with a poor PM utilization and is generally used with lower energy product magnets like ferrite. The V-shape IPM in Fig. 1-5(d) is characterized by a low PM flux leakage and mild to moderate reluctance torque capability. Compared to the I-shape, the V-shape uses the space in the rotor laminations better by having the flux barrier segmented and at an angle to the rotor surface. When the total magnet length in one rotor pole is greater than the pole pitch, the rotor topology is flux focusing. The spoke IPM and the PM assisted synchronous reluctance machine (PMaSynRM) rotor topologies can also achieve this but with a significantly higher leakage compared to the V-shape IPM due to the number of flux leakage paths. The V-shape IPM only has a maximum of 3 leakage paths around one rotor pole, and the majority of the magnet close to the rotor surface. In the spoke IPM, although the number of leakage paths around one pole is only 2, the leakage at the inner rotor radius is more severe. The PMaSynRM rotor topologies in Fig. 1-5(e) and Fig. 1-5(f) exhibit the highest PM flux leakage but also the highest saliencies and reluctance torque capabilities. The PMaSynRM have the thinnest magnets due to the space constraints and are, thus, the most susceptible to local irreversible demagnetization.

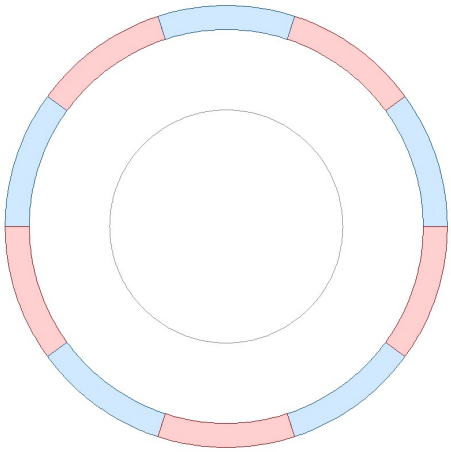

Fig. 1-4 Non-salient surface permanent magnet rotor topology.

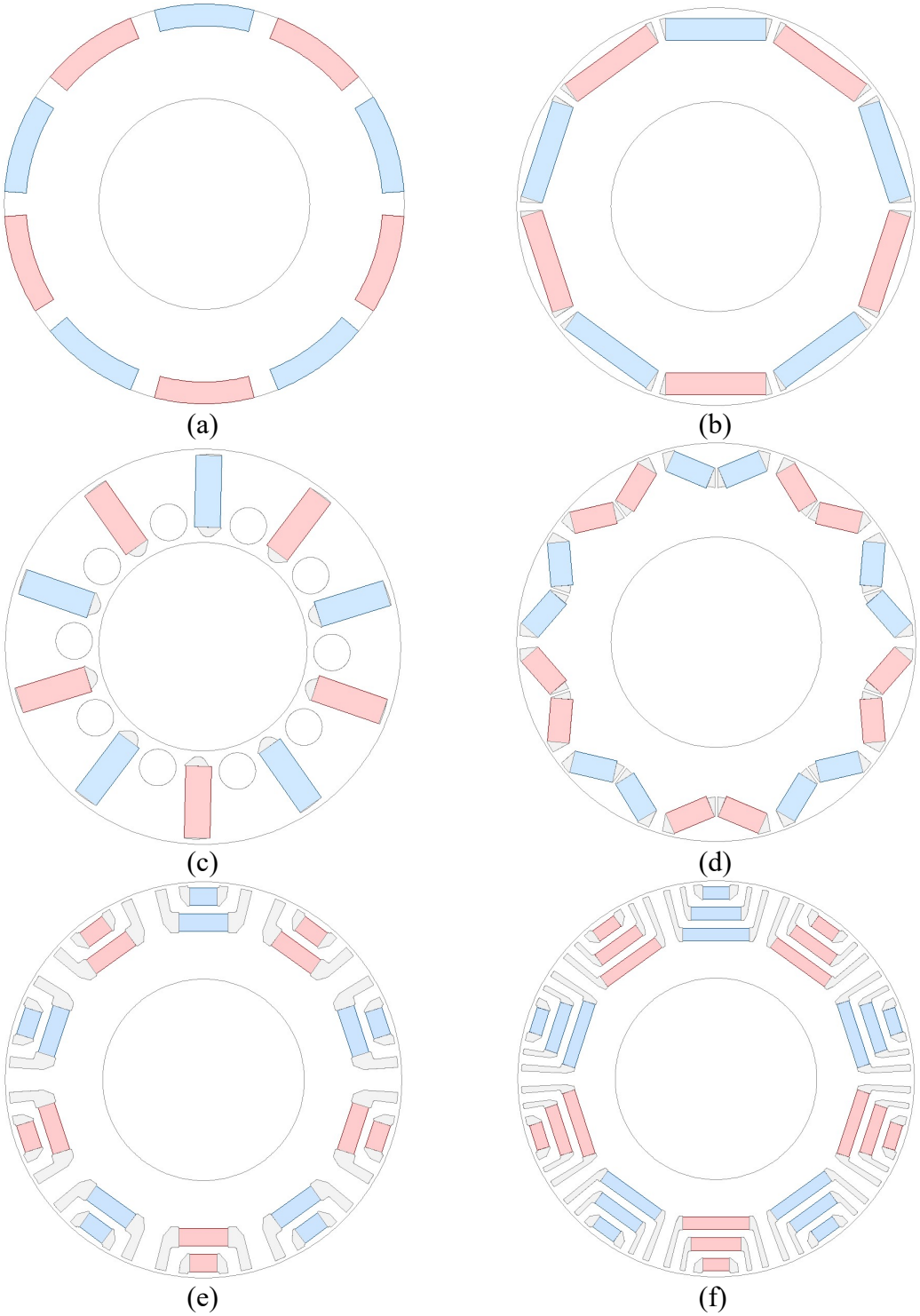

Fig. 1-5 Salient PM rotor topologies: (a) inset SPM, (b) I-shape IPM, (c) spoke IPM (d) V-shape IPM, (e) two barrier PMaSynRM and, (f) three barrier PMaSynRM.

For the investigations presented in this thesis the V-shape rotor topology was used for the IPM as it offers the best compromise between the flux leakage and the flux focusing and the reluctance torque capabilities.

1.4 Thesis outline and contribution

Chapter 1:

It presents the background of the PM machines optimized for direct drive applications and highlights their advantages and limitations.

Chapter 2:

A hybrid FE and analytical technique is used to segregate the average PM and reluctance torque contributions in a salient machine with a reduced number of FE simulations. Results of the fast estimation technique are compared to results obtained using the conventional partial flux-coupling flux segregation technique in a small size Prius 2010 IPM motor and in large outer diameter machines for direct drive applications. A "goodness" ratio of the reluctance torque over PM torque capabilities is introduced. The ratio is used to explain the influence of key parameters like the air gap length, the number of rotor poles and the current amplitude on the average torque capabilities of the machine. The emphasis is on the different optimum number of rotor poles for maximum torque or maximum torque per cost or torque per volume for the SPM and IPM machines.

Chapter 3:

A closed loop finite element optimization technique is introduced. Machines equipped with SPM and V-shape IPM rotors are optimized for minimum cost, volume or mass. NdFeB and ferrite magnets are used to show the influence of the PM energy product on the optimum design. The cost, mass and volume material breakdown of the optimized machines are compared.

Chapter 4:

The fault and demagnetization withstand capability analyses in electrical machines are presented. Analytic models for the permanent magnet working point and for the peak current during the symmetrical three phase to ground converter short circuit transient are used to investigate the demagnetization withstand capabilities of the minimum cost machines optimized in chapter 3. The demagnetization performance of the minimum cost machines in chapter 3 is reported. The key parameters governing the demagnetization withstand capability are tweaked. The machine with the minimum cost increase that yields no irreversible demagnetization due to the fault is selected for each combination of rotor type and magnet grade. Finally, the cost of the machines without irreversible demagnetization is reported and their rated load performance is compared.

Chapter 5:

In chapter 5, an experimental investigation on the accuracy of Cobham Opera's Vector Fields demagnetization solver is presented. Experimental locked rotor demagnetization results of the open circuit back-EMF and static torque are compared to results computed using Vector Fields demagnetization solver for a small size SPM machine.

Chapter 6:

The conclusions of chapters 1 to 5 are summarized and general conclusions and consideration for future trends are formulated.

Contributions:

- Developed closed loop parameter optimization process for SPM and IPM machines;
- Optimized and compared the electromagnetic performance and the materials used in PM machines optimized for maximum torque per cost, torque per volume or torque per mass for a direct drive application;
- Investigated demagnetization performance of PM machine for direct drive applications;
- Determined parameters of minimum cost PM machines without irreversible demagnetization for machines equipped with SPM and IPM rotors and with NdFeB and ferrite magnets.

2. Interior Permanent Magnet Generators for Wind Turbine Applications

2.1 Introduction

This chapter investigates the potential application of IPM generators for direct drive (DD) wind power applications, with particular focus on the reluctance torque capability. A hybrid FE and analytical method to segregate the PM and reluctance torque components of large data sets of IPM generators with a reduced number of FE simulations is presented. The accuracy of the proposed torque segregation method is compared to that of the conventional method for the Toyota Prius 2010 IPM machine and the DD generators equipped with IPM rotors, respectively. A ratio is introduced to account for the average contributions of the PM torque and of the reluctance torque, and to quantify the utility of the reluctance torque in the machine equipped with high energy product rare-earth magnets.

The proposed torque segregation method and ratio are used to assess the reluctance torque capabilities of generators designed for DD applications. The influence of key design parameters such as the air gap length and the slot-pole number combinations on the reluctance torque capability is investigated.

2.2 Reluctance torque calculation

2.2.1 Method 1: Partial coupling method

Different methods can be used to estimate the contribution of the reluctance torque based on how the inductances are defined. The partial coupling method is one of the well-established techniques where the d-q axis inductances are computed with the aid of finite element tools [16]. The computation of self and mutual inductances is done using the flux linkage values computed with finite element method. The flux linkage is segregated considering the contribution of the PM to the flux linkage as a function of q-axis current only.

$$\Psi_{PM(0,I_q)} = \Psi_d(I_d = 0, I_q) \tag{2.1}$$

where Ψ_{PM} is average d-axis PM flux linkage which is a function of the q-axis current amplitude. I_d and I_q are the d-q axes current amplitudes.

The average inductances along d and q-axes are computed by dividing the flux linkage due to the armature reaction by the current amplitude. For the d-axis, it means removing the flux linkage due to the PM first.

$$L_d = \frac{\Psi_d(I_d, I_q) - \Psi_{PM}(0, I_q)}{I_d} \tag{2.2}$$

$$L_q = \frac{\Psi_q(I_d, I_q)}{I_q} \tag{2.3}$$

$$M_{dq} = \frac{\Psi_d(I_d, I_q) - \Psi_d(I_d, 0)}{I_q} \tag{2.4}$$

$$M_{qd} = \frac{\Psi_q(I_d, I_q) - \Psi_q(0, I_q)}{I_d} \tag{2.5}$$

where L_d and L_q are the average self inductances and M_{dq} and M_{qd} are the mutual inductances of the d-q axes. $\Psi_{d \text{ and }} \Psi_q$ are the average d-q axes flux linkage.

2.2.2 Method 2: Fast estimation method

Similar to the partial coupling method, in the proposed method, the average PM torque is estimated using finite element method. In this method, the *d*- axis PM flux linkage is assumed to be constant for the rated current amplitude, I_r, regardless of the current angle as in (2.6).

$$\Psi_{PM} = \Psi_d(I_d = 0, I_q = I_r) \tag{2.6}$$

$$T_{PM(I_d,I_q)} = \frac{3}{2} p \cdot \Psi_{PM(0,I_r)} \cdot I_q \tag{2.7}$$

This simplification implies the d-axis PM flux linkage, $\Psi_{PM,}$ is constant for a fixed total current amplitude, I_r, not a function of the current angle or I_q. The PM torques at different current angles are calculated by using the constant Ψ_{PM} as in (2.7). The reluctance torque is then estimated by subtracting the reluctance torque from the total torque computed using finite element method.

The proposed method is similar to the constant parameter method in the sense that the contribution of the PM towards the flux linkage is assumed constant regardless of the current angle. However, compared to the constant parameter method, in the proposed fast estimation method, no assumptions are made about the average *dq* axis inductances. The reluctance torque is calculated, by subtracting the average PM torque from the average torque computed by FE.

$$T_{reluctance(I_d,I_q)} = T_{FE(I_d,I_q)} - T_{PM(I_d,I_q)} \tag{2.8}$$

Using the reluctance torque value from the above equation, one can compute the inductance difference L_q-L_d. However, there is insufficient data to calculate the average inductance along each of the d-q axes.

$$T_{reluctance(I_d,I_q)} = \frac{3}{2} p \, (L_d - L_q) \cdot I_d I_q \tag{2.9}$$

In Fig. 2-2 the torque components of an IPM machine are segregated using the proposed fast estimation technique. The only information required for the torque segregation is the average torque at a particular current angle and the average torque at 0 deg. current angle. Both these values can be obtained directly with the aid of two finite element simulations.

In terms of computational complexity, the proposed fast estimation technique only requires 31 finite element simulations to obtain Fig. 2-2 while the partial coupling technique would require 93 finite element simulations (with either I_d, I_q or both I_d and I_q excitations. Overall, it is expected that the proposed method will be three times less computational intensive.

Furthermore, the proposed method computes the reluctance torque contribution directly and hence it is not possible to compute the individual *d*- and *q*- axis inductances. Hence, a direct comparison with the inductances predicted using the conventional partial coupling method is not possible. The accuracy of the proposed method in computing the torque segregation can be evaluated by their prediction of average permanent magnet and reluctance torques, as presented in sections 2.2.3 and 2.2.4.

2.2.3 Validation of proposed technique for the estimation of torque components - Toyota Prius 2010 IPM machine

As the proposed method 2 cannot predict the *d*- and *q*- axis inductances, the average amplitude of the reluctance torque will be used to validate the accuracy of the method.

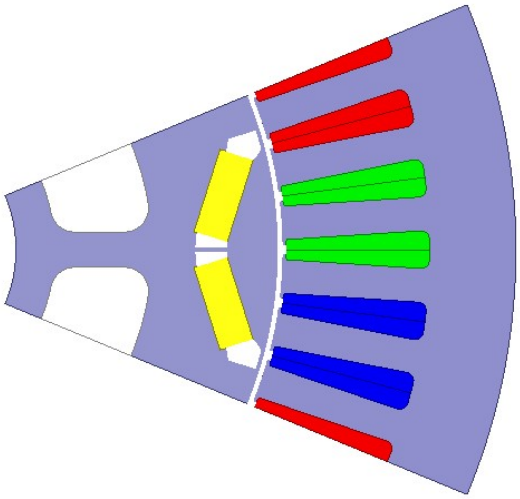

Fig. 2-1 Cross section of Toyota Prius 2010 IPM machine (one pole).

Fig. 2-2 shows a graphical representation of the segregated torque of the Toyota Prius 2010 IPM machine [17] using the fast estimation method presented in section 0. The total average torque (blue line in Fig. 2-2) vs current angle is computed with the FE tool. The PM torque is directly proportional to the total torque at 0 current angle and to the cosine of the current angle, β. The reluctance torque is then computed by subtracting the PM torque contribution from the total average torque computed using FE.

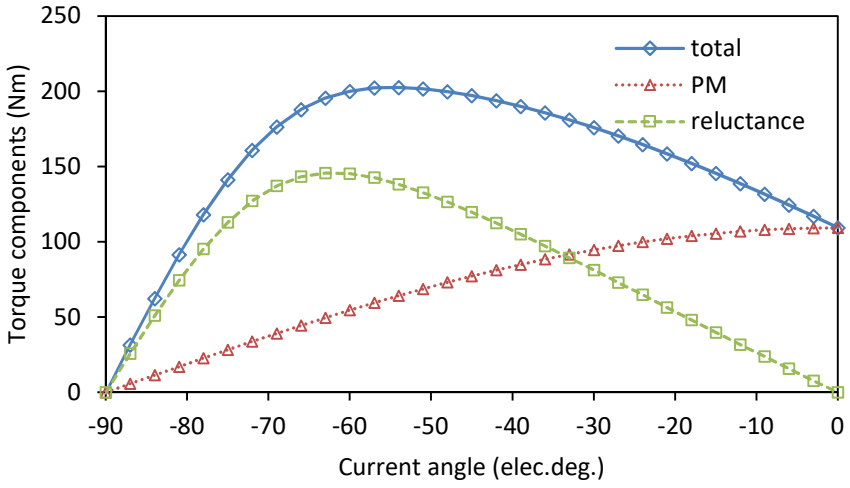

Fig. 2-2 Torque segregation of Toyota Prius 2010 IPM machine for *I*=200A using fast estimation method.

The most significant difference between these two methods of torque segregation is caused by the cross-coupling between the *d*- and the *q*- axes. For the conventional

partial coupling method, the effect of the *q*-axis current on the *d*- axis is considered: the PM flux linkage is a function of the *q*-axis current as in (2.1) while for the fast method the PM *d*-axis flux linkage is assumed constant (Fig. 2-3). As flux weakening current is applied, the average *d*-axis PM flux linkage calculated with the partial coupling method increases. This can be explained with reference to the saturation of magnetic circuit due to the two flux linkage sources: when the armature reaction field is the opposite direction to the PM field, the working point of the steel is lower and the effective flux linkages due to each individual source is higher in amplitude than in the case where the armature reaction field would only partially oppose the magnetic field (i.e. when aligned with the rotor *q*- axis). The discrepancy between the PM flux linkages calculated using the two methods increases as the amplitude of the excitation is increased and the cross-coupling is more severe.

The difference in Fig. 2-4 is caused by the estimation of the *d*-axis PM flux linkage in Fig. 2-3.

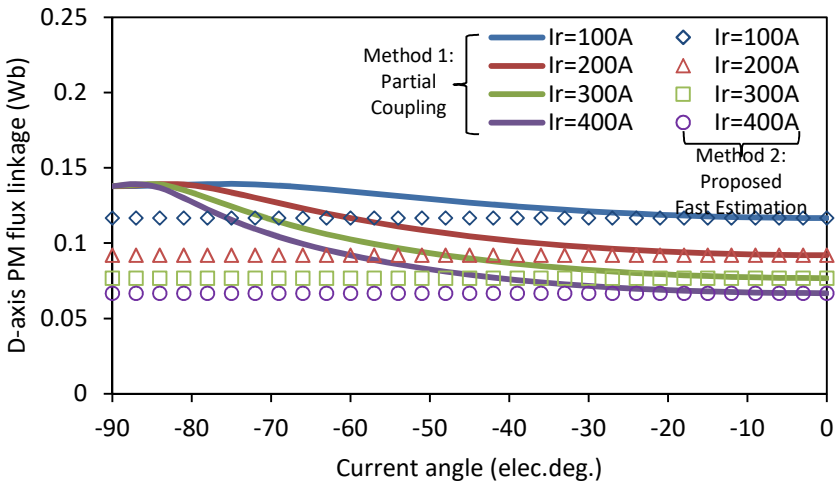

Fig. 2-3 *D*- axis PM flux linkage calculated using partial coupling method. Fast estimation method uses marked value at 0 elec.deg. for all other current angles.

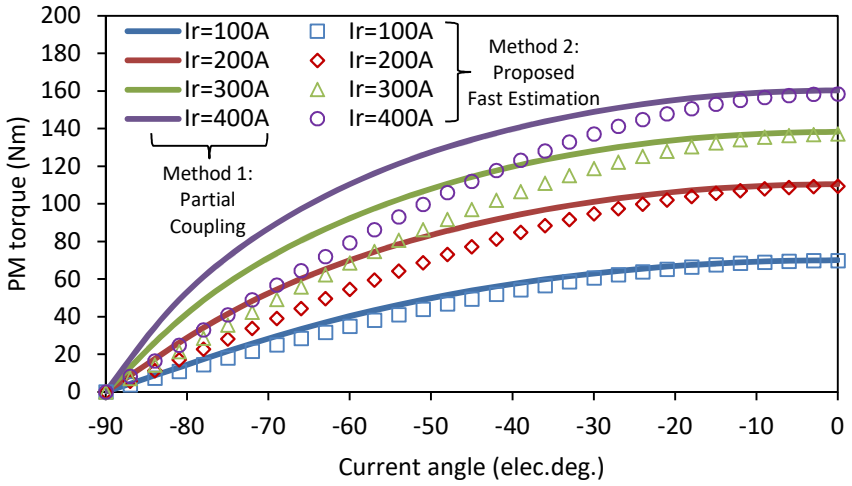

Fig. 2-4 Permanent magnet torque prediction by partial coupling and fast estimation methods.

The calculation error of fast estimation method for the PM torque is shown in Fig. 2-5. The error is computed using (2.10).

$$\varepsilon = (T_{M1} - T_{M2})/T_{M1} * 100 \tag{2.10}$$

The amplitude of the error can be up to 50% for values of β<-60 elec.deg, where the amplitude of the average PM torque tends to zero. This is caused by the severe effect of the *d*- axis demagnetizing armature reaction field on the saturation of the magnetic circuit. In Fig. 2-6 the reluctance torque computed with the aid of the two methods is presented. As the contribution of the PM torque is underestimated when the fast estimation method is used, and consequently, the contribution of the reluctance torque will be overestimated.

The error of calculating the contribution of the reluctance torque towards the total average torque increases with the current amplitude and the magnitude of the current angle. This is due to cross-coupling affecting the *d*- axis PM flux linkage and causing the error in predicting the PM, and thus reluctance torques as in Fig. 2-7.

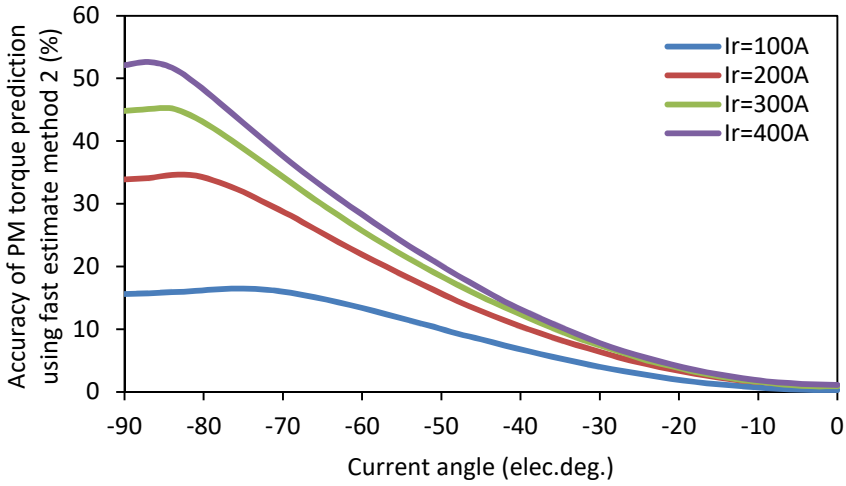

Fig. 2-5 Difference between average PM torque computed using partial coupling and fast estimation methods.

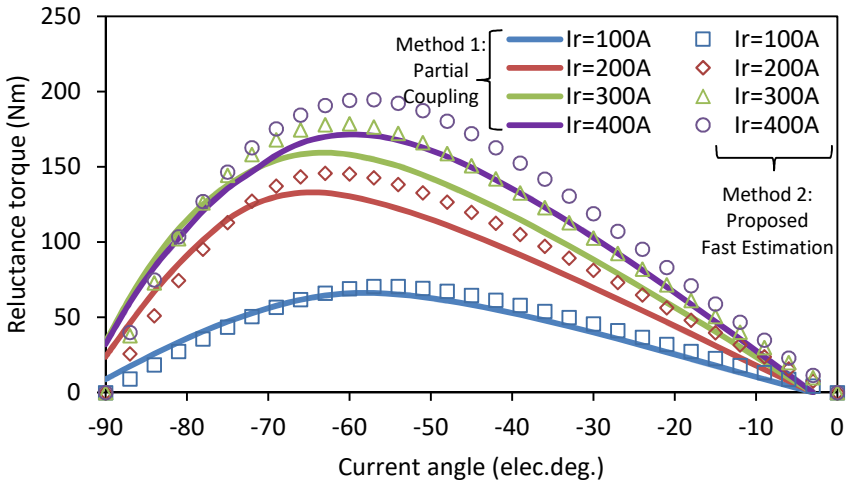

Fig. 2-6 Reluctance torque prediction by partial coupling and fast estimation methods.

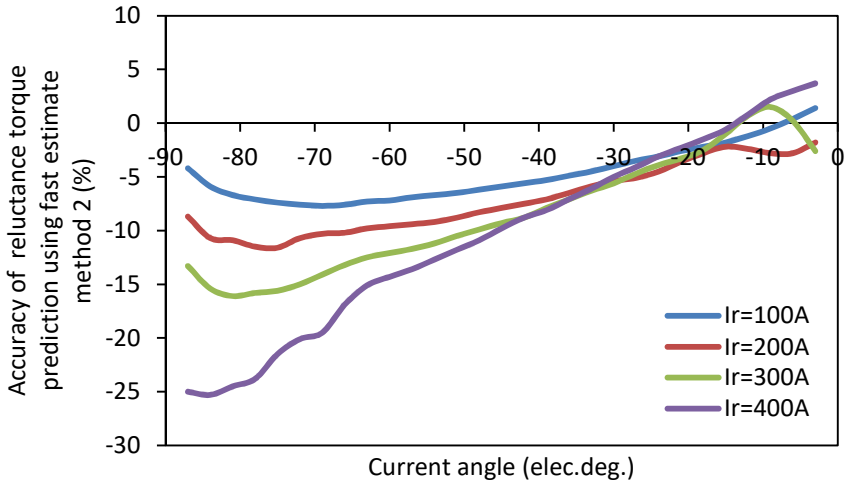

Fig. 2-7 Difference between average reluctance torque computed using fast estimation and partial coupling methods.

2.2.4 Accuracy of reluctance torque calculation in large scale DD IPM machines for wind power generation

The aim of this part is to assess the accuracy of the reluctance torque estimation method for different IPM generators. The parameters that have the most influence on the reluctance torque are the air gap length and the stator magneto-motive force, $N{\cdot}I$: the distribution of phase windings by coils and the electrical excitation amplitude. Hence, the most important parameters for the average reluctance torque are listed below.

Parameters:

- air gap length
- number of slot/poles (distribution of turns in coils and number of rotor poles)
- current amplitude

To reduce the number of simulations, the key parameters above are scanned in pairs: in one scan the air gap length and current amplitude and in the other scan the air gap length and the slot/pole number. The investigation was carried out on the 3kW prototype generator frame whose design parameters are shown in the appendix.

In the first finite element scan the air gap length and current amplitude are varied for a 84slot-28pole IPM machine. In the second finite element scan the air gap length and slot/pole number are varied for a fixed current excitation $I=5I_r$=21.2A.

Table 2-1 shows the number of values for each scanned parameters takes during the scans described above and the total number of FE simulations required for the conventional method 1 and the fast estimation method 2.

Table 2-1 Number of finite element simulations required for torque segregation using the two methods for the two parameter scans.

	Number of scanned parameter values				Numbers of required FE simulations	
	air gap length	current amplitude	number of rotor poles	current angle	Method 1	Method 2
scan 1	10	10	1 (p=28)	17	**5100**	**1700**
scan 2	6	1 ($I=5\cdot I_r$)	19	17	**5814**	**1938**

In Fig. 2-8 the reluctance torque increases with current amplitude faster than a linear rate. It was expected that the average reluctance torque would be directly proportional to the square of the current amplitude. However, at high current amplitude conditions the saturation of the magnetic circuit, especially along the q- axis, limits the average reluctance torque amplitude. The average reluctance torque will quadruple when the amplitude of the current excitation is doubled if the magnetic circuit is linear. The average reluctance torque predicted by the partial coupling and the proposed fast estimation methods are 3.73 times and 3.92 times larger when the amplitude of the current is doubled from I_r=12.7A to I_r=25.4A. However, for the I_r=21.2A to I_r=42.2A range the reluctance torque increases only 3 times according to the partial coupling method and by 3.17 times according to the proposed method due to saturation.

The air gap length is also an important parameter for reluctance torque generation as shown in Fig. 2-9. The reluctance torque rate of reduction with air gap length is also faster than linear due to the effect of the additional air gap which has on the *d*- and *q*-axis inductances. Increasing the air gap length generally yields a reduction in L_d and L_q. However, the effect of the additional air gap has a much more severe effect in the *q*-axis where the effective air gap length is small and the saturation caused by the armature reaction is more significant. Effectively, when the air gap is increased, the average value of L_q reduces faster than that of L_d. This has a detrimental effect on the average reluctance torque.

The error in predicting the average reluctance torque using the fast estimation method compared to the conventional partial cross-coupling method is plotted in Fig. 2-10 for the air gap length and current amplitude scan and in Fig. 2-12 for the air gap length and number of rotor poles scan.

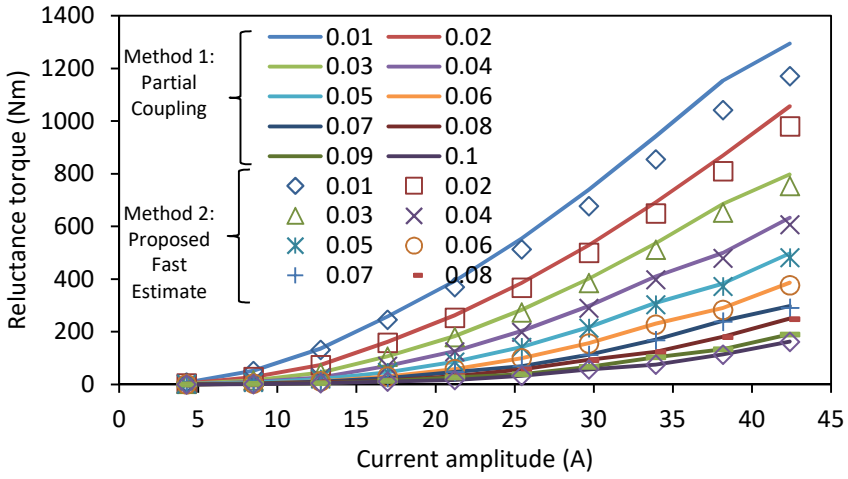

Fig. 2-8 Reluctance torque vs. current amplitude and air gap length to 38.5mm ratio.

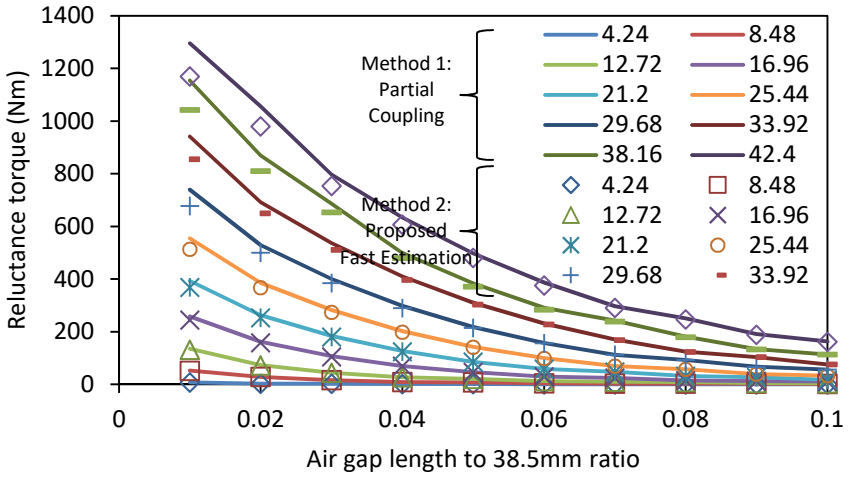

Fig. 2-9 Reluctance torque vs. air gap length to 38.5mm ratio and current amplitude.

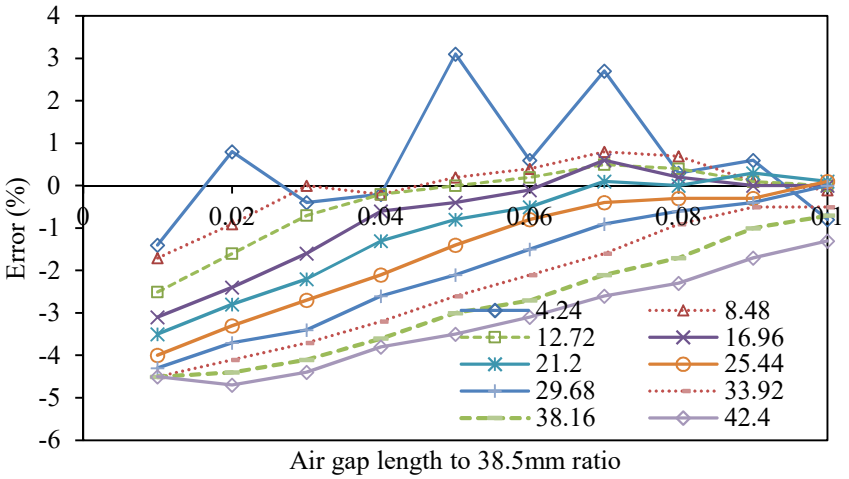

Fig. 2-10 Error in computing the reluctance torque contribution using method 2, referred to method 1 (scan 1-air gap length and current amplitude, p=28).

The number of rotor poles is fixed to p=28 in the air gap length and current amplitude scan. The error for the average reluctance torque prediction is lower than 5% and is caused by the inaccurate prediction of the PM flux linkage due to saturation caused by the armature reaction field as explained in Section 2.2.3.

For a machine with a fixed number of turns per phase, the air gap magnetizing inductance is inversely proportional to the number of rotor poles, p. This is because the per pole air gap magnetizing inductance is directly proportional to the square of the number of turns per coil. The number of turns per coil is inversely proportional to p, and

hence neglecting the non-linearity of the magnetic circuit, the air gap magnetizing inductance is proportional to $p \cdot p^{-2}$. As the air gap magnetizing inductance is proportional to the average reluctance torque capabilities of an electrical machine, for a machine with a fixed number of turns per phase and fixed number of slots per pole per phase, the average reluctance torque will be inversely proportional to p, as shown in Fig. 2-21.

For the parametric scan of air gap length and number of rotor poles, the error in average reluctance torque prediction is higher at a low pole number. This is because the inductance of the generators is the highest when the phase winding is grouped into the minimum number of coils at a low pole number. Furthermore, the error in predicting the reluctance torque decreases with the increase of air gap length, as shown in Fig. 2-12.

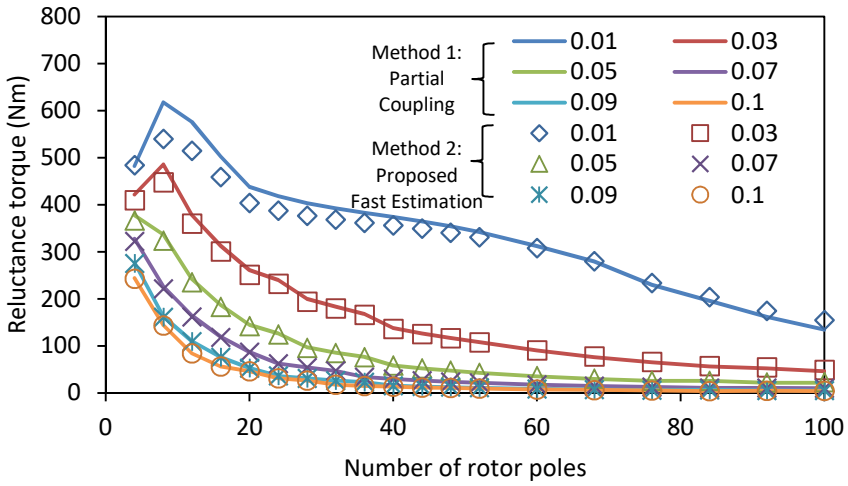

Fig. 2-11 Reluctance torque vs. slot/pole combinations (Ns=3p) and air gap length to 38.5mm ratio.

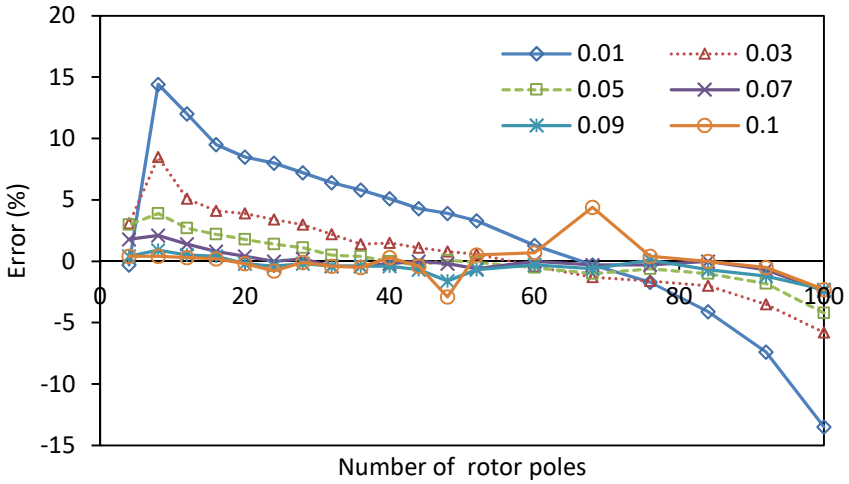

Fig. 2-12 Error in computing the reluctance torque contribution using method 2, referred to method 1 (scan 2-air gap length and number of rotor poles).

Fig. 2-11 can be rearranged into Fig. 2-13 to show the decrease of reluctance torque with the increase of pole number and the distribution of the turns of one phase into multiple coils. Furthermore, the machines with the largest air gap lengths experience the sharpest reduction of reluctance torque with the pole number.

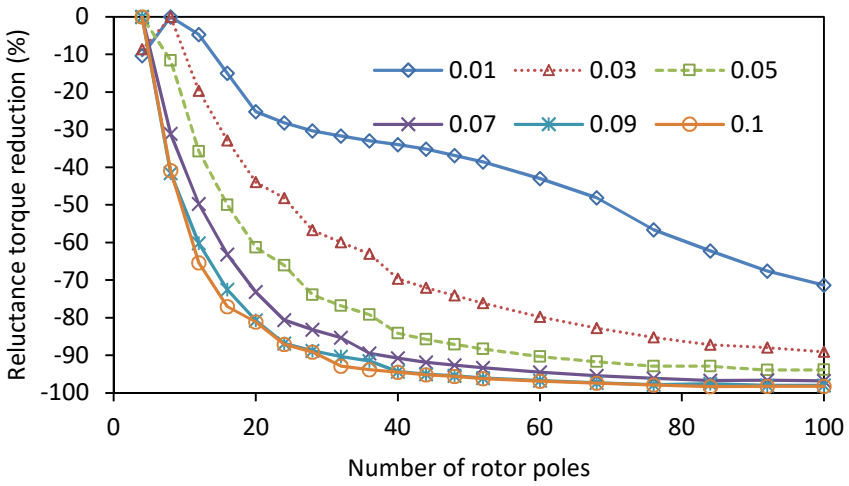

Fig. 2-13 Reduction of reluctance torque with number of rotor poles referred to machine with p=4 for different air gap lengths to 38.5mm ratios.

The nominal design has an air gap length of g=1.925mm which corresponds to an air gap length to pole pitch ratio of l_{gr}=0.05 when the generator has the nominal pole number p=28 and an air gap radius of R_g=0.1962m. If the air gap is a function of the

pole pitch, any adjustment in pole number will also affect the air gap length. Hence, the air gap length will be expressed as a ratio to a fixed pole pitch, that of the machine with the nominal pole number p=28.

In Fig. 2-14, the average reluctance torque monotonically decreases as the pole number is increased. Referring to the average reluctance torque at p=4, the average reluctance torque is reduced by 76.8% when the pole number is increased to the nominal p=28. In Fig. 2-14, the average reluctance torque decreases as the square of the number of turns per coil decreases. This decrease is faster than linear.

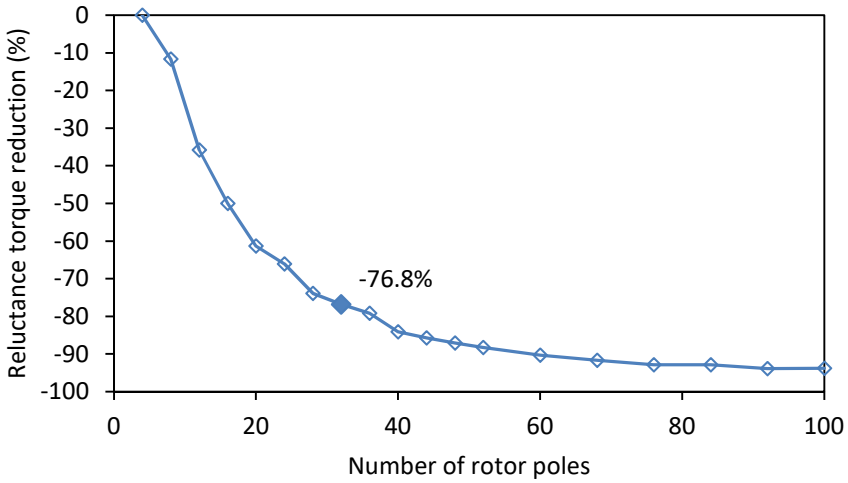

Fig. 2-14 Reduction of reluctance torque with number of rotor poles referred to machine with p=4 for nominal air gap length of 1.925mm (l_{gr}=0.05).

Fig. 2-15 and Fig. 2-16 portray the influence of the air gap length on the average reluctance torque of generators with different numbers of poles.

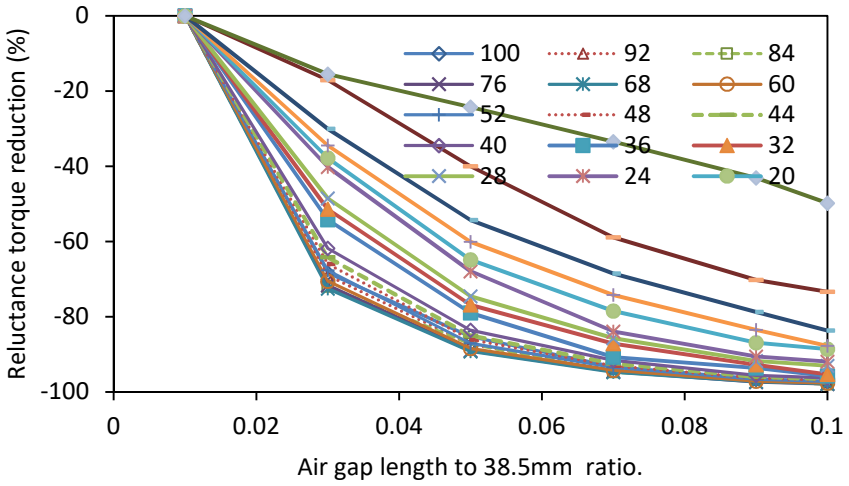

Fig. 2-15 Reduction of reluctance torque with air gap length referred to machine with minimum air gap length for different rotor poles.

The average reluctance torque has reduced by 76.9% from g=0.385mm at l_{gr}=0.01 to g=1.925mm at l_{gr}=0.05. It is purely coincidental that the reduction of the average reluctance torque with the pole number, p (Fig. 2-14), and the reduction with the air gap length, g (Fig. 2-16) have similar amplitudes.

If both the distribution of the winding into coils (inversely proportional to p) and the increase of d and q ax-s inductances due to the increase in air gap length are considered, the generator with l_{gr}=0.05 and p=28 (nominal 3kW design) will exhibit roughly 5% of the average reluctance torque of a generator with l_{gr}=0.01 and p=4. The rated current used for this study is 5 times larger than the rated current of the 3kW prototype.

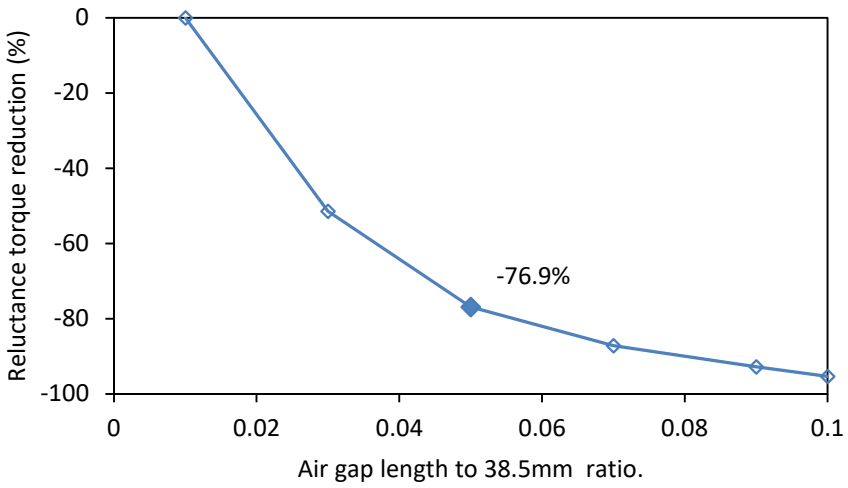

Fig. 2-16 Reduction of reluctance torque with air gap length referred to machine with minimum air gap length for nominal p=28.

2.3 Utility of reluctance torque in PM machine

The torque equation for a salient synchronous motor in the dq axis reference frame is:

$$T = \frac{m}{2} p[\Psi_{PMd} I_q - \Psi_{PMq} I_d - (L_d - L_q) I_d I_q + M_{dq} I_q^2 - M_{qd} I_d^2] \qquad (2.11)$$

where m is the number of phases, I_d, I_q, ψ_{PMd}, ψ_{PMq}, L_d, L_q, M_{dq}, M_{qd} are the d- and q-axis current amplitudes, the average PM flux linkages and the average self and mutual inductances. In salient machines the 1st and 3rd terms, i.e. the PM alignment and reluctance torque components, are the major contributors towards the average output torque. The average q-axis flux linkage due to the PM, ψ_{PMq}, is usually very low and assumed to be zero.

The PM alignment torque is proportional to the current amplitude while the reluctance torque capability is directly proportional to the square of the current. In the benchmark 3kW SPM machine, the PM alignment torque has the most contribution. It has a high magnetic loading and a low electrical excitation to minimize the copper losses and

maximize the annual energy gain. It has a ψ_{PMd}=1.13Wb, a rated current density of 1.9A/mm^2 and copper losses of around 100W (neglecting the end windings).

This electrical excitation is appropriate for producing 196 Nm PM torque. However, the reluctance torque capabilities for this current excitation, even with an IPM rotor are modest (Fig. 2-21, Fig. 2-25 and Fig. 2-26).

Most of the contribution towards the average torque in the non-salient machine equipped with an SPM rotor is given by:

$$T_{SPM} = \frac{m}{2} p \Psi_{SPM} I_q \tag{2.12}$$

while for the salient machines equipped with an IPM rotor, neglecting the mutual inductances and cross-coupling:

$$T_{IPM} = \frac{m}{2} p[\Psi_{IPM} I_q + (L_d - L_q) I_d I_q] \tag{2.13}$$

$$I_d = \sin(\beta)\, I_r \tag{2.14}$$

$$I_q = \cos(\beta)\, I_r \tag{2.15}$$

where

$$-\pi/2 < \beta < 0 \tag{2.16}$$

The IPM machines will exhibit a higher PM flux leakage and thus a lower flux linkage. Consequently, a leakage factor can be used to account for the difference in flux linkage:

$$\Psi_{IPM} = k_{leak} * \Psi_{SPM} \tag{2.17}$$

where $k_{leak.}$ is the ratio between the flux linkage of the IPM over that of the SPM.

$$\mathrm{k}_{leak} < 1 \tag{2.18}$$

For two machines with equal average output torque, equating (2.12) and (2.13):

$$T_{SPM(\beta=0)} = T_{IPM(\beta)} \tag{2.19}$$

$$\Psi_{SPM} I_r = k_{leak} \Psi_{SPM} I_q + \left(L_d - L_q\right) I_d I_q \tag{2.20}$$

$$\Psi_{SPM} I_r [1 - k_{leak} * \cos(\beta)] = \frac{1}{2}\left(L_d - L_q\right) I_r^2 \sin(2\beta) \tag{2.21}$$

$$L_d - L_q = \frac{2\Psi_{SPM}[1 - k_{leak} * \cos(\beta)]}{I_r \sin(2\beta)} \tag{2.22}$$

Equation (2.22) is an approximation of the difference in *d*- and *q*-axis inductances required for an IPM machine to exhibit the same average output torque as an SPM machine. This equation assumes there is no cross-coupling and that the mutual inductance has no influence on the average torque. In practice, these approximations lead to a difference between results obtained using (2.22) and finite element results. Moreover, the current-inductance characteristic is highly non-linear, further increasing the error in predicting the rated current at which the SPM and IPM machines exhibit equal average output torque.

The terms in (2.22) can be rearranged as in (2.23): the *dq* axis average inductances, the rated current and the d- axis PM flux linkage on one side and the leakage factor and current angle arguments on the other side.

- This ratio can be used to assess a PM machine average reluctance torque capabilities, referred to its average PM alignment torque.
- $R=R_{required}$ or (2.23) is the condition for equal average torque of the SPM and IPM machines.
- The value of fraction in (2.25) is only a function of k_{leak} and can be plotted for the flux weakening range $-90<\beta<0$ to determine its minimum value as in Fig. 2-18.

$$\frac{(L_d - L_q) I_r}{2\Psi_{SPM}} = \frac{1 - k_{leak} * \cos(\beta)}{\sin(2\beta)} \tag{2.23}$$

$$R = \frac{(L_d - L_q) I_r}{2\Psi_{SPM}} \tag{2.24}$$

$$R_{required} = \frac{1 - k_{leak} * cos(\beta)}{sin(2\beta)} \tag{2.25}$$

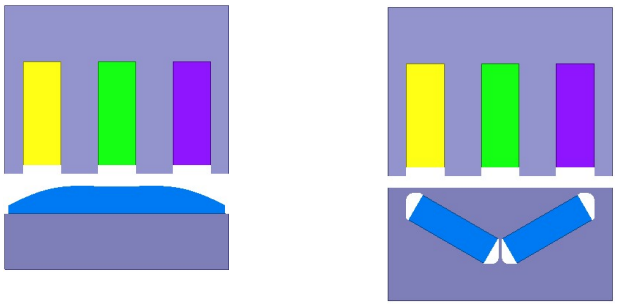

Fig. 2-17 Cross section of compared SPM and IPM machines with overlapping distributed winding and equal PM volume.

The $R_{required}$ from (2.25) is plotted in Fig. 2-18 for all values of β from -90 to 0 elec.deg. and for different leakage factors k_{leak}. There is a minimum value for $R_{required}$ for every value of k_{leak}, marked with a dot on the curves in Fig. 2-18. As k_{leak} increases, the minimum value of $R_{required}$ also increases and occurs at current angle closer to -45 elec.deg.

If R=R_{req_min}, the maximum average torque of the IPM machines will be equal to that of the SPM machine (k_{leak}=1). The average torque of the IPM machine as shown in (2.13) vs. current angle with different k_{leak} factors designed to satisfy (2.19) is plotted in Fig. 2-19.

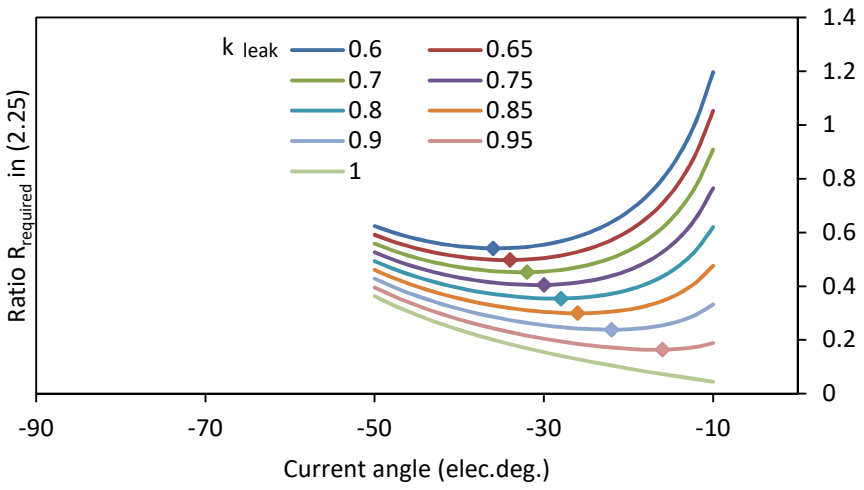

Fig. 2-18 Variation of ratio $R_{required}$ with current angle for different IPM leakage factors (k_{leak}).

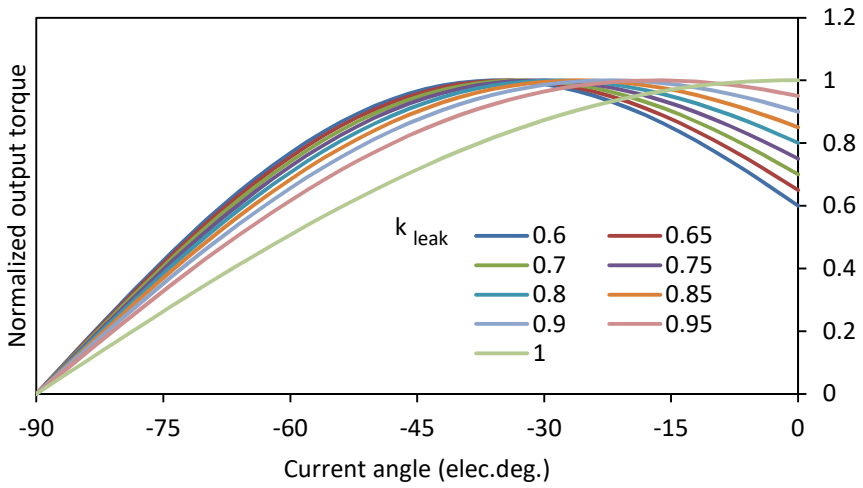

Fig. 2-19 Normalized output torque of IPM machines that have direct and quadrature inductance difference equal to minimum in Fig. 2-18 and different leakage factors compared to the equivalent SPM machine.

The ratio $R/R_{required}$ can be used to quantitatively assess the reluctance torque capabilities. In section 2.4, the influence of the air gap length is presented in different machines: the 3kW small size prototype frame and the optimized 3MW generator.

Equation (2.23) is the condition for the IPM machine to exhibit the same maximum average torque as its SPM counterpart, when the magnetic loading of the IPM is k_{leak} times that of the SPM. When $R/R_{required}<1$, the average torque of the IPM machine will be less than that of the SPM. For $R/R_{required}>1$ the IPM machine will exhibit a higher average torque. However, $R/R_{required}>1$ only occurs for short air gap lengths and low pole numbers in section 2.4.

2.4 Influence of air gap length and slot-pole combination on average reluctance torque

The following parametric scans present the influence of key parameters on a 3kW DD small size prototype generator with a low electrical excitation and on the 3MW DD generator with a typical electrical loading used in the wind power industry.

The air gap length in sections 2.4.1, 2.4.2 and 2.4.3 is expressed as a ratio of the pole pitch. This is the general approach for PM machine design. For a constant air gap to pole pitch ratio, the air gap length decreases as the number of rotor poles increases and the pole pitch decreases. However, in large diameter generators, the minimum air gap length is limited by the air gap diameter due to mechanical tolerances and should not be decreased for machines with a higher rotor pole number. Due to mechanical feasibility issues, for large diameter generators, the lower limit for the air gap length is 0.1% of the air gap diameter [4].

To isolate the effect of the reducing air gap L_d-L_q inductance difference and the varying air gap length when the number of rotor poles is increased and the air gap length to pole pitch ratio is fixed, an additional scan is carried out. In Section 2.4.4, the air gap length does not vary with the number of rotor poles as it is simply expressed as a length in millimeters. The fixed air gap lengths of the generators in Section 2.4.4 are between 0.03%and 0.3%of the air gap diameter, in steps of 0.03%.

The $R/R_{required}$ ratio of the machine with the stator of the 3kW SPM prototype or 3MW SPM generator and a V-shaped IPM rotor is presented at the beginning of each section in 2.4. This is only for a numerical reference as the ratio is expected to vary with the number of rotor poles and the air gap length.

2.4.1 Air gap/pole pitch ratio in 3kW prototype machine at rated load

For a machine with the stator of the 3kW prototype SPM machine, with p=28 and l_{gr}=0.05 and a V-shaped NdFeB IPM rotor, $R/R_{required}$ =0.093<<1. The reluctance torque

capability of this machine is expected to be negligible at this number of rotor poles and air gap length.

When the air gap length is expressed as a ratio of pole pitch, the air gap length effectively decreases when the number of rotor poles is increased for a constant air gap to pole pitch ratio. Generally, the flux leakage in both stator and rotor increases as the numbers of slots and poles increase. However, decreasing the air gap length when the pole number is increased effectively reduces the rotor flux leakage.

Fig. 2-20 shows the influence of air gap length to pole pitch ratio and pole number on the average torque of the SPM generator. The optimum pole number for maximum average torque occurs at a large pole number, and increases as the air gap to pole pitch ratio is reduced. The optimum number of rotor poles is between p=52 for l_{gr}=0.01 to p=96 for l_{gr}=0.1.

The variation of the average torque of an IPM machine with the air gap to pole pitch ratio and the number of rotor poles is presented in Fig. 2-21. The IPM generators have the same air gap diameters and total PM volume, as well as electrical loading as the SPM generator in Fig. 2-20. The optimum number of rotor poles for the IPM machines is between p=24 for l_{gr}=0.01 to p=52 for l_{gr}=0.1. This is lower compared to the SPM machines due to the increased PM flux leakage in the IPM machines caused by the buried rotor topology as at this low $R/R_{required}$ ratio, the reluctance torque contribution is negligible.

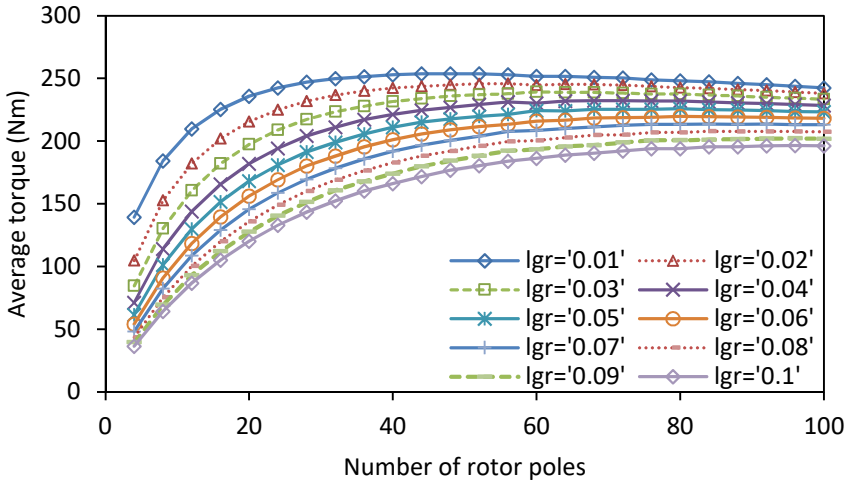

Fig. 2-20 Average torque of SPM machines with different pole number and air gap to pole pitch ratios.

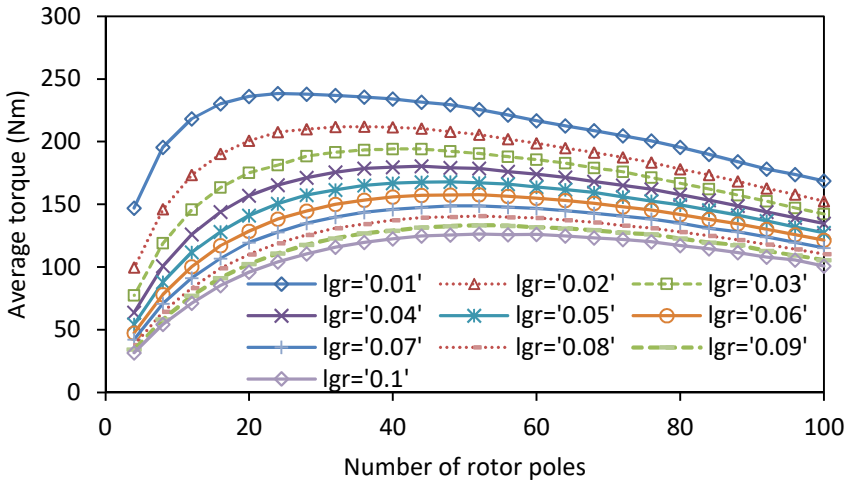

Fig. 2-21 Average torque of IPM machines with different pole number and air gap to pole pitch ratios.

These are linear models for PM machines with high numbers of slots and poles and that are located around the edges of the design space where the diameter is >90% of the outer diameter. As these machines are hollow, only the regions between the stator and the rotor back irons (including the back irons) are considered for the active volume of the machine.

The average torque per volume monotonically increases with the pole number in the SPM machine (Fig. 2-23). This is because the required back irons reduce as the slot/pole

combination increases. However, the torque/active volume increase is small for high number of rotor poles and, in practice, the manufacturing cost will limit the maximum number of rotor poles of a high pole number direct drive SPM machine.

In contrast to the SPM machines, the average torque per volume in the IPM machine still have an optimum well within the scanned rotor pole range, around p=60 (Fig. 2-24). This is due to the higher flux leakage in the IPM machine; the expected torque reduction is more severe in the IPM at high pole number. The optimum rotor pole numbers for maximum torque/volume can be explained using the average torque characteristic, as the active volume vs number of rotor pole characteristic is similar regardless of the rotor typology. The SPM machine with peak average torque between p=52 for l_{gr}=0.01 and p=96 for l_{gr}=0.1 yields the maximum torque per volume for p>100. The IPM machine with the peak average torque between p=24 for l_{gr}=0.01 and p=52 for l_{gr}=0.1 yields a maximum torque/volume for a rotor pole number between p=60 and p=76 as in Fig. 2-22. As the back irons reduce with the increase of p, the highest torque/volume characteristic will be at a number of rotor poles higher than the optimum p for maximum average torque.

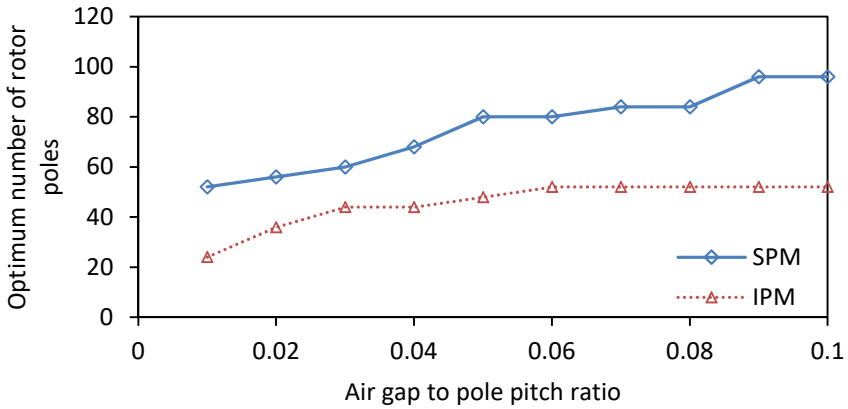

Fig. 2-22 Optimum pole number vs. air gap to pole pitch ratio for NdFeB SPM and IPM machines.

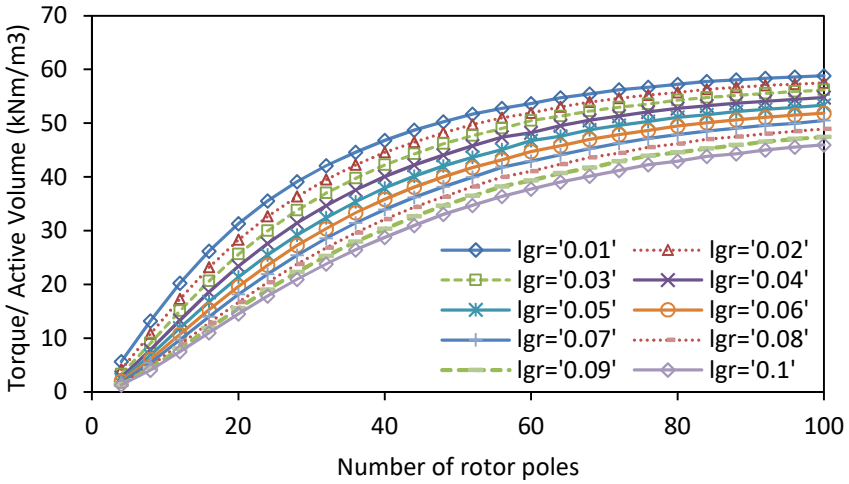

Fig. 2-23 Average torque per volume of SPM motors with different pole number and air gap to pole pitch ratios.

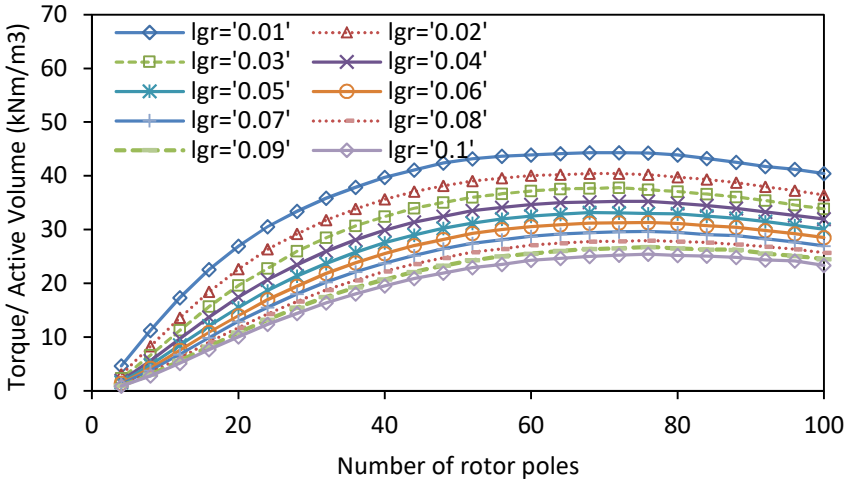

Fig. 2-24 Average torque per volume of IPM motors with different pole number and air gap to pole pitch ratios.

At the low current excitation of the 3kW prototype, the PM torque in Fig. 2-25 makes up for most of the total torque in Fig. 2-20. The maximum reluctance torque contribution, for the shortest air gap in Fig. 2-26, is roughly 10% of the total torque in Fig. 2-20. For the nominal air gap of the 3kW prototype the reluctance torque contribution is less than 3% of the total average torque.

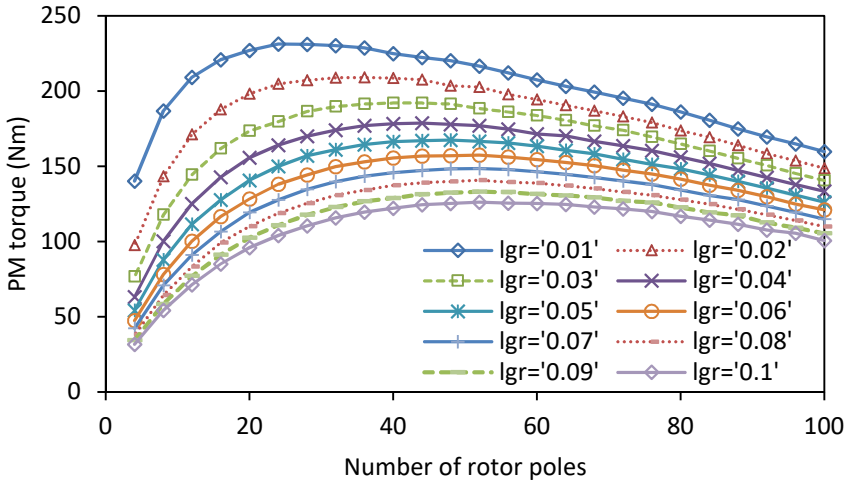

Fig. 2-25 Average permanent magnet torque of IPM motors at MTPA with different pole number and air gap to pole pitch ratios.

If the generators have a fixed number of turns per phase, N_{ph}, the number of turns per coil is equal to N_{ph}/p while the inductance is proportional to $p\cdot(N_{ph}/p)^2=N_{ph}^2/p$. When the air gap length, g, is expressed as a ratio of the pole pitch and this ratio is fixed, it is inversely proportional to the number of rotor poles, $g \propto 1/p$. Consequently, as the number of rotor poles is increased, the stator MMF decreases and the air gap length also decreases. The overall effect is that the reluctance torque component shows a flat behavior versus pole number, as shown in Fig. 2-26. However, this is just a coincidence due to the fact that the stator MMF is decreasing and the air gap length is also reducing for the same air gap to pole pitch ratio. Section 2.4.4 refers to the case where the air gap length does not vary with the number of rotor poles, and the influence of the number of rotor poles on the average reluctance torque is thus isolated from the effect of the varying air gap length.

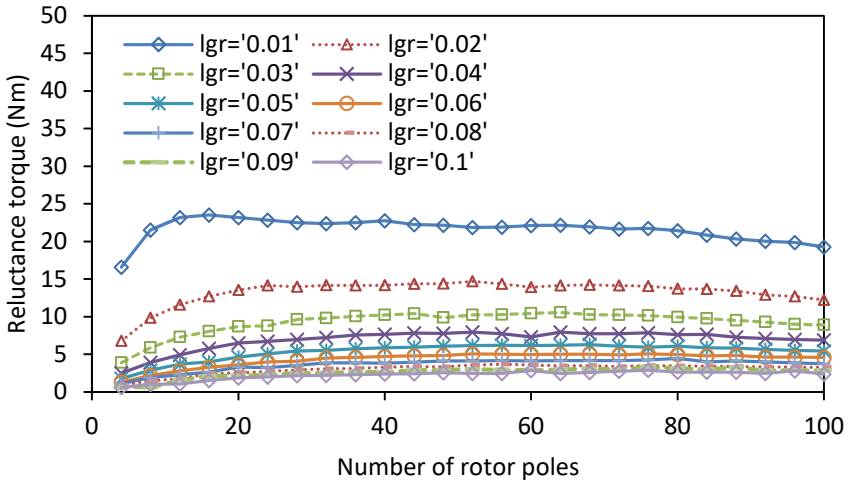

Fig. 2-26 Average reluctance torque of IPM machines at MTPA with different pole number and air gap to pole pitch ratios.

Fig. 2-27 to Fig. 2-29 portray the influence of changing the air gap length to pole pitch ratio on the PM and reluctance torque components of IPM machines with different number of rotor poles (p=16, p=52 and p=80).

For the rated current excitation, the contribution of the reluctance torque is limited at less than 10% of the total torque when the air gap is only 1% of the pole pitch (Fig. 2-27c). Even though the contribution of the reluctance torque is modest, increasing the air gap length to pole pitch ratio reduces the reluctance torque capabilities at a rate faster than a linear decrease. In fact, at 5% air gap length to pole pitch ratio the average reluctance torque has reduced to roughly 17% of the average reluctance torque of the IPM machine with 1% air gap length to pole pitch ratio. This trend is consistent regardless of the pole number and can be seen in Fig. 2-27b to Fig. 2-29b.

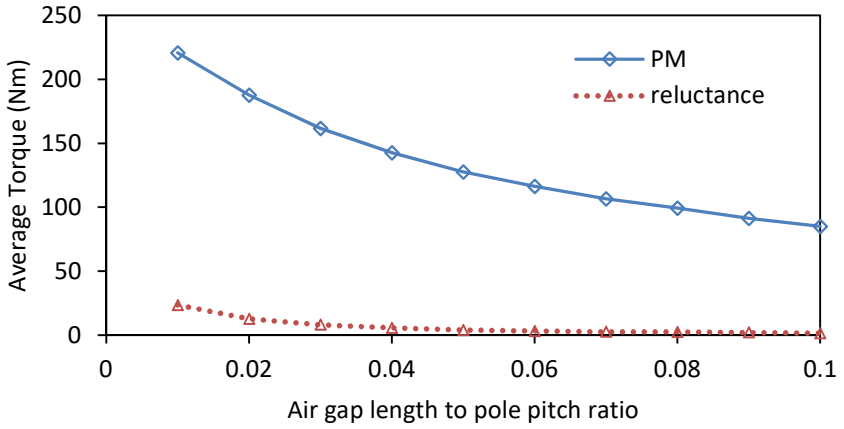

(a)

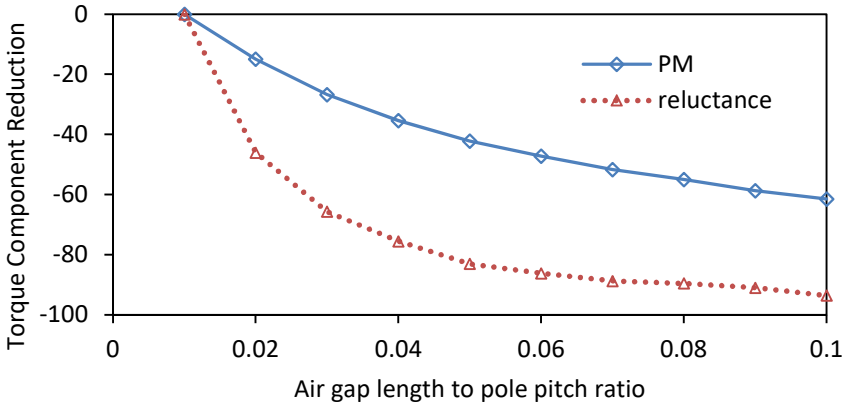

(b)

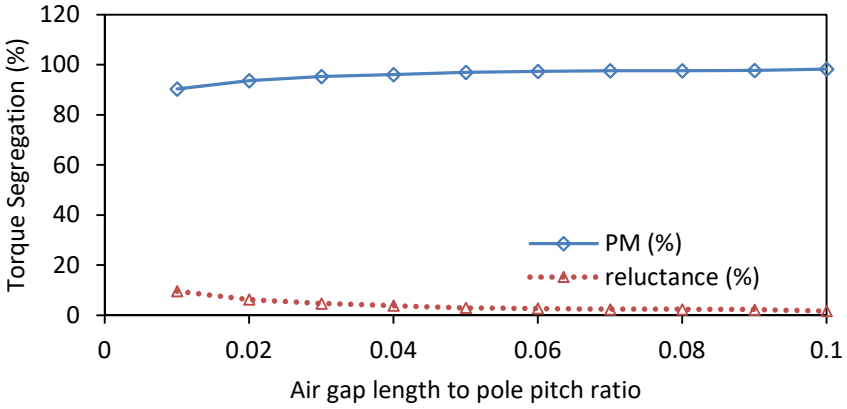

(c)

Fig. 2-27 Torque segregation IPM machines with *p*=16 at different air gap to pole pitch ratios. (a) PM and reluctance torque (b) PM and reluctance torque reduction with air gap length increase and (c) average torque composition.

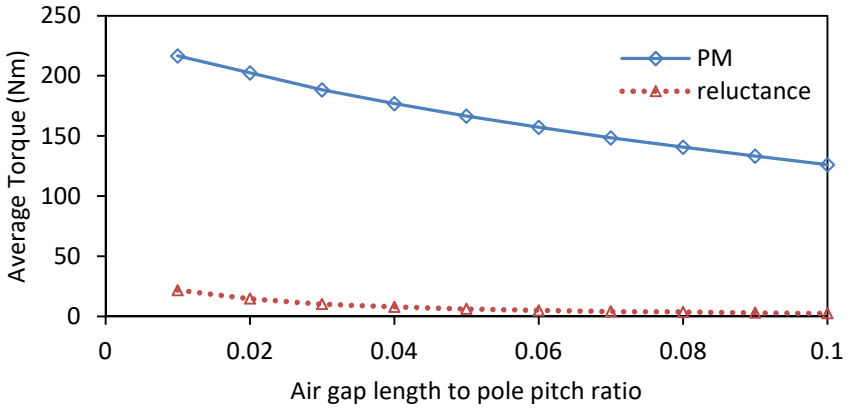

(a)

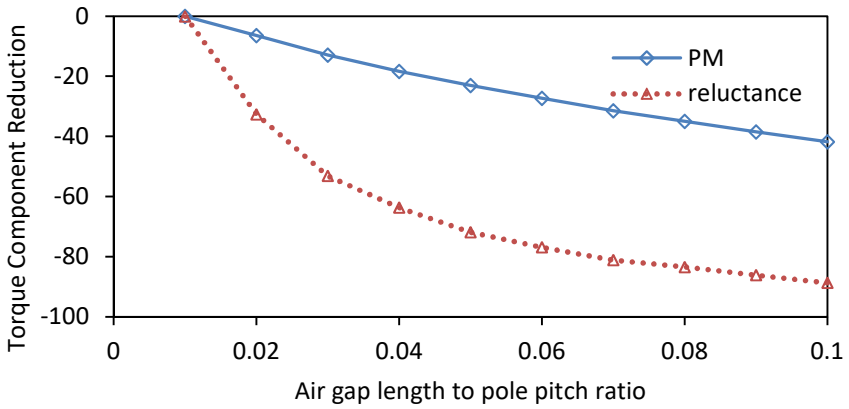

(b)

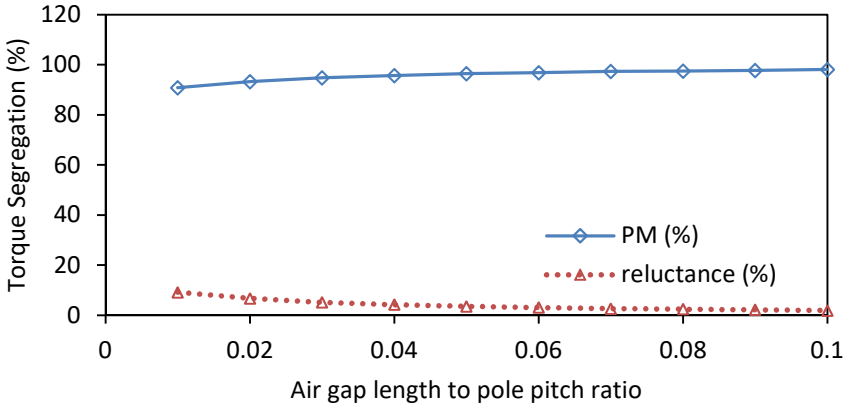

(c)

Fig. 2-28 Torque segregation IPM machines with *p*=52 at different air gap to pole pitch ratios. (a) PM and reluctance torque (b) PM and reluctance torque reduction with air gap length increase and (c) average torque composition.

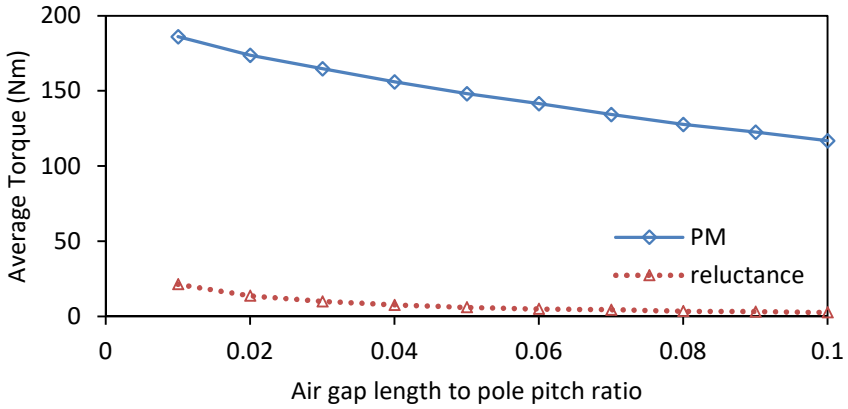

(a)

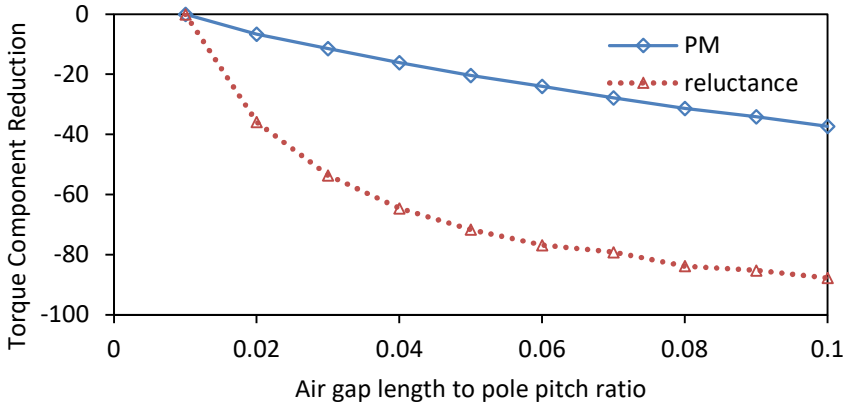

(b)

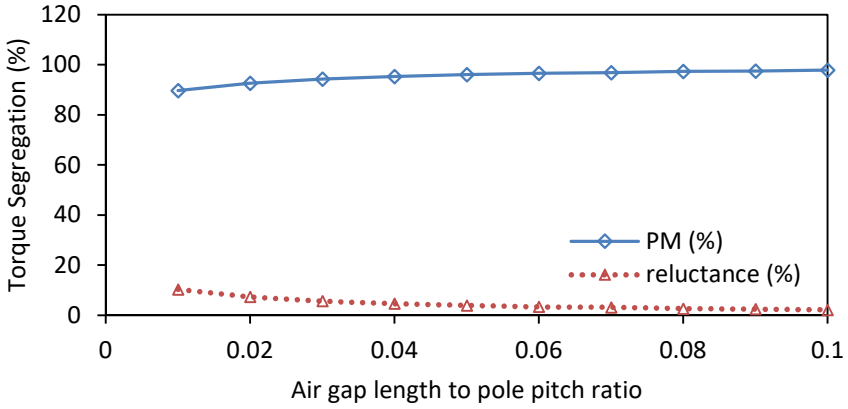

(c)

Fig. 2-29 Torque segregation IPM machines with *p*=80 at different air gap to pole pitch ratios. (a) PM and reluctance torque (b) PM and reluctance torque reduction with air gap length increase and (c) average torque composition.

2.4.2 Air gap/pole pitch ratio in 3kW prototype machine at 10x rated load

For a machine with the stator of the 3kw prototype SPM machine with 10x the rated load, p=28, l_{gr}=0.05 and a V-shaped NdFeB IPM rotor, $R/R_{required}$ =0.93. Hence, the IPM machine will exhibit less average torque for p=28, l_{gr}=0.05, but can also exhibit higher torque when the number of rotor poles is decreased or the air gap length to pole pitch ratio is reduced as shown in Fig. 2-30 and Fig. 2-31. The decrease of p and of l_{gr} yields an increase of $R/R_{required}$.

From a thermal management point of view, this scenario is not feasible as the copper losses would be 100 times higher. However, this scenario is used to investigate the influence of the air gap length and number of rotor poles at a higher current excitation, where $R/R_{required} \approx 1$. As the average PM torque is proportional to the current while the reluctance torque is proportional to the current squared, when a current excitation 10 times the rated one is used, the reluctance torque contribution of the IPM drive is enhanced more than the PM torque contribution. With these higher excitations, besides the amplitude which is roughly ten times higher, the shapes of the average torque vs. pole number curves for the SPM in Fig. 2-20 and Fig. 2-30 and for the IPM in Fig. 2-21 and Fig. 2-31 look similar. Again, the optimum pole number for the SPM machines is higher than that of the IPM machines (Fig. 2-32). Furthermore, the average torque is more sensitive to the air gap to pole pitch ratio in the IPM machine due to the presence of the reluctance torque.

The maximum average torque of the IPM machine (Fig. 2-31) is higher than that of the SPM machine (Fig. 2-30) when the number of rotor poles is low (i.e. p=24).

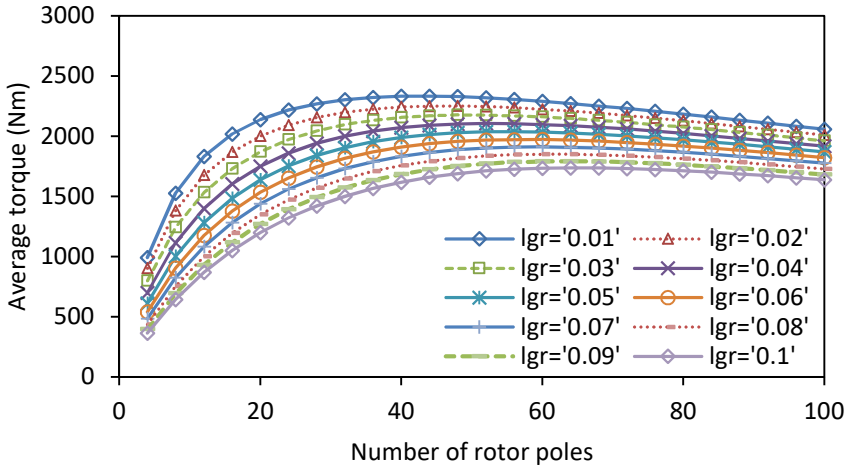

Fig. 2-30 Average torque of SPM machines with different pole number and air gap to pole pitch ratios (10 times of rated current excitation).

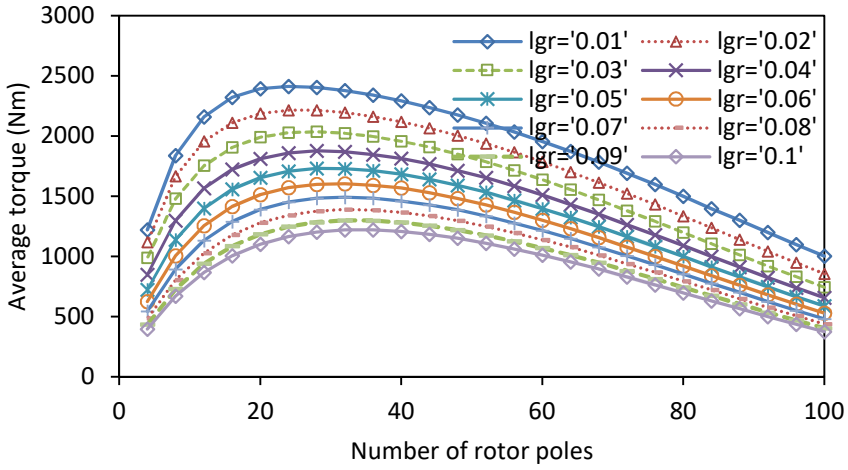

Fig. 2-31 Average torque of IPM machines with different pole number and air gap to pole pitch ratios (10 times of rated current excitation).

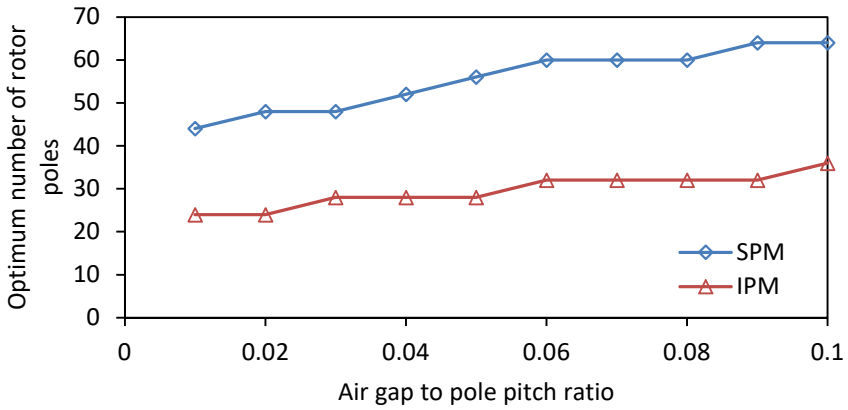

Fig. 2-32 Optimum pole number vs. air gap to pole pitch ratio for NdFeB SPM and IPM machines.

In terms of torque per volume, the IPM machine was found to always exhibit a poorer performance when compared to the SPM machine (Fig. 2-33, Fig. 2-34).

The maximum torque per volume is roughly 20% higher for the SPM machines. Furthermore, optimum pole numbers are significantly different for SPM and IPM machines. While for the IPM machines there clearly is a global optimum around 40<p<60, the optimum for the SPM machines occurs at a significantly higher pole number 80<p<100.

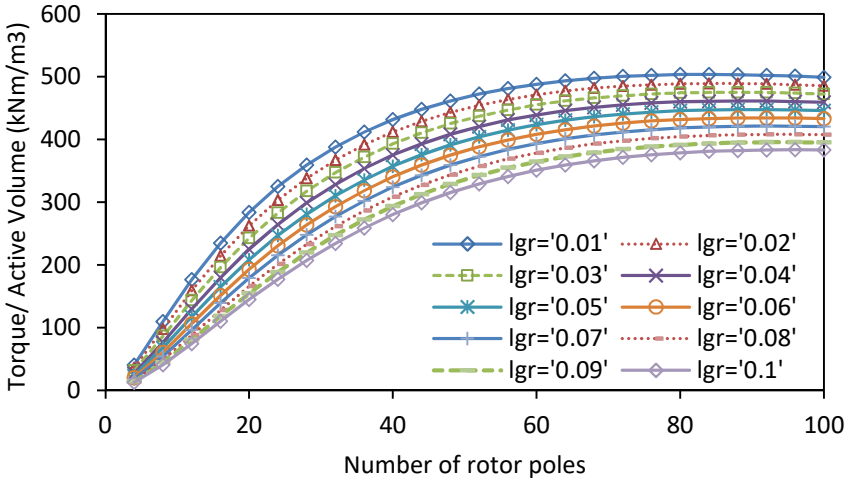

Fig. 2-33 Average torque per volume of SPM machines with different pole number and air gap to pole pitch ratios (10 times of rated current excitation).

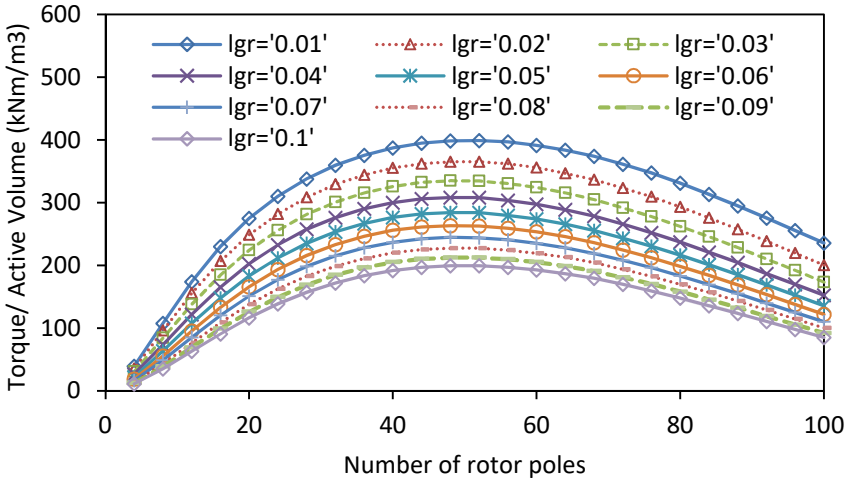

Fig. 2-34 Average torque per volume of IPM machines with different pole number and air gap to pole pitch ratios (10 times of rated current excitation).

The maximum average PM and reluctance torque capabilities are of similar amplitude as shown in Fig. 2-35 and Fig. 2-36. The PM torque increases linearly with the current excitation amplitude. The average PM torque of the PM machines have increased 10 times from Fig. 2-20 to Fig. 2-30 and Fig. 2-25 to Fig. 2-35. As the average reluctance torque is proportional to the square of current amplitude, the increase from Fig. 2-26 to Fig. 2-36 is 100 times for l_{gr}=0.05 and 60 times for the saturated l_{gr}=0.01.

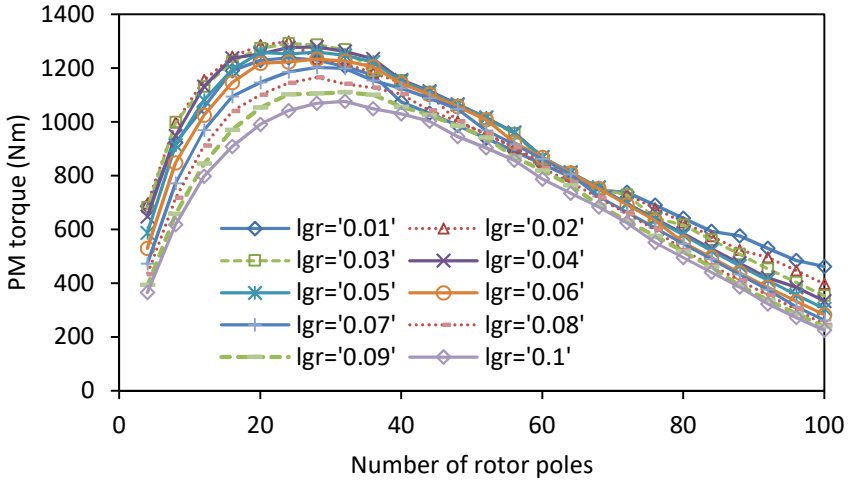

Fig. 2-35 Average permanent magnet torque of IPM motors at MTPA with different pole number and air gap to pole pitch ratios (10 times of rated current excitation).

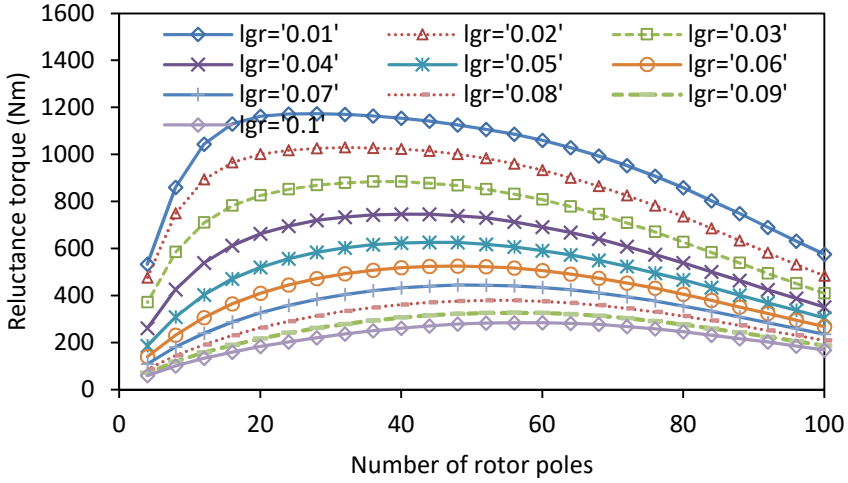

Fig. 2-36 Average reluctance torque of IPM machines at MTPA with different pole number and air gap to pole pitch ratios (10 times of rated current excitation).

The air gap is expressed as a ratio to the pole pitch so the air gap length decreases as the rotor pole number increases. On the other hand, the inductance of the IPM machine also

decreases with the number of rotor poles and consequently the reluctance torque exhibits the behavior versus the number of rotor poles as shown in Fig. 2-36.

For 10 times the rated current excitation, the average PM and reluctance torques have similar values for a 1% air gap to pole pitch ratio. As the air gap to pole pitch ratio is increased to 2-3%, the contribution of the PM torque slightly increases (Fig. 2-37a). This is due to the rapid decrease in inductance which causes a change in MTPA current angle.

The amplitude of the average reluctance torque decreases by 40-65% for different pole numbers as the air gap to pole pitch ratio is increased from 1 to 5%.

In Fig. 2-37 to Fig. 2-39, the average, normalized average and percentage average PM and reluctance torque are segregated for different pole numbers. The average reluctance torque decreases due to an increase in air gap length to pole pitch ratio from l_{gr}=0.01 to l_{gr}=0.05 was found to be 58%, 45% and 44%.

However, the average PM torque will suffer from a maximum of 10% reduction in average torque when l_{gr} is increased from l_{gr}=0.01 to l_{gr}=0.05 for a high pole number generator (Fig. 2-39b). For small pole numbers (Fig. 2-37, Fig. 2-38) due to the aforementioned abrupt decrease in reluctance torque with the increase of l_{gr}, the MTPA current angle also gets closer to 0, effectively increasing the average PM torque. This explains why the average PM torque slightly increases and then decreases when moving from l_{gr}=0.01 to l_{gr}=0.05.

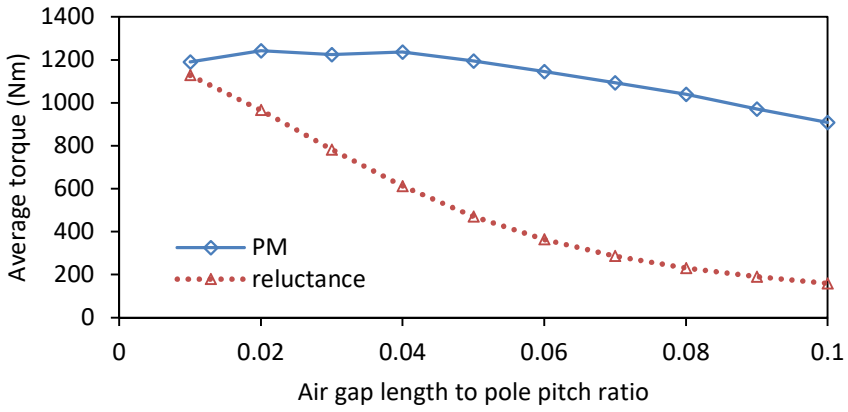

(a)

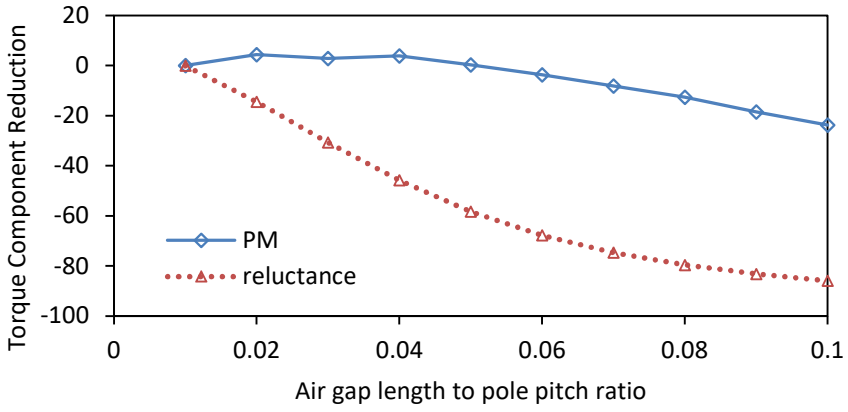

(b)

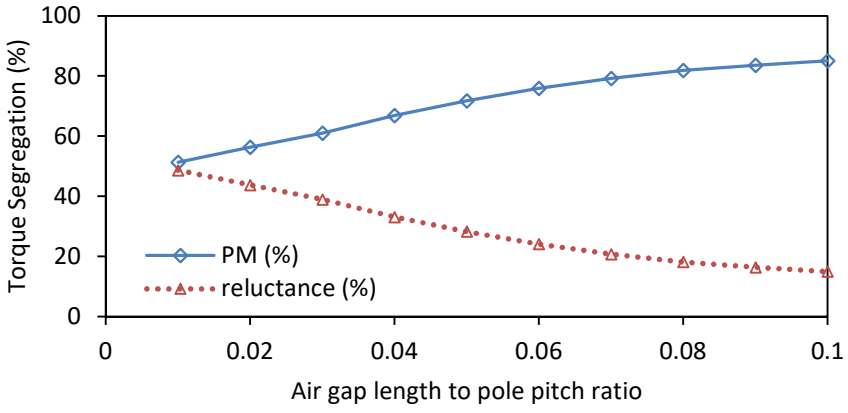

(c)

Fig. 2-37 Torque segregation IPM machines with p=16 at different air gap to pole pitch ratios. (a) PM and reluctance torque (b) PM and reluctance torque reduction with air gap length increase and (c) average torque composition (10 times of rated current excitation).

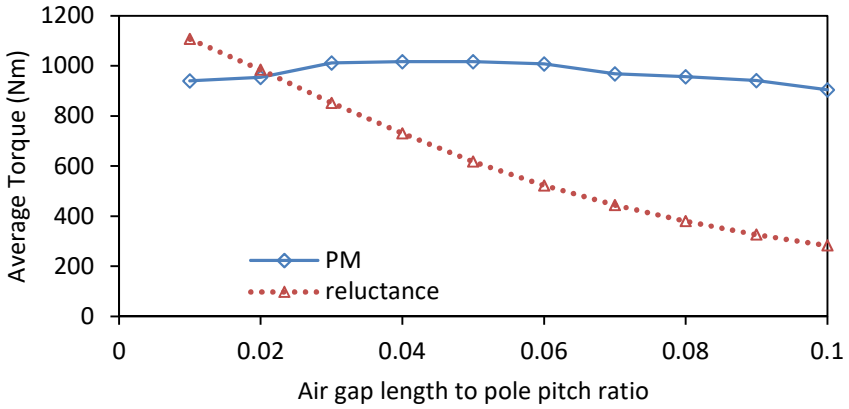

(a)

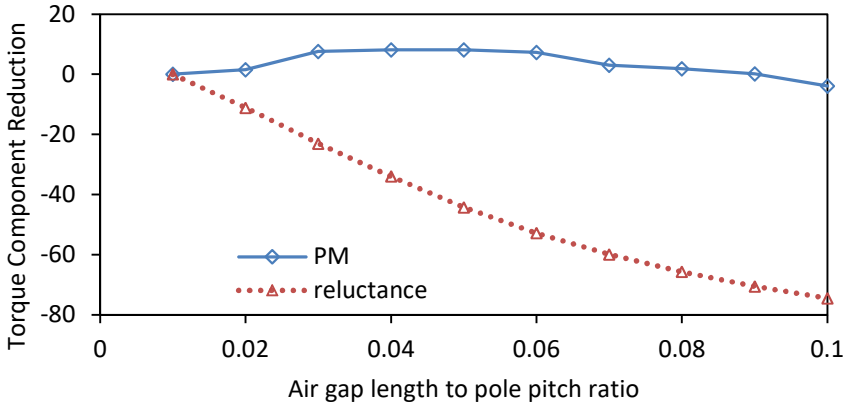

(b)

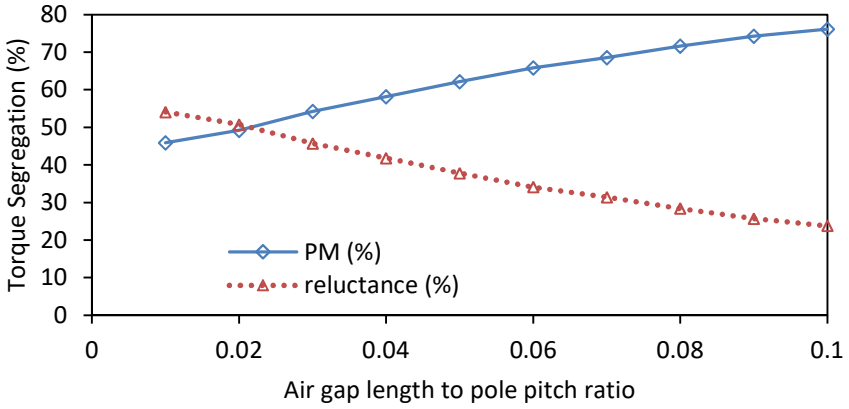

(c)

Fig. 2-38 Torque segregation IPM machines with *p*=52 at different air gap to pole pitch ratios. (a) PM and reluctance torque (b) PM and reluctance torque reduction with air gap length increase and (c) average torque composition (10 times of rated current excitation).

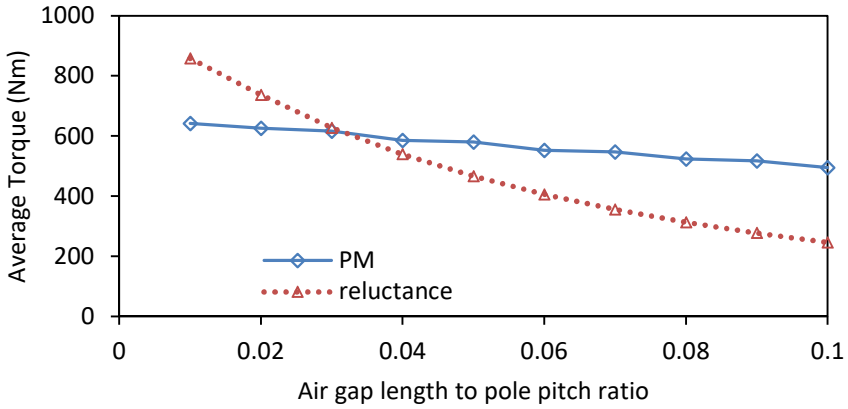

(a)

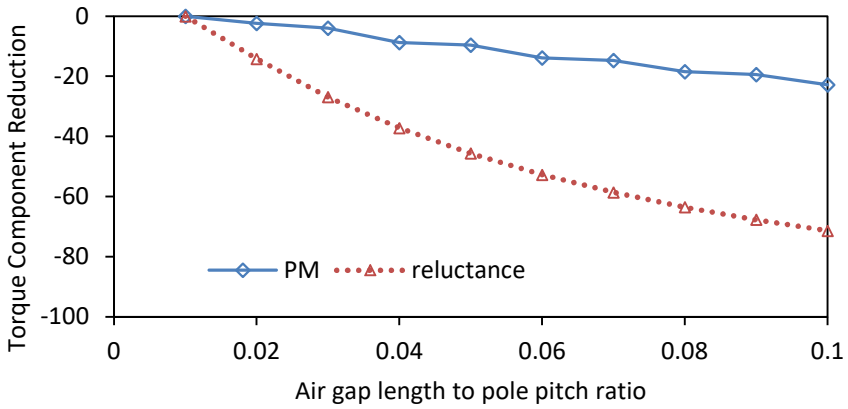

(b)

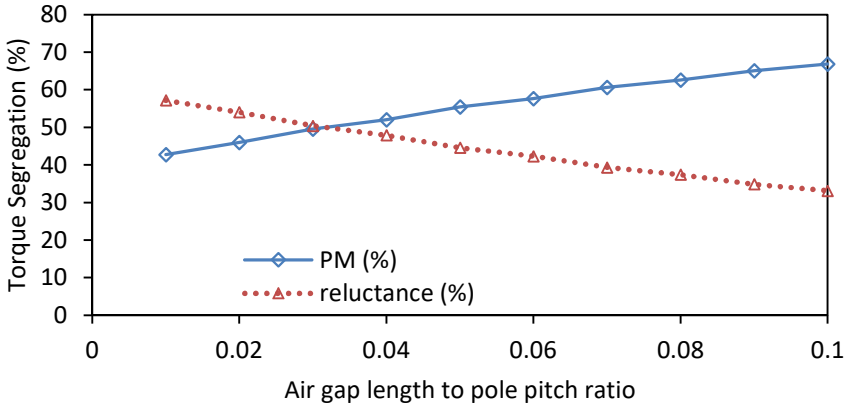

(c)

Fig. 2-39 Torque segregation IPM machines with *p*=80 at different air gap to pole pitch ratios. (a) PM and reluctance torque (b) PM and reluctance torque reduction with air gap length increase and (c) average torque composition (10 times of rated current excitation).

2.4.3 Air gap/pole pitch ratio in 3MW generator at rated load

For a machine with the stator of the 3MW SPM generator at rated load with p=108, l_{gr}=0.05 and a V-shaped NdFeB IPM rotor, $R/R_{required}$ =0.61 For a sub unitary value, the average torque of the IPM will be lower than that of the SPM machine, but it can increase over 1 for fewer rotor poles or a shorter air gap length.

Fig. 2-40 shows the average torque of the 3MW SPM machine at different pole numbers and different air gap lengths. The optimum number of rotor poles is between p=104 for l_{gr}=0.01 and p=168 for l_{gr}=0.1. In Fig. 2-41, the average torque of the IPM machine with the number of rotor poles and air gap length is presented. The optimum pole number varies from p=72 at l_{gr}=0.01 to p=132 at l_{gr}=0.1. The average torque of the IPM machine is more sensitive to the air gap length compared to the SPM generator, as shown in Fig. 2-40. The optimum number of rotor poles vs, the air gap length in Fig. 2-42 shows the lower optimum value for the IPM machines.

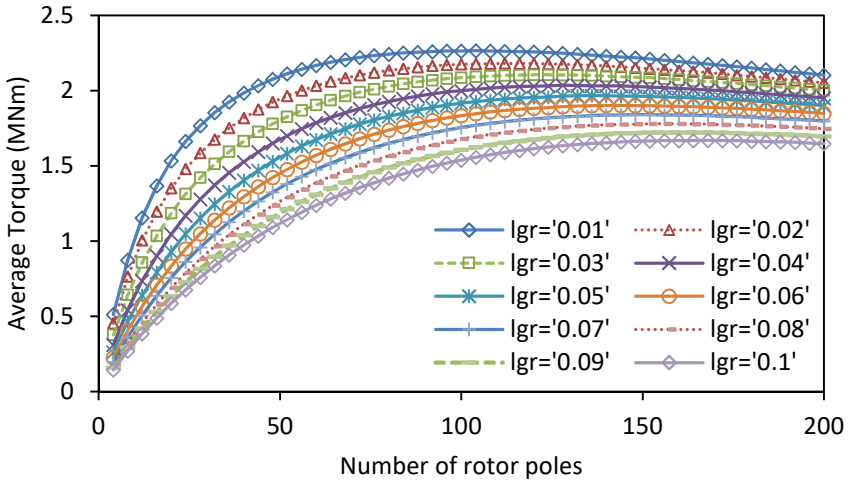

Fig. 2-40 Average torque of SPM machines with different pole number and air gap to pole pitch ratios.

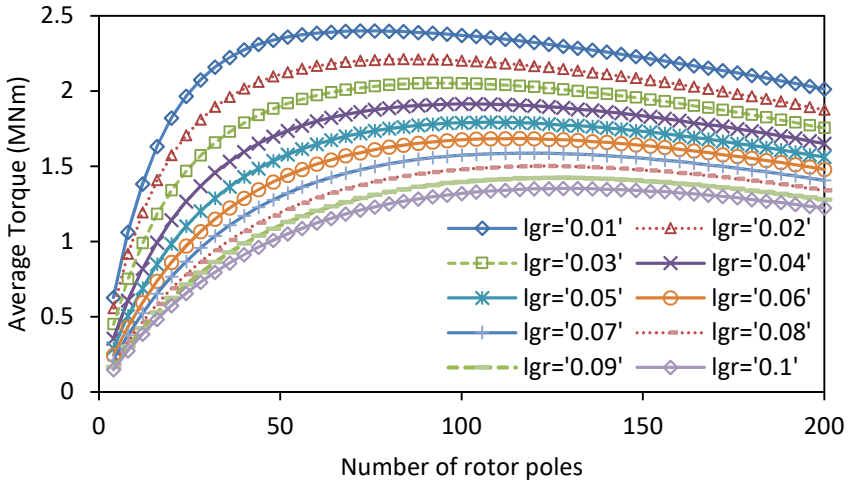

Fig. 2-41 Average torque of IPM motors with different pole number and air gap to pole pitch ratios.

In terms of torque/active machine volume, the SPM will always have a better performance as shown in Fig. 2-43 and Fig. 2-44. For a short air gap length i.e. l_{gr}=0.01 the torque/active volume of the IPM machine can get close to that of the SPM machine. However, as l_{gr} is increased, the difference between the torque/active volume of SPM an IPM machines increases.

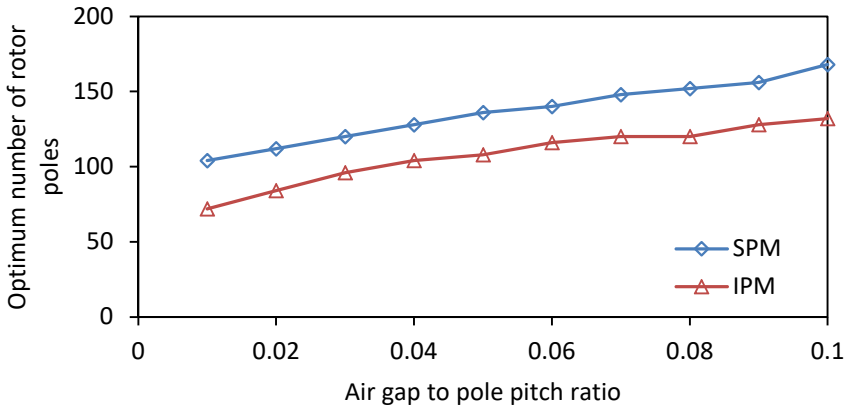

Fig. 2-42 Optimum pole number vs. air gap to pole pitch ratio for NdFeB SPM and IPM machines.

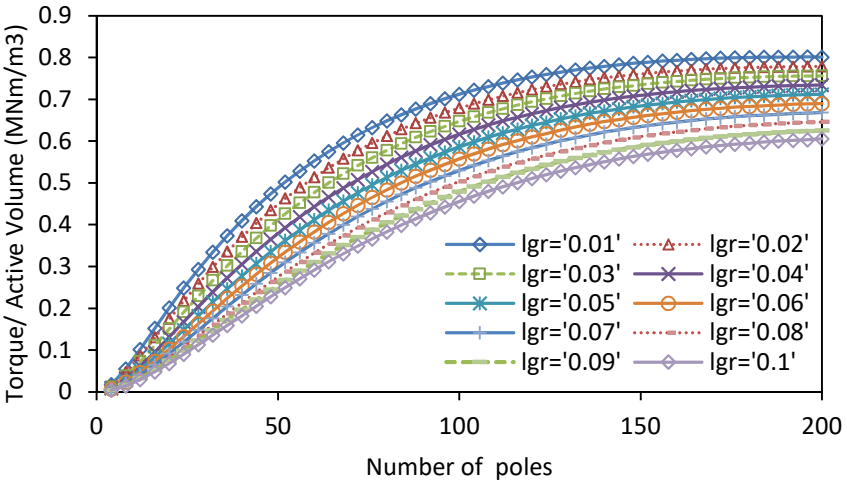

Fig. 2-43 Average torque per volume of SPM machines with different pole number and air gap to pole pitch ratios.

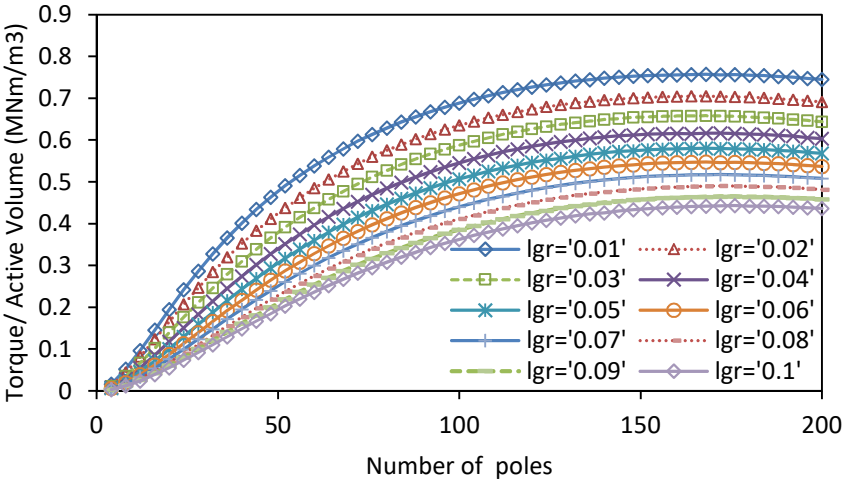

Fig. 2-44 Average torque per volume of IPM machines with different pole number and air gap to pole pitch ratios.

In Fig. 2-45, the average PM torque of the IPM generator was plotted versus the number of rotor poles for different air gap lengths. When moving from l_{gr}=0.01 to l_{gr}=0.04 the average PM torque has similar values. This is caused by the abrupt decrease of the reluctance torque when the air gap is increased and the consequent reduction of the current angle.

As the air gap length is expressed as a ratio to the pole pitch and this ratio is fixed, increasing the number of rotor poles also decreases the air gap length. The reluctance torque contribution will increase as the air gap length is decreased. When the air gap to

pole pitch ratio is used, as explained in the previous section, the average reluctance torque versus the number of rotor poles characteristic curves in Fig. 2-46 show almost flat regions. However, this is due to the air gap length reducing for a higher number of rotor poles and the same air gap to pole pitch ratio.

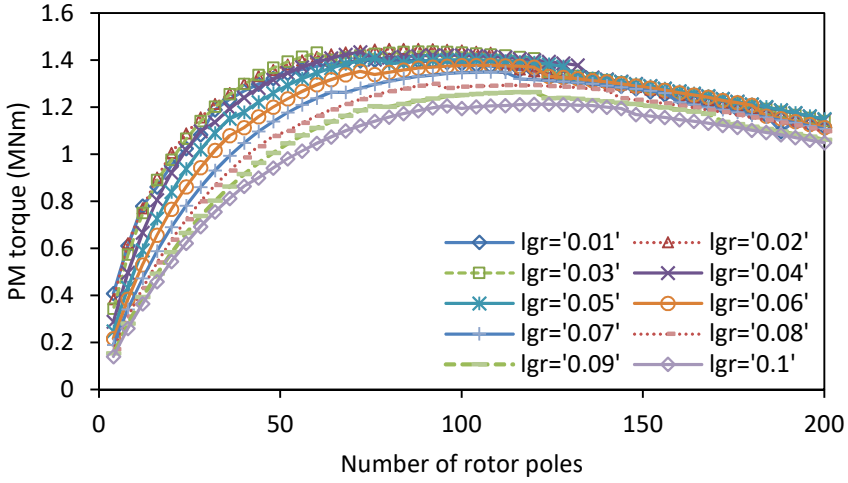

Fig. 2-45 Average permanent magnet torque of IPM machines at MTPA with different pole number and air gap to pole pitch ratios.

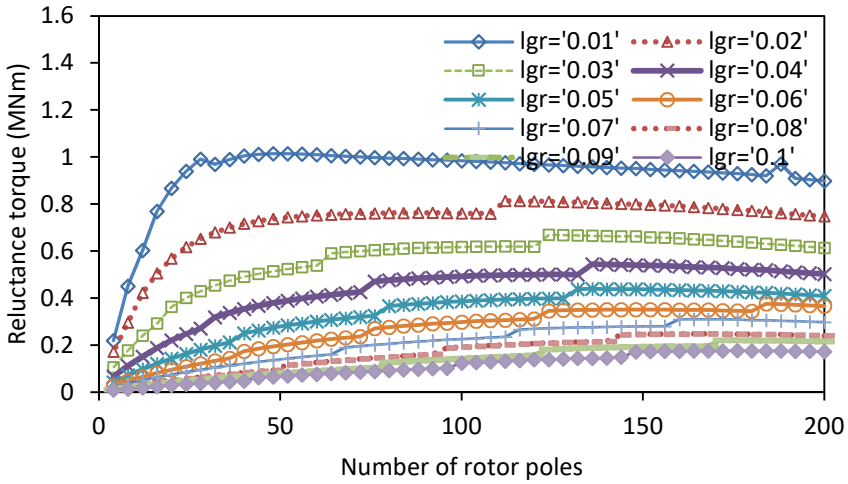

Fig. 2-46 Average reluctance torque of IPM machines at MTPA with different pole number and air gap to pole pitch ratios.

In Fig. 2-47 to Fig. 2-49 the average reluctance torque contribution decreases by 84%, 72% and 60% for p=16, p=52, and p=80 respectively. The abrupt decrease of the average reluctance torque contribution causes the MTPA current angle to move closer to

zero, and consequently, the contribution of the average PM torque can increase from l_{gr}=0.01 to roughly l_{gr}=0.03.

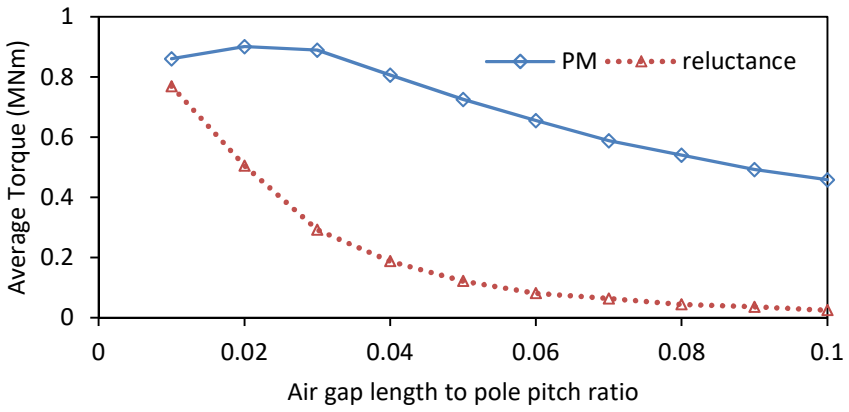

(a)

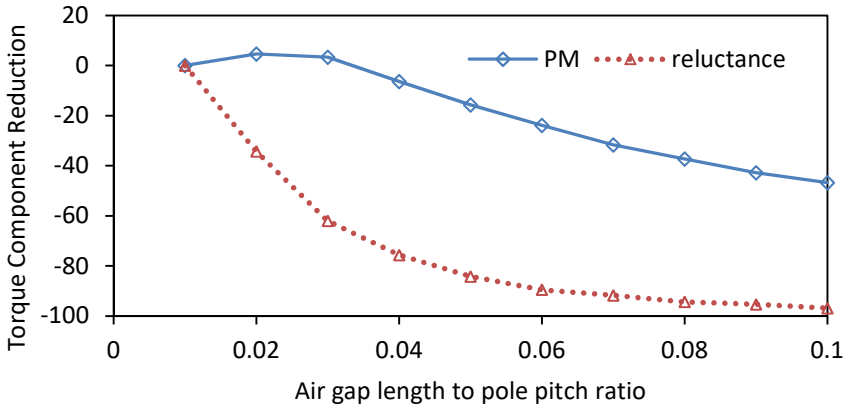

(b)

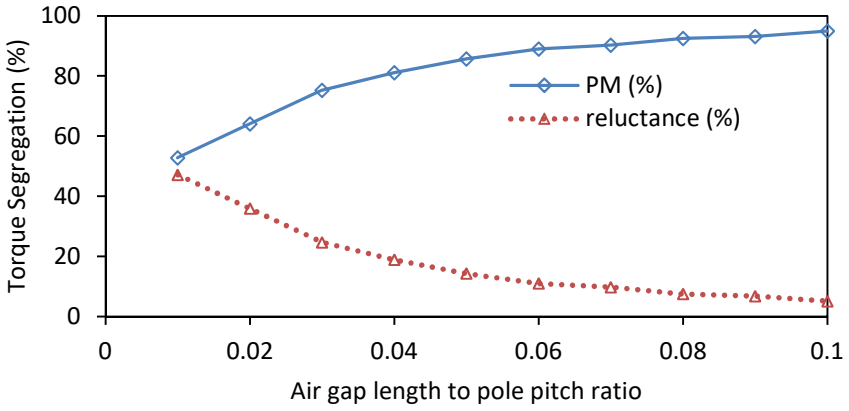

(c)

Fig. 2-47 Torque segregation IPM machines with p=16 at different air gap to pole pitch ratios. (a) PM and reluctance torque (b) PM and reluctance torque reduction with air gap length increase and (c) average torque composition.

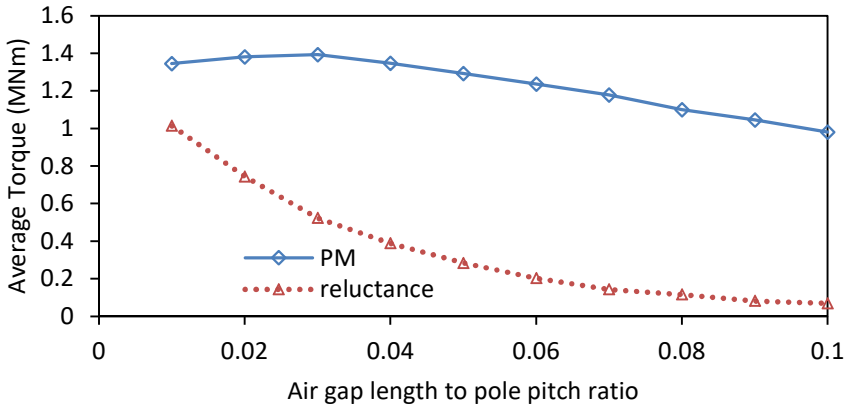

(a)

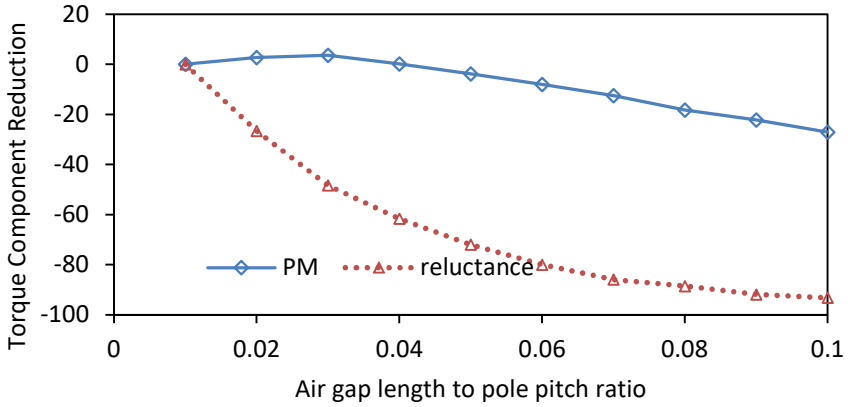

(b)

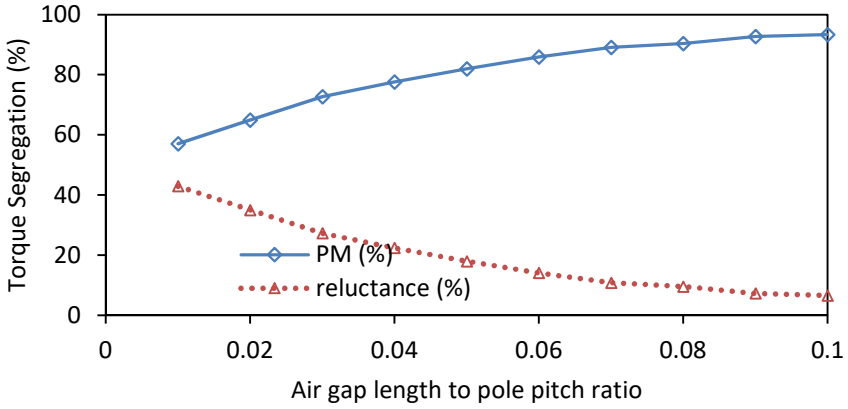

(c)

Fig. 2-48 Torque segregation IPM machines with p=52 at different air gap to pole pitch ratios. (a) PM and reluctance torque (b) PM and reluctance torque reduction with air gap length increase and (c) average torque composition.

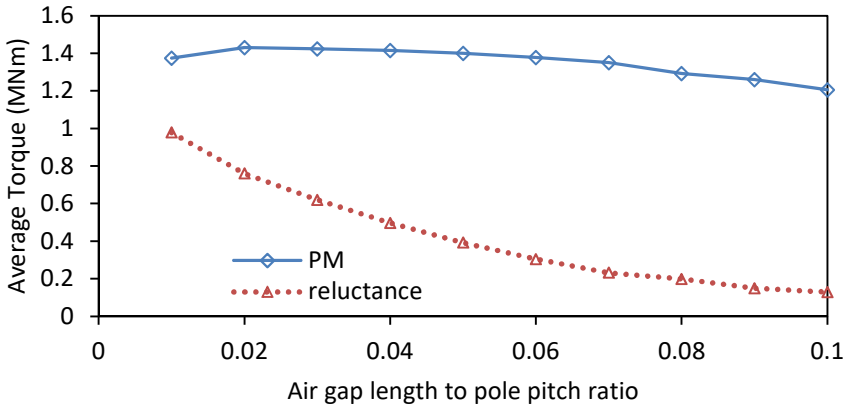

(a)

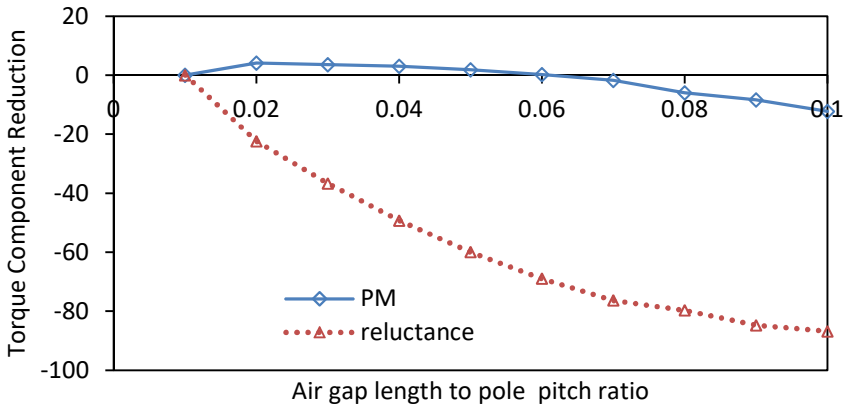

(b)

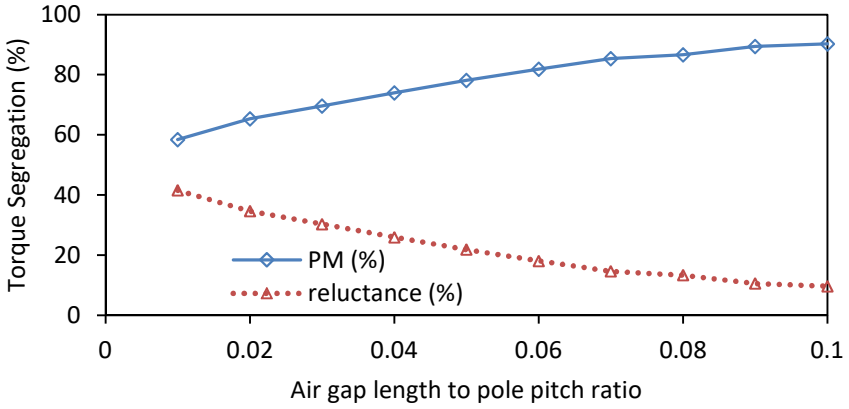

(c)

Fig. 2-49 Torque segregation IPM machines with *p*=80 at different air gap to pole pitch ratios. (a) PM and reluctance torque (b) PM and reluctance torque reduction with air gap length increase and (c) average torque composition.

In large diameter machines, the mechanical limits of the minimum air gap length are generally related to the outer diameter, not to the pole pitch. In other words, even when designing a machine with a high number of rotor poles the lower limit for the air gap

length should be constant. By varying the air gap length rather than using an air gap to pole pitch ratio (i.e. the air gap length will no longer vary with the number of rotor poles), the reluctance torque versus number of rotor poles characteristic curve will not be flat any more. This will be investigated in the next section.

2.4.4 Air gap length in 3MW generator frame at rated load

Fig. 2-50 and Fig. 2-51 portray the variation of average torque of the SPM and IPM machines with the number of rotor poles for different air gap lengths. The optimum pole number varies from p=88 at g=1.18mm to p=68 at g=11.8mm for the SPM machines and from p=56 at g=1.18mm to p=32 at g=11.8mm for the IPM machines. For a short air gap length of g=1.18mm, their optimum pole numbers only differ by 32%, while for a large g=11.8mm, their optimum pole numbers differ by 55% (Fig. 2-52).

In Fig. 2-22, Fig. 2-32 and Fig. 2-42 the optimum number of rotor poles increases with the increase of the air gap to pole pitch ratio. In Fig. 2-52 the more familiar characteristic of the decreasing optimum number of rotor poles with the increase of the air gap length is plotted.

The ratio of $R/R_{required}$=0.61 is valid only for p=108 and g=5.89mm and it is not constant throughout the air gap length and pole number scan. The difference in dq-axis inductances increases as the pole number decreases from p=108. In the low pole region, the inductance difference times the current can compensate for the lower PM flux linkage ($R/R_{required}$ >1) so the IPM machines exhibit a higher torque compared to the conventional SPM machines.

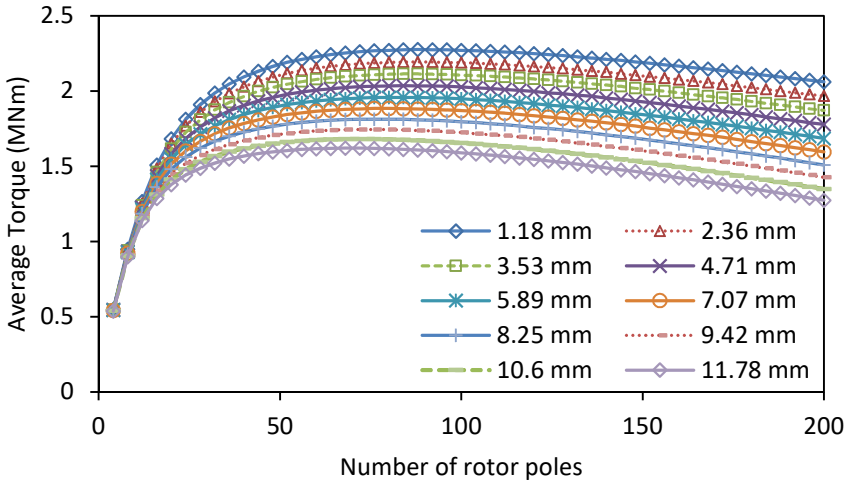

Fig. 2-50 Average torque of SPM machines with different pole number and air gap lengths.

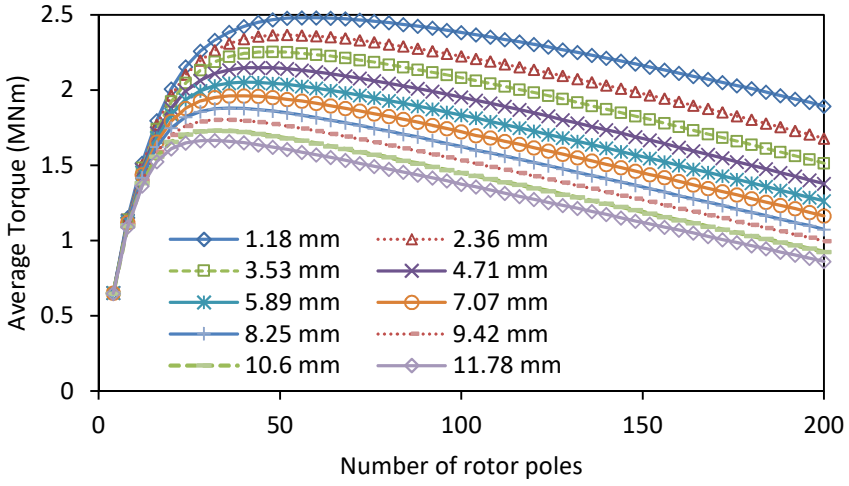

Fig. 2-51 Average torque of IPM machines with different pole number and air gap lengths.

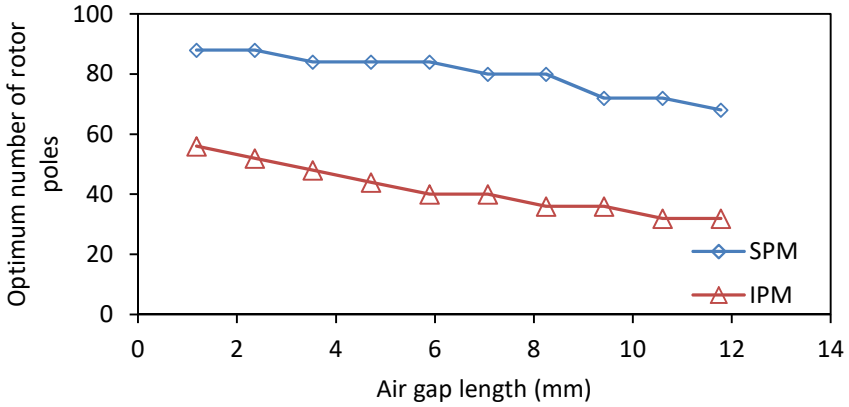

Fig. 2-52 Optimum pole number vs. air gap to pole pitch ratio for NdFeB SPM and IPM machines.

Fig. 2-53 and Fig. 2-54 show the conventional SPM machines always have the higher torque per active volume. This suggests that if they are designed for the same average output torque, the SPM machines will have a higher torque density and hence will be lighter and the material cost will be cheaper. Of course, a numerical optimization should be carried out for each of the candidate topologies before the conclusions can be drawn.

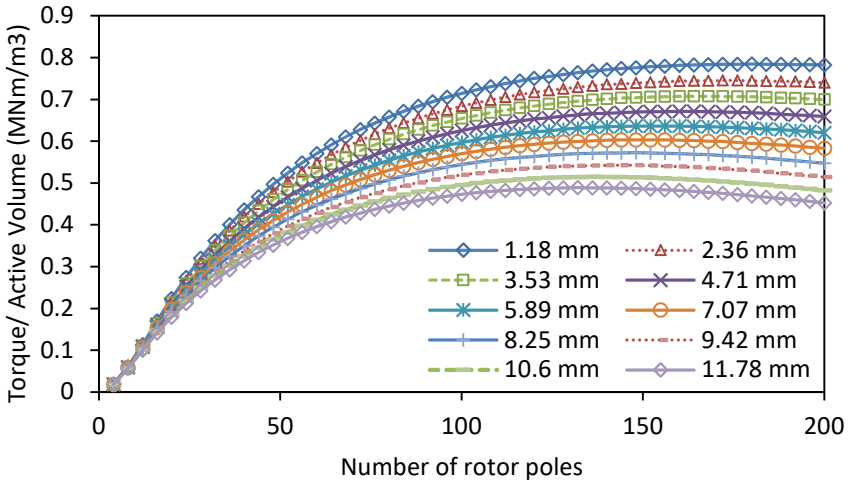

Fig. 2-53 Average torque per volume of SPM machines with different pole number and air gap lengths (mm).

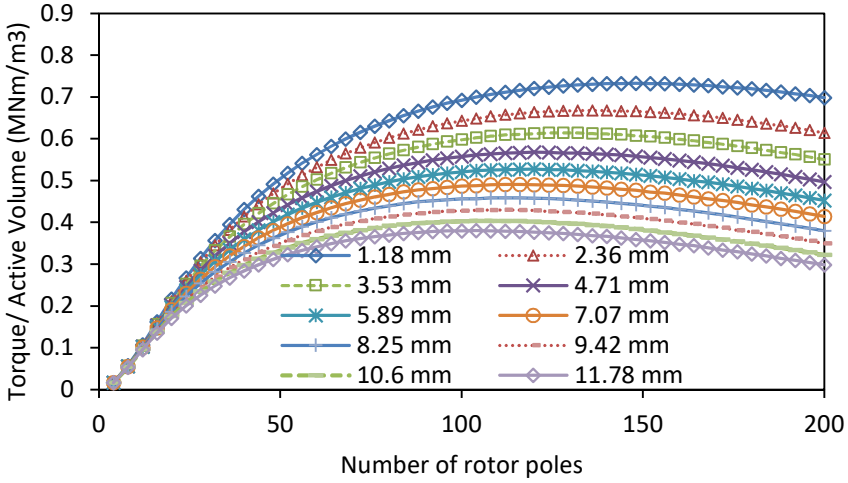

Fig. 2-54 Average torque per volume of IPM machines with different pole number and air gap lengths (mm).

The average PM torque at MTPA of the IPM machines in Fig. 2-55 does not change by a significant margin when the air gap length is increased for an IPM machine with a

small number of rotor poles. When the air gap length is increased, the most significant decrease is of the average reluctance torque as shown in Fig. 2-56. This yields a decrease of the MTPA current angle, β, that can increase the contribution of the PM torque.

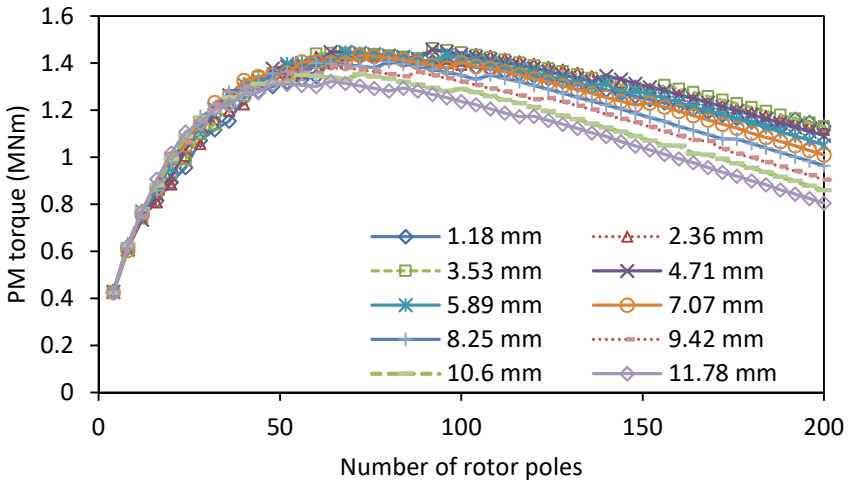

Fig. 2-55 Average permanent magnet torque of IPM machines at MTPA with different pole number and air gap lengths.

Fig. 2-56 shows the variation of the average reluctance torque of the IPM machines versus the number of rotor poles for different air gap lengths. The steps are due to the use of discrete values for the current angle (multiples of 3) to reduce the simulation time. For any air gap length, when moving from a very low pole number the reluctance torque firstly increases sharply due to the reduction of the d- axis inductance. At low pole numbers, the air gap magnetizing inductance and, hence, the reluctance torque capabilities are the highest. However, the q- axis is considerably more saturated compared to the d- axis where the magnetic circuit includes a high reluctance rotor flux barrier. An increase in the average reluctance torque can be achieved by employing a higher slot-pole combination to reduce the q-axis saturation. Even though the air gap magnetizing inductance is constantly decreasing as the number of rotor poles is increased, the rate at which the non-saturated d-axis inductance decreases is higher than

the rate at which the saturated q-axis inductance decreases in this low pole number region. This can be observed in Fig. 2-56 for the $8<p<24$ range where the average reluctance torque increases. The average reluctance torque monotonically decreases with the pole number after reaching its maximum. This can be explained by the constant air gap length and by the monotonically decreasing air gap magnetizing inductance.

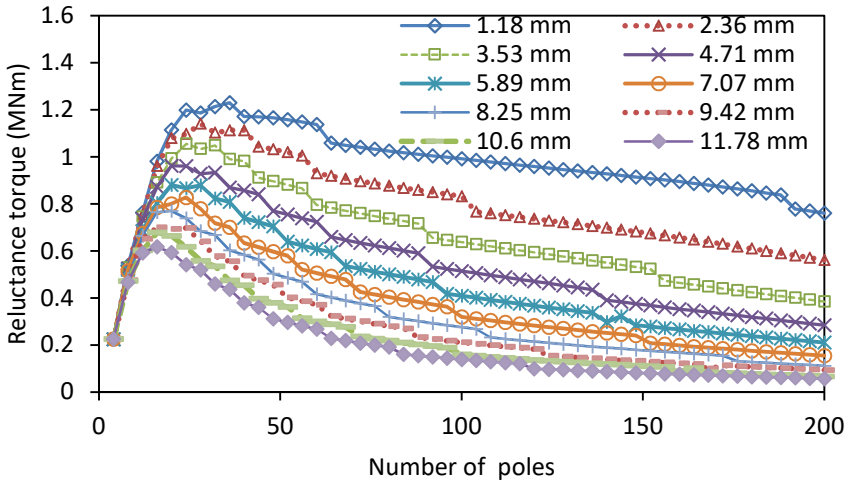

Fig. 2-56 Average reluctance torque of IPM machines at MTPA with different pole number and air gap lengths.

For a low pole number where $R/R_{required}$ >1 the reluctance torque monotonically decreases with the air gap length. On the other side, the PM torque appears to be constant (Fig. 2-57). However, as mentioned before, this is just a side-effect of the MTPA current angle which becomes closer to zero as the reluctance torque contribution is decreased. This effectively enhances the contribution of the PM torque. This phenomenon can be observed for small air gaps in Fig. 2-57 to Fig. 2-59.

The reductions in reluctance torque when the air gap length is increased from 1.18mm to 5.89mm are 18% for p=16, 45% for p=52 and 60% for p=80. The average PM torque is less sensitive to the air gap length. However, this is partially due to the MTPA current angle changing with the air gap length.

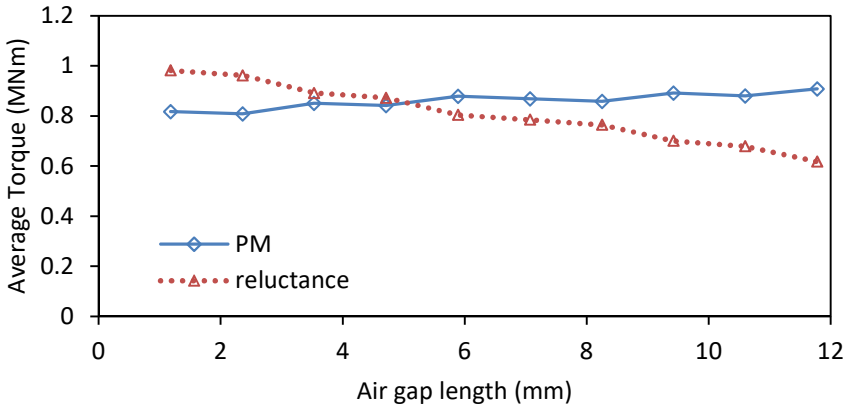

(a)

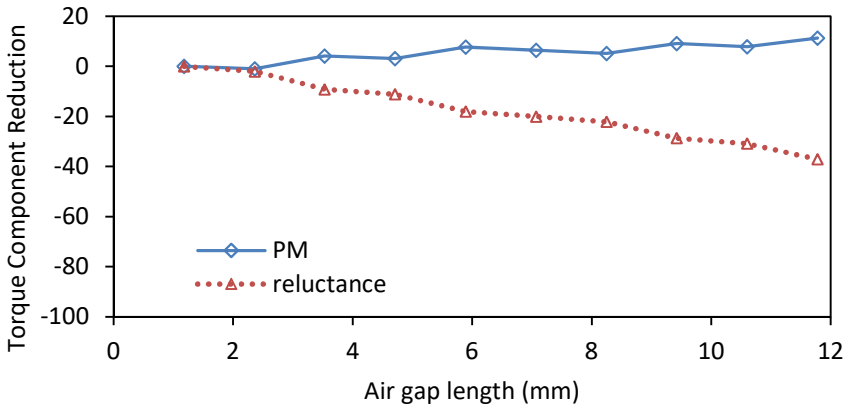

(b)

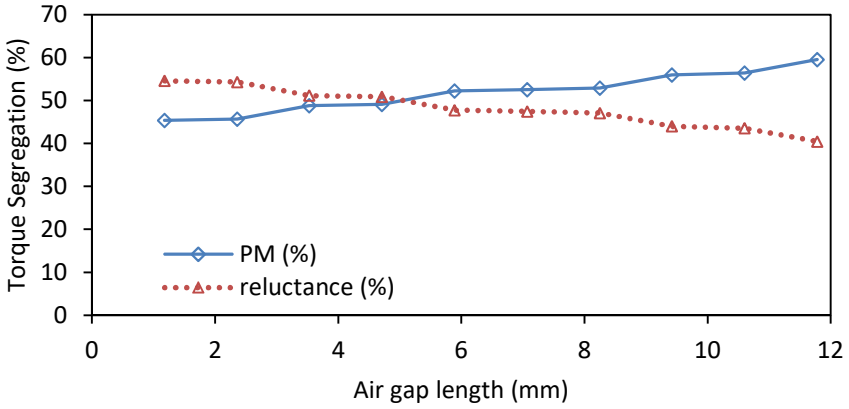

(c)

Fig. 2-57 Torque segregation IPM machines with *p*=16 at different air gap to pole pitch ratios. (a) PM and reluctance torque (b) PM and reluctance torque reduction with air gap length increase and (c) average torque composition.

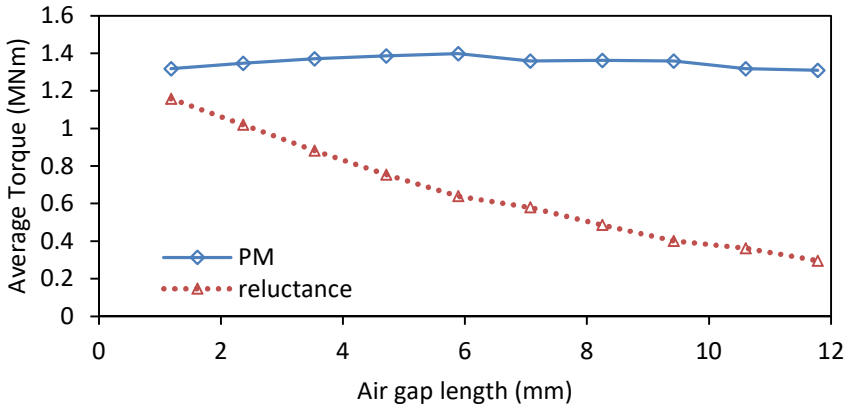

(a)

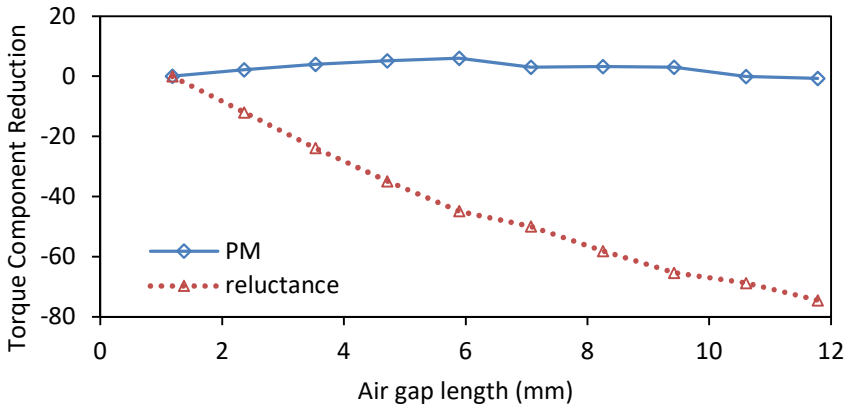

(b)

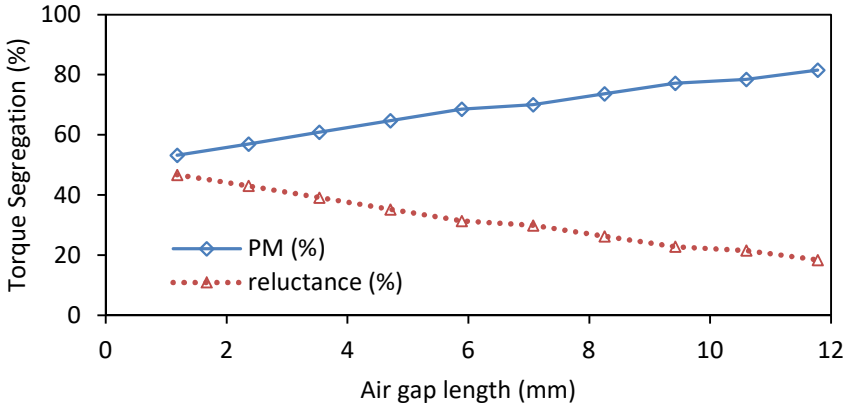

(c)

Fig. 2-58 Torque segregation IPM machines with *p*=52 at different air gap to pole pitch ratios. (a) PM and reluctance torque (b) PM and reluctance torque reduction with air gap length increase and (c) average torque composition.

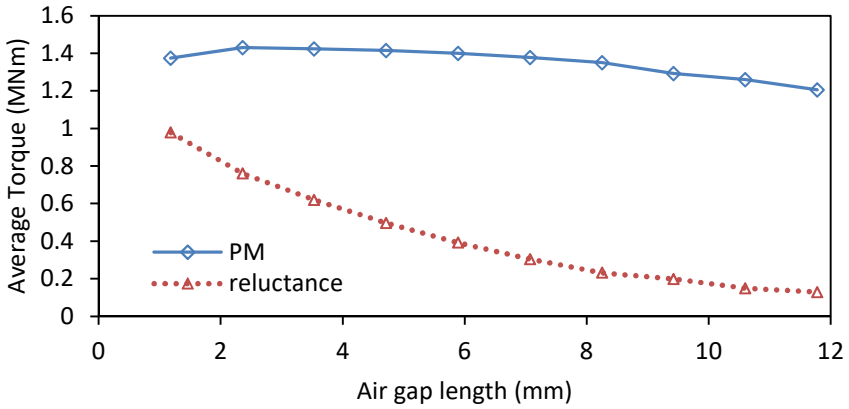

(a)

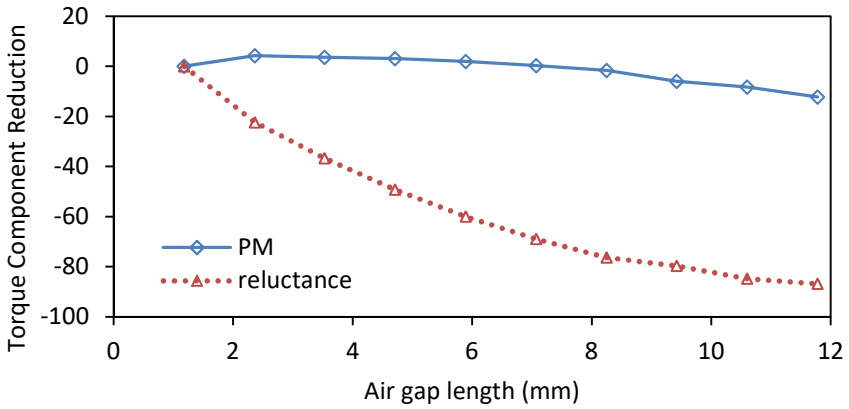

(b)

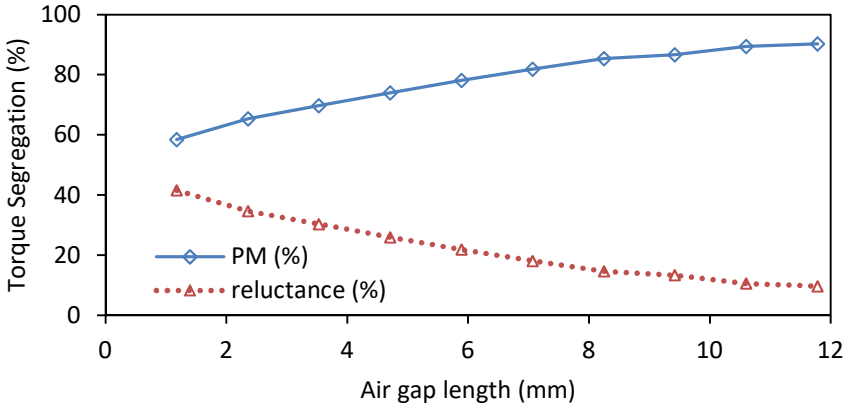

(c)

Fig. 2-59 Torque segregation IPM machines with *p*=80 at different air gap to pole pitch ratios. (a) PM and reluctance torque (b) PM and reluctance torque reduction with air gap length increase and (c) average torque composition.

2.5 Influence of slot/pole combination on active machine material cost

This section presents the effect of the number of slots and poles on the active generator material cost and on the machine average torque per cost. In Fig. 2-60, the cross-sections of four SPM machines with the same air gap diameter and an increasing number of slots and poles are shown. For this q=1 slot per pole per phase integer slot overlapping winding arrangement, the rotor and stator back-iron thicknesses are 3/2 of the tooth thickness as the back-iron needs to carry the flux corresponding to three teeth, half of it being in clockwise direction and the other half in counterclockwise direction. As the tooth thickness to slot pitch ratio is kept constant at 0.5, the stator and rotor back-iron thicknesses will decrease as the pole number is increased and the slot pitch decreased.

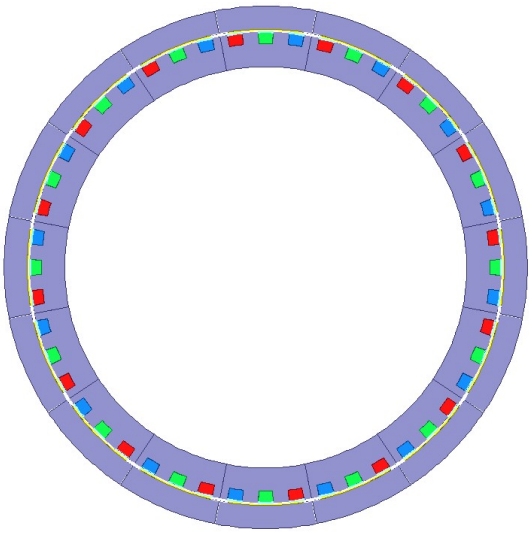

(a) p=16

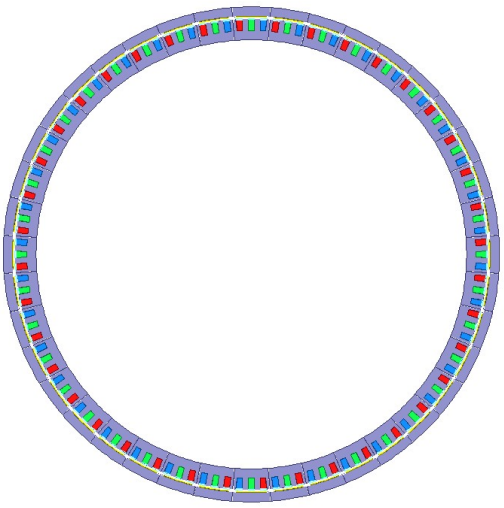

(b) p=40

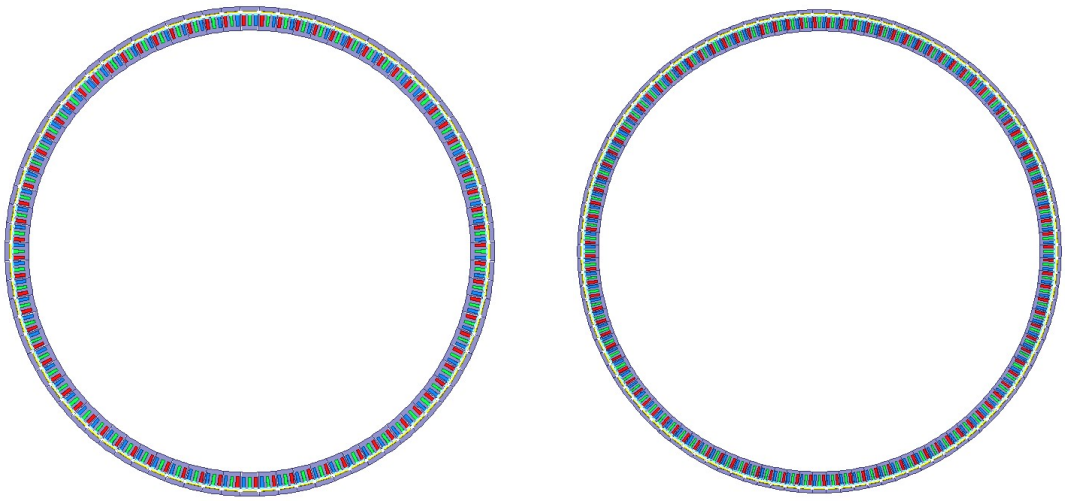

(c) p=80 (d) p=108

Fig. 2-60 Cross sections of SPM machine active materials at different pole numbers.

The cost per kg and the mass density of the active materials in the NdFeB PM machines is presented in Table 2-2.

Table 2-2 Cost per mass and mass density of materials in a PM machine [2] [18].

	Cost (€/kg)	Mass density (kg/m^3)
Copper	8.5	8960
Steel	1.5	7600
NdFeB	25	7500

For this comparison of SPM vs IPM machines, a couple of constraints are imposed:

Fixed parameters:

- air gap diameter 4050mm
- air gap length 5.89mm
- slot height 93mm
- PM height 18.2mm
- number of turns per phase 1242
- current amplitude 222A
- tooth pitch to slot pitch ratio 0.5

Varying parameters:

- number of rotor poles
- number of turns per coil

In the SPM machine the PM and copper winding volumes do not vary with the number of rotor poles. The required steel cost decreases from 87.5k€ at p=16 to 21.5k€ at

p=108. Effectively, the steel laminations would make up for 45% of the total cost at p=16 and only about 17% of the total cost at p=108.

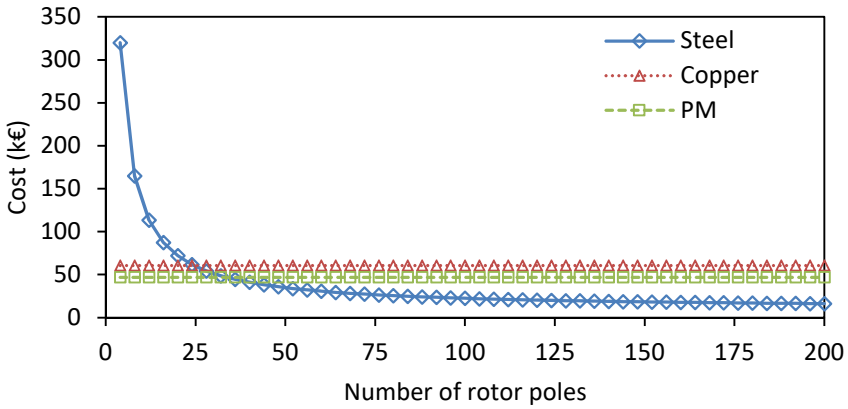

Fig. 2-61 SPM machine active material cost versus number of rotor poles.

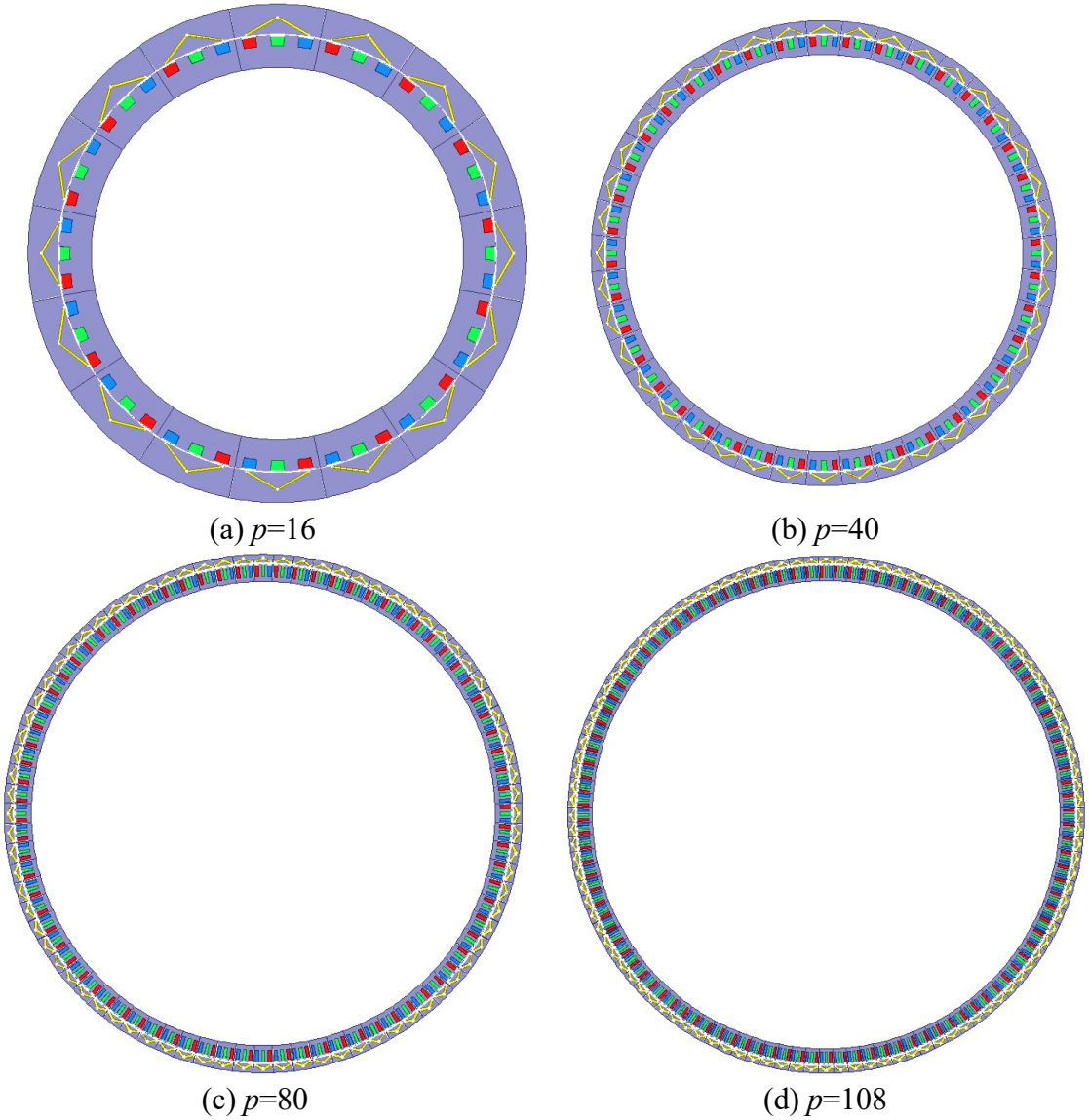

(a) p=16 (b) p=40

(c) p=80 (d) p=108

Fig. 2-62 Cross sections of IPM machine active materials at different pole numbers.

The most significant difference in terms of required materials between the SPM and the IPM machines is that of the steel cost. Due to its PM being buried inside the rotor, the rotor steel needs to be laminated to reduce the parasitic losses. Furthermore, the steel volume required by the rotor in the IPM topology is inherently larger. Because the V-barrier pitch to pole pitch ratio and the magnet thickness are kept constant, the PM volume slightly decreases when the pole number is increased in Fig. 2-63. This is due to the spatial requirements of a PM barrier at an angle (i.e. the barrier thickness limits the barrier length in a finite space). However, the investigations in this section is based on constant barrier thickness since the reluctance torque component is sensitive to the barrier thickness.

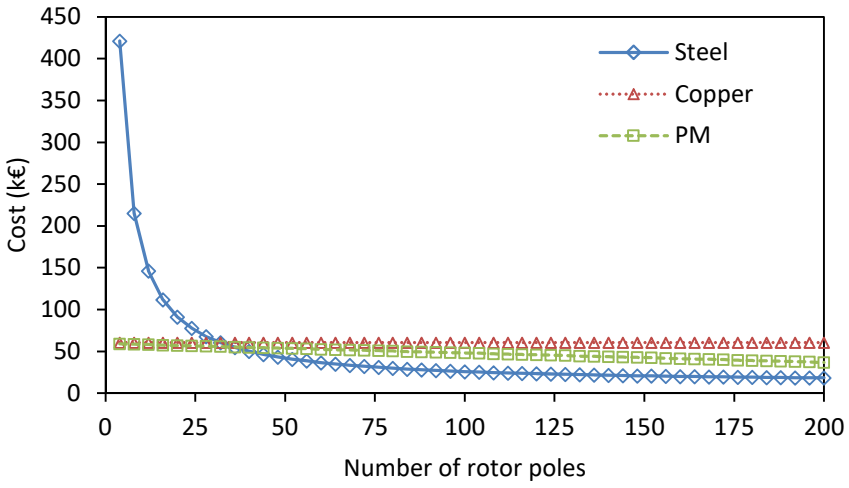

Fig. 2-63 IPM machine active materials cost versus number of rotor poles.

Referring to Fig. 2-64, the SPM machine average torque increases with number of rotor poles. As the number of slots increases with the number of rotor poles, the slot pitch and hence the slot opening are reduced. The Carter factor reduces with the decrease of the slot opening; thus, for a fixed mechanical air gap length, the effective air gap length reduces and the average torque increases for a higher number of rotor poles. The

average torque vs number of rotor poles characteristic is almost flat between p=80 and p=120 for the SPM machine. For p>120 the average torque of the SPM decreases due to flux leakage. Furthermore, at low pole numbers the stator MMF has a large amplitude due to the high number of turns per coil, and hence, a high inductance. This yields higher parasitic losses induced by the stator armature reaction field in both the PM and steel.

Owing to its buried magnet, the IPM machine has a higher rotor PM flux leakage compared to the SPM machine. This is the first reason why the optimum number of rotor poles of the IPM machine is lower compared to the SPM machine. At low pole numbers, the IPM machine exhibits significant average reluctance torque. The rapid decrease of the average reluctance torque with the pole number is the second reason for the fact that the optimum number of rotor poles of the IPM machine is lower. This was presented in Section 2.4.4, Fig. 2-56.

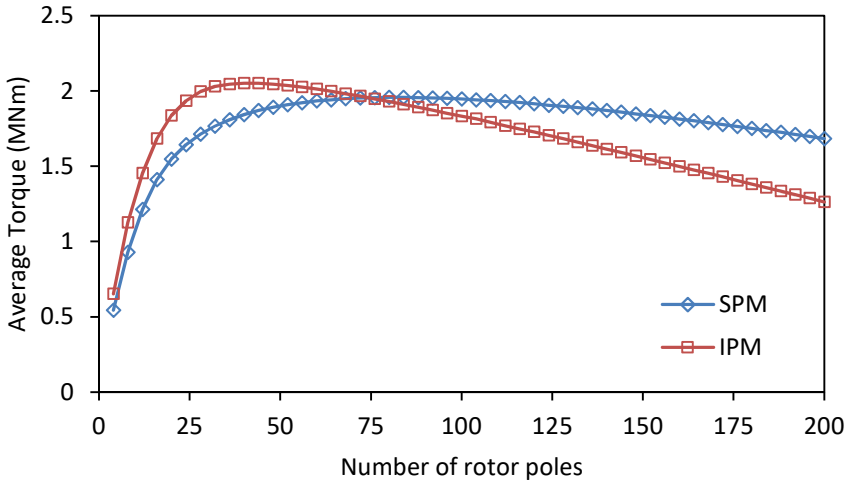

Fig. 2-64 Average torque of SPM and IPM machine versus number of rotor poles.

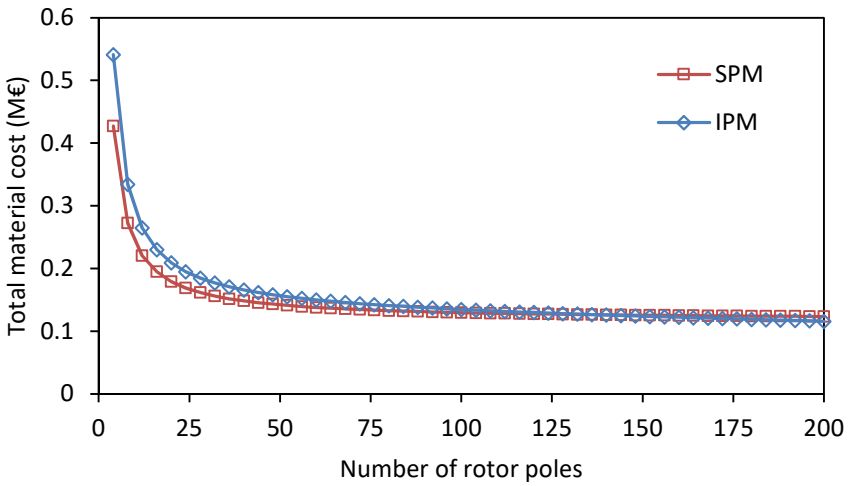

Fig. 2-65 Total active material cost of SPM and IPM machines versus number of rotor poles.

As the optimum number of rotor poles for maximum average torque is significantly different for SPM and IPM machines as shown in Fig. 2-64, the maximum torque per cost will also occur at a lower pole number for the IPM. For machines with the pole number lower than 150, the material cost of the IPM machine is always higher. This is the reason why the torque per cost of the IPM machine is always lower for the scanned conditions.

In the low pole region, p=40, the average torque of the IPM machine can be higher as shown in Fig. 2-64. However, the material cost of the steel is significantly higher at p=40 compared to the optimum pole number for maximum torque per cost, p=80.

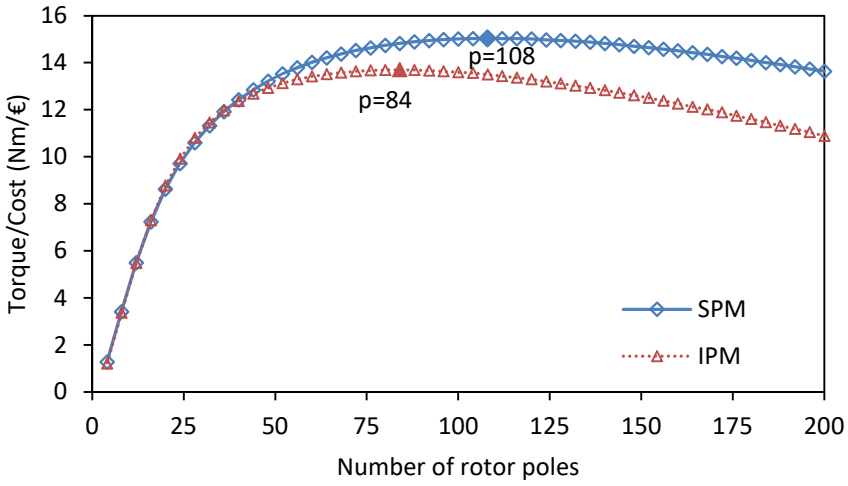

Fig. 2-66 Torque per active material cost of SPM and IPM generator versus number of rotor poles.

2.6 Summary

A hybrid FE and analytical method to segregate the PM and reluctance torque components of large data sets of IPM generators with a reduced number of FE simulations was presented. Its results were compared to the results of the conventional partial coupling flux segregation method. The proposed method was used to investigate the influence of the air gap length and the number of rotor poles on the average torque of SPM and V-shaped IPM machines based on the 3kW prototype and the 3MW generator geometries. Table 2-3 presents a summary of the conditions for scans presented in this section. The numerical data is for an air gap to pole pitch ratio of l_{gr}=0.05 for the first 3 sections and for g=5.9mm for the last section. The optimum number of rotor poles is always significantly lower for the IPM machine, regardless of the current excitation or air gap conditions. As the $R/R_{required}$ <1 for all cases the IPM machine always exhibits a lower average torque with an air gap to pole pitch ratio l_{gr}=0.05 or g=5.9mm.

Table 2-3 Summary of electrical excitation, air gap and optimum number of rotor poles of the SPM and IPM machines with l_{gr}=0.05 or g=5.9mm.

Section	Machine geometry	Current excitation	Air gap	$R/R_{required}$	p for max torque	
					SPM	IPM
2.4.1	3kW	rated	Air gap / pole pitch	0.093	80	48
2.4.2	3kW	10x rated	Air gap / pole pitch	0.93	56	28
2.4.3	3MW	rated	Air gap / pole pitch	0.61	136	108
2.4.4	3MW	rated	Air gap length	0.61	84	40

The torque per cost metric can be used as a single and sufficient quantifier for the material cost of a generator. If multiple generators are to be designed to produce the same average torque, the one with a higher torque per cost is expected to be proportionally cheaper.

A more comprehensive comparison is required for the machine material cost comparison. A numerical optimization algorithm is to be used to determine the optimum cross section for minimum material cost for each of the candidate rotor topologies.

3. Design Optimization and Comparative Study of PM Generators

3.1 Introduction

Permanent magnet (PM) electrical machines are a popular research topic due to their high torque density, high efficiency and relatively simple manufacturing [19] [20]. The interior permanent magnet (IPM) machine has been extensively investigated and was found to be an attractive solution for hybrid electric vehicles applications. There are a plethora of publications on the IPM machines for HEV. Some of them offer an overview of the state of PM machines for HEV applications [14] [21] [22] [23] [24] [25] [26] [27] [28] [29] [30] [31] [32] [33] [34] [35] [36] [37] [38] [39] [40]. Other publications compare the performance characteristics of some of the machine topologies. There is a very rich literature on comparison of small size IPM with other machine topologies suitable for HEV.

Most of the publications on the design of large scale PM generators for wind power applications are about the surface permanent magnet (SPM) topology. The author of [6] highlights the advantages and the trade-offs of PM machines for DD applications. A small air gap length is crucial for high torque density but is one of the major challenges for large diameter generators due to mechanical limitations. A general design approach based on the maximization of the power factor for DD SPM generators is presented in [41] [42]. The authors of [43] propose an analytical design process to maximize the torque of a SPM generator with an outer diameter constraint and with or without an inner diameter constraint. The influence of the rotor pole number on the active material cost, inductance, power factor and demagnetization performance is reported in [44]. In

[1] a system level cost comparison of a DD DC excited synchronous generator, a PMSG (DD, with single stage gearbox), doubly-fed induction generator (DFIG) (with single and three stage gearbox) are presented. The DD PMSG was found to be a cheaper solution compared to the DD DC excited synchronous generator. The single stage PMSG was the cheapest overall. In [2] a genetic algorithm is used to minimize the total system cost for a PMSG (DD, with single and three stage gearbox), for a DD DC excited synchronous generator and for a DFIG (DD, with single and three stage gearbox). The DFIG with a single stage gearbox had the highest annual energy production (AEP) per cost. The AEP of the DD PMSG was higher than that of the DD DC excited synchronous generator. In [5] PMSG (DD, with single and three phase gearbox) and DFIG with a three stage gearbox are compared. At low wind speeds the DD PMSG have the highest AEP due to the absence of gearing losses. At high wind speeds the single stage gearbox PMSG was found to have the highest AEP. Radial and axial field, and inner and outer rotor geared generators are compared in [45]. The conclusions are that the axial field generators have the higher torque density and that for the radial generators the outer rotor was better due to the larger air gap diameter.

Some papers are on the spoke-type IPM topology for DD applications, which exhibits limited reluctance torque due to the high pole number. The spoke-type IPM PMSGs in [46] [47] [48] utilize the flux focusing feature of the topology but have limited reluctance torque. Only a qualitative comparison with some basic performance are presented in [46] [47]. The authors of [48] present a GA optimization design process for a FSCW DD spoke-type IPM PMSG for a micro-wind farm. The basic performance characteristics of un-optimized SPM and IPM (spoke, inset and I-shaped with no inter-magnet laminations) are presented in [49]. The inset IPM was reported to be the most

suitable due to having the highest reluctance torque. This is a reasonable conclusion when considering that in the investigated I-shaped topology the inter-magnet steel is completely missing, increasing the effective air gap length along the q-axis of the generator. The authors of [50] use a differential evolution algorithm to optimize integer slot distributed winding (ISDW) and fractional slot concentrated winding (FSCW) SPM and IPM generators. The ISDW SPM is reported to have the highest torque per unit length, and therefore, it is expected that it will be the cheapest if designed for equal average torque. A NdFeB SPM PMSG is compared to a ferrite IPM PMSG in [18] and in [51]. In [18] the generators are optimized using a multi-objective cost function to minimize the generator active material costs and maximize the AEP. The ferrite IPM PMSG was found to have a competitive price compared to the NdFeB SPM PMSG, but its AEP was always lower due to its higher losses. Furthermore, the optimum ferrite IPM PMSG was found to weight more than the NdFeB SPM PMSG. The influence of the pole number on the different generator active materials is investigated for a DD FSCW SPM PMSG and a DD FSCW IPM PMSG in [52]. The cost minimization was done by scanning the key parameters in a 2D time stepping FEA model. The DD IPM PMSG was found to have a lower optimum number of rotor poles for minimum active material cost. No quantitative comparison of material costs of the optimized generators is presented. Some basic demagnetization performance was reported. With the exception of [52] none of the other comparative papers report on the demagnetization issues during converter faults.

This chapter covers the optimization of synchronous generators equipped with SPM and IPM rotors with either NdFeB or ferrite magnets. The objective is to investigate the feasibility of the IPM generator for DD applications by direct comparison with the well-

established SPM generator. The demagnetization performance of the optimum generators for minimum cost will be investigated in the following chapter and the key parameter values will be adjusted for the rotor magnets to withstand the demagnetization fields during a symmetrical three phase short-circuit.

As demonstrated in the previous chapter, the average reluctance torque is sensitive to the slot-pole number. Therefore, for a fair comparison it is important to compare generators optimized for the same objective, which will have a different optimum number of rotor poles. It was found that the optimum pole number is always lower for the IPM generators, regardless of the optimization target (volume, mass or cost). This is the case because of two reasons: the leakage is higher in the IPM generator and a lower pole number can alleviate the issue, and the average reluctance torque has higher average amplitude for a lower number of rotor poles.

The computer aided design (CAD) process involves the generators key parameter optimization using a 2D finite element simulation controlled by a genetic algorithm optimizer.

SPM and IPM generators using both NdFeB and ferrite magnets were designed. The 4 generators, all rated at 2.4MNm, are optimized for minimum cost, mass and volume. A comparison between the SPM and the IPM generators resulting from the each optimization is presented. Lastly, a comparison between the material contributions to the optimizer cost function is presented for all the optimization objectives and for all the optimized generators.

3.2 Design optimization process for electrical generator

The diagram below summarizes the optimization process used for the minimization of the active material cost in an electrical generator.

Process:

1. The set of generator parameters and constraints are inputs for the FE solver;
2. A time stepped FE analysis is carried out for each set of parameters and constraints;
3. The average torque and average active material cost of the 1m axial length generator are post-processed from the FE results;
4. The axial length required for the generator to achieve the target average torque is calculated;
5. The total cost of the active materials of the generator is calculated by multiplying the cost per axial length by the length required (calculated in the previous step).

Alternatively, the average torque per cost can be computed in step 3. Maximizing this performance metric is equivalent to minimizing the total cost of a generator required to achieve any target average torque.

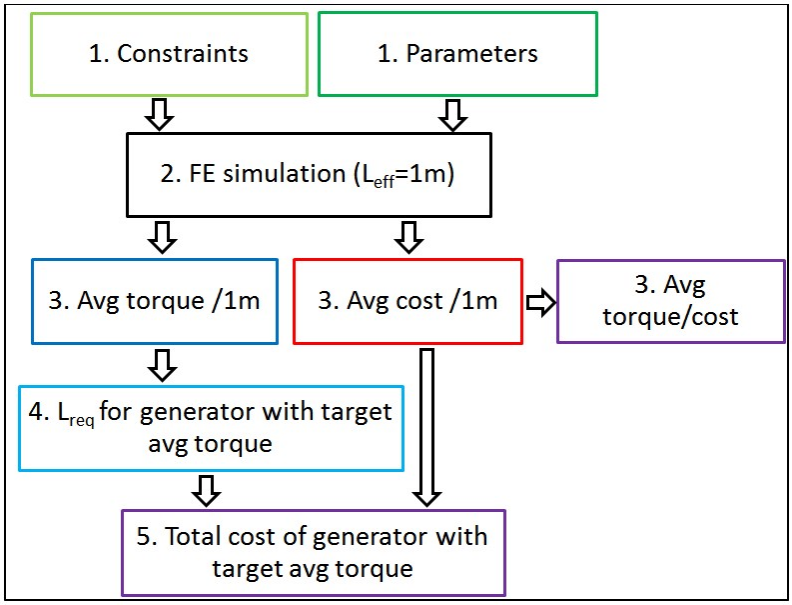

Fig. 3-1 Design optimization process of electrical generator.

3.3 Optimization of SPM and IPM generator cross sections for 2.4MNm at 16 rpm

3.3.1 Cost optimization with fixed copper loss per unit length

3.3.1.1 Surface permanent magnet generator optimization

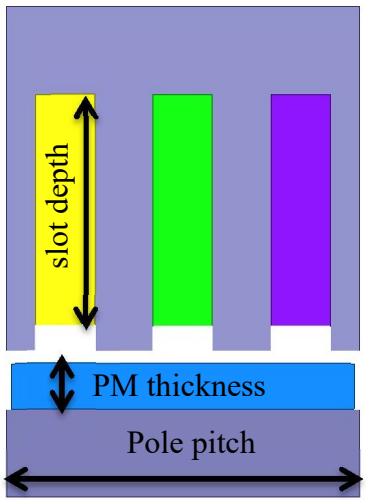

Fig. 3-2 Parameters for SPM generator cross section cost optimization. The 4th parameter is p, the number of rotor poles. Pole pitch, $\tau_p = 2\pi \cdot R_g / p$.

Constraints:

R_g	- air gap radius	- 2025 mm
P_{cu}	- copper loss	- 100kW/1m axial length
g	- air gap length	- 5 mm
tps	- tooth pitch to slot pitch ratio	- 0.5
pmp	- PM pitch to pole pitch ratio	- 0.97

Parameters for optimization:

t_m - PM thickness

p - number of rotor poles

s_d - slot depth

Post processing:

L_{eff} - axial length (m) required for 2.4MNm average torque

Cost - cost of generator of L_{eff} axial length

Volume - volume of generator of L_{eff} axial length

Mass - mass of generator of L_{eff} axial length

The active material cost of the generators resulting from the optimization process can be plotted versus either axial length or versus the other parameters used in the optimization. This reveals the influence of each of the parameters on the generator with minimum active material cost.

The cost per kg and the mass density of the active materials in the generators optimized for cost is presented in Table 3-1.

Table 3-1 Cost and mass density of all active generator materials used in optimization [2] [18].

	Cost (€/kg)	Mass density (kg/m^3)
Copper	8.5	8960
Steel	1.5	7600
NdFeB	25	7500
ferrite	2.5	4900

Due to the constant copper loss optimization condition, when the slot depth is decreased the current density increases. As the torque/cost of electrical machines is directly proportional to the current density, the generators with a shorter slot depth will have a higher torque/cost and thus they will be cheaper for the same rated average torque. This explains why the active material cost of generator decreases in Fig. 3-3 for higher axial lengths. Following the parameter trend along the minimum envelope of the population cost in Fig. 3-3:

- active material cost decreases as the torque/cost increases due to the higher current density in shallow slot generators
- generators with shallow slots have the same total copper loss per cross sectional area and also a higher current density (Fig. 3-18-Fig. 3-20)
- optimum PM thickness decreases as the pole number increases
- optimum slot depth decreases as the pole number increases

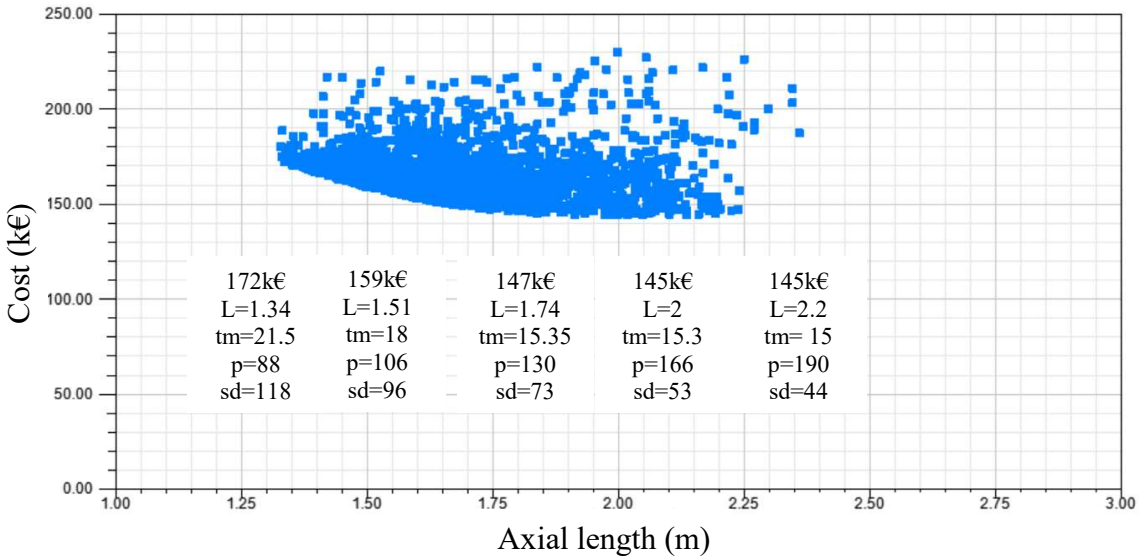

Fig. 3-3 NdFeB SPM material cost vs axial length required to achieve target average torque.

The optimum number of rotor poles for the minimum active material cost in the surface permanent magnet is higher than 100, around 160. In the high pole number region the generator cost is almost constant as the cost vs pole number characteristic curve exhibits a flat region. For even higher number of rotor poles it is expected that the cost will start to increase as the stator teeth become thinner and the stator leakage becomes more significant. This occurs when the pole number is increased beyond 180.

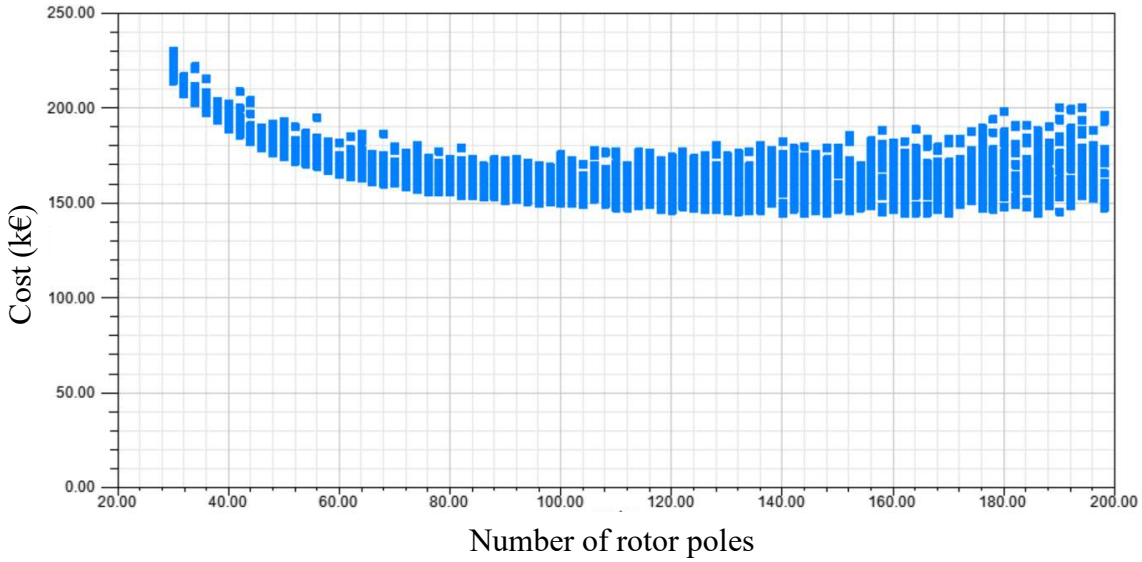

Fig. 3-4 NdFeB SPM cost vs number of rotor poles.

The cost versus slot depth characteristic curve has a global minimum around 50mm because of the constant copper loss condition used for this optimization. This is the case because the cost linearly increases with slot depth while the torque has a less than linear increase due to the stator leakage as seen in Fig. 3-20.

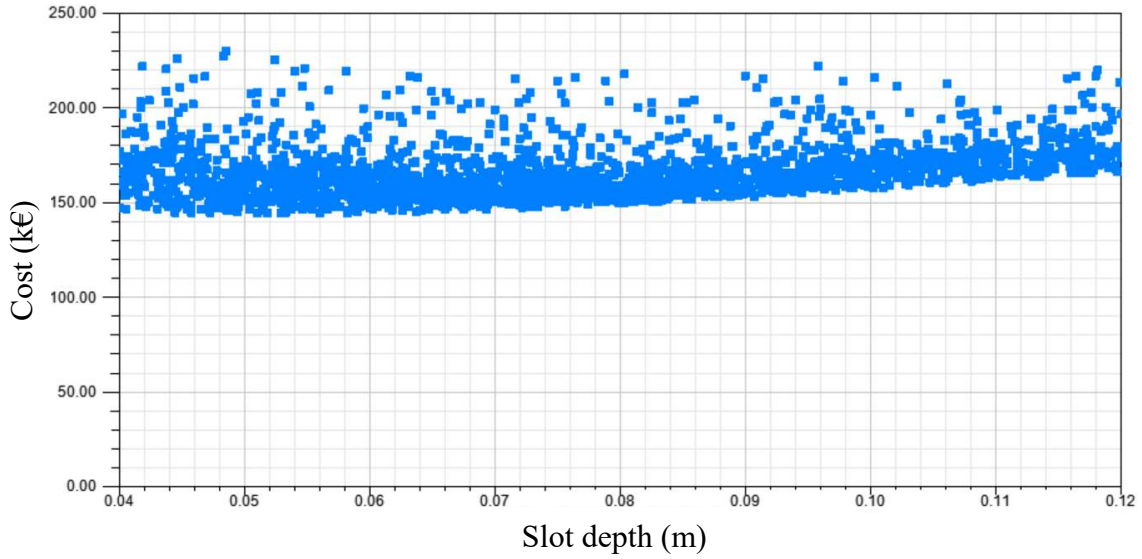

Fig. 3-5 NdFeB SPM cost vs slot depth.

The optimum magnet thickness for minimum active material cost for the SPM generator with the constant copper loss condition is around 15mm for an air gap length of 5mm. Thicker magnets can be used to increase the torque/cross sectional area or the

demagnetization withstand capabilities but this will reduce the average torque/cost and increase the total active material cost as shown in Fig. 3-6.

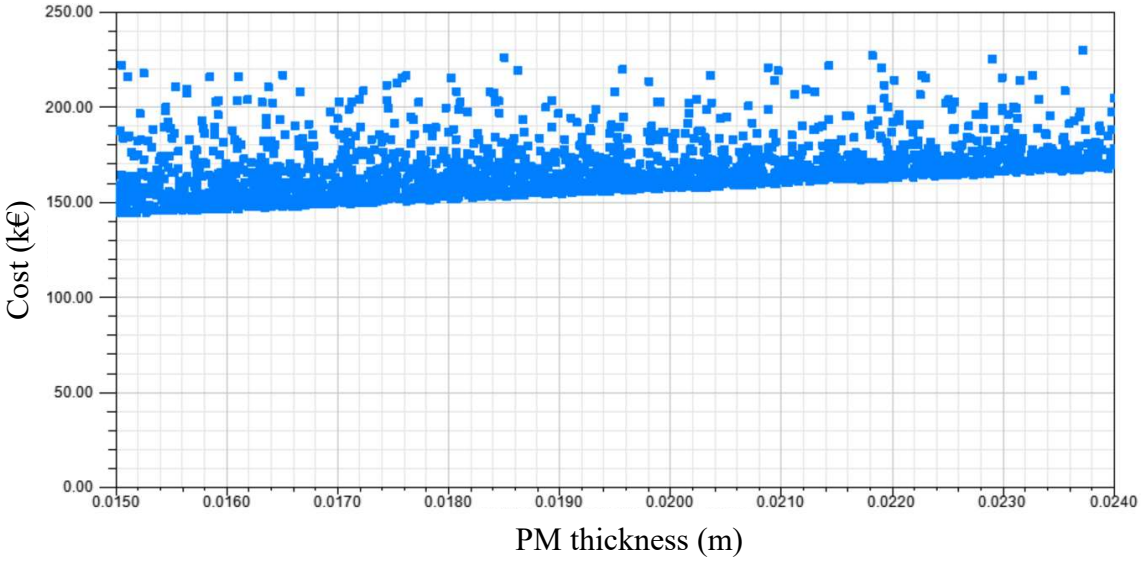

Fig. 3-6 NdFeB SPM cost vs PM thickness.

3.3.1.2 Interior permanent magnet generator optimization

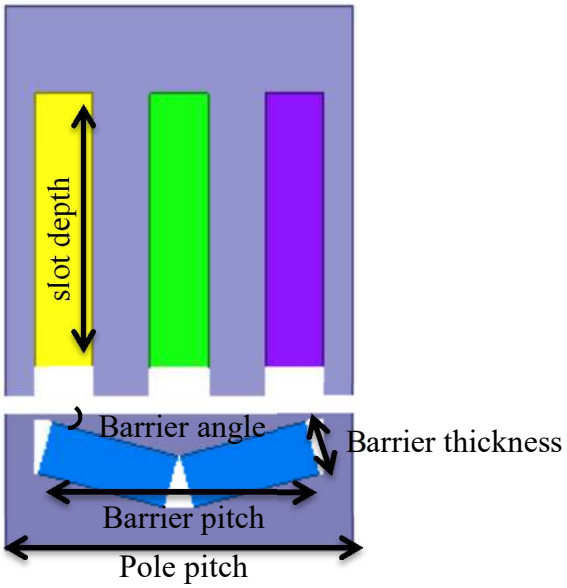

Fig. 3-7 Parameters for IPM generator cross section cost optimization. The 6th parameter is β, the current angle. Pole pitch, $\tau_p=2\pi \cdot R_g/p$.

Constraints:

R_g	- air gap radius	- 2025 mm
P_{cu}	- copper loss	- 100kW/1m axial length
g	- air gap length	- 5 mm
tps	- tooth pitch to slot pitch ratio	- 0.5
bp	- barrier pitch	- 5/6
bd	- barrier depth	- 2 mm
a	- barrier angle	- 15°

Parameters for optimization:

β	- current angle
p	- number of rotor poles
s_d	- slot depth
t_m	- barrier thickness

Post processing:

L_{eff}	- axial length (m) required for 2.4MNm average torque
Cost	- cost of generator of L_{eff} axial length
Volume	- volume of generator of L_{eff} axial length
Mass	- mass of generator of L_{eff} axial length

An interior permanent magnet generator has a higher number of parameters to optimize compared to the conventional surface permanent magnet. The most important additional parameters are the barrier angle and barrier pitch. However, the average torque/ material cost characteristic vs. these two parameters is flat around their values. To reduce the complexity of the problem presented to the numerical optimization solver and for a continuous minimum envelope with respect to all of the scanned parameters the PM barrier pitch (5/6) and the barrier angle (15°) are kept constant throughout the optimization process.

Following the parameter trend along the minimum cost envelope in Fig. 3-8:

- active material cost decreases as the torque/cost increases due to the higher current density in shallow slot generators

- generators with shallow slots have the same total copper loss per cross sectional area and also higher current density (Fig. 3-18-Fig. 3-20)
- optimum PM thickness decreases as the pole number increases
- optimum slot depth decreases as the pole number increases

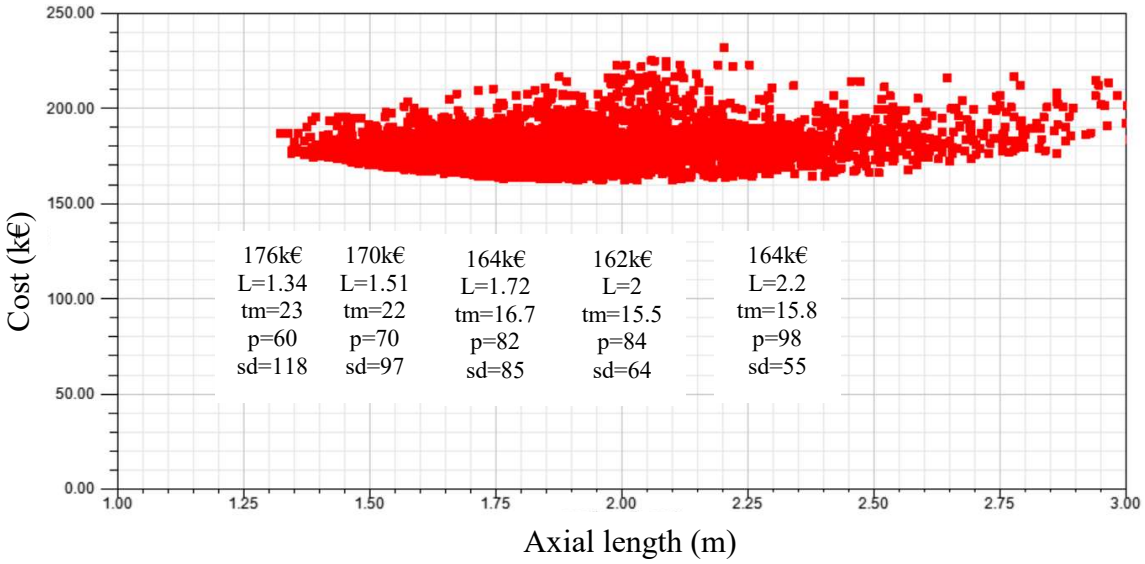

Fig. 3-8 NdFeB IPM material cost vs axial length required to achieve target average torque.

The optimum number of rotor poles for the cheapest IPM generator is around 84. For higher number of rotor poles the IPM generator will be more expensive due to the increased stator flux leakage. Furthermore, the IPM generator base inductance and thus the average reluctance torque decrease when the number of rotor poles is increased.

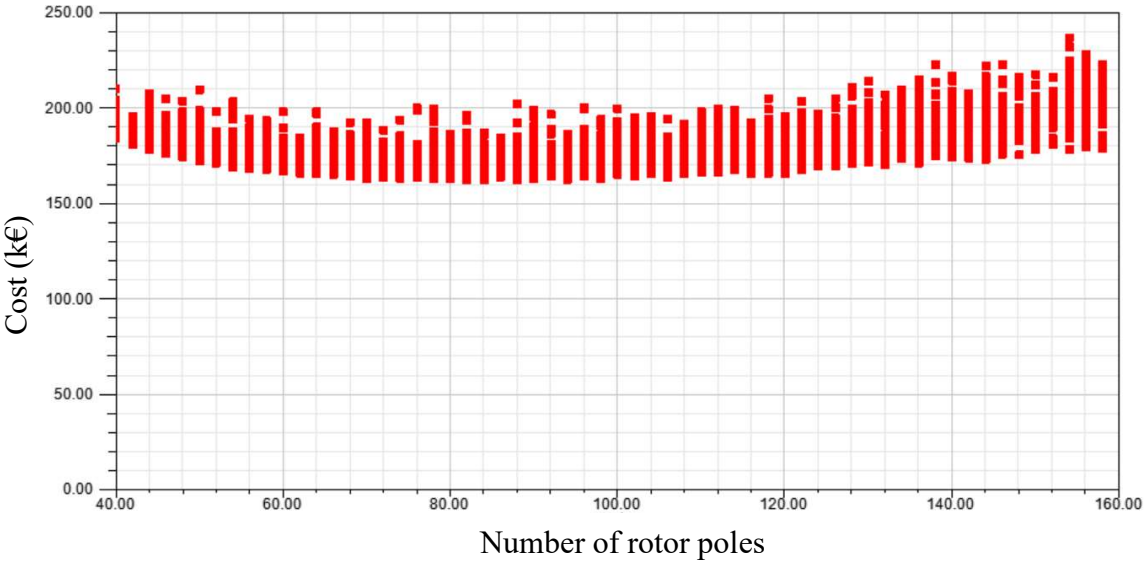

Fig. 3-9 NdFeB IPM cost vs number of rotor poles.

The optimum slot depth for minimum active material cost is roughly 80mm. The explanation for the existence of this cost minimum is similar to that for the SPM generator and is summarized in Fig. 3-18-Fig. 3-20.

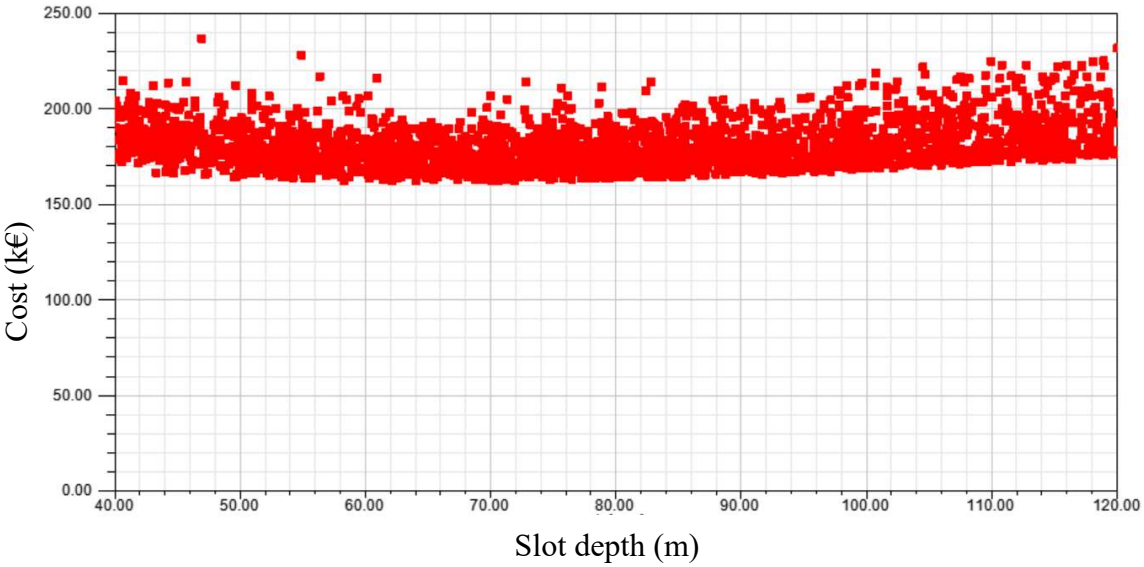

Fig. 3-10 NdFeB IPM cost vs slot depth.

The PM thickness for minimum cost for the IPM machine topology is around 15-16mm, 3 times the 5mm air gap length and similar to the optimum in the SPM machine topology.

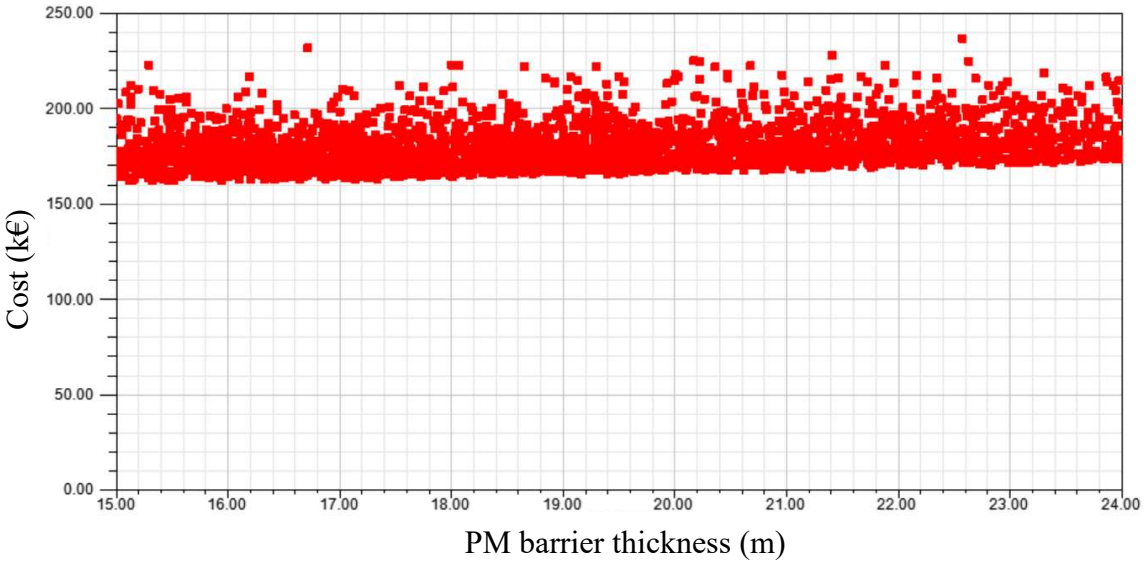

Fig. 3-11 NdFeB IPM cost vs PM barrier thickness.

3.3.1.3 Comparison of SPM and IPM generators with fixed copper losses per unit length and NdFeB magnets

The constant copper loss per unit length condition is related to the heat dissipation capabilities of the electrical generator. Generators with identical cross sections but of different axial lengths will have equal copper loss per unit length and different total copper losses.

In Fig. 3-12 the minimum cost generators have different axial lengths, suggesting the optimum electric loading is higher in the IPM generators since the optimum IPM will have a higher axial length and hence higher copper losses.

The parameters of the IPM generator with the same average torque as the nominal SPM generator are presented in Fig. 3-12. There are three reasons for these differences: the flux leakage, the saturation and the reluctance torque of the IPM generators. The generators equipped with an IPM rotor have a higher flux leakage due to the PM being buried inside the rotor. This also makes the effective air gap length shorter and yields a higher inductance. Thus, the saturation is higher compared to the generators equipped with a SPM rotor, making the leakage issue more severe.

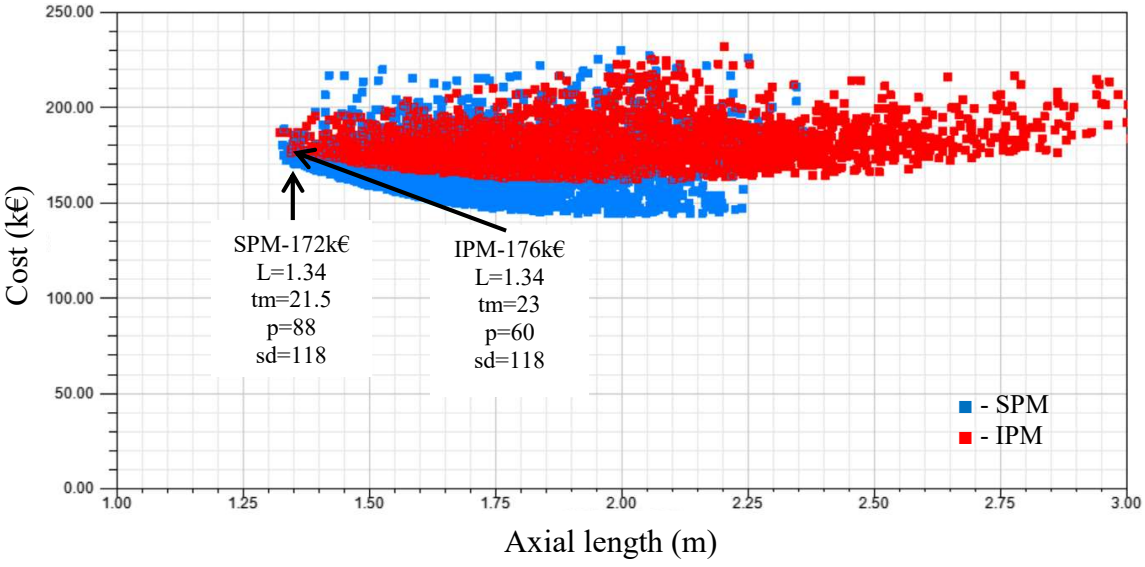

Fig. 3-12 NdFeB SPM(blue) and IPM(red) material cost vs axial length required to achieve target average torque.

The reluctance torque decreases with the increase of the number of rotor poles as the square of the number of turns in each coil decreases. The effect of all these is that the optimum pole number for the IPM generators is significantly lower than the SPM generators to reduce the leakage and to generate more reluctance torque as seen in Fig. 3-13.

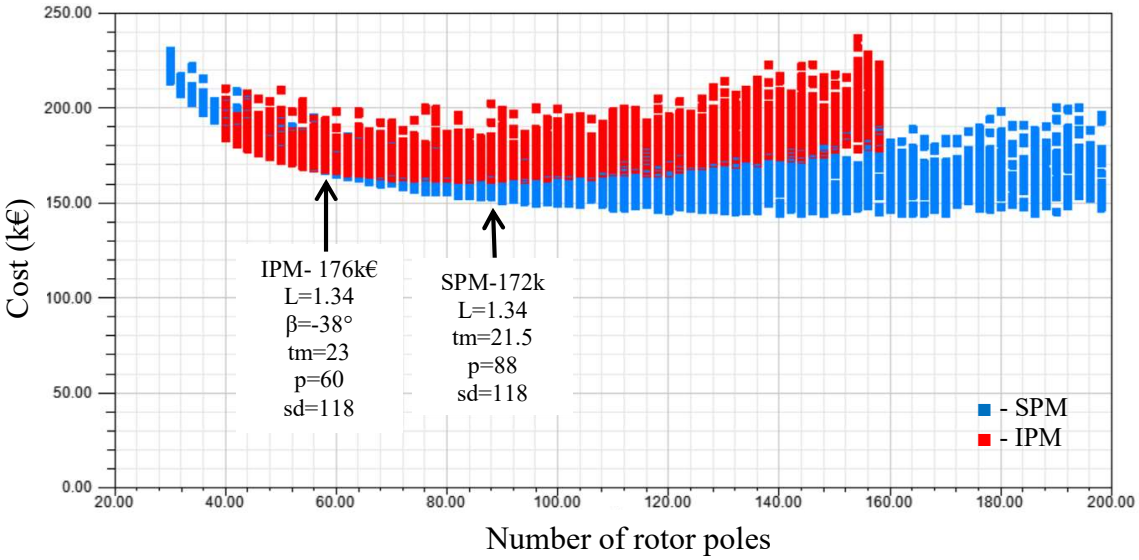

Fig. 3-13 NdFeB SPM(blue) and IPM(red) cost vs number of rotor poles.

The global optimum slot depth for minimum cost is around 60mm for the SPM and higher, around 80mm, for the IPM (Fig. 3-14). This was expected because of the lower optimum pole number and higher optimum electric loading of the IPM generator. The significantly lower pole number alleviates the leakage issue so the optimum slot depth is also higher compared to the SPM machine topology.

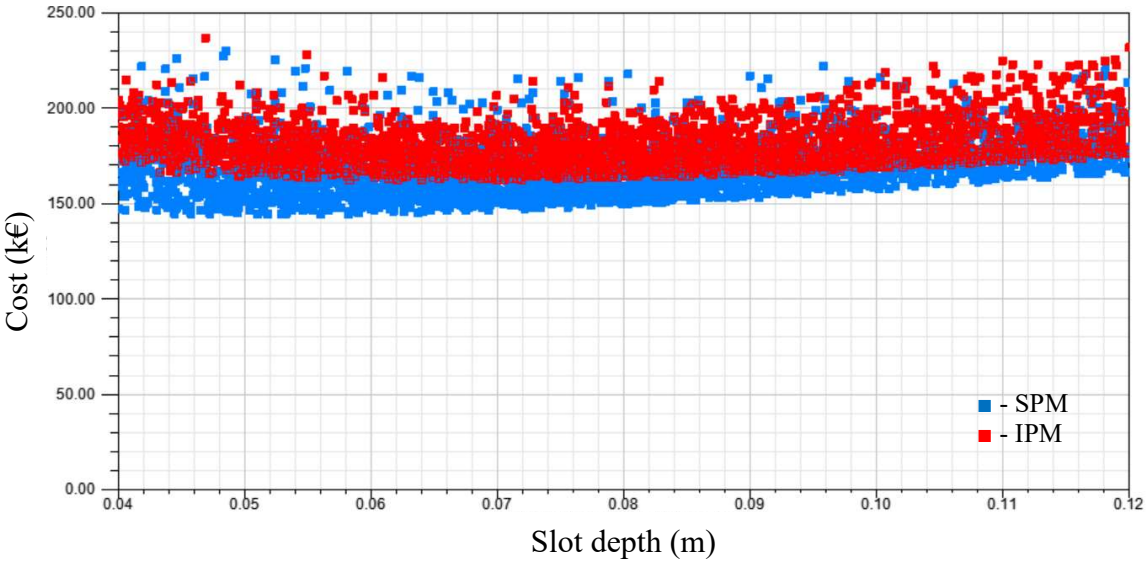

Fig. 3-14 NdFeB SPM(blue) and IPM(red) cost vs slot depth.

The optimum PM thickness in terms of active material cost is lower than 15mm for the SPM drive but the optimization algorithm lower limit for the magnet thickness was 3 times the air gap length. This was done because the nominal SPM generator already has a thicker 18.2mm PM to withstand the demagnetization during a symmetrical 3 phase short-circuit transient.

The costs of the SPM and IPM generators increase linearly with the PM thickness. However, the slope of the IPM cost vs PM thickness is flatter. This is due to the significantly lower optimum pole number of the IPM generator and due to the fact that a thicker barrier decreases the d-axis inductance and enhances the reluctance torque capabilities.

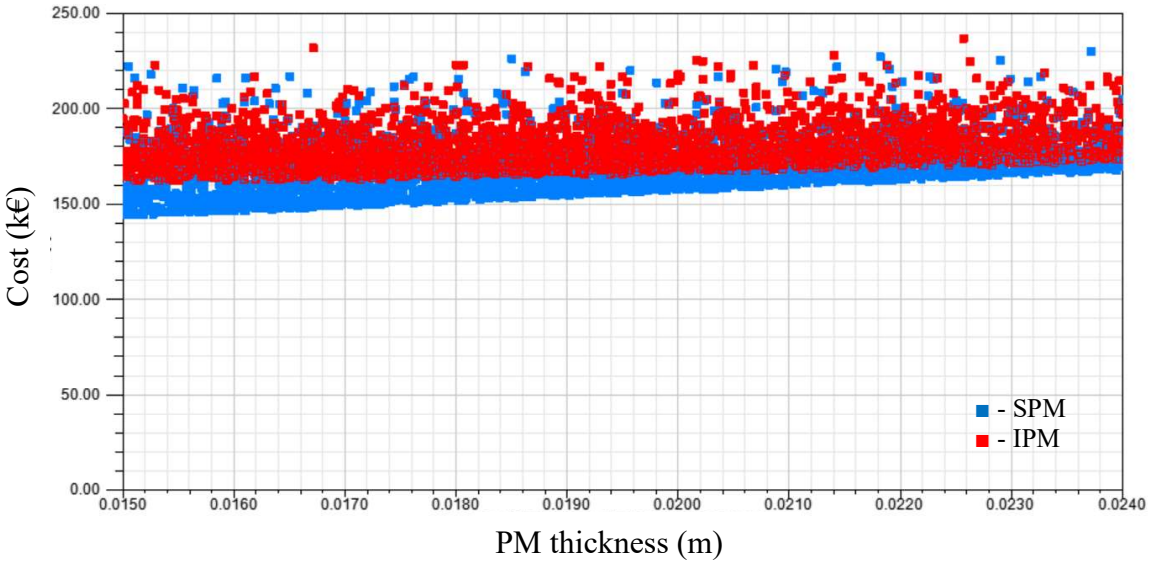

Fig. 3-15 NdFeB SPM(blue) and IPM(red) cost vs PM thickness.

Comparing the minimum cost SPM and IPM for the same axial length:

- the cost is always lower for the SPM
- the optimum number of rotor poles is higher for the SPM
- the slot depth is lower in the SPM
- the PM thickness is lower in the SPM

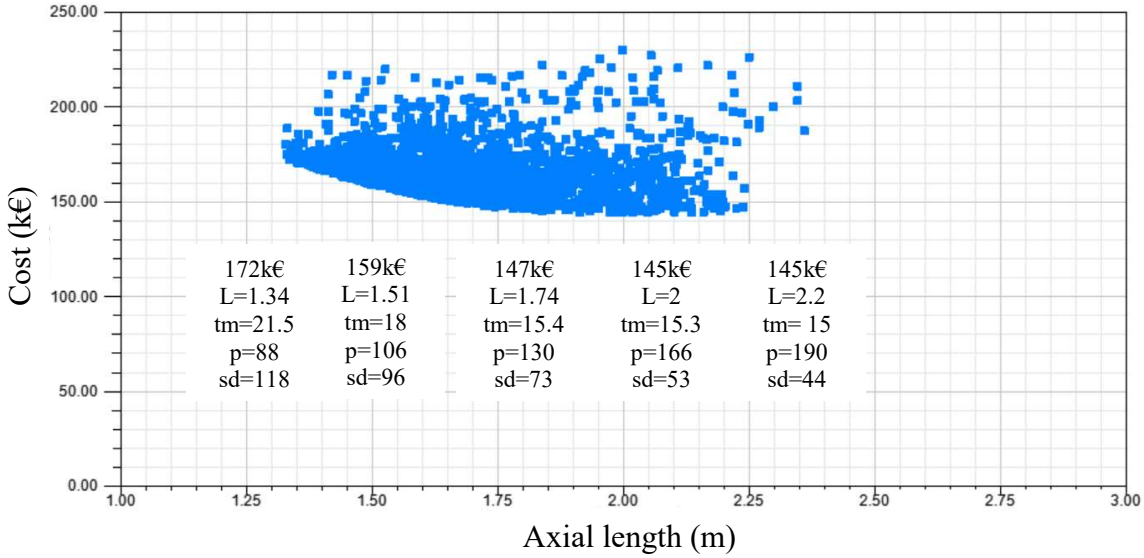

Fig. 3-16 NdFeB SPM material cost vs axial length required to achieve target average torque.

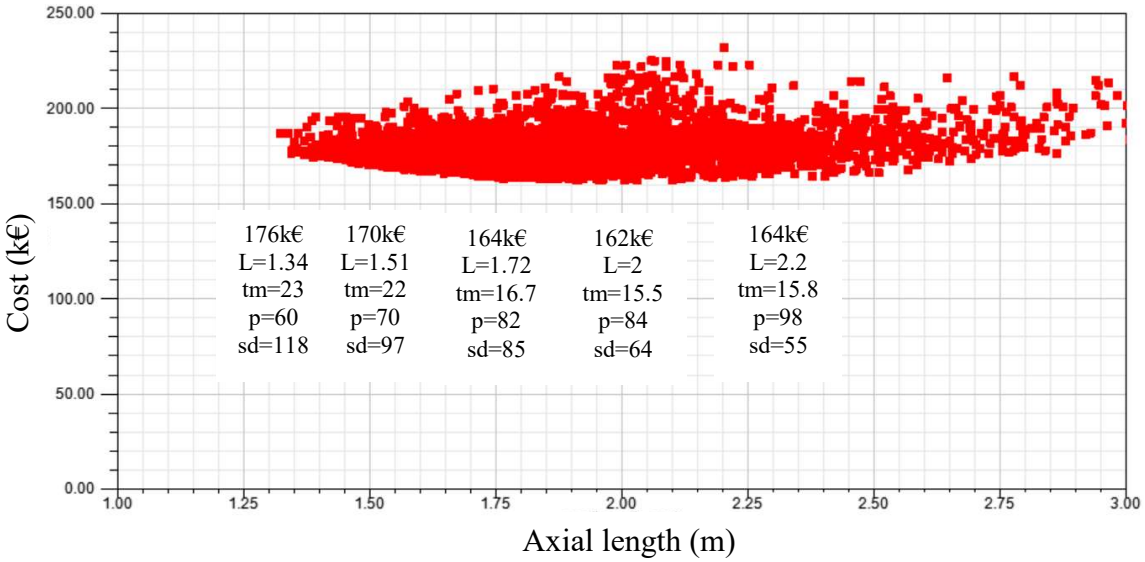

Fig. 3-17 NdFeB IPM material cost vs axial length required to achieve target average torque.

Table 3-2 Key parameter values of minimum cost NdFeB generators with similar axial lengths and fixed copper loss per unit length.

NdFeB SPM					
Axial length (m)	1.34	1.51	1.74	2	2.2
Magnet thickness (mm)	21.5	18	15.4	15.3	15
Number of rotor poles	88	106	130	166	190
Slot depth (mm)	118	96	73	53	44
Cost (k€)	172	159	147	145	145
NdFeB IPM					
Axial length (m)	1.34	1.51	1.72	2	2.2
Magnet thickness (mm)	23	22	16.7	15.5	15.8
Number of rotor poles	60	70	82	84	98
Slot depth (mm)	118	97	85	64	55
Cost (k€)	176	170	164	162	164

For the constant copper loss condition presented in Section 3.3.1.3, the current density can increase when the slot depth is reduced, increasing the temperature of the middle-slot hotspot. This has an important effect on the optimum slot depth for minimum generator cost. As seen in Fig. 3-18 and Fig. 3-19, the optimum slot depth is around 60mm for the constant copper loss condition and monotonically increasing for the constant current density condition. This trend can be explained by the higher current density specific to a smaller area slot and fixed copper losses.

For the constant current density case, the number of turns is directly proportional to the slot depth. The torque/cost monotonically increases with the slot depth in this case (Fig. 3-18). The rate of increase of torque/cost decreases as the slot becomes deeper and the stator PM flux leakage becomes more severe.

For constant copper loss the number of turns squared is directly proportional to the slot depth. In this case, the current density decreases as the slot depth is increased, causing the torque/cost characteristic to exhibit a maximum region, in this case around 60mm slot depth.

With the constant copper loss condition, the optimum generator for minimum cost will have shorter slot depth and a higher current density. This yields a higher torque/cost for the generator at the cost of a more severe winding hotspot problem. This generator would have a shorter slot, the same copper loss but a higher current density and a longer axial length to compensate for the shorter slot depth.

The most significant difference in terms of optimization results can be seen by comparing the cost vs length for the two optimizations with either fixed copper loss (Fig. 3-12) or fixed current density (Fig. 3-21). In Fig. 3-12 the cost vs. axial length initially decreases, reaches a minimum and then monotonically increases. This trend is due to the effect of the constant copper losses condition on the current density and thus torque/cost of the generator as explained above.

3.3.1.4 Influence of electrical load conditions on optimum slot depth for maximum torque/cost

In Fig. 3-18 the torque/cost is plotted versus slot depth for the two cases: constant slot copper loss and constant slot current density. The reference slot depth is at 93 mm; the generator geometries and electrical loads will be identical at this point for the two

conditions. For the constant copper loss case, the number of turns times current amplitude is directly proportional to square root the slot area while for the constant current density case the turns times current is directly proportional to the slot area.

In the constant slot current density case the torque/cost monotonically increases with the slot depth. As the slot becomes deeper, it yields diminishing returns in terms of torque/cost. This is due to the higher slot leakage and higher stator saturation caused by the increased slot depth and electric loading.

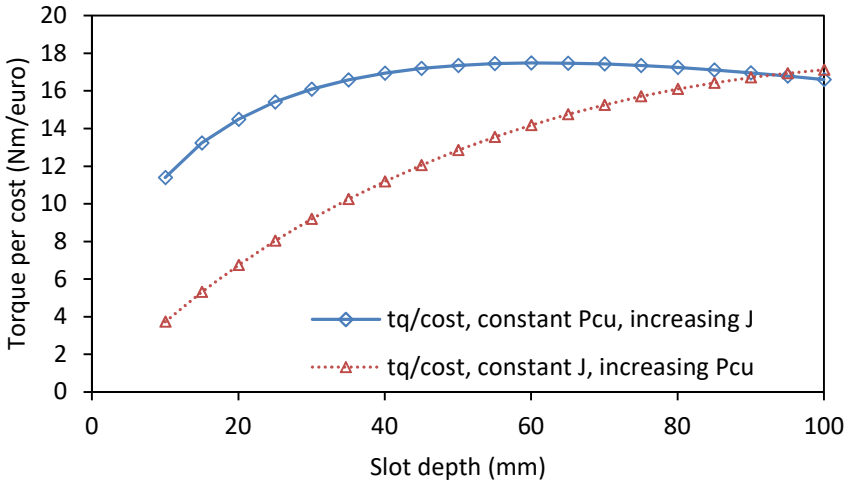

Fig. 3-18 Average torque per cost vs. slot depth for different conditions.

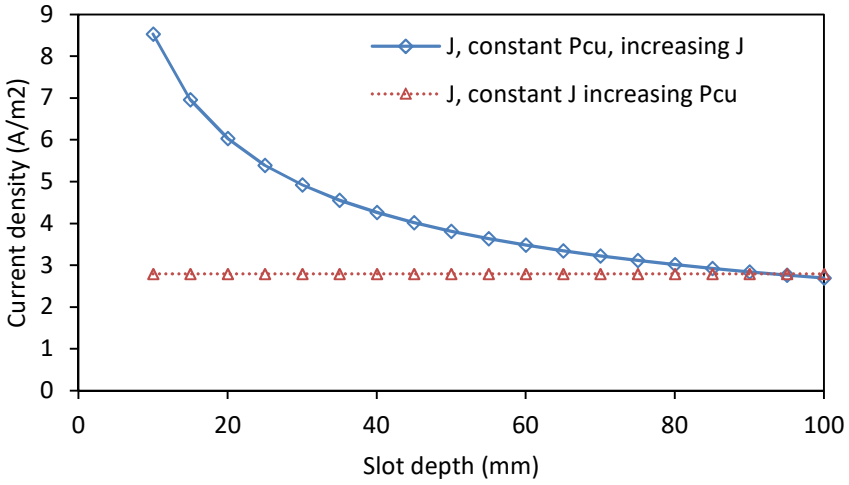

Fig. 3-19 Current density vs. slot depth for different conditions.

In the constant copper loss case, there exists an optimum slot depth for maximum torque/cost around 60mm slot depth. This can be explained with the aid of Fig. 3-20. The material cost increases linearly with slot depth while the average torque increase rate is less than the linear case due to the increase of stator flux leakage. This causes the torque/cost performance metric to exhibit an optimum as shown in Fig. 3-18.

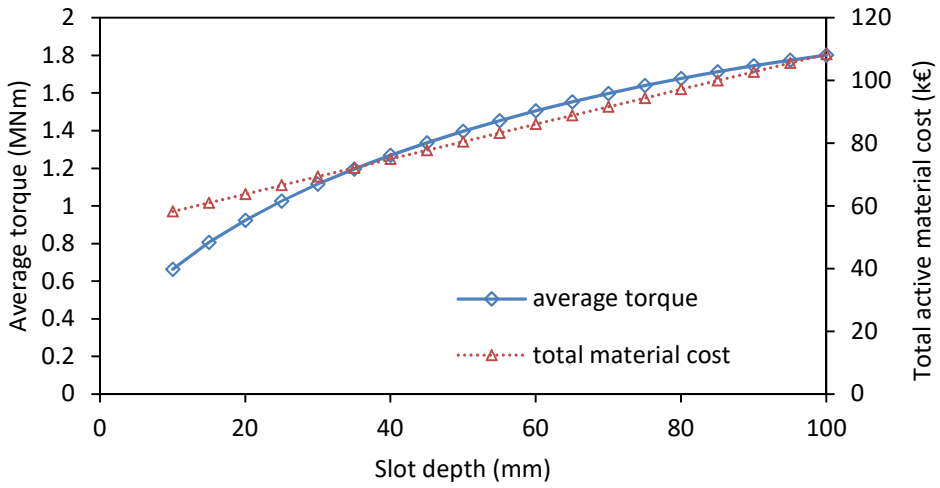

Fig. 3-20 Average torque and total active material cost vs slot depth. The copper loss is constant while the slot depth is varied.

3.3.2 Cost optimization with fixed current density

3.3.2.1 Fixed current density and NdFeB magnets

The conditions for this optimization are the same as the conditions in Section 3.3.1.1 for the SPM and the same as in Section 3.3.1.2 for the IPM. The only different condition is for the electrical loading, i.e. constant current density. This condition is suitable for the optimization search for a DD wind power generator as limiting factor for the electrical loading is the middle-slot hotspot temperature.

The trend of the cost in Fig. 3-21 is to increase when the axial length is increased to compensate for a lower torque/unit and achieve the same target average torque. In this case, the generators with shorter slot depths and longer axial length will have a lower

torque/cost because the torque/cost monotonically increases with slot depth in this case (Fig. 3-18). This explains why the minimum cost increases with axial length in Fig. 3-21.

This causes the cost of the individuals in the population to exhibit a minimum versus axial length and increase monotonically for longer axial lengths.

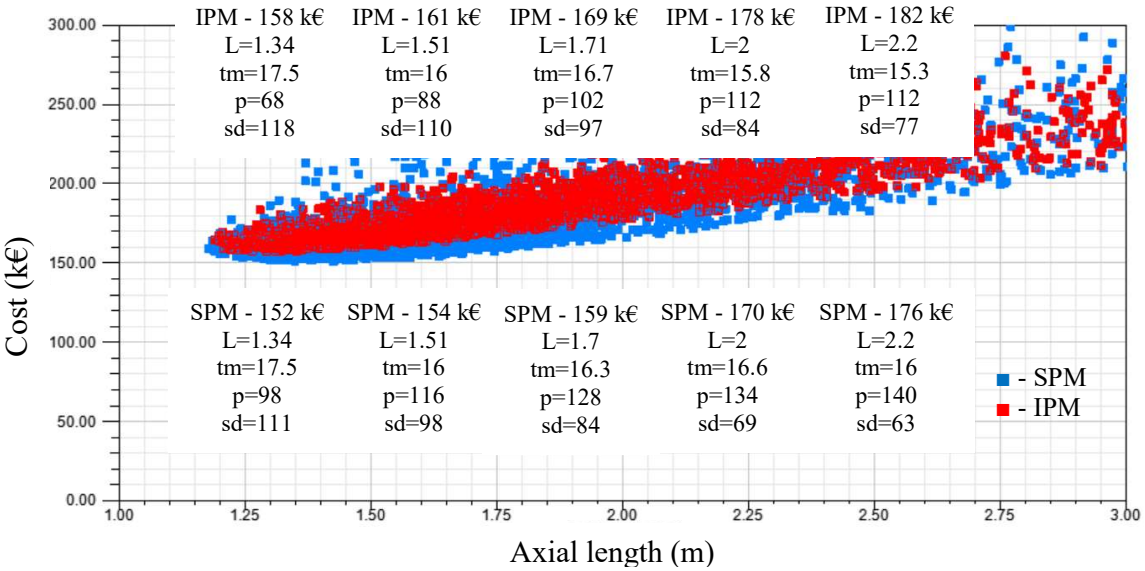

Fig. 3-21 NdFeB SPM(blue) and IPM(red) material cost vs axial length required to achieve target average torque.

Table 3-3 Key parameter values of minimum cost NdFeB generators with similar axial lengths and fixed current density.

NdFeB SPM					
Axial length (m)	1.34	1.51	1.7	2	2.2
Magnet thickness (mm)	17.5	16	16.6	16.6	16
Number of rotor poles	98	116	128	134	140
Slot depth (mm)	111.4	98.3	84	69	62.5
Cost (k€)	153	154	159	170	176.8
NdFeB IPM					
Axial length (m)	1.34	1.51	1.71	2	2.2
Magnet thickness (mm)	17.5	16	16.7	15.8	15.3
Number of rotor poles	68	88	102	112	112
Slot depth (mm)	118	110	97	84	77
Cost (k€)	158	161	169	178	182

In Fig. 3-22 the costs of the SPM and IPM generators were plotted against the number of rotor poles. The SPM generators have an optimum minimum cost around 100 rotor poles while the IPM generators minimum cost is around 60-70 rotor poles. The trend of minimum cost versus the number of rotor poles is similar to that in Fig. 3-13, where the copper loss is fixed. Again, for the same outer diameter and air gap length constraints, the IPM generators have an optimum pole number lower than the optimum of the SPM. This is due to the increase of average reluctance torque when the winding turns are grouped into the minimum number of coils, i.e. at low pole number, and due to the higher PM flux leakage.

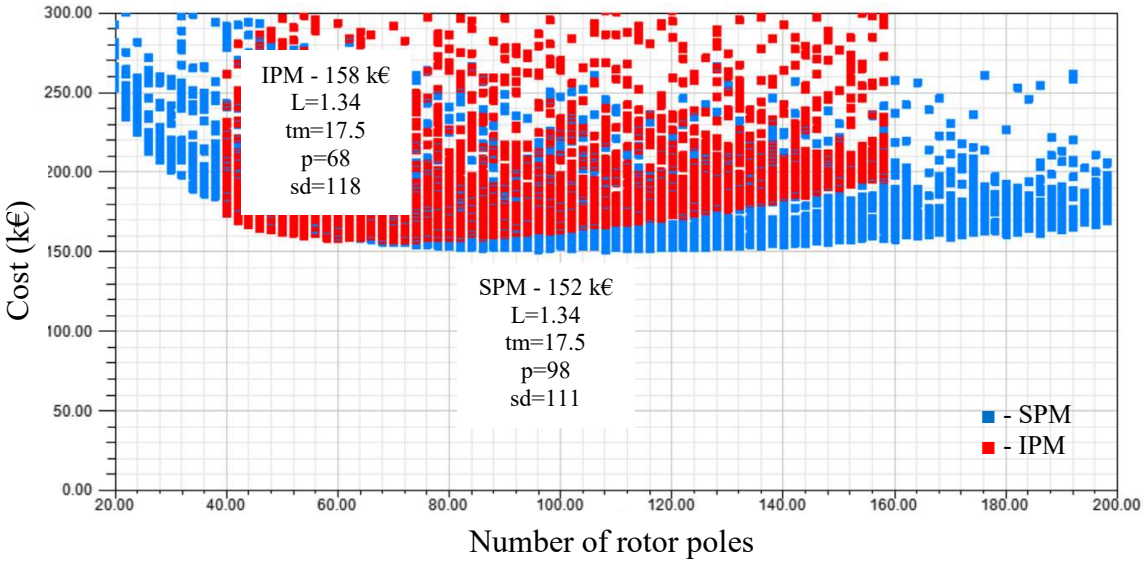

Fig. 3-22 NdFeB SPM(blue) and IPM(red) cost vs number of rotor poles.

When the number of turns is directly proportional to the slot depth (i.e. constant current density) the cost versus slot depth monotonically decreases for both SPM and IPM generators. In Fig. 3-23, the SPM generators reach a flat region of minimum for slot depths higher than 100mm.

For the IPM generators the minimum cost would occur at a slightly higher slot depth compared to the SPM, mainly due to the lower optimum number of rotor poles which mitigates the stator leakage issues and effectively increases the optimum slot depth.

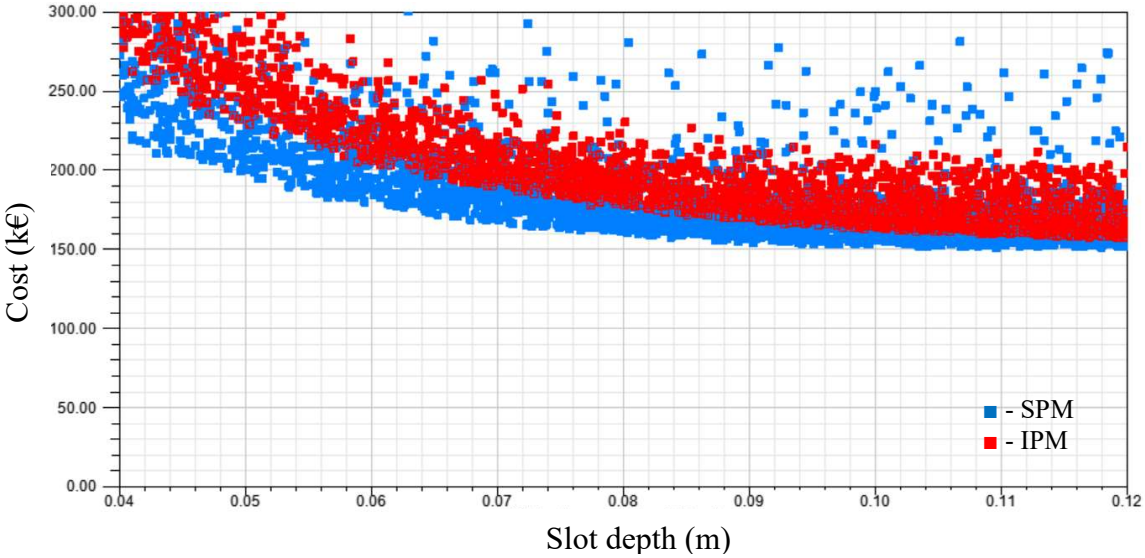

Fig. 3-23 NdFeB SPM(blue) and IPM(red) cost vs slot depth.

The optimum thickness for minimum cost is at the lower limit of 3 times the air gap length for both SPM and IPM (Fig. 3-24). However, the rate of cost increase for the SPM versus PM thickness is higher than that of the IPM. This suggests that even though the active material cost of the IPM is larger, it is less sensitive to the optimum magnet volume for minimum total cost. This is beneficial if there will be a need to increase the demagnetization withstand capabilities which is generally achieved by increasing the magnet thickness.

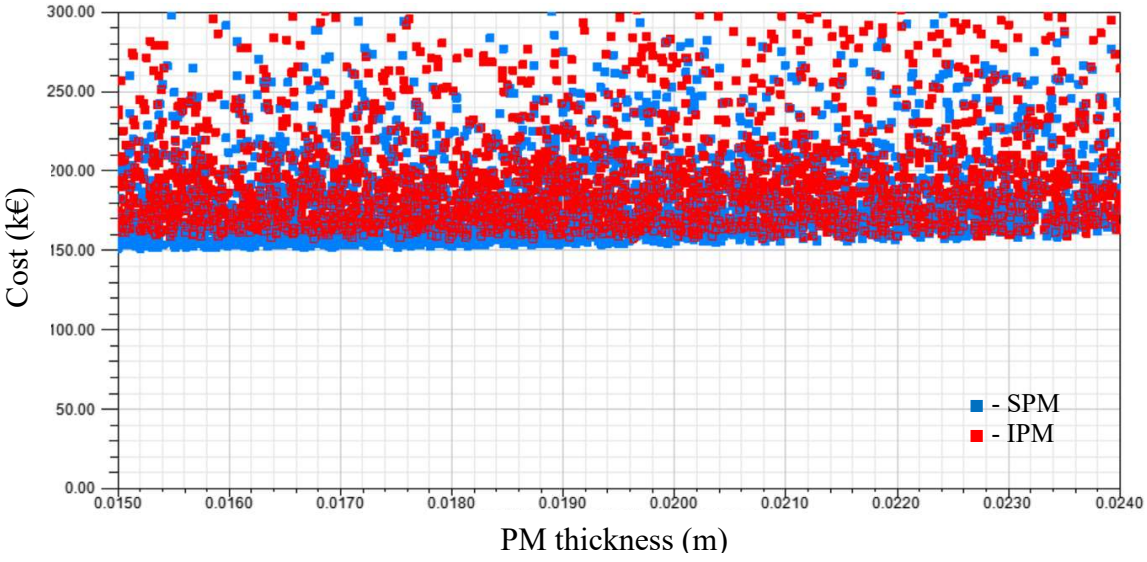

Fig. 3-24 NdFeB SPM(blue) and IPM(red) cost vs PM thickness.

Fig. 3-25 and Fig. 3-26 portray the effect of the different conditions for the electrical loading of the generator. The trend of the optimum number of rotor poles and slot depth is similar with either condition: when the pole number increases the optimum slot depth for minimum cost decreases.

In the case of the constant copper loss generator, the decrease of slot depth from 120mm to 60mm yields an increase of the average torque per cost as shown in Fig. 3-18 and hence the total cost of the generator reduces.

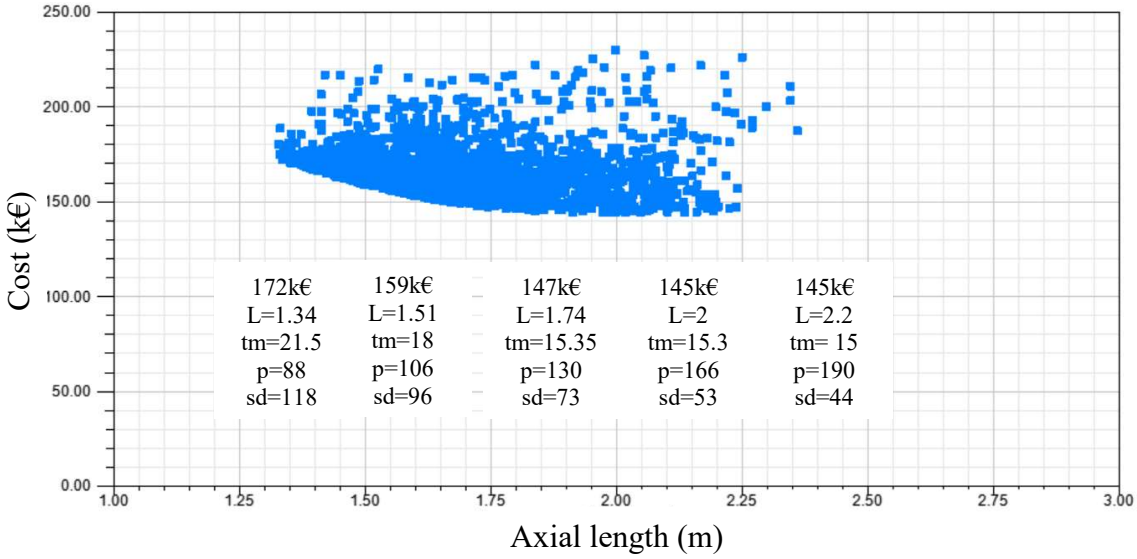

Fig. 3-25 NdFeB SPM material cost vs axial length required to achieve target average torque (constant copper loss).

For the generators optimized with fixed current density, any decrease in slot depth below 100mm causes a decrease of the average torque per cost (Fig. 3-18) and hence, yields a higher active material cost generator. This explains why, for the constant current density conditions, when the slot depth decreases in Fig. 3-26, the total cost will increase.

The relationship between the average torque per cost and the slot depth for the two different electrical excitation conditions is responsible for the differences in the trends plotted in Fig. 3-25 and Fig. 3-26.

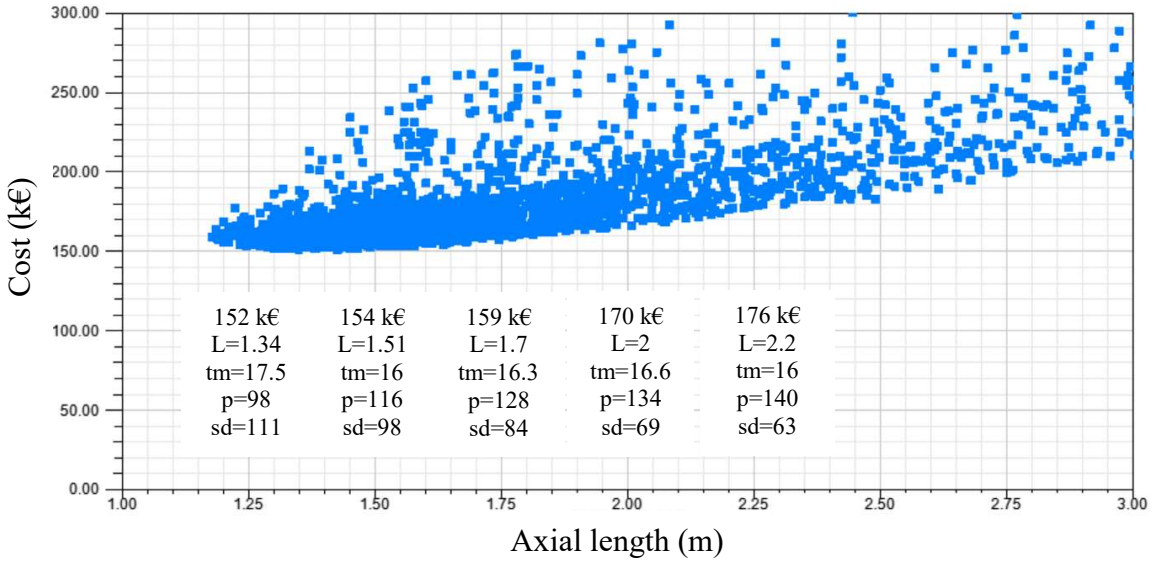

Fig. 3-26 NdFeB SPM material cost vs axial length required to achieve target average torque (constant current density).

3.3.2.2 Fixed current density and ferrite magnets

In this section, the optimization with fixed current density conditions is repeated for SPM and IPM generators equipped with cheaper, lower energy density ferrite magnets. The upper limit for the optimization PM thickness was increased from 24mm for the NdFeB generators to 70mm for the ferrite generators.

The cost vs axial length of all the generators in the optimization process is plotted in Fig. 3-27. For generators equipped with the ferrite magnets, the IPM topology will yield lower cost generators compared to the SPM. This is due to the IPM cross-section higher torque/cost which is owed to the presence of the reluctance torque. Compared to the generators equipped with high energy density NdFeB magnets, the generators equipped with the ferrite magnet have a considerably higher $R/R_{required}$ ratio. This is the case because the average PM flux linkage in the denominator of R will be significantly reduced, roughly 3 times, when the remanence flux density is reduced from B_r=1.2T (NdFeB) to B_r=0.4T (ferrite magnet). Considering the $R/R_{required} \approx 0.61$ for the 3MW

DD generator with NdFeB at for p=108 and g=5mm, it is expected that for a ferrite IPM generator $R/R_{required} \approx 1.83$ for the same pole number and air gap length. When the $R/R_{required} > 1$, the direct and quadrature inductance difference is larger than the required value for the average IPM torque to be greater than the average SPM torque. Hence, the torque/cost of the ferrite IPM cross-section is higher and thus the minimum cost is lower compared to the ferrite SPM.

Even though it is considerably cheaper compared to the ferrite SPM (235 k€), the ferrite IPM (168 k€) is still more expensive when compared to either the NdFeB IPM (158 k€) or the NdFeB SPM (152 k€) from section 3.3.2.1.

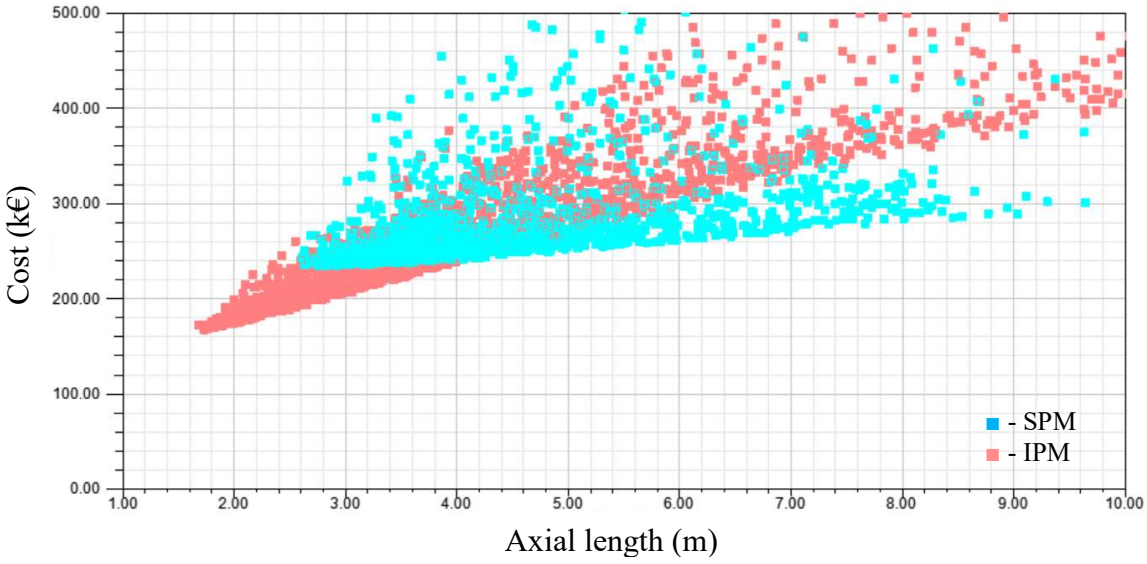

Fig. 3-27 Ferrite SPM(light blue) and IPM(light red) material cost vs axial length required to achieve target average torque.

Table 3-4 Key parameter values of minimum cost ferrite generators with similar axial lengths.

ferrite SPM						
Axial length (m)		2.625	3	4.05	5	5.95
Magnet thickness (mm)		61.4	45.35	32.45	34.6	30.3
Number of rotor poles		72	94	128	128	174
Slot depth (mm)		120	109.8	83.8	67	59.4
Cost (k€)		235	236	242	254	261

ferrite IPM						
Axial length (m)	1.734	1.987	3	4	4.9	6
Magnet thickness (mm)	60.1	67	47.8	32.8	26.8	26.5
Number of rotor poles	52	58	72	78	80	90
Slot depth (mm)	119.5	106.7	82.7	71.3	63.5	58.4
Cost (k€)	168	173	206.6	239.4	266.8	297

The cost vs number of rotor poles in Fig. 3-28 shows that the optimum number of rotor poles for minimum generator active material costs is around 100 for the SPM and significantly lower, around 50 for the IPM. This trend is consistent regardless of the current excitation conditions or the PM energy density and can be also seen in Fig. 3-13 in section 3.3.1.3 and in Fig. 3-22 in section 3.3.2.1.

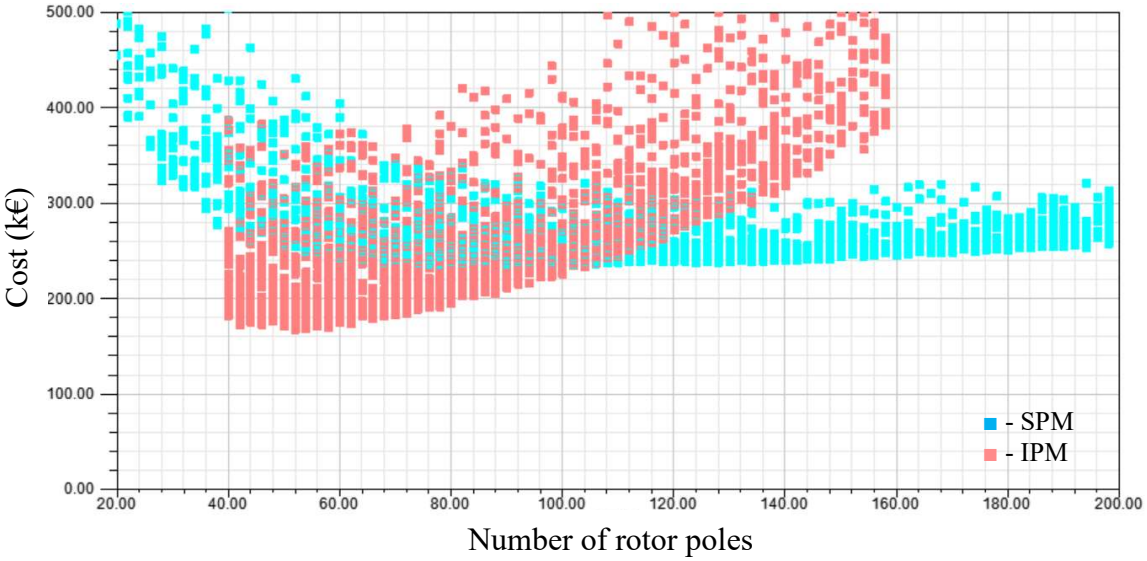

Fig. 3-28 Ferrite SPM(light blue) and IPM(light red) material cost vs number of rotor poles.

For the constant slot current density condition, the total cost decreases as the slot depth is increased. The optimum slot depth of the IPM generator will be higher compared to the SPM, due to the lower optimum pole number which alleviates the stator leakage.

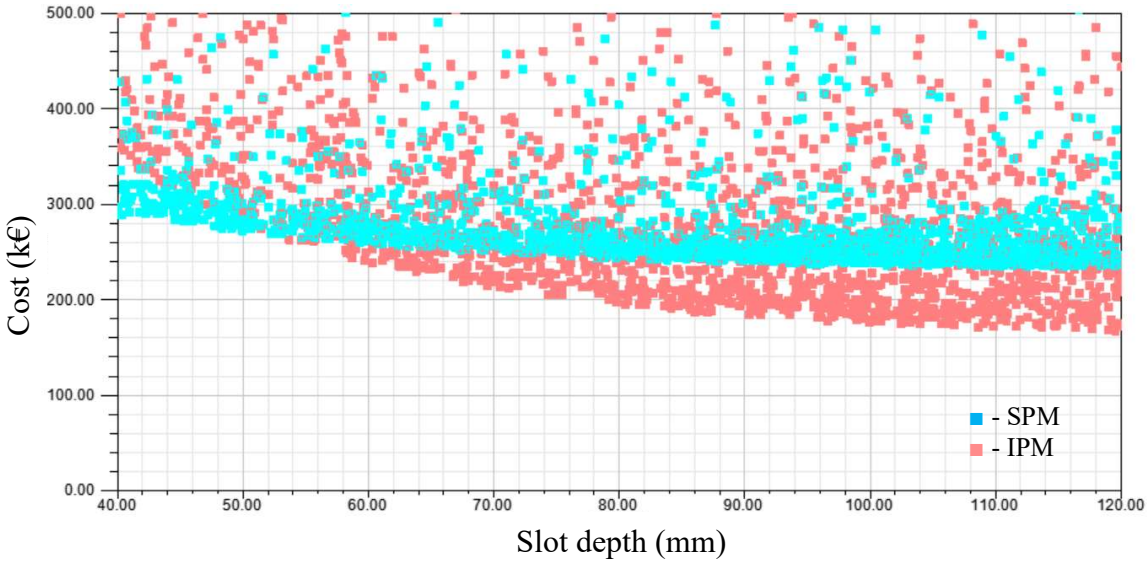

Fig. 3-29 Ferrite SPM(light blue) and IPM(light red) material cost vs slot depth.

For the generators equipped with ferrite magnets, the optimum magnet thickness for minimum generator cost is significantly higher compared to the NdFeB generators. This is mostly due to the significantly lower cost of ferrite, 2.5€/kg compared to 25€/kg for NdFeB.

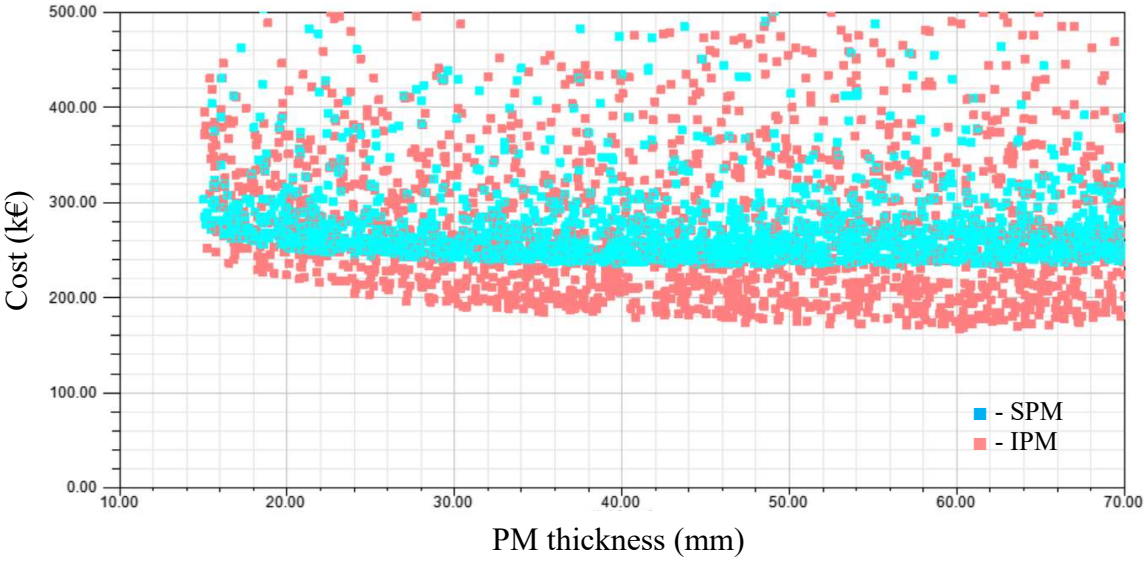

Fig. 3-30 Ferrite SPM(light blue) and IPM(light red) material cost vs PM thickness.

3.3.2.3 Summary of generators optimized for minimum cost

Table 3-5 summarizes the key parameter values of the SPM and IPM generators optimized for minimum active material cost. Fig. 3-31 shows that in order from cheapest to most expensive, the generators are NdFeB SPM, NdFeB IPM, ferrite IPM and ferrite SPM. The prices of the NdFeB SPM, IPM generators and that of the ferrite IPM generators are similar between 150 and 170k€ while the price of the ferrite SPM is significantly higher, around 240k€.

A similar trend can be observed for the mass and volume (Fig. 3-32, Fig. 3-33) with the ferrite SPM having a significantly higher mass and volume.

The SPM generators have a similar total d-axis PM flux linkage as this is directly proportional to their torque capabilities. The magnet is significantly thinner in the NdFeB SPM compared to the ferrite SPM. The thicker ferrite magnets yield a longer effective air gap length and thus the difference between the average direct to quadrature axis inductances is lower than those of the NdFeB SPM generators. This explains why the optimum current angle for MTPA is -12 elec.deg. for the NdFeB SPM generator and very close to 0 for the ferrite SPM generator.

The SPM generators exhibit a minor difference between the average direct and quadrature axis inductances. This is due to the saturation of the d-axis caused by the PM flux linkage.

The IPM generators have a lower d-axis PM flux linkage, the NdFeB IPM is only 13% lower while the ferrite IPM has a roughly 47% lower magnetic loading compared to the SPM generators.

For the NdFeB generators, the SPM has the higher power factor at MTPA due to the low large d-axis PM flux linkage and due to the low values of average inductances. The

power factor of the ferrite SPM is significantly lower, even though the air gap length is larger. This is due to the significantly lower average air gap flux density when using the lower energy density ferrite magnets which increases the axial length required for achieving the target torque. The longer axial length and the lower optimum rotor pole number are the main reasons why the d- and q- axis inductances of the ferrite SPM generator are roughly 3 times larger average amplitude than those of the NdFeB SPM. Hence, the power factor of the ferrite SPM generators is lower since the SPM generators had equal magnetic loading.

The SPM generator has a higher power factor than the IPM generator at MTPA for the NdFeB generators and vice versa for the ferrite magnet.

Table 3-5 Optimum parameters of SPM and IPM generators with equal average torque capabilities and minimum active material cost.

	NdFeB Br=1.2T		**Ferrite Br=0.4T**	
	SPM	**IPM**	**SPM**	**IPM**
Axial length (m)	1.344	1.346	2.625	1.73
Active materials cost (k€)	151	158	234.7	167.5
Active material volume (m^3)	3.37	4.52	9.1	7.15
Active material mass (t)	26.9	35.6	66.5	53.6
Copper loss (kW)	157.6	170	336	221.4
MTPA current angle (elec.deg.)	-12	-36	-1	-45
Number of rotor poles	98	68	72	52
Slot depth (mm)	111.4	114	119.5	119.5
PM/barrier thickness (mm)	17.5	17.5	61.4	60.1
Number of turns per phase	1470	1564	1584	1586
Number of turns per coil	30	46	44	61
Rated current amplitude (A)	222	222	222	222
Per pole d-axis PM flux linkage (Wb)	145.3	181.5	198.5	146.7
Total d-axis PM flux linkage (Wb)	7122	6171	7147	3816
Average L_d (H)	0.42	0.9	1.32	1.43
Average L_q (H)	0.49	1.39	1.34	3.05
Power factor at rated load	0.88	0.77	0.56	0.6

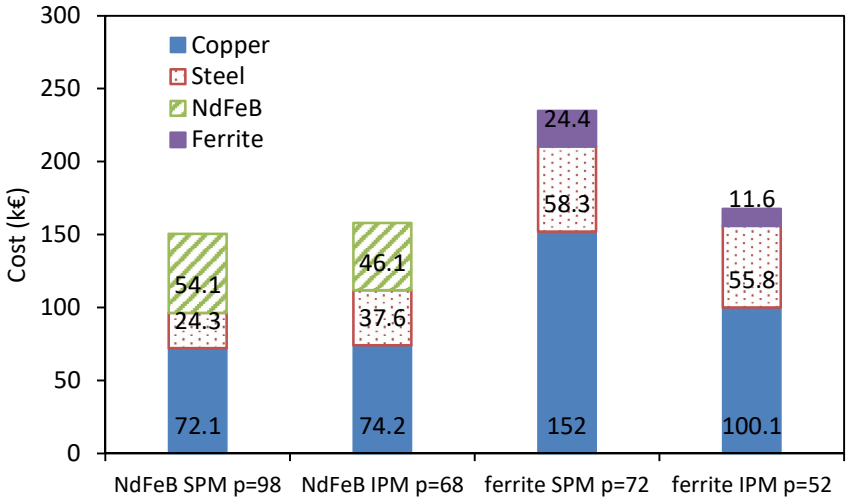

Fig. 3-31 Active material cost breakdown comparison for minimum cost SPM and IPM generators.

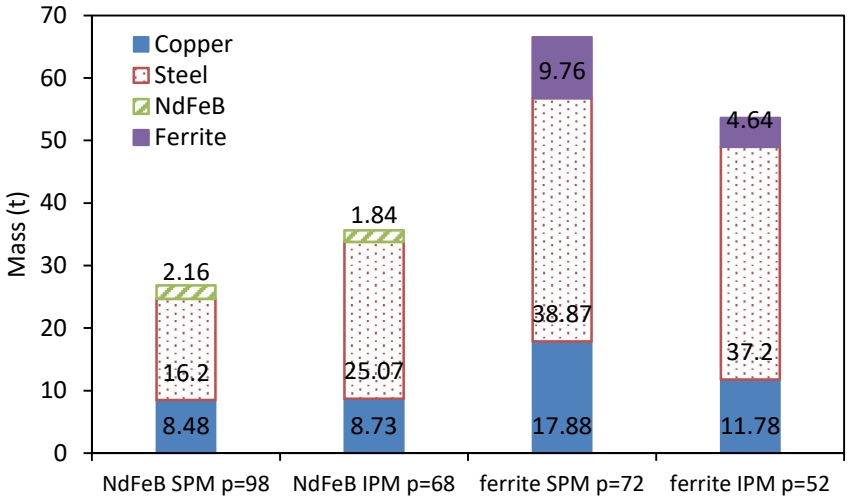

Fig. 3-32 Active material mass breakdown for minimum cost SPM and IPM generators.

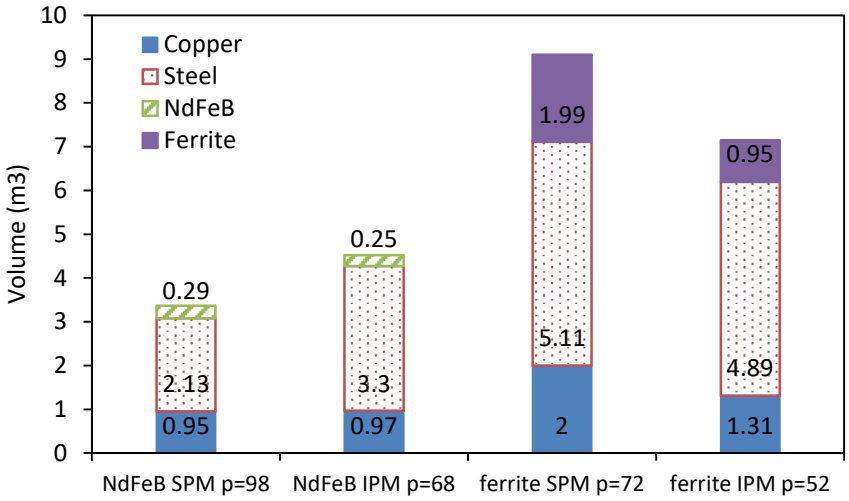

Fig. 3-33 Active material volume breakdown for minimum cost SPM and IPM generators.

3.3.3 Volume optimization with fixed current density

The maximization of the generator torque per volume is the objective for designing high torque density machines. This technique is useful for applications where the torque density is a priority i.e.: aerospace, medical industries. In this section, the SPM and IPM generators equipped with either NdFeB or ferrite magnets are optimized for maximum torque density (torque per volume).

The generators optimized for minimum volume are to be compared with the ones optimized for minimum cost in terms of both cost and volume.

3.3.3.1 Fixed current density and NdFeB magnets

The fixed current density condition used for the torque per volume optimization yields a volume vs axial length characteristic as in Fig. 3-34. For both SPM and IPM generators there exists an axial length for which the total generator volume is minimum. The volume increases monotonically with the axial length after the optimum around L_{eff}=1.4m.

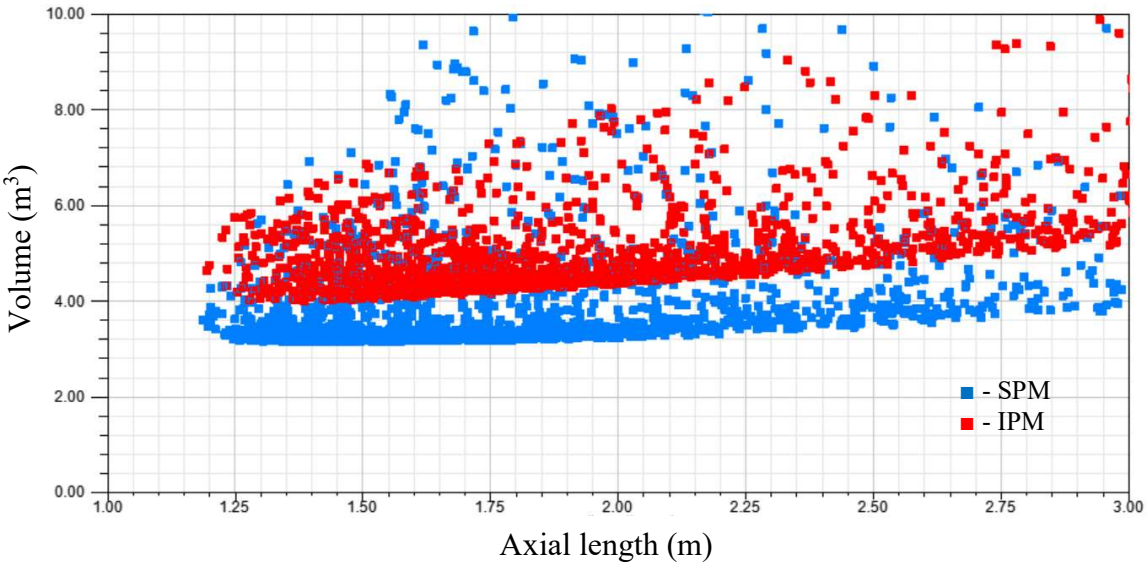

Fig. 3-34 NdFeB SPM(blue) and IPM(red) material volume vs axial length.

The optimum number of poles for minimum volume are p=140 for the SPM and p=100 for the IPM. These are significantly higher compared to to the generators optimized for minimum cost. This can be explained by the torque/volume performance characteristic which tends to increase with the number of rotor poles or when the backiron thicknesses become thinner.

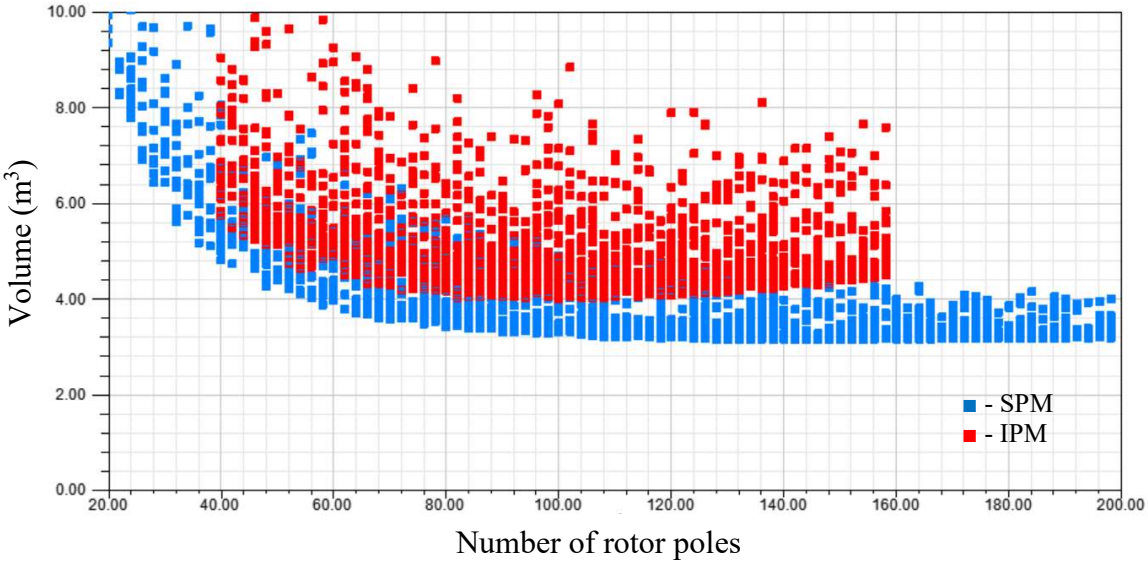

Fig. 3-35 NdFeB SPM(blue) and IPM(red) material volume vs number of rotor poles.

The volume of the SPM and IPM generators vs slot depth was plotted in Fig. 3-36. The SPM shows a flat characteristic for deep slots. The IPM can benefit from deeper slots in terms of maximizing its torque/volume as the number of poles is significantly lower compared to the SPM.

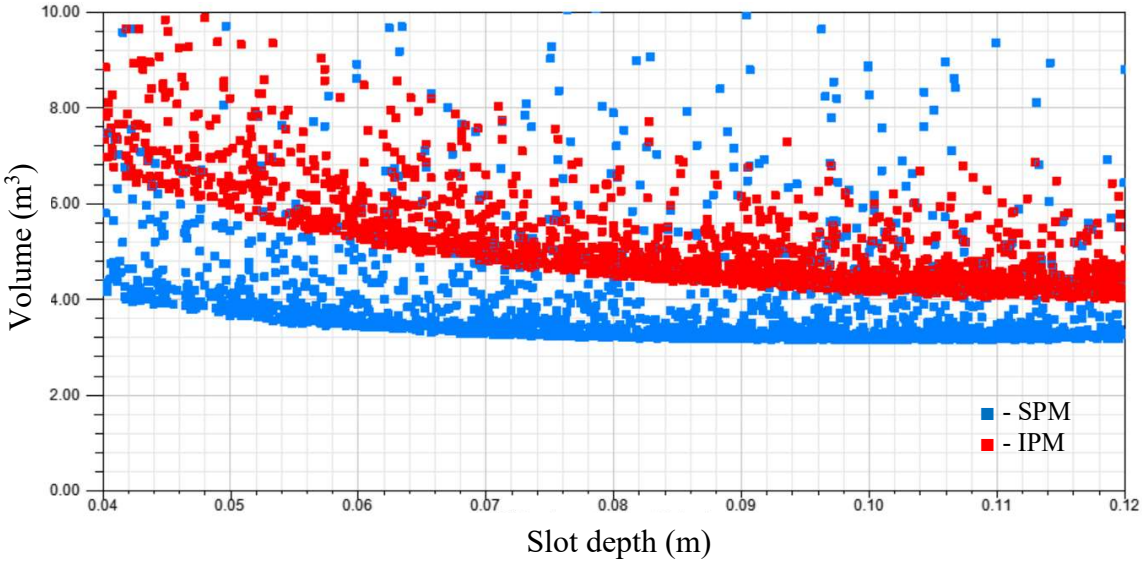

Fig. 3-36 NdFeB SPM(blue) and IPM(red) material volume vs slot depth.

The optimum PM thickness for minimum generator volume (Fig. 3-37) is closer to the upper limit of 24mm, considerably higher than the optimum PM thickness for minimum generator cost which was close to the lower limit of 15mm. This is due to the change in the ratio of the materials contribution to the optimizer cost function and will be further explained in Section 3.3.3.4.

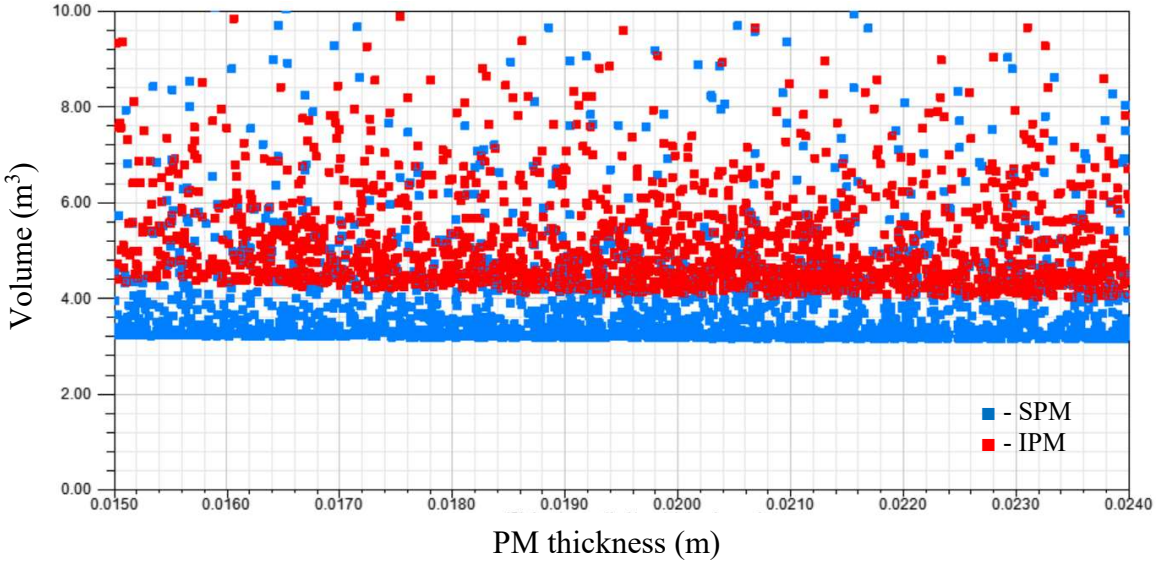

Fig. 3-37 NdFeB SPM(blue) and IPM(red) material volume vs PM thickness.

3.3.3.2 Fixed current density and ferrite magnets

The active material volumes vs axial length of the ferrite SPM and ferrite IPM generators are plotted in Fig. 3-38. The minimum volume of the ferrite IPM is lower than that of the ferrite SPM.

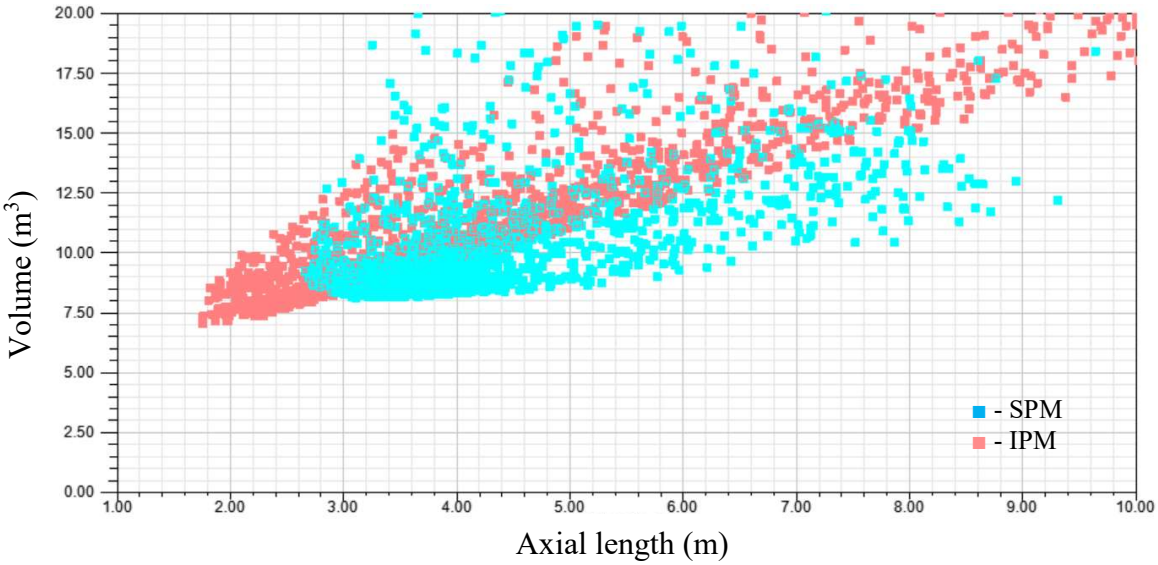

Fig. 3-38 Ferrite SPM(light-blue) and IPM(light-red) material volume vs axial length.

The optimum number of rotor poles for minimum volume is lower for the ferrite IPM generator, around p=60, compared to p=140 for the ferrite SPM. Furthermore, when increasing the number of rotor poles beyond the optimum value for minimum volume, the SPM exhibits a flat behavior while the volume of the IPM increases abruptly. The higher leakage and the reduction of the average reluctance torque with the number of poles is the cause of the lower optimum rotor pole number for the IPM topology.

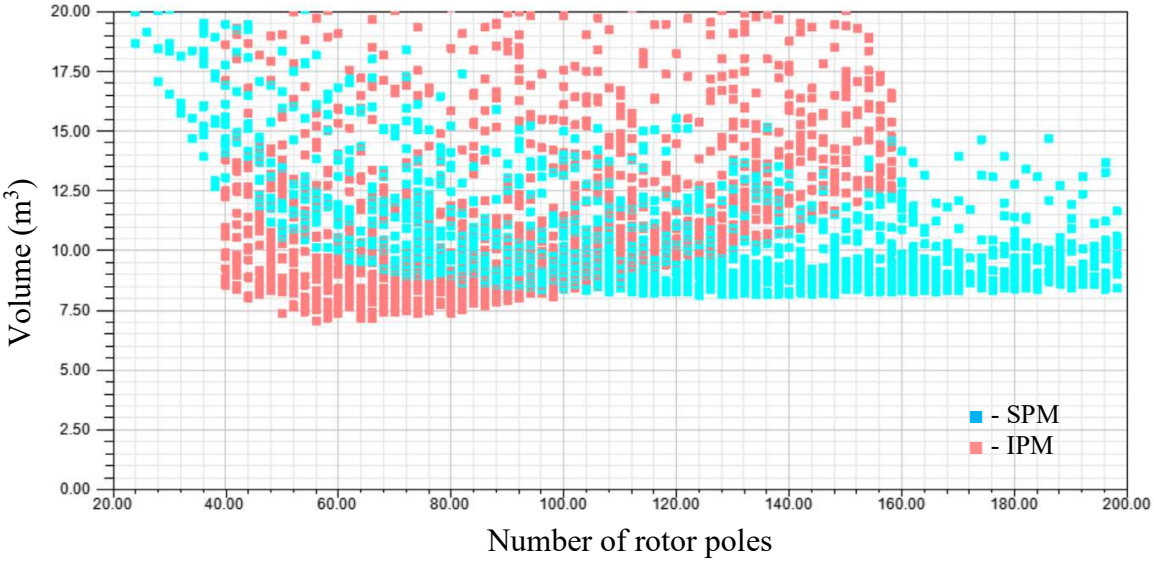

Fig. 3-39 Ferrite SPM(light-blue) and IPM(light-red) material volume vs number of rotor poles.

The SPM volume vs slot depth characteristic curve shows a flat region above 100mm. The optimum slot depth of the IPM is higher but was limited to 120mm in an effort to limit the slot leakage.

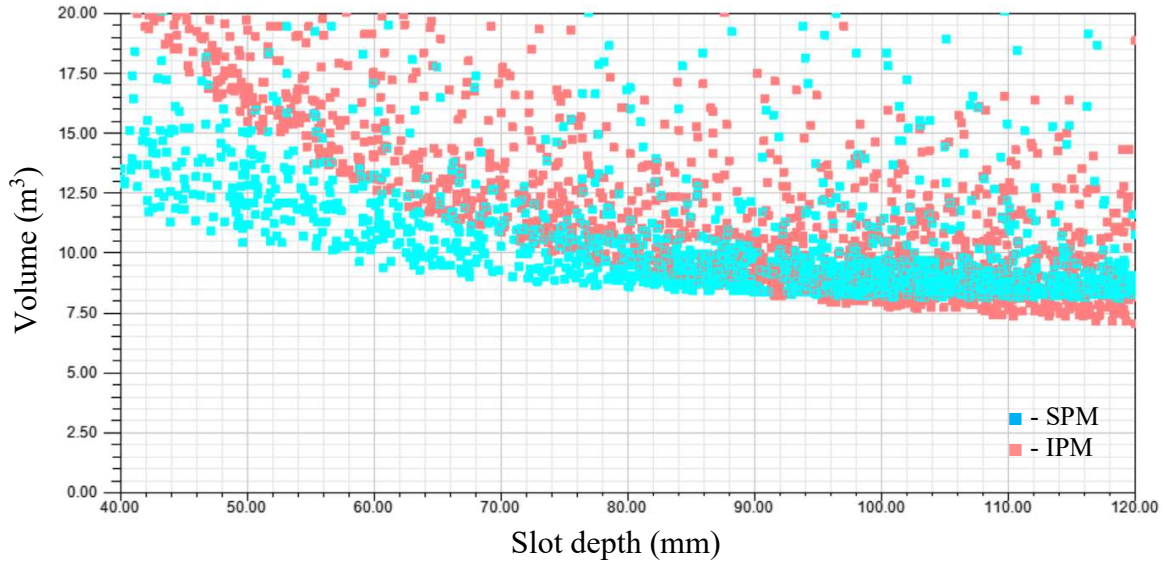

Fig. 3-40 Ferrite SPM(light-blue) and IPM(light-red) material volume vs slot depth.

The optimum PM thickness for maximum torque density of ferrite SPM generator is around 30mm for an air gap length of 5mm. Further increasing the PM thickness yields diminishing returns as the PM thickness is already 6 times larger that of the air gap length.

For the ferrite IPM generator the optimum PM thickness for minimum volume is considerably higher, around 60mm, roughly double that of the ferrite SPM generator. This is the case because, for the IPM topology, the barrier thickness influences both the average air gap flux density and the saliency. Increasing the PM barrier thickness of the IPM also yields a higher saliency.

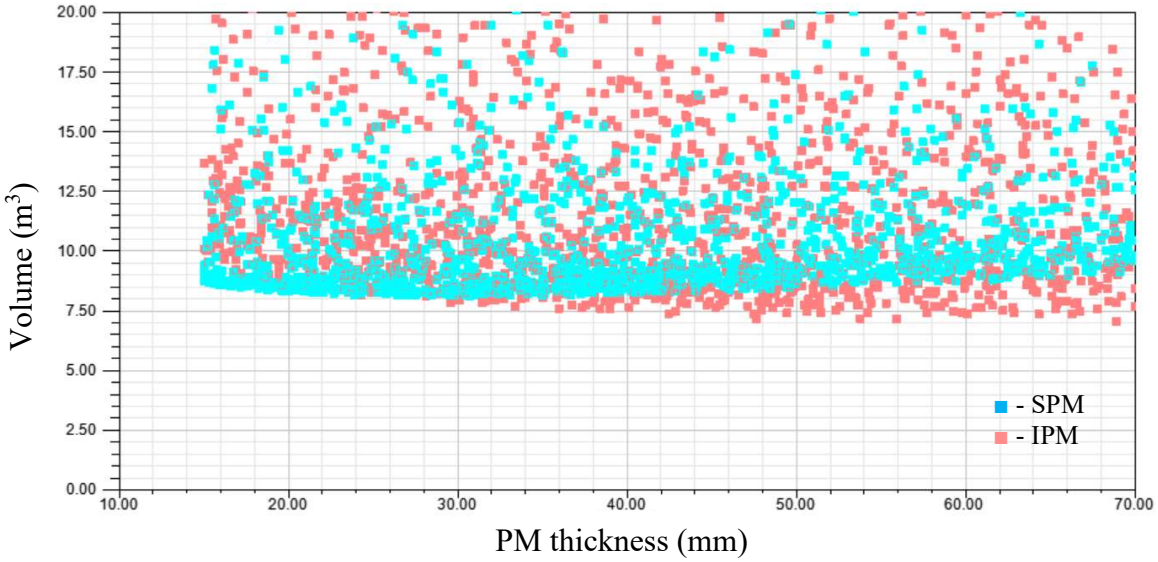

Fig. 3-41 Ferrite SPM(light-blue) and IPM(light-red) material volume vs PM thickness.

3.3.3.3 Summary of generators optimized for minimum volume

Table 3-6 summarizes the key parameter values of the SPM and IPM generators optimized for maximum torque per active material volume. In order of their active material volumes the generators are: the NdFeB SPM, NdFeB IPM, ferrite IPM and ferrite SPM.

As this optimization focuses on maximizing the torque density, the most significant difference to the generators optimized for maximum torque per cost occurs in the utilization of the most expensive material.

The generators optimized for maximum torque per volume always have a higher rotor pole number compared to the generators optimized for torque per cost. This is due to the

stator and rotor back-iron thicknesses reducing with the increase of the number of rotor poles. When optimizing for torque per cost, the thicker back-irons are not of much concern since they are made out of the cheapest material.

For the NdFeB the generators optimized for minimum volume use significantly more PM (41% extra) compared to the NdFeB generator optimized for minimum cost. Consequently, the NdFeB generators optimized for minimum volume will be roughly 9% more expensive than the one optimized for minimum cost.

For the ferrite generators, the relatively most expensive material is the copper winding. Hence, the ferrite generators optimized for torque per volume will use more copper and less PM compared to the ferrite generators optimized for torque per cost. This effect is opposite to that for the NdFeB generators.

Table 3-6 Optimum parameters of SPM and IPM generators with equal average torque capabilities and minimum active material volume.

	NdFeB Br=1.2T		**Ferrite Br=0.4T**	
	SPM	**IPM**	**SPM**	**IPM**
Axial length (m)	1.4	1.38	3.1	1.76
Active materials cost (k€)	165.8	167.3	244.8	168.6
Active material volume (m^3)	3.07	3.98	8.08	7.08
Active material mass (t)	24.55	31.64	61.42	52.77
Copper loss (kW)	151.6	175.1	394.8	226.4
MTPA current angle (elec.deg.)	-12	-36	-3	-45
Number of rotor poles	146	100	124	56
Slot depth (mm)	101.1	118.4	118.8	120
PM/barrier thickness (mm)	23.85	23.64	30.67	68.87
Number of turns per phase	1350	1580	1587	1602
Number of turns per coil	18.5	31.6	25.6	57.2
Rated current amplitude (A)	222	222	222	222
Per pole d-axis PM flux linkage (Wb)	96.72	125.1	114.4	134.7
Total d-axis PM flux linkage (Wb)	7060	6255	7092	3772
Average Ld (H)	0.23	0.6	1.16	1.32
Average Lq (H)	0.31	1	1.19	2.77
Power factor at rated load	0.89	0.77	0.41	0.58

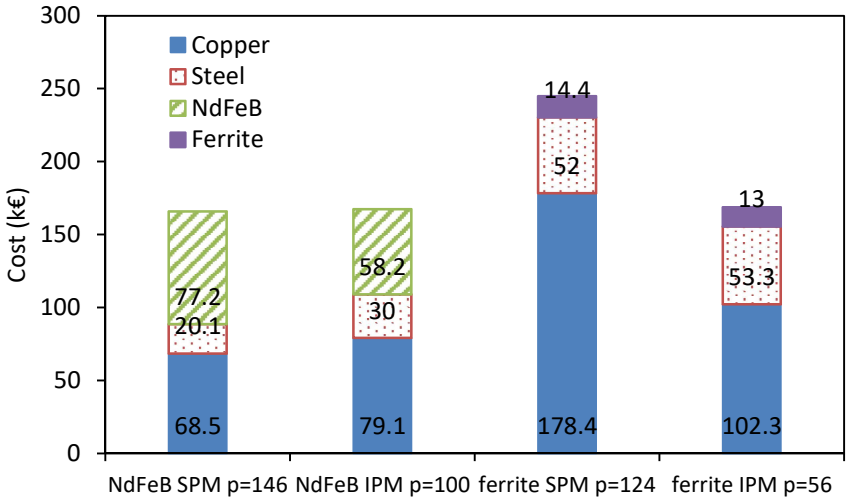

Fig. 3-42 Active material cost breakdown for minimum volume SPM and IPM generators.

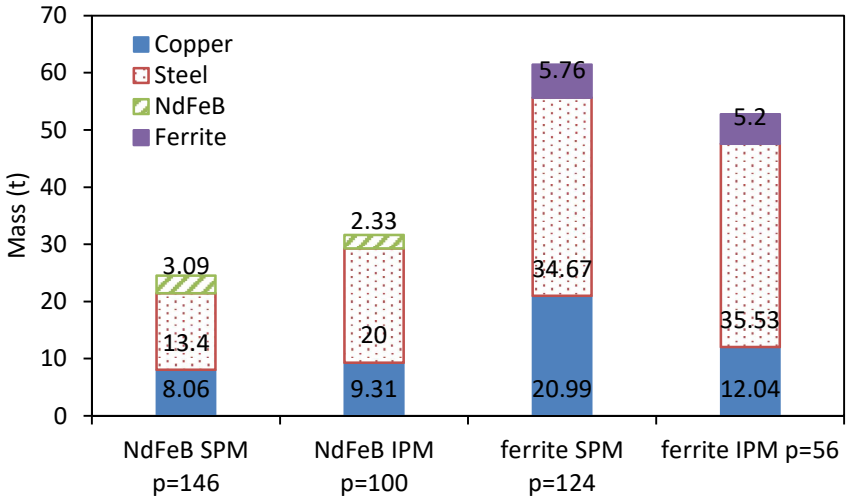

Fig. 3-43 Active material mass breakdown for minimum volume SPM and IPM generators.

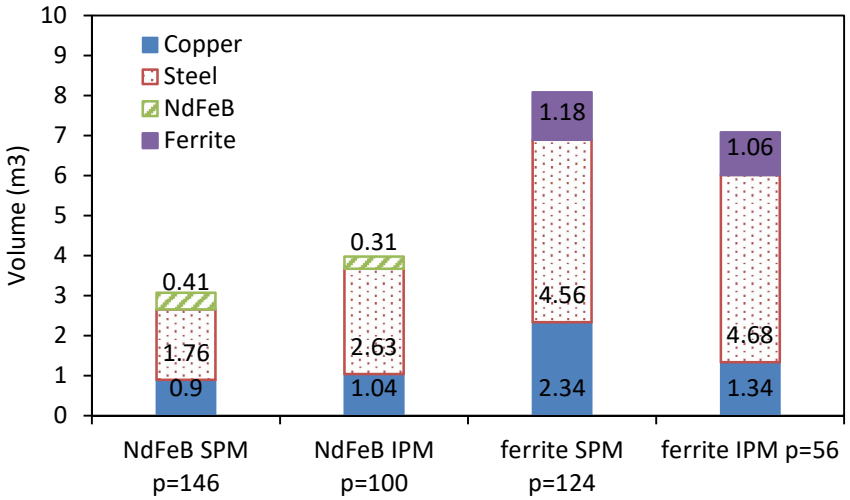

Fig. 3-44 Active material volume breakdown for minimum cost SPM and IPM generators.

3.3.3.4 Comparison of optimization populations for minimum cost and minimum mass

A genetic optimization algorithm was used for the torque per cost, torque per volume and torque per mass optimizations. The genetic optimization algorithm varies the parameters randomly and assigns a higher priority in the reproductive setup to the fitter individuals (lower cost).

This design technique is not only useful for finding the set of optimum parameter values which maximize a particular performance metric, but can also be used to investigate the influence of key parameters on the cost function like in section 3.3.

In this section, the cost of the generators optimized for minimum volume is presented versus axial length and versus the number of rotor poles. The idea is that even though the optimization targets are different (i.e. torque/volume and torque/cost), the cost vs axial length and cost vs the number of rotor pole characteristic curves exhibit identical minimum envelopes as seen in Fig. 3-21, Fig. 3-22 and in Fig. 3-45, Fig. 3-46.

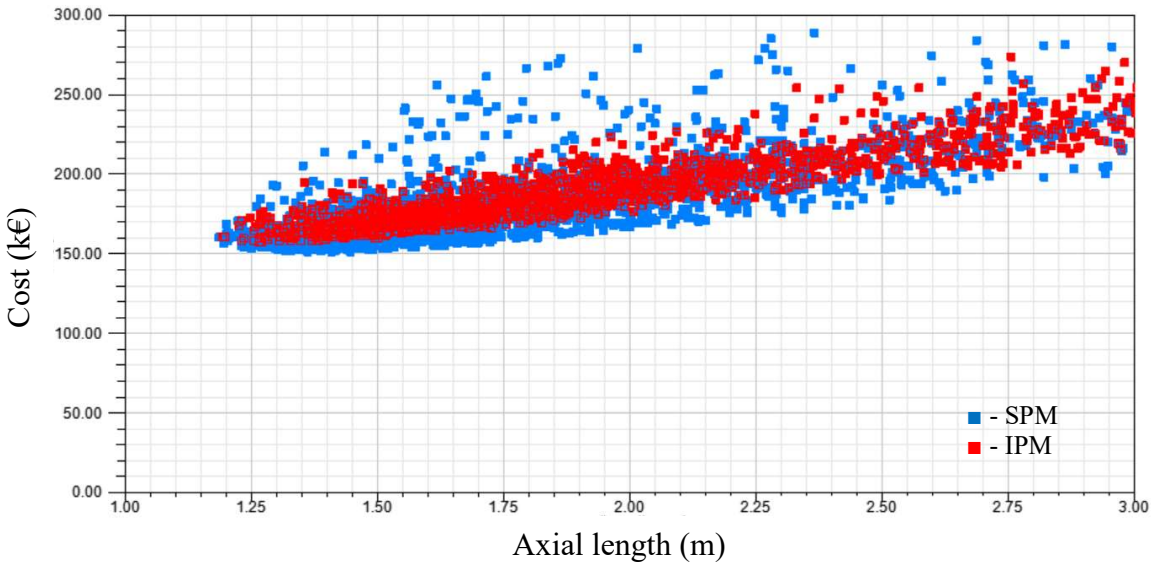

Fig. 3-45 Cost of NdFeB SPM(blue) and IPM(red) optimized for minimum material volume vs axial length.

Even though the optimum number of rotor poles of the NdFeB SPM optimized for minimum volume is around p=140 (Fig. 3-35), plotting the cost vs number of rotor poles of the same population optimized for minimum volume, one would find the optimum number of poles for minimum cost around p=70, exactly like the result during the cost minimization optimization. Similarly for the NdFeB IPM, the optimum number of poles for minimum volume is around p=100 (Fig. 3-35). If the cost of same population is plotted versus the number of rotor poles (Fig. 3-46), the optimum pole number for minimum cost is around p=70, like the one found during the torque/cost optimization (Fig. 3-22).

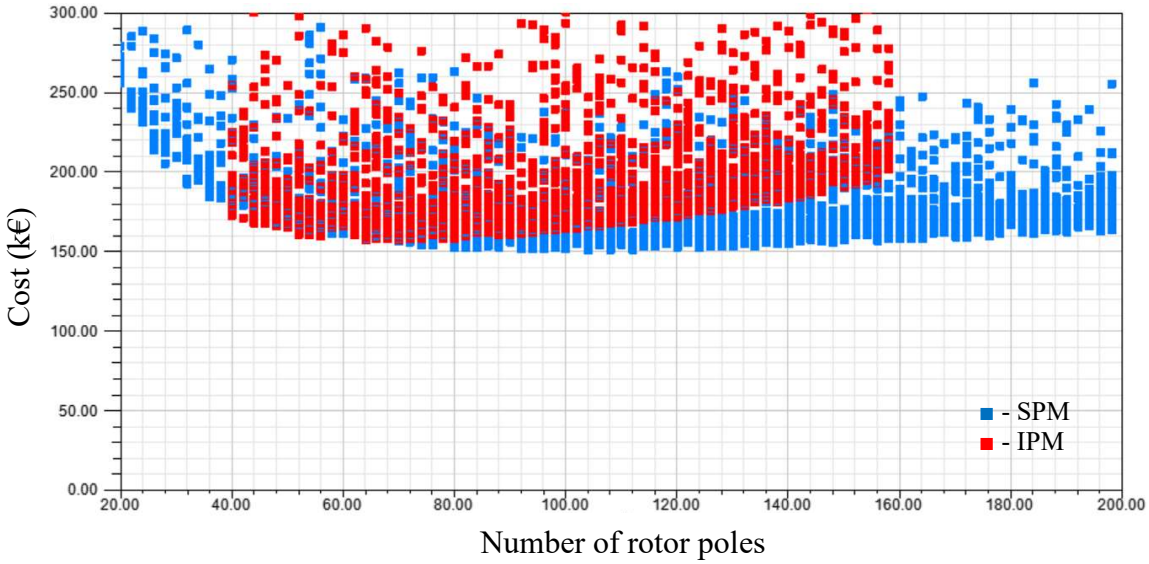

Fig. 3-46 Cost of NdFeB SPM(blue) and IPM(red) optimized for minimum material volume vs number of rotor poles.

In terms of cost vs axial length and cost vs number of rotor poles, the ferrite SPM and IPM generators optimized for minimum volume exhibit the same minimum envelopes as the ferrite generators optimized for minimum material cost as seen in Fig. 3-23, Fig. 3-24 and in Fig. 3-47, Fig. 3-48.

In general, any performance metric versus any parameter characteristic curve will have the same minimum envelope regardless of the optimization objective. The location of the minimums will depend on the optimization conditions and setup.

The genetic optimization algorithm varies the parameters randomly, and thus, the resulting generators have a wide range of parameters values. Furthermore, the genetic optimization converges due to the higher priority of the fitter individuals in the reproductive setup, a natural numerical optimization technique which has the inherited benefit of being less likely to stop at a local optimum. In contrast, the traditional pattern search optimization algorithm investigates the rate of change of the cost function with the parameter values and tries to identify the highest rate of increase for the fitness (or decrease of cost). This makes the pattern search algorithm susceptible to stopping at local minimums and makes it less likely that the population during a pattern search will have parameter values spanning along the whole range.

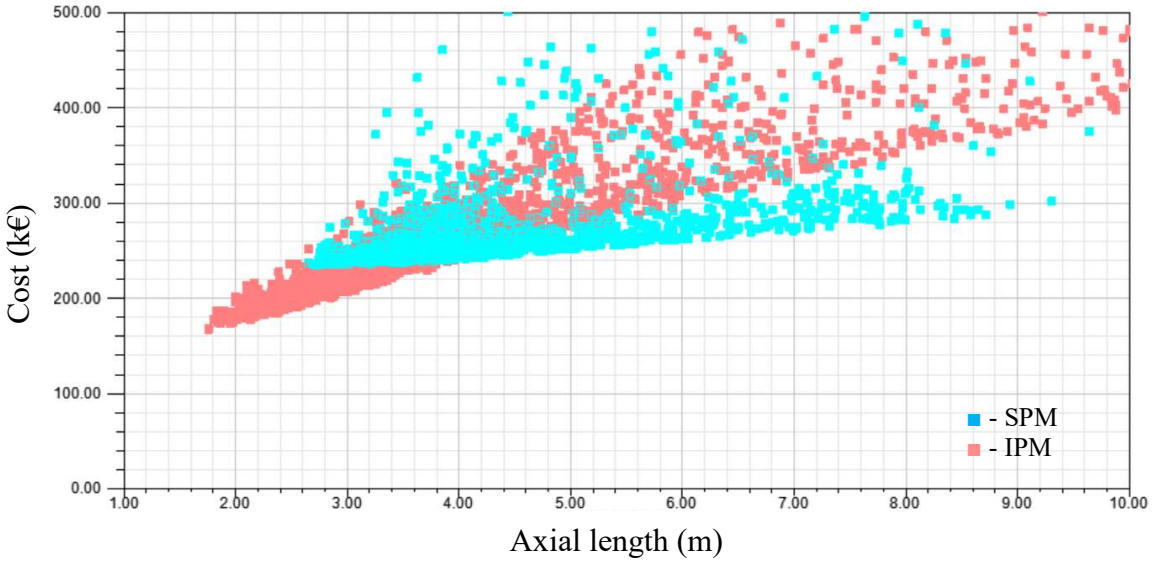

Fig. 3-47 Cost of ferrite SPM(light-blue) and IPM(light-red) optimized for minimum material volume vs axial length.

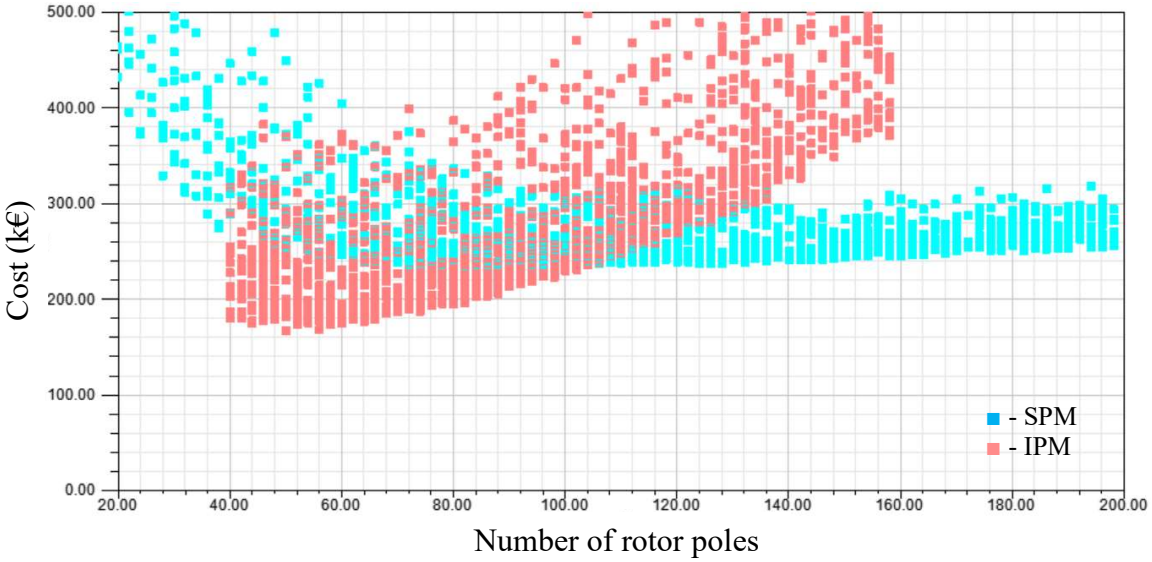

Fig. 3-48 Cost of ferrite SPM(light-blue) and IPM(light-red) optimized for minimum material volume vs number of poles.

3.3.4 Mass optimization with fixed current density

3.3.4.1 Fixed current density and NdFeB magnets

The mass of the generators equipped with NdFeB are plotted vs axial length in Fig. 3-49. The IPM generators are heavier, weighting a minimum of around 32t while the SPM only weight about 25t. The total mass of the generators increases when a shorter slot depth and a longer axial length are used to produce the same average output torque.

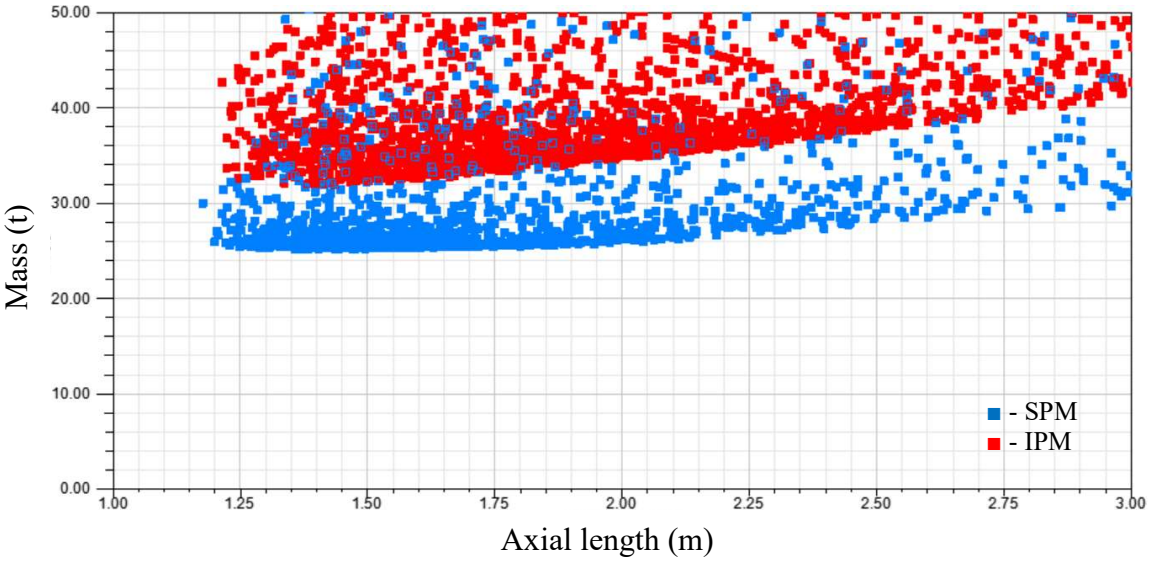

Fig. 3-49 NdFeB SPM(blue) and IPM(red) material volume vs axial length.

When optimized for minimum mass the optimum number of rotor poles for the NdFeB generators are p=138 for the SPM and p=112 for the IPM, similar to p=146 and p=100 for the SPM and IPM optimized for minimum volume. Furthermore, this optimum number of poles is considerably higher than when the optimization process is minimizing the total cost as in Section 3.3.2, where p=98 for SPM and p=68 for IPM.

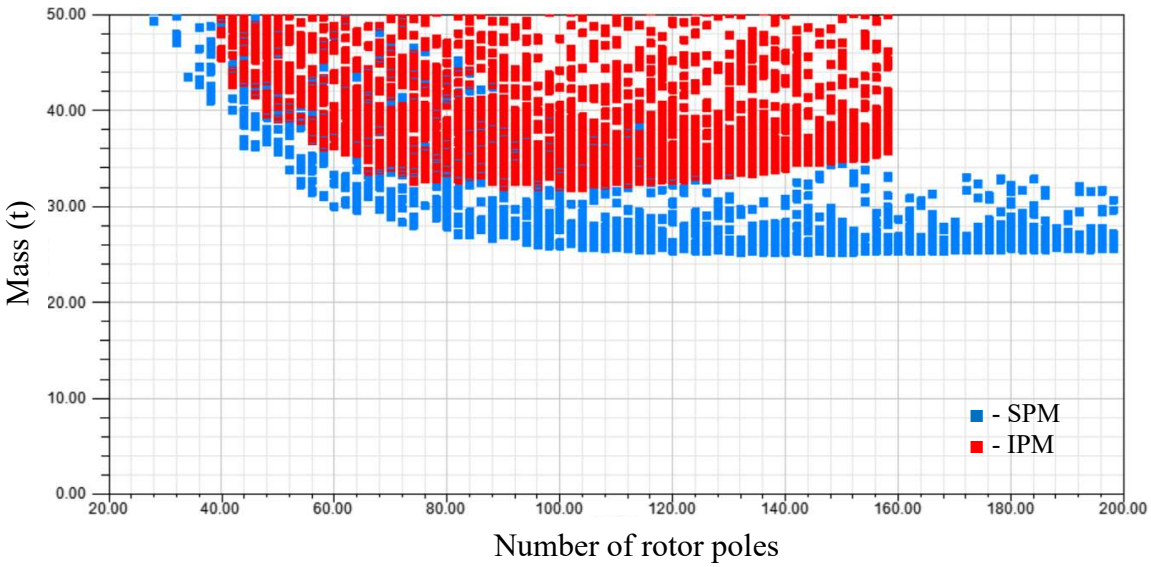

Fig. 3-50 NdFeB SPM(blue) and IPM(red) material volume vs number of rotor poles.

The optimum slot depths for minimum costs are around 110mm for the SPM and around 120mm for the IPM, owing to the lower number of rotor poles. They exhibit a flat behavior vs cost in the optimum region which spans across a wider range for the SPM.

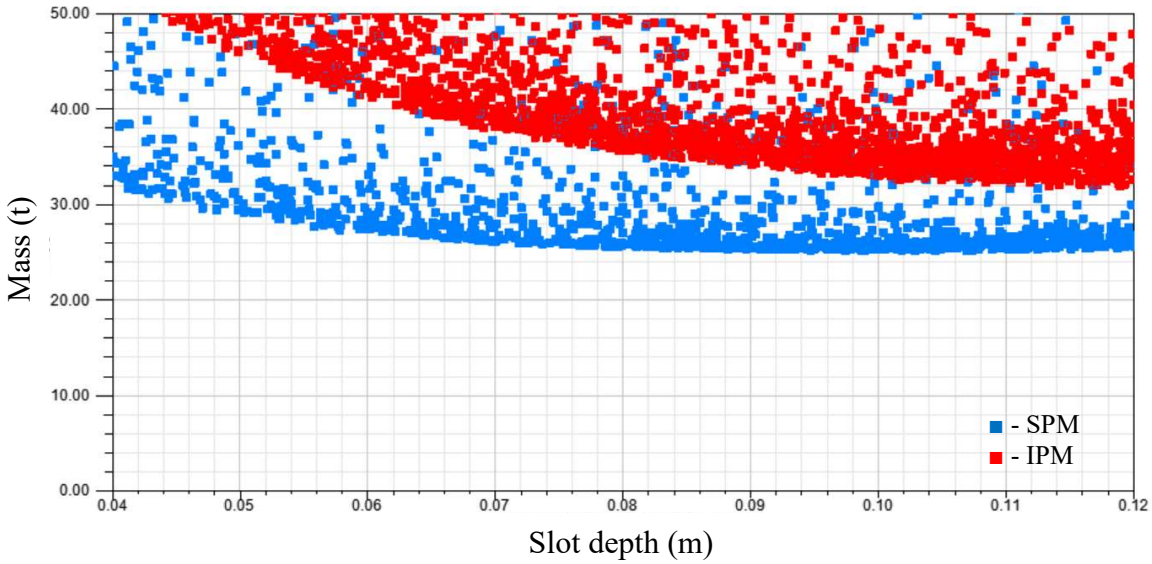

Fig. 3-51 NdFeB SPM(blue) and IPM(red) material volume vs slot depth.

The optimum PM thicknesses for the minimum mass NdFeB generators tend towards the upper limit, 24mm, similarly to the generators optimized for minimum volume. This is because the optimizer can slightly reduce the total mass by increasing the amount of rare earth magnet material. However, this will yield a more expensive generator.

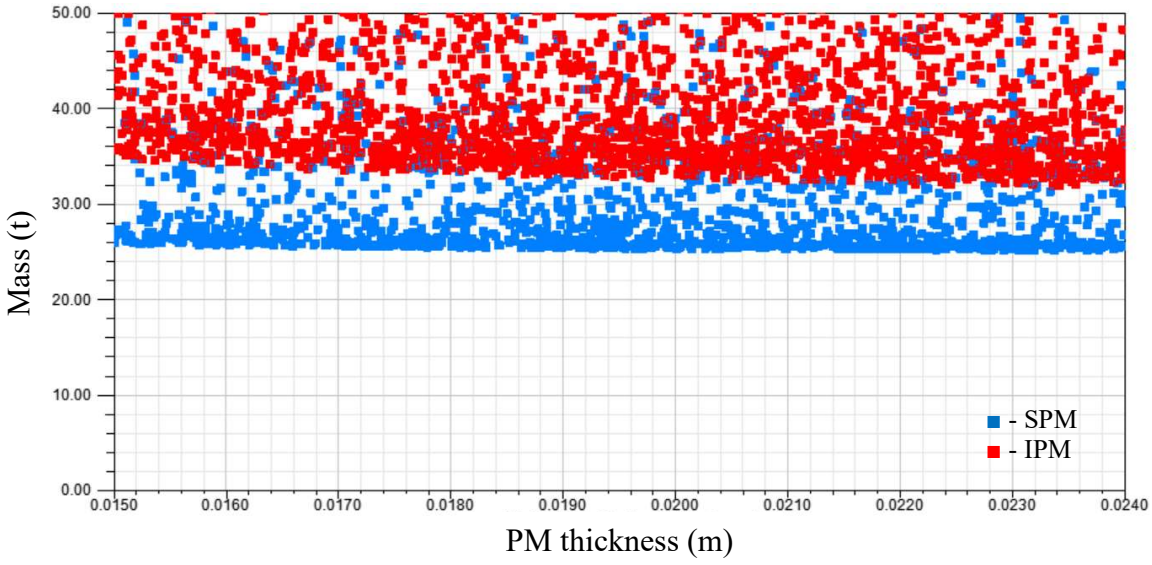

Fig. 3-52 NdFeB SPM(blue) and IPM(red) material volume vs PM thickness.

3.3.4.2 Fixed current density and ferrite magnets

For generators equipped with ferrite magnets, the IPM topology is lighter and shorter compared to the SPM. This is because the average reluctance torque contribution is of comparable amplitude to the PM torque when using the lower energy product ferrite magnets. The reluctance torque goodness ratio $R/R_{required}>1$ for the ferrite IPM generator. The ferrite IPM generator is thus lighter and shorter compared to the ferrite SPM, as there is more than enough direct to quadrature inductance difference to compensate for the lower PM alignment torque.

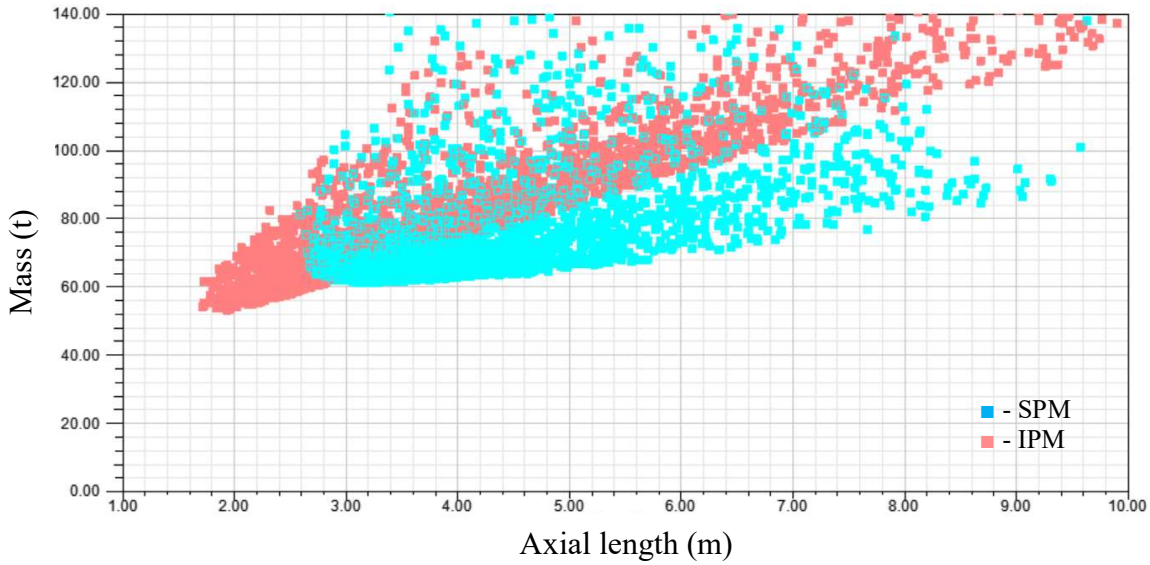

Fig. 3-53 Ferrite SPM(light-blue) and IPM(light-red) material volume vs axial length.

The optimum number of rotor poles for minimum mass is similar to the optimum for minimum volume and higher than the optimum for minimum cost. For the minimum mass, the optimum number of poles is p=124 for the SPM and p=66 for the IPM.

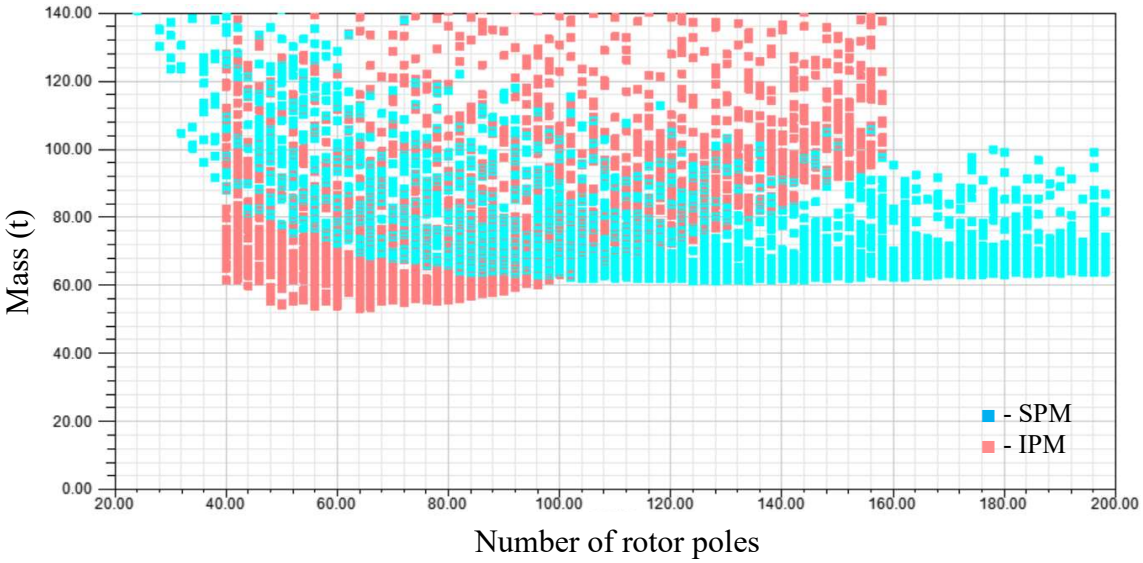

Fig. 3-54 Ferrite SPM(light-blue) and IPM(light-red) material volume vs number of rotor poles.

The slot depth vs cost characteristic in Fig. 3-55 are flat for p>100 for the SPM. The optimum slot depth for the minimum cost IPM generators is slightly higher, around 120mm due to their lower optimum pole number which alleviates the stator leakage.

In Fig. 3-56 the optimum PM thickness of the SPM is significantly lower than that of the IPM. For the SPM the optimum PM thickness will be limited to a value where the air gap flux density is close to B_r. For the IPM, increasing the PM barrier thickness beyond this point will yield an increase of the average reluctance torque as it decreases the direct axis inductance and thus enhances the direct to quadrature inductance difference. This causes the optimum barrier thickness of the ferrite IPM generator to be significantly higher than that of the ferrite SPM generator as seen in Fig. 3-56.

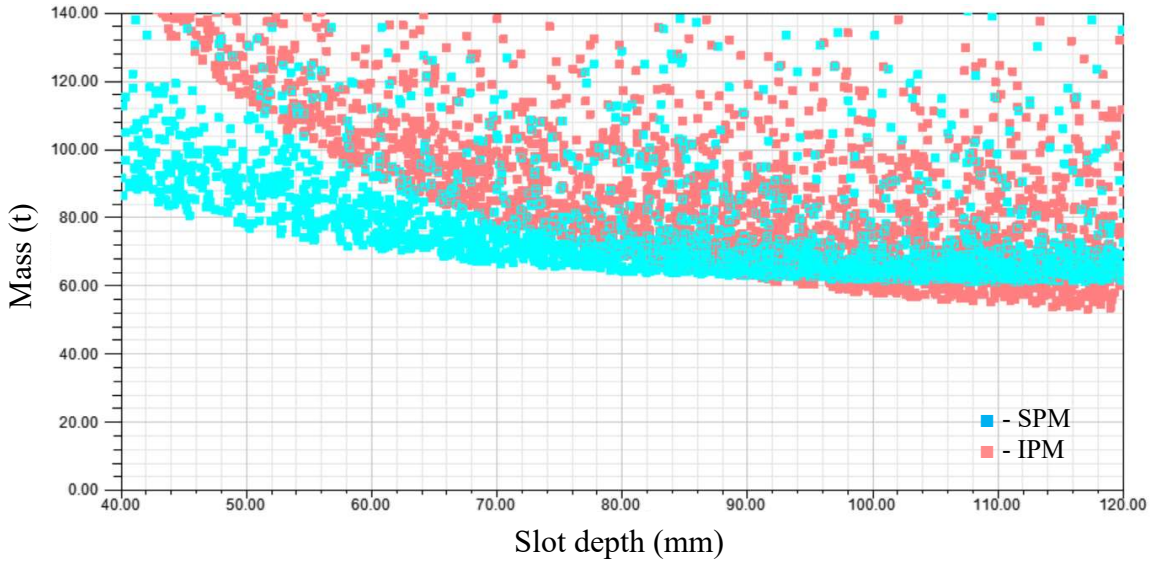

Fig. 3-55 Ferrite SPM(light-blue) and IPM(light-red) material volume vs slot depth.

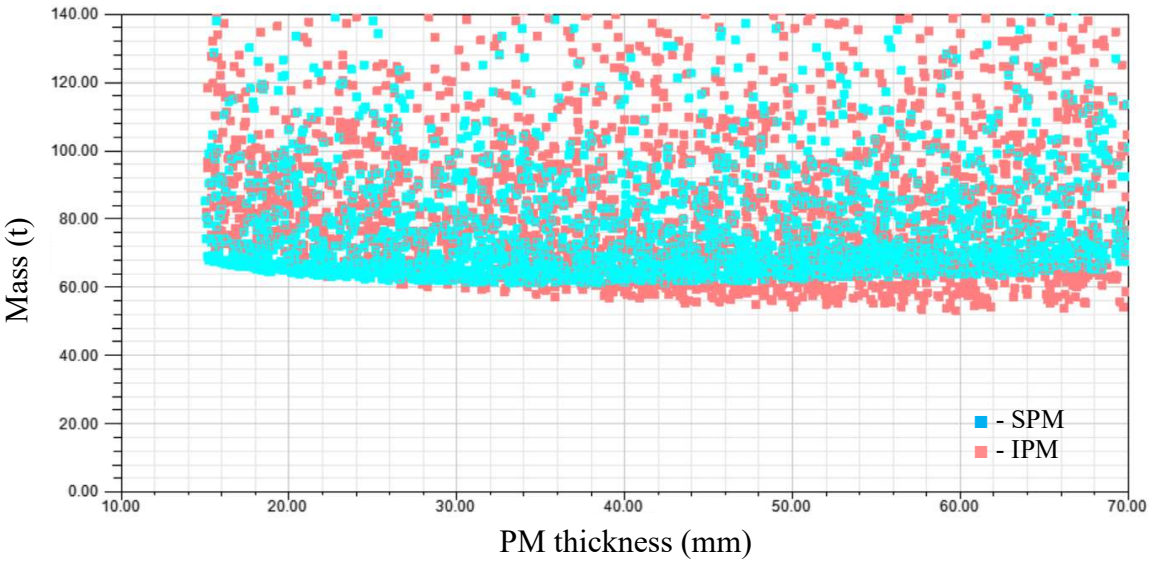

Fig. 3-56 Ferrite SPM(light-blue) and IPM(light-red) material volume vs PM thickness.

3.3.4.3 Summary of generators optimized for minimum mass

Table 3-7 presents the key parameter values of the SPM and IPM generators optimized for maximum torque per active material mass.

The generators obtained using the torque per mass optimization technique have similar parameters to the generators optimized for torque per volume. This can be explained by referring to Table 3-9 and the normalized volume and normalized mass columns. For

the torque per mass optimization, the cost of NdFeB relative to the steel is the same as in the torque per volume optimization. The highest relative cost of any material vs another material is 1 for the torque per volume optimization, 1.83 for the torque per mass optimization (1.2 if ferrite is disregarded) and 16.45 for the torque per cost optimization. This indicates that, in fact, the torque per volume and torque per mass optimization objectives are similar as relative contribution of the materials to each optimization cost function is similar.

Table 3-7 Optimum parameters of SPM and IPM generators with equal average torque capabilities and minimum active material mass.

	NdFeB Br=1.2T		**Ferrite Br=0.4T**	
	SPM	**IPM**	**SPM**	**IPM**
Axial length (m)	1.34	1.54	3.13	1.952
Active materials cost (k€)	160.8	175.7	237.9	177.1
Active material volume (m^3)	3.07	4.05	8.15	7.13
Active material mass (t)	24.53	32.23	61.01	53.35
Copper loss (kW)	153.6	179	373.7	247.1
MTPA current angle (elec.deg.)	-12	-33	-3	-45
Number of rotor poles	138	112	124	66
Slot depth (mm)	106.9	108.4	111.3	118.1
PM/barrier thickness (mm)	22.9	23.9	37.9	61.3
Number of turns per phase	1428.3	1450	1488	1578
Number of turns per coil	20.7	25.9	24	47.8
Rated current amplitude (A)	222	222	222	222
Per pole d-axis PM flux linkage (Wb)	102.2	113	114.5	116.6
Total d-axis PM flux linkage (Wb)	7052	6328	7099	3847.8
Average Ld (H)	0.26	0.51	1.01	1.26
Average Lq (H)	0.35	0.84	1.04	2.48
Power factor at rated load	0.89	0.77	0.45	0.55

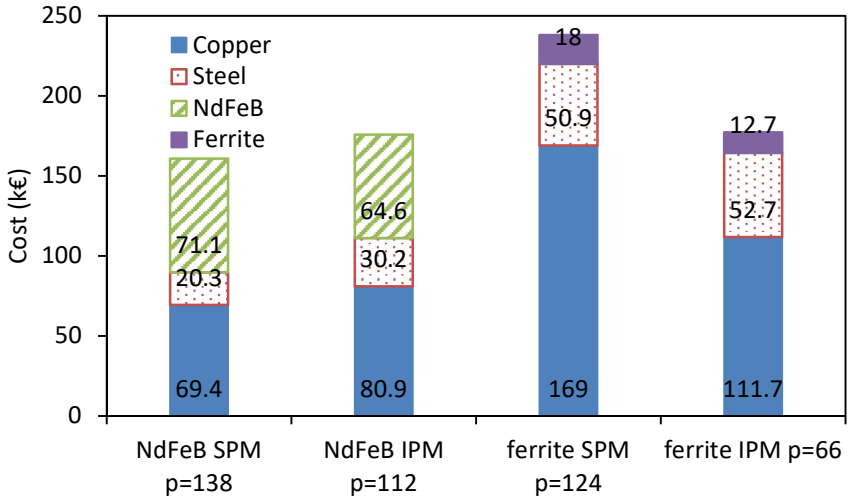

Fig. 3-57 Active material cost breakdown for minimum mass SPM and IPM generators.

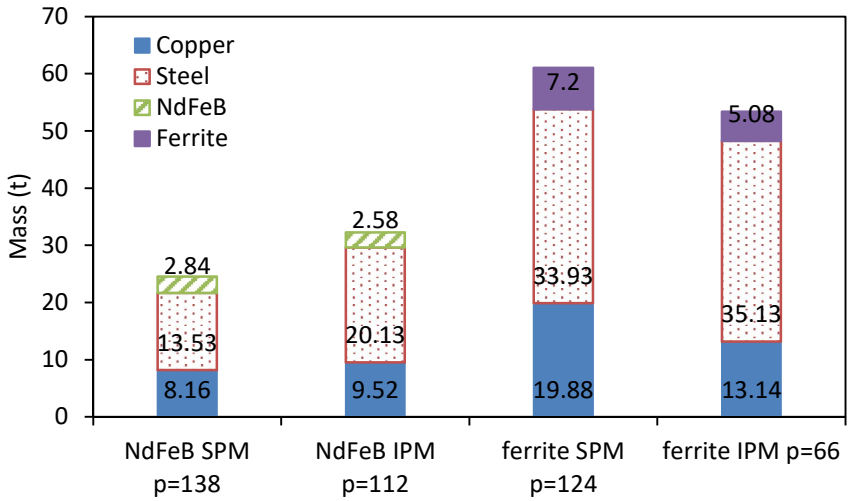

Fig. 3-58 Active material mass breakdown for minimum mass SPM and IPM generators.

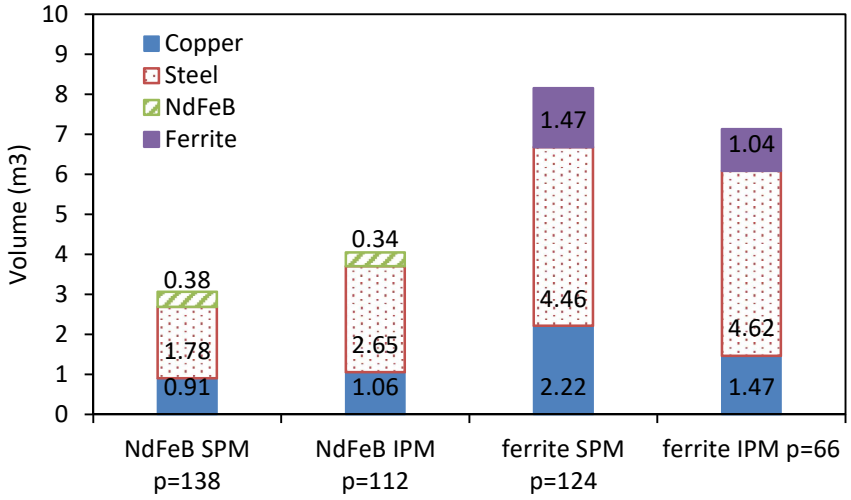

Fig. 3-59 Active material volume breakdown for minimum mass SPM and IPM generators.

3.3.5 Cross sections and trimetric views of machines optimized for minimum cost

The specification, parameters and performance of the minimum cost machines are summarized in Table 3-8. Cross sections of the minimum cost machines are shown in Fig. 3-60 - Fig. 3-63. Trimetric views are presented in Fig. 3-64.

Table 3-8 Optimum parameters of SPM and IPM generators with equal average torque capabilities and minimum active material cost.

	NdFeB Br=1.2T		**Ferrite Br=0.4T**	
	SPM	**IPM**	**SPM**	**IPM**
Axial length (m)	1.344	1.346	2.625	1.73
Active materials cost (k€)	151	158	234.7	167.5
Active material volume (m^3)	3.37	4.52	9.1	7.15
Active material mass (t)	26.9	35.6	66.5	53.6
Copper loss (kW)	157.6	170	336	221.4
MTPA current angle (elec.deg.)	-12	-36	-1	-45
Number of rotor poles	98	68	72	52
Slot depth (mm)	111.4	114	119.5	119.5
PM/barrier thickness (mm)	17.5	17.5	61.4	60.1
Number of turns per phase	1490	1574	1595	1596
Number of turns per coil	30.4	46.3	44.3	61.4
Rated current amplitude (A)	222	222	222	222
Per pole d-axis PM flux linkage (Wb)	145.3	181.5	198.5	146.7
Total d-axis PM flux linkage (Wb)	7122	6171	7147	3816
Average Ld (H)	0.42	0.9	1.32	1.43
Average Lq (H)	0.49	1.39	1.34	3.05
Power factor at rated load	0.88	0.77	0.56	0.6

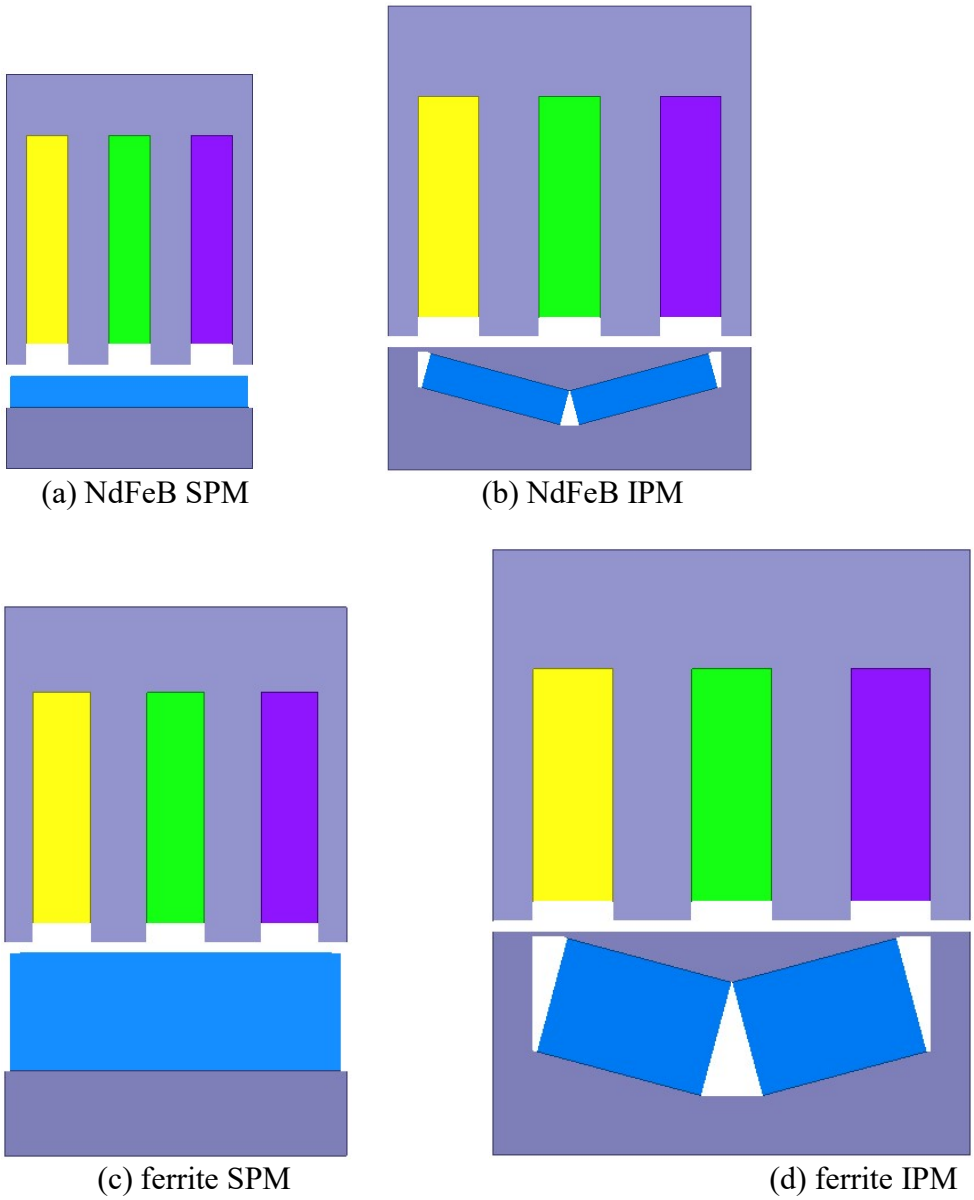

Fig. 3-60 Cross section of periodic unit of minimum cost SPM and IPM generators (to scale).

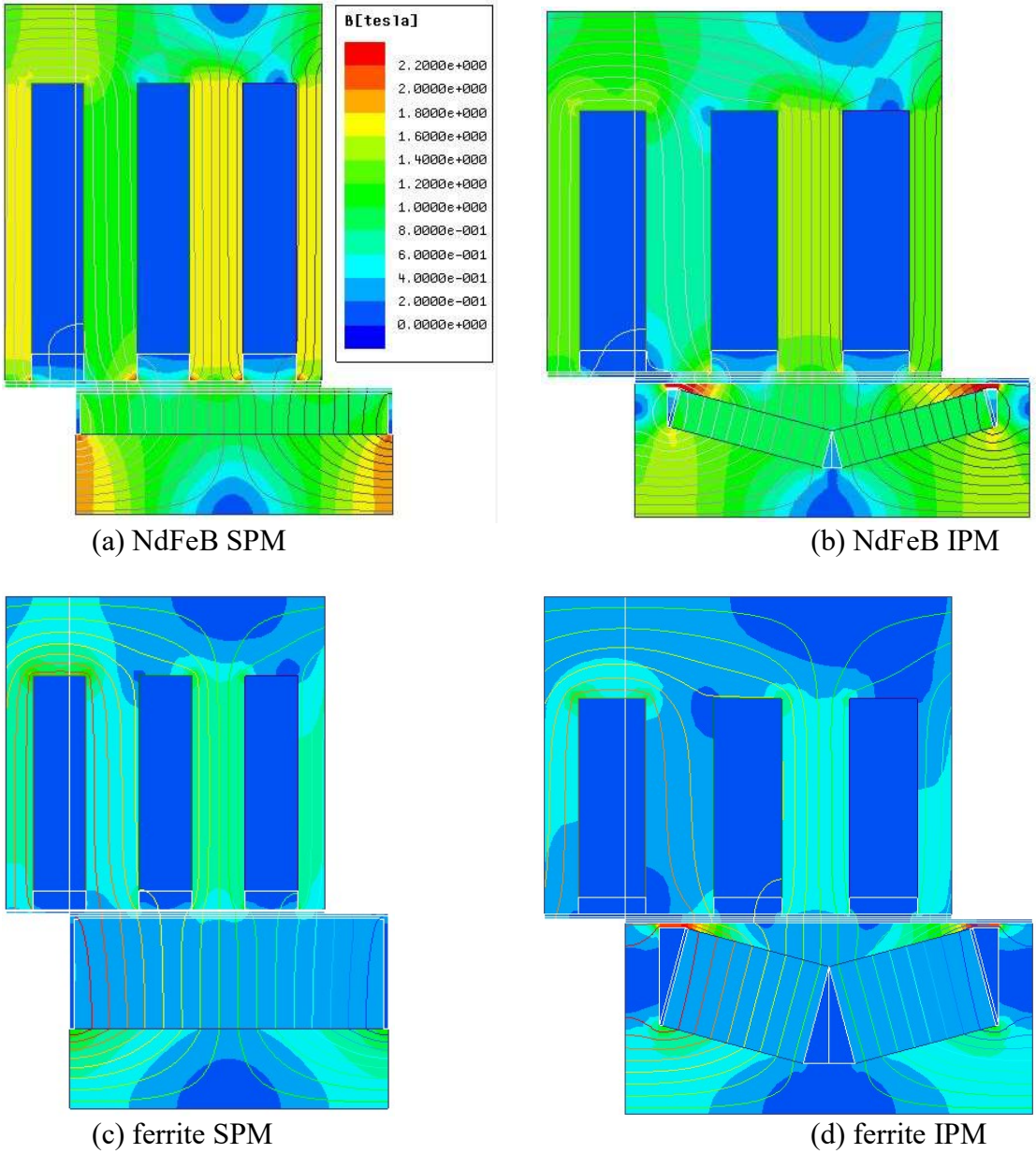

Fig. 3-61 Cross section of minimum cost SPM and IPM generators with equal flux lines and contour plot of flux density at open circuit.

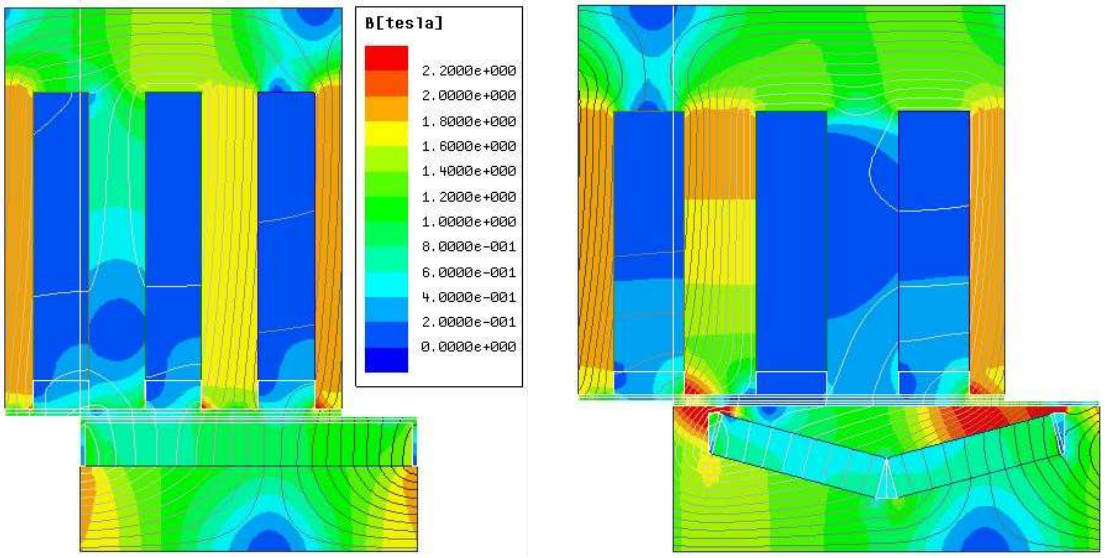

(a) NdFeB SPM (b) NdFeB IPM

(c) ferrite SPM (d) ferrite IPM

Fig. 3-62 Cross section of minimum cost SPM and IPM generators with equal flux lines and contour plot of flux density at rated load. SPM load: Ir=222A, β=-10°; IPM load: Ir=222, β=-30°.

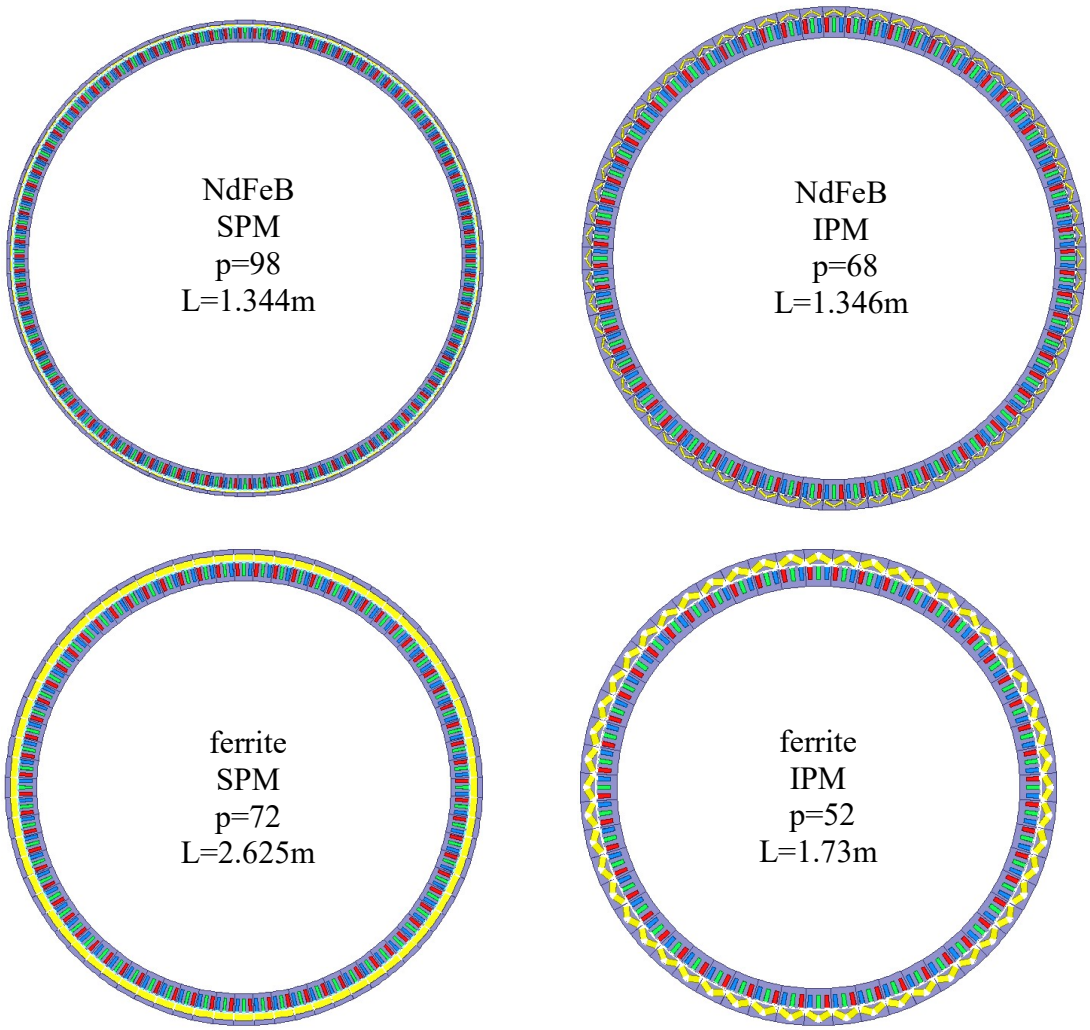

Fig. 3-63 Cross sectional view of minimum cost SPM and IPM generators equipped with NdFeB and ferrite PM.

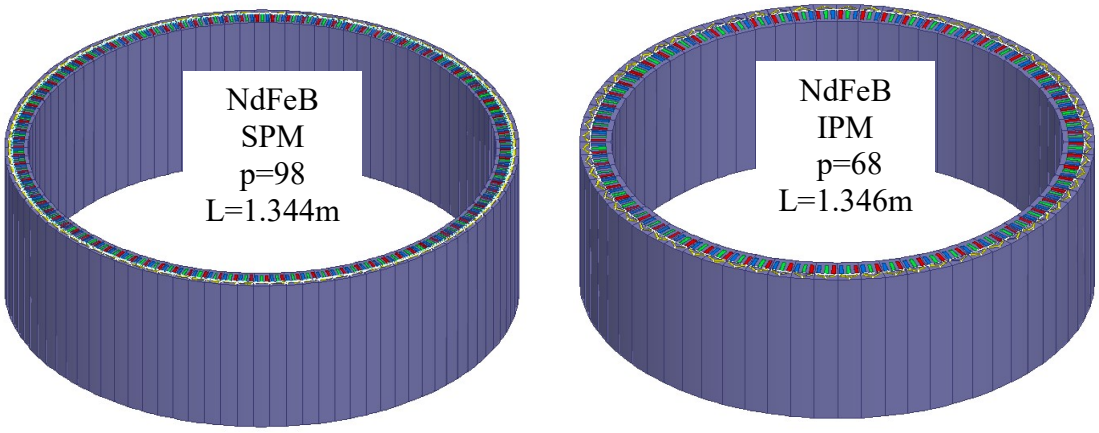

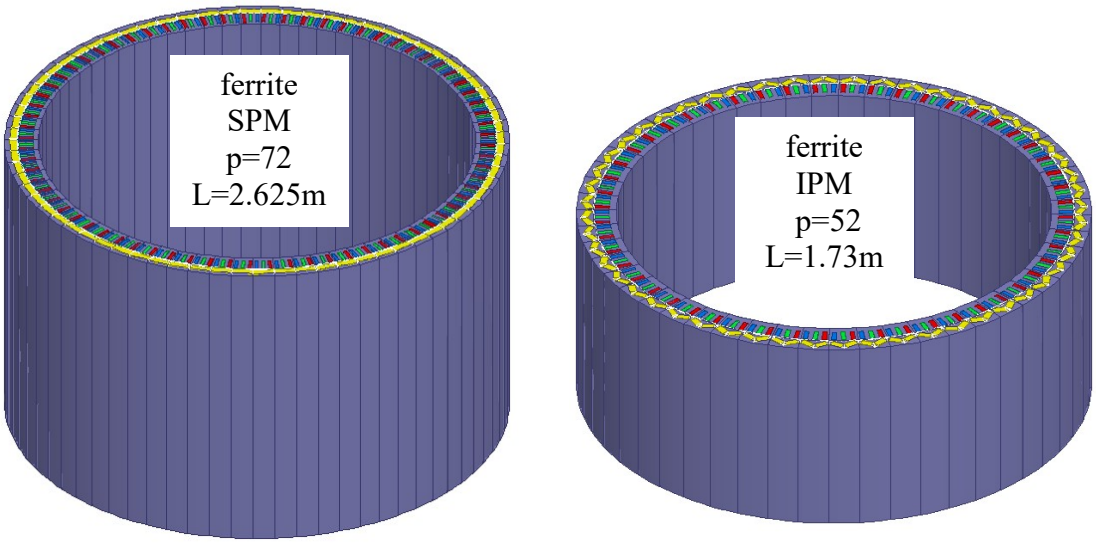

Fig. 3-64 Trimetric view of minimum cost SPM and IPM generators equipped with NdFeB and ferrite PM.

3.3.6 Cost, volume and mass of all optimized generator

3.3.6.1 Cost

The cost optimization yields the minimum cost generators for both NdFeB/ferrite and SPM/IPM as seen in Fig. 3-65 - Fig. 3-69. The torque per cost optimization reveals that the NdFeB SPM is the best candidate for a DD application as the required materials have the minimum total cost.

The cost of NdFeB in the minimum cost generators is lower than that of the generators optimized for volume or mass and vice versa for the cost of the ferrite in the minimum cost generators.

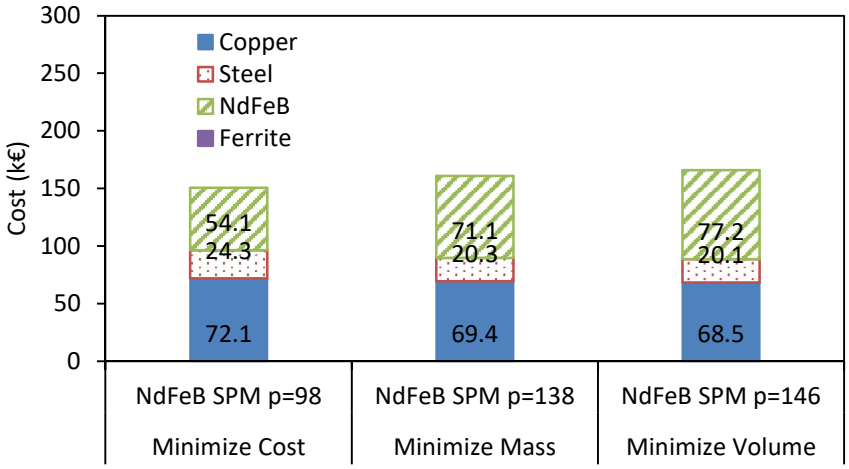

Fig. 3-65 Cost breakdown of NdFeB SPM generators optimized for different objectives.

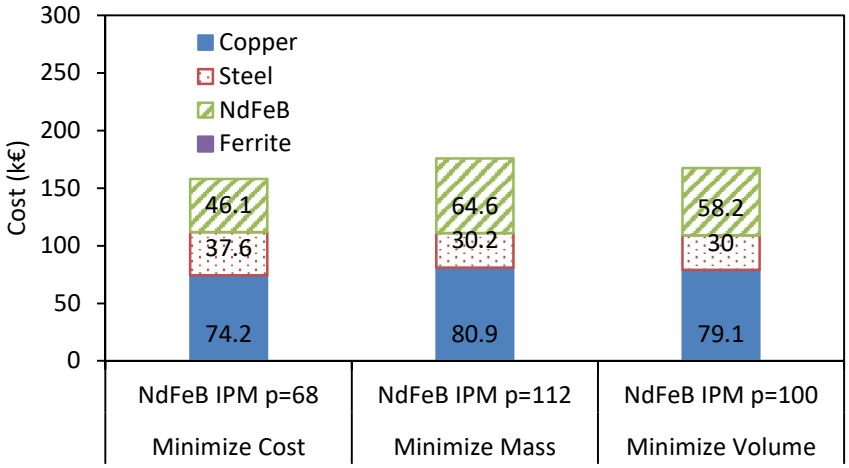

Fig. 3-66 Cost breakdown of NdFeB IPM generators optimized for different objectives.

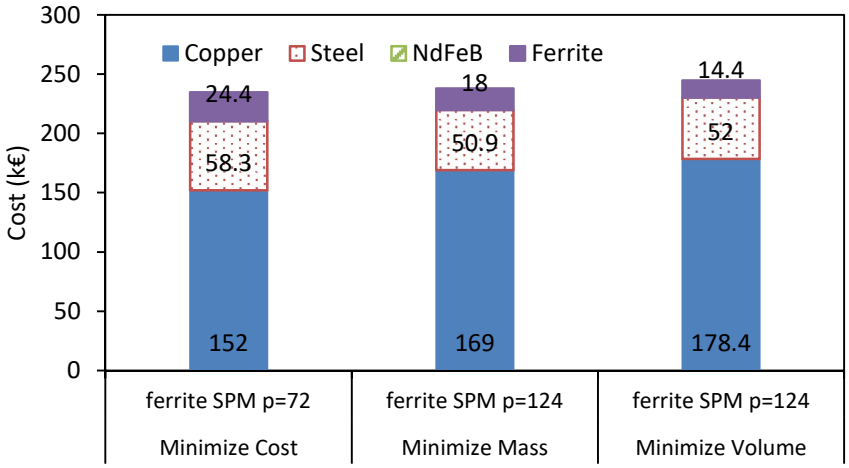

Fig. 3-67 Cost breakdown of ferrite SPM generators optimized for different objectives.

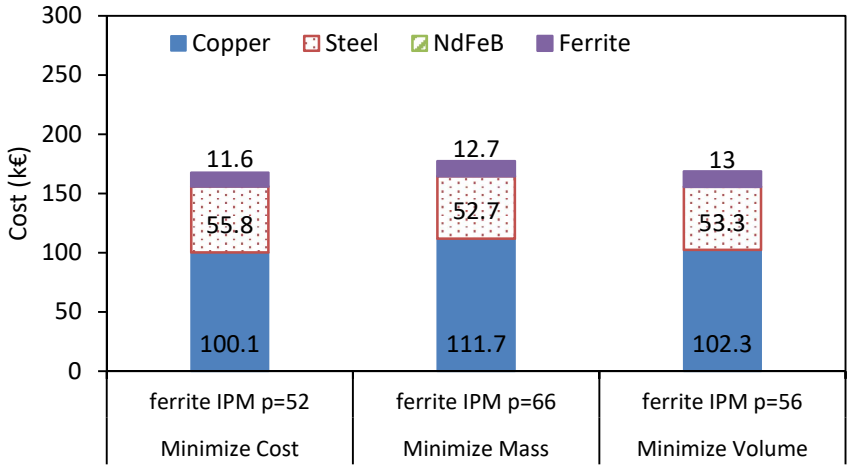

Fig. 3-68 Cost breakdown of ferrite IPM generators optimized for different objectives.

3.3.6.2 Volume

The torque per volume maximization is the objective when designing high torque density generators. Because the contribution towards the optimizer cost function is relatively the same for all materials in the torque per volume optimization, the NdFeB generators designed using this technique will have thicker magnets and will be more expensive than the NdFeB generators optimized for minimum cost. This is the main reason that the torque per cost is more appropriate for the price sensitive large scale industrial DD application.

In Fig. 3-69 - Fig. 3-70 the NdFeB generators optimized for minimum volume use a higher volume of the most expensive NdFeB material compared to the minimum cost generators.

The minimum volume ferrite generators also use a higher volume of their most expensive material, the copper windings, as shown in Fig. 3-71 - Fig. 3-72. The ferrite volume is higher in the minimum cost ferrite generators, the opposite behavior compared to the NdFeB generators.

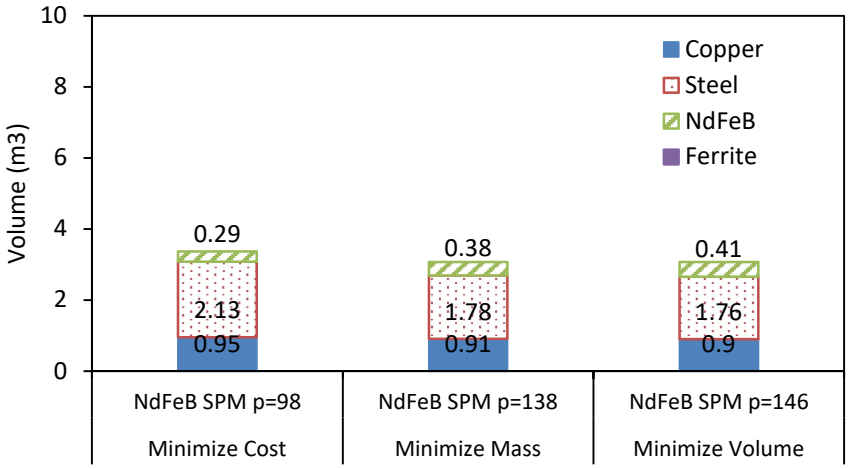

Fig. 3-69 Volume breakdown of NdFeB SPM generators optimized for different objectives.

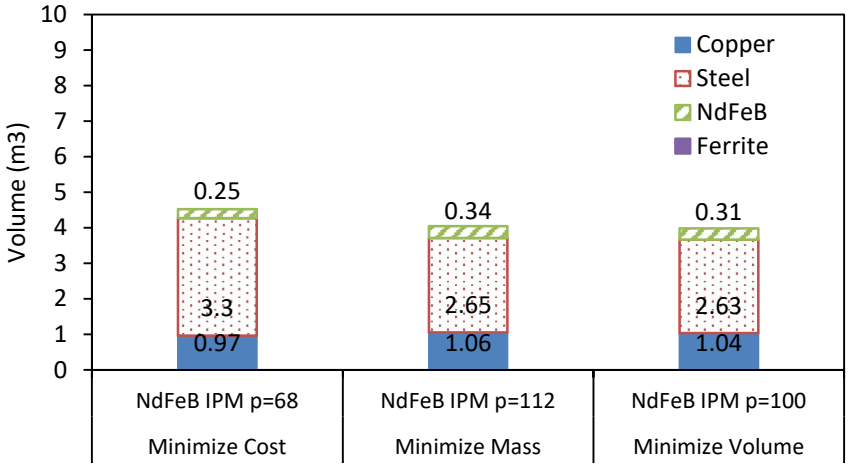

Fig. 3-70 Volume breakdown of NdFeB IPM generators optimized for different objectives.

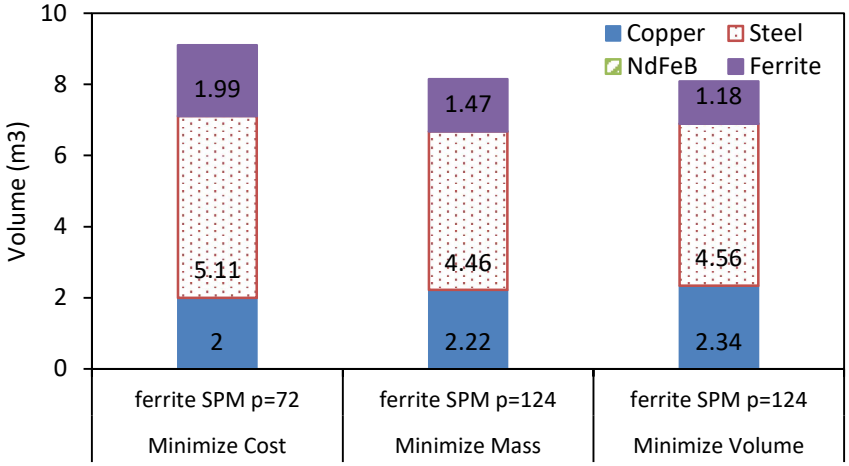

Fig. 3-71 Volume breakdown of ferrite SPM generators optimized for different objectives.

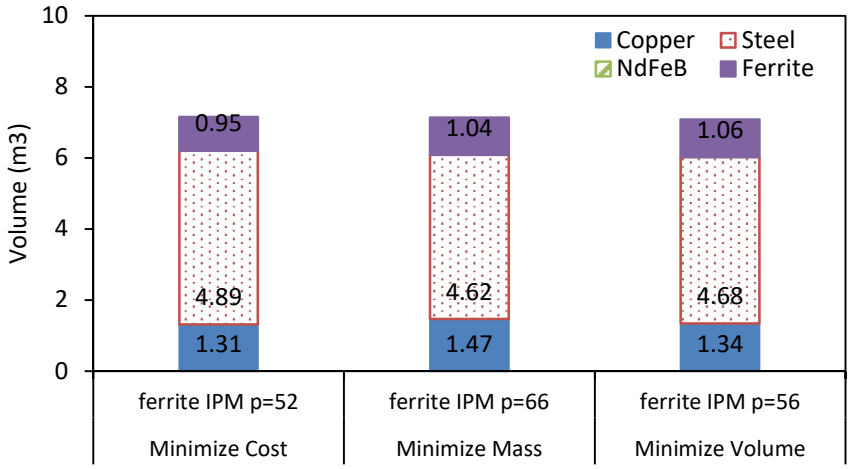

Fig. 3-72 Volume breakdown of ferrite IPM generators optimized for different objectives.

3.3.6.3 Mass

The torque per mass optimization is relevant for large diameter generators. As the mass of the generator increases, the cost of the tower, foundation, bearings and other mechanical systems increase. Hence, the total mass is an important performance metric of a large scale DD electrical generator. The generators resulting from the torque per mass optimization were found to have similar parameter values to the generators optimized for torque per volume. They also use similar amounts of the active materials. This is due to the normalized material contribution to the optimization cost function being similar in the volume and in the mass optimizations.

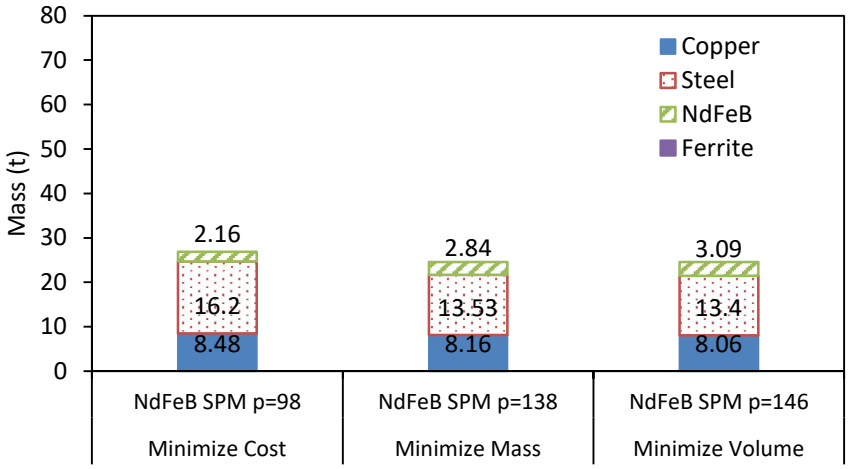

Fig. 3-73 Mass breakdown of NdFeB SPM generators optimized for different objectives.

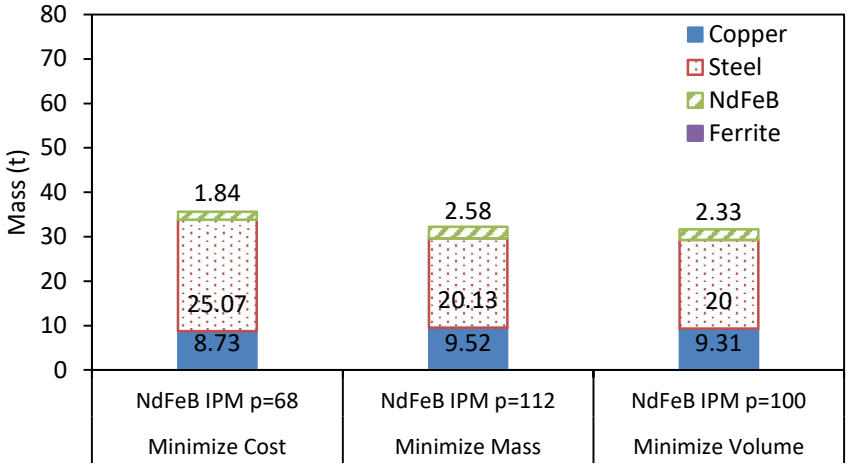

Fig. 3-74 Mass breakdown of NdFeB IPM generators optimized for different objectives.

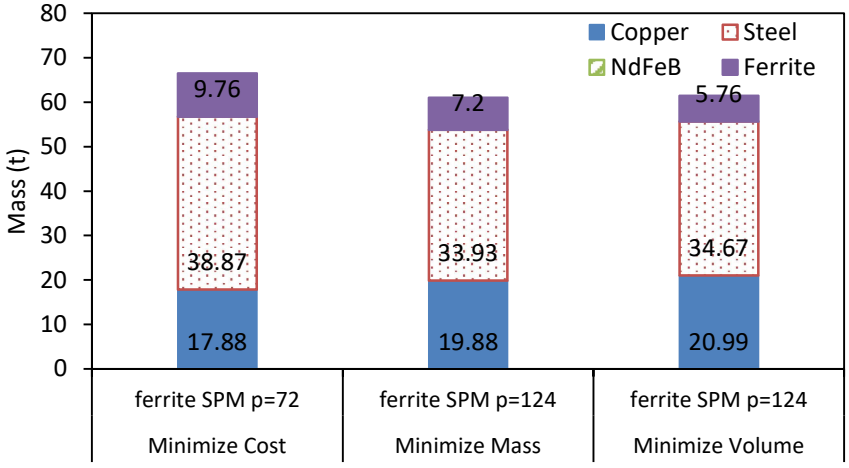

Fig. 3-75 Mass breakdown of ferrite SPM generators optimized for different objectives.

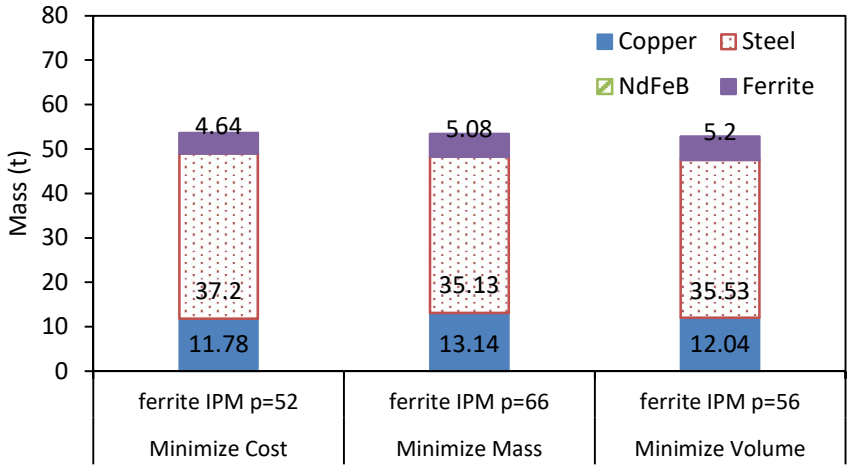

Fig. 3-76 Mass breakdown of ferrite IPM generators optimized for different objectives.

3.3.7 Discussion on the optimization objective

The cost and mass density of the copper windings, steel laminations and PM materials are presented in Table 3-9. This will aid with explaining the differences between the generators optimized for different objectives.

Table 3-9 Cost, mass density and cost and ratio of generator materials contribution to the cost functions.

	Cost (€/kg)	Mass density (kg/m^3)	Normalized volume	Normalized mass	Normalized cost
Copper	8.5	8960	1	1.83	6.68
Steel	1.5	7600	1	1.55	1
NdFeB	25	7500	1	1.53	16.45
ferrite	2.5	4900	1	1	1.07

For the torque per volume optimization, the total volume is simply the sum of all volumes.

The cost of the generator can be computed by adding up all the materials volumes multiplied by the mass density and their costs per mass. This yields a material contribution to cost function ratio as seen in the normalized cost column in Table 3-9.

For the torque per mass optimization, the mass density will determine the contribution of each material volume to the optimizer cost function. The ratios are shown in the normalized mass column in Table 3-9.

The normalized mass and cost columns in Table 3-9 express the mass and cost respectively, normalized to the minimum values. A higher relative value of one material compared to the other corresponds to a higher contribution of that material to the optimization cost function. Consequently, the materials with a higher normalized volume, mass or cost will be used less for the generator optimized for that particular objective i.e. the copper has the most contribution to the cost function of the mass optimization while the NdFeBs contribution is 16.45 times that of steel and 2.46 times that of copper for the cost optimization.

By analyzing the normalized volume, cost and mass columns in Table 3-9, the factors of the torque per volume and torque per mass optimizations are similar. With the exception of the ferrite which only has 66% of the contribution towards the generator mass compared to the other materials, the contributions of the steel, NdFeB and copper towards the total mass are similar. This explains why the optimum NdFeB generators for minimum volume or minimum mass have about the same key parameters values (number of rotor poles, PM thickness and slot depth).

For NdFeB, the cost optimization yields the generators with a lower PM volume compared to the volume and mass optimizations. For the ferrite magnet, the cost optimization increases the used ferrite volume and reduces the volume of the more expensive copper windings compared to the volume optimization. This is because the NdFeB is more expensive while the ferrite is cheaper than the copper windings.

4. Fault and Demagnetization Analyses of SPM and IPM Machines

4.1 Introduction

PM machines are a popular solution for electromechanical energy conversion due to their power density, high efficiency and cheap manufacturing [19], due to the PM excitation which is, most of the time, installed on the rotor. As the PM material can be irreversibly demagnetized if the working point is pushed under the knee point, not only does the PM need to withstand the demagnetizing fields during normal operation, the PM machines has to be designed with fault ride-through capabilities.

PM machines can be designed with a high degree of fault tolerance [53] [54] [55] [56]. Several multi-phase machine systems can be used so that when a fault occurs, a part of the machine can still deliver power. Furthermore, these multi-phase machine systems can be electrically, magnetically and thermally isolated from each other to limit the interactions during a fault. The PM machine can be designed with a per unit inductance which would limit the steady state current during a converter short circuit to the rated current [53].

However, these techniques for the design of a fault tolerant PM machine also have a detrimental effect on the torque density and performance characteristic. For a mechanical isolation between the systems and the phases, only alternate teeth wound fractional slot concentrated windings are possible [54]. All teeth wound FSCW can be used in multi-phase machine system configurations but the electrical, magnetic and thermal isolation between the phases is lost [57]. Integer slot distributed windings (ISDWs) can be used in multi-phase machine system configurations albeit also without satisfying the isolation condition to achieve fault tolerance. The ISDWs are sometimes

preferred over the FSCW configurations due to their lower inductance and due to the absence of sub-harmonic orders in the stator magnetic field. The lower inductance makes the ISDW machines an especially attractive solution for DD applications where the minimization of the inductance is a common objective. This is done to maximize the power factor of the machine, and hence, to reduce the reactive power and the cost of the converters.

A single turn short circuit is one of the most severe types of winding fault. The problem with this type of fault is that the inductance of a 1 turn coil is negligible compared to the inductance of the whole coil. As the resistance of a coil is proportional with the number of turns and as its inductance is proportional to the square of the number of turns, it is expected that fault current in the single turn short circuit will mostly be limited by the resistance. This can cause a very large current to flow in this single faulty turn which can cause large local heat dissipation. If the fault is detected fast enough, a fault control strategy that applies a symmetrical three phase short circuit to the converter terminals of the faulty system can be used to reduce the fault severity [53].

For large scale off-shore wind power generation, there is a requirement that the PM withstand the demagnetizing fields due to a symmetrical three phase to ground converter short circuit. This is because the consequences due to the more severe types of faults can be avoided by using a fault ride-through strategy, i.e. applying a symmetrical three phase to ground short circuit if an inter-turn fault is detected. Even though the probability of an electrical fault is low, the cost of replacing the whole rotor and the downtime associated with the off-shore generation make the magnet demagnetization withstand capability a design priority.

There is a plethora of papers on the demagnetization of PM machines for medium and high speed applications, mostly for HEV. In [58] the authors investigate the demagnetization in I-shaped, V-shaped and dovetail IPM rotors using magnetic circuit models. [59] presents an analytical technique to assess the demagnetization in tubular linear Halbach magnetized SPM machines. The electrical machine is designed so that its magnets withstand the demagnetization during rated load conditions. A FE investigation on the demagnetization of a mixed magnet grades dovetail IPM rotor is presented in [60]. Using a higher coercivity magnet closer to the rotor surface and a higher remanence magnet in the deeper rotor barriers was suggested as a good compromise between power density and demagnetization withstand capability. [61] presents a FE study on the use of damper bars to improve the demagnetization withstand capability of a PM assisted synchronous reluctance machine. In [62] the response of IPM machines designed for HEV applications to symmetrical and asymmetric converter faults is investigated. The authors of [63] present a magnet minimization technique for an IPM machine. There general trend for the HEV is that the machine will be designed to withstand the demagnetization during rated load and overload conditions, but not during a stator winding fault. A FE study on the influence of the initial load conditions on the demagnetization transient is presented in [64] along with details on the V-shape IPM rotor topology particularities during a fault. A nodal decomposition method which stores the magnetization of each element of the PM is used in [65]. In [66] analytical and experimental demagnetization results are compared for a FSCW SPM machine during symmetrical and asymmetric converter faults.

The authors of [67] propose a closed loop model for the transient response of a salient machine to a symmetrical three phase short circuit. Equations for the steady state fault currents are provided. The paper also highlights the issues due to the short circuit

transient which can subject the machine to currents higher than the steady state fault currents. An analytical model based on machine parameters for predicting the fault current due to the initial current and due to the back EMF during a symmetrical three-phase short circuit is presented in [68]. These analytical models provide insight about the PM machine behavior during a symmetrical three phase converter short circuit and about the influence parameters on the fault currents.

There is considerably less information available in literature on the demagnetization of low speed PM machines for DD applications compared to medium and high speed PM machines for HEV. A comprehensive approach for the design of a FSCW SPM machines for DD applications which can withstand the demagnetization due to a symmetrical three phase short circuit is presented in [69]. The authors highlight the importance of the pole number on the amplitude of the air gap magnetizing inductance, which is related to the demagnetization withstand capability. The influence of the pole number on the demagnetization withstand capability is also mentioned in [5] and a more in depth analysis on the influence of the pole number on the inductance, power factor and demagnetization performance is presented in [44].

The demagnetization of IPM machines for DD applications has received little attention, mostly recently as the popularity of the DD PM machines increases. In [70] the authors present an FE study on the demagnetization of a 7MW FSCW generator with a double layer winding. The influence of the number of slots per pole per phase was investigated. The demagnetization performance of a SPM generator equipped with NdFeB is compared to that of an IPM generator equipped with a ferrite magnet spoke type rotor [71]. The generators use the same stator which has been optimized for the NdFeB SPM generator.

In this chapter analytical and FE models are used to investigate the response of the SPM and IPM machine equipped with NdFeB and ferrite magnets to a symmetrical three phase converter short circuit.

First, an analytical model that can accurately predict the fault currents due to a symmetrical three phase to ground converter short circuit is presented. Analytical predictions of the fault current are compared to the FE model prediction for the NdFeB SPM machines optimized for minimum cost in the previous chapter.

The influence of key parameters, the number of poles and the PM thickness is investigated and presented.

The demagnetization performance of the minimum cost machines optimized in the previous chapter is reported. Each of the machines is tweaked for it to be able to withstand the demagnetization during a symmetrical three phase converter short circuit. Finally, the cost of the machines capable of withstanding the demagnetization is updated and compared.

4.2 Synchronous PM machine transient response to symmetrical three phase converter short circuit

4.2.1 Analytical model

The analytical model for the prediction of the *d*- and *q*-axes short circuit currents during a symmetrical three phase converter short circuit assumes that the speed of the machine and the magnetization of the PM remain unchanged during the short circuit transient. Furthermore, average values for Ψ_{PM}, the *d*-axis PM flux linkage, L_d and L_q, the *d*- and the *q*- axis average inductances, are used for this calculation. The accuracy of this analytical prediction depends on the accuracy of average parameters used. As both Ψ_{PM} and the average inductances are influenced by the amplitude of the current excitation, the accuracy of the predicted short circuit currents decreases for electrical machines which experience fault currents significantly higher than the rated currents.

$$\begin{bmatrix}0\\0\end{bmatrix}=\begin{bmatrix}R & -\omega L_q\\ \omega L_d & R\end{bmatrix}\begin{bmatrix}I_d(t)\\I_q(t)\end{bmatrix}+\begin{bmatrix}L_d & 0\\0 & L_d\end{bmatrix}\frac{d}{dt}\begin{bmatrix}I_d(t)\\I_q(t)\end{bmatrix}+\begin{bmatrix}0\\E\end{bmatrix} \tag{4.1}$$

The machine response can be decomposed into the current and EMF responses. For a salient pole machine, $L_d \neq L_q$, the current and EMF responses are given by [68]:

Current response:

$$I_d(t)_I = I_q(0)\frac{L_q}{L_d\cos\theta_0}e^{-t/\tau}\sin(\omega_d t) \tag{4.2}$$

$$I_q(t)_I = I_q(0)\frac{1}{\cos\theta_0}e^{-t/\tau}\cos(\omega_d t+\theta_1) \tag{4.3}$$

EMF response:

$$I_d(t)_E = -\frac{\omega^2 L_q\Psi_{pm}}{\omega^2 L_d L_q+R^2}\left[1-\frac{1}{\sin\varphi}e^{-t/\tau}\sin(\omega_d t+\varphi)\right] \tag{4.4}$$

$$I_q(t)_E = -\frac{\omega R\Psi_{pm}}{\omega^2 L_d L_q+R^2}\left[1-\frac{\omega L_d}{\mathrm{R}\sin\varphi}e^{-t/\tau}\cos(\omega_d t+\varphi-\theta_1)\right] \tag{4.5}$$

where

$$\tau=\frac{2L_d L_q}{R(L_d+L_q)} \tag{4.6}$$

$$\omega_d = \sqrt{\omega^2 - \left(\frac{R(L_d - L_q)}{2L_dL_q}\right)^2} \tag{4.7}$$

$$\varphi = \operatorname{acos}\left(\frac{R(L_d + L_q)}{2L_dL_q}\sqrt{\frac{L_dL_q}{\omega^2 L_dL_q + R^2}}\right) \tag{4.8}$$

$$\theta_1 = asin\left(\frac{R(L_d - L_q)}{2\omega L_dL_q}\right) \tag{4.9}$$

R – phase resistance

ω – synchronous angular electrical frequency

L_d – average d-axis inductance

L_q – average q-axis inductance

t - time

τ – time constant

I_d – d-axis current

I_q – q-axis current

Ψ_{PM} – average d-axis PM flux linkage

E – Electromotive force – $E=\omega\cdot\Psi_{PM}$

For a non-salient electrical machine, $L_d=L_q$, the responses to a symmetrical 3-phase short circuit are:

Current response:

$$I_d(t)_I = I_q(0)e^{-t/\tau}\sin(\omega t) \tag{4.10}$$

$$I_q(t)_I = I_q(0)e^{-t/\tau}\cos(\omega t) \tag{4.11}$$

EMF response:

$$I_d(t)_E = -\frac{\omega^2 L\Psi_{pm}}{\omega^2 L^2 + R^2}\left[1 - \frac{1}{\sin\varphi}e^{-t/\tau}\sin(\omega t + \varphi)\right] \tag{4.12}$$

$$I_q(t)_E = -\frac{\omega R\Psi_{pm}}{\omega^2 L^2 + R^2}\left[1 - \frac{1}{\cos\varphi}e^{-t/\tau}\cos(\omega t + \varphi)\right] \tag{4.13}$$

$$I_{dq}(t)_E = \frac{\omega\Psi_{pm}}{\sqrt{\omega^2 L^2 + R^2}}\sqrt{1 - 2\cos(\omega t)\,e^{-t/\tau} + e^{-2t/\tau}} \tag{4.14}$$

where

$$\tau = L/R \tag{4.15}$$

$$\varphi = \text{atan}\left(\frac{\omega L}{R}\right) = \text{atan}(\omega\tau) \tag{4.16}$$

The peak *d*- and *q*-axis currents during the short circuit transient occur at π and π/2 elec.rad. after the short circuit and are given by:

$$I_{d_{peak}} = I_d(\theta = \pi) = \frac{\Psi_{pm}}{L}\frac{\omega^2 L^2}{\omega^2 L^2 + R^2}[1 + e^{-R\pi/(\omega L)}] \tag{4.17}$$

$$I_{q_{peak}} = I_q(\theta = \pi/2) = \frac{\Psi_{pm}}{L}\frac{\omega L R}{\omega^2 L^2 + R^2}[1 + \frac{\omega L}{R}e^{-R\pi/(2\omega L)}] \tag{4.18}$$

This analytical model provides good insight into the influence of key parameters on the amplitudes of the *d*- and *q*-axes currents during the fault.

The amplitudes of the current pulsations are affected by the $\omega L/R$ ratio. Fig. 4-1, Fig. 4-3 and Fig. 4-5 are plots for different values of $\omega L/R$ of the terms between square brackets from (4.12), (4.13) and the terms under the square root on the right-hand side of (4.14), respectively. For the *d*-axis, the per unit current pulsations are limited to $2\cdot\Psi_{PM}/L$, twice the value of the steady state *d*-axis fault current. Fig. 4-2 shows the per unit *d*-axis current tends asymptotically to 2 for large values of $\omega L/R$.

The amplitude of the per unit *q*-axis current pulsations are significantly higher than the *d*-axis per unit pulsations as shown in Fig. 4-3 and Fig. 4-4. However, the normalization base, the amplitude of the steady state *q*-axis current decreases with the increase of $\omega L/R$.

The total current amplitude will be limited to $2\cdot\Psi_{PM}/L$ as shown in Fig. 4-5 and Fig. 4-6, where the normalization base is the total steady state fault current amplitude, Ψ_{PM}/L.

The peak current during the symmetrical three phase converter short circuit will correspond to a rotor position between the positions for the maximum *q*- and maximum *d*-axis currents at π/2 and π after the occurrence of the short circuit fault.

One of the design characteristics of PM machines for DD applications is their low inductance due to the high pole numbers and large effective air gap lengths. Furthermore, another typical design objective is the maximization of Ψ_{PM}, the *d*-axis magnetic flux linkage. This helps to reduce the current amplitude required to produce the rated torque and yields a high efficiency electrical machine. However, these two design objectives make the PM DD machine susceptible to demagnetization due to the fault currents being significantly larger than the rated currents.

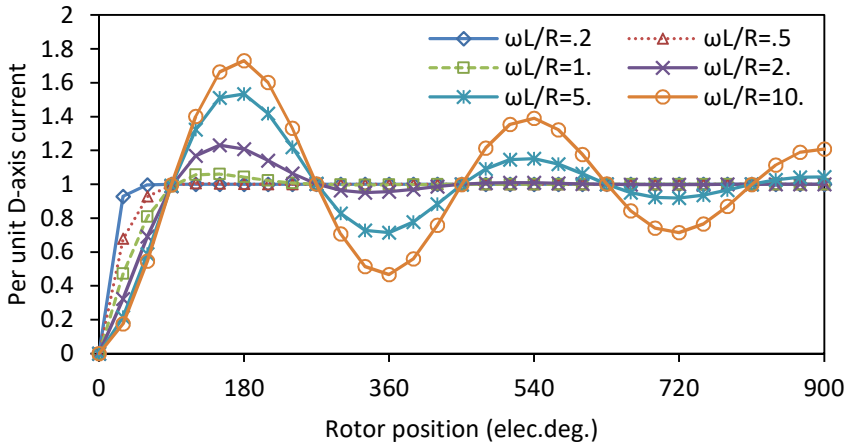

Fig. 4-1 Per unit *d*-axis current vs. rotor position during three phase symmetrical converter short circuit.

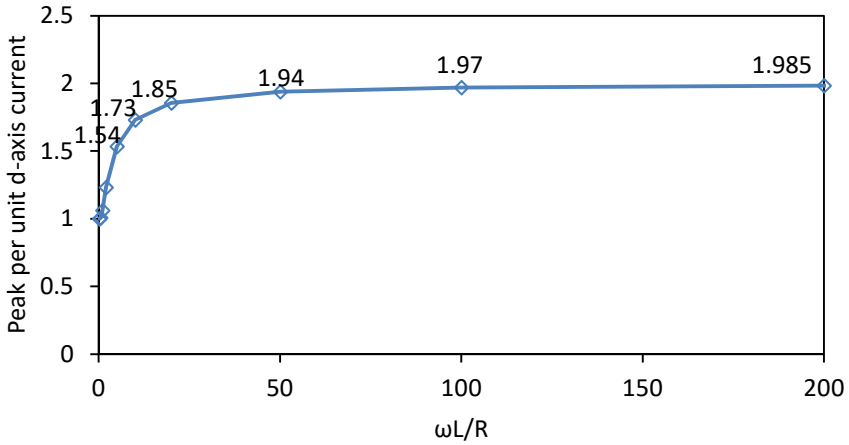

Fig. 4-2 Influence of $\omega L/R$ on the peak per unit *d*-axis current during a three phase symmetrical converter short circuit.

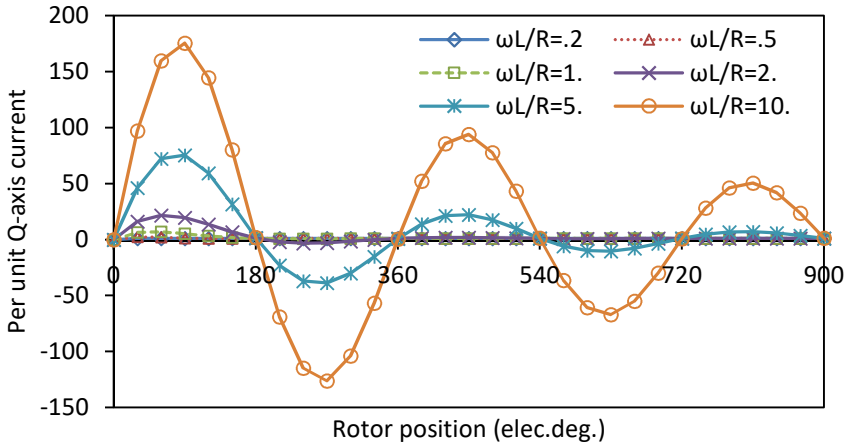

Fig. 4-3 Per unit *q*-axis current vs. rotor position during a three phase symmetrical converter short circuit.

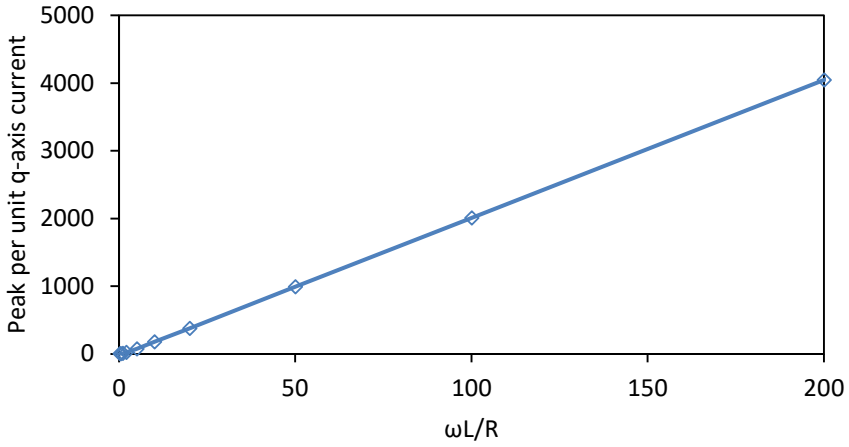

Fig. 4-4 Influence of $\omega L/R$ on the peak per unit *q*-axis current during a three phase symmetrical converter short circuit.

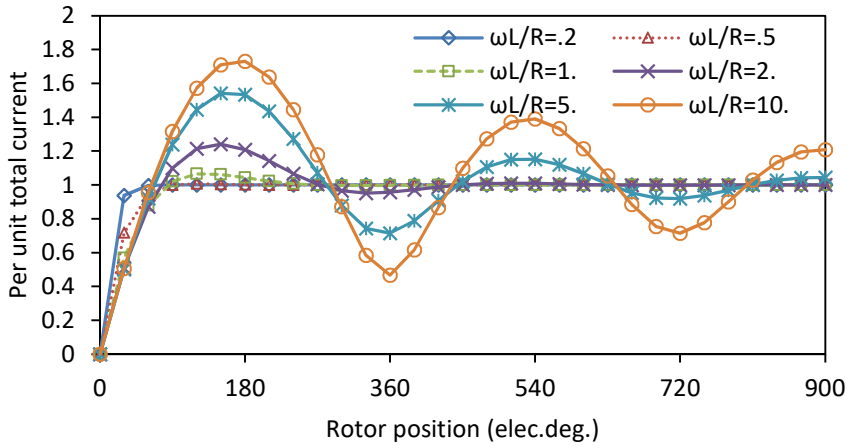

Fig. 4-5 Per unit total current vs. rotor position during a three phase symmetrical converter short circuit.

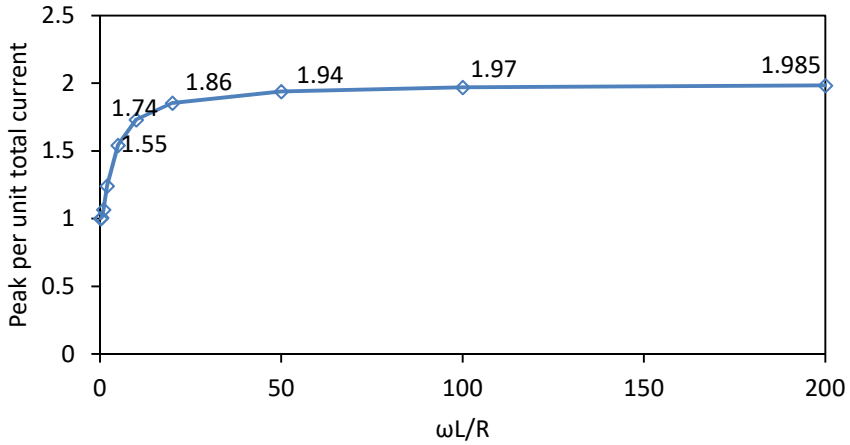

Fig. 4-6 Influence of $\omega L/R$ on the peak per unit total current during a three phase symmetrical converter short circuit.

4.2.2 Finite Element model

A time stepping 2D finite element (FE) analysis was used to investigate the transient behavior of SPM and IPM machines during a symmetrical three phase to ground converter short circuit. The FE analysis was used to accurately predict the working point of the PM for each of the minimum cost machines in Chapter 3 and assess whether the PM is subjected to irreversible demagnetization. The minimum and average values of the B and H-fields over each magnet in the direction of the magnetization are monitored. Using an FE tool for the demagnetization analysis is the preferred solution

as it can accurately predict the magnetic fields due to complex shaped magnets or rotor surfaces, particularly around the corners and surface of the PMs. An example of this will be showed in this section. Furthermore, an analytical model capable of accurately predicting these localized demagnetization areas would need to be adjusted for any changes in the topology and is impractical.

Fig. 4-8 shows the circuit model used for the 2D time stepping FE simulation in ANSYS Maxwell. Fig. 4-9 is a simplified version which shows the star connected three phase SPM machine and the switches used to apply the symmetrical three phase to ground short circuit. The phase inductance is that of the 2D FE model including the slot leakage, air gap leakage and air gap magnetizing inductances.

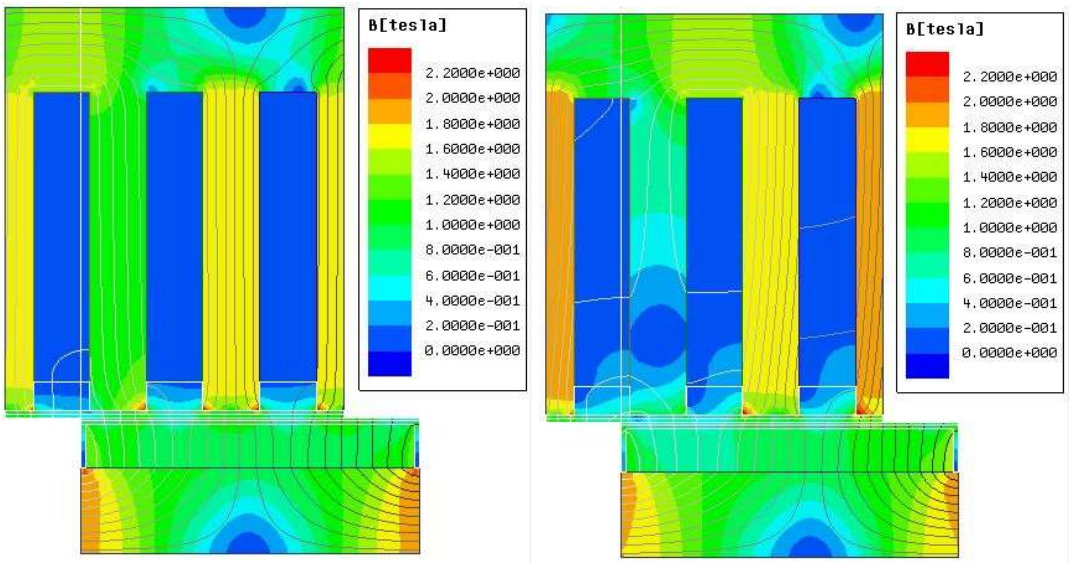

(a) (b)

Fig. 4-7 Cross section of 1 pole of minimum cost SPM machine with equal flux lines and contour plot of flux density (a) at open circuit and (b) at rated load, Ir=222A, β=-10°.

Table 4-1 Optimum parameters of minimum cost SPM machine.

	SPM
Air gap diameter (m)	4.05
Axial length (m)	1.344
Active materials cost (k€)	151
Active material volume (m^3)	3.37
Active material mass (t)	26.9
Copper loss (kW)	157.6
MTPA current angle (elec.deg.)	-12
Number of rotor poles	98
Slot depth (mm)	111.4
PM/barrier thickness (mm)	17.5
Number of turns per phase	1490
Number of turns per coil	30.4
Rated current amplitude (A)	222
Per pole *d*-axis PM flux linkage (Wb)	145.3
Total *d*-axis PM flux linkage (Wb)	7122
Average Ld (H)	0.42
Average Lq (H)	0.49
Power factor at rated load	0.88

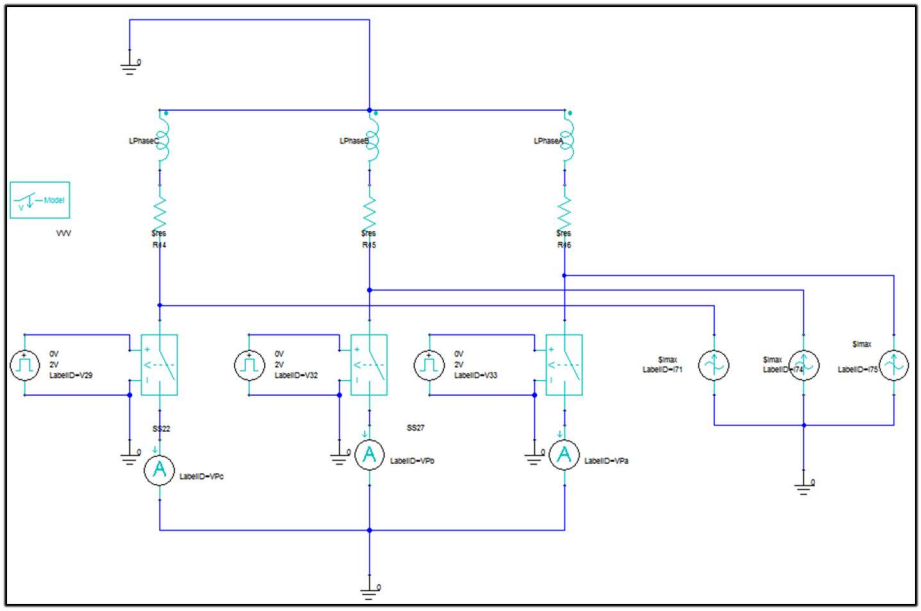

Fig. 4-8 Circuit model for the 2D time stepping FE simulation of the three phase symmetrical converter short circuit.

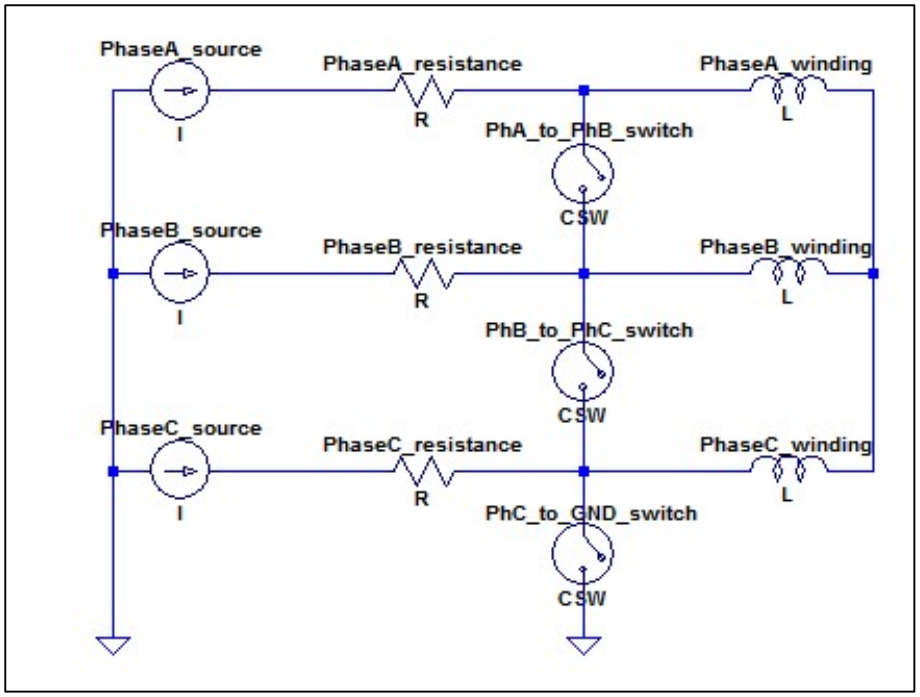

Fig. 4-9 Simplified diagram of the PM machine connections during the three phase symmetrical converter short circuit.

4.2.3 Comparison of predicted fault currents using analytical and finite element models

In this section the NdFeB SPM machine optimized for minimum cost is used to show a typical example of a PM machine during a symmetrical three phase to ground converter short circuit. The *d*- and *q*-axis fault currents predicted using the analytical model are compared to the FE model simulation results and are shown in Fig. 4-10 to Fig. 4-13. Both the non-salient and salient machine analytical models are used to predict the fault current amplitude in the NdFeB SPM machine. Even though it is a non-salient pole rotor topology, the saturation along the *d*-axis caused by the PM field reduces the *d*-axis inductance and yields a machine with a very mild saliency. In this case the average *d*- and *q*-axes inductances are L_d=0.42H and L_q=0.49H. This also explains the non-zero maximum torque per ampere current advance angle.

The current response to a symmetrical three phase to ground short circuit at open circuit at the rated speed is purely an EMF response. The analytical model overestimates the *d*-axis current during this fault by around 7% as shown in Fig. 4-10 and Fig. 4-11. This is due to the fact that the PM flux linkage is assumed constant in the analytical model. In the non-linear FE simulation, the average PM flux linkage driving the short circuit fault reduces due to the saturation caused by the short circuit armature reaction field.

All models in Fig. 4-10 to Fig. 4-13 Fig. 4-13 tend towards $I_d=\Psi_{PM}/L_d$, $I_q=0$ steady state fault current during a symmetrical three phase to ground converter short circuit current.

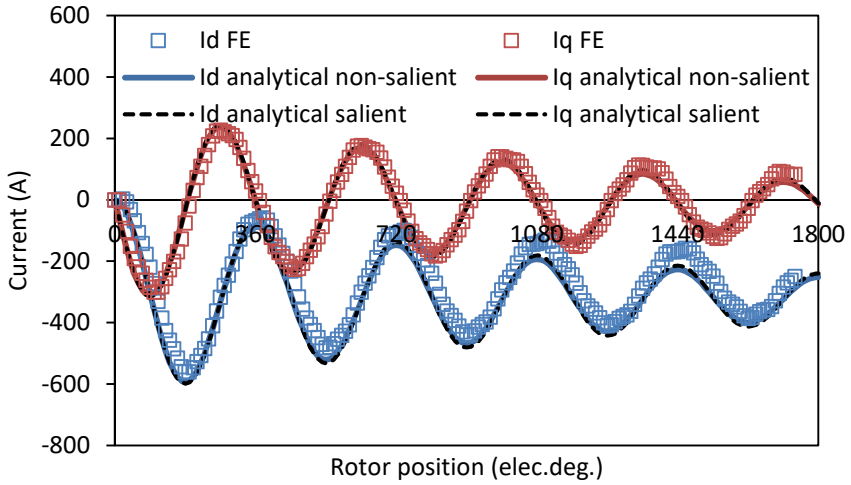

Fig. 4-10 FE and analytical predicted *d*- and *q*-axes currents during three phase to ground short circuit for open circuit at rated speed pre fault condition, *Iq*=0, 16 rpm.

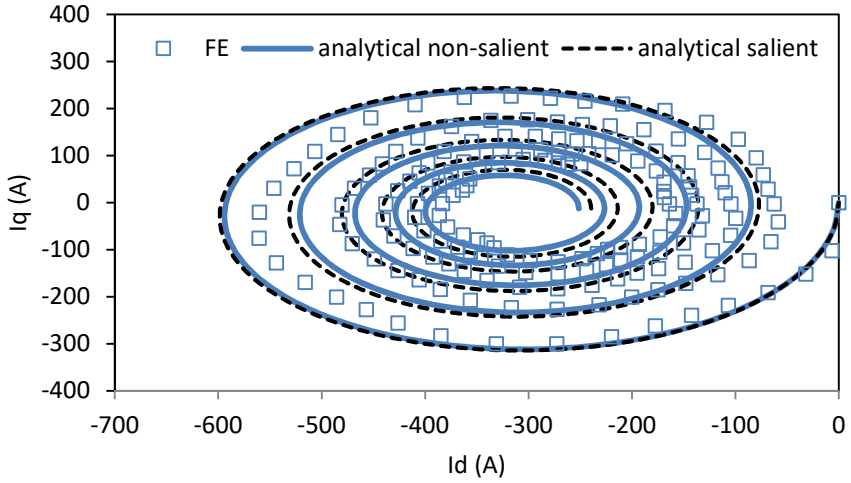

Fig. 4-11 FE and analytical fault current during three phase to ground short circuit in the *d*-*q* plane for open circuit at rated speed pre fault condition, *Iq*=0, 16 rpm.

The *d*-axis current prediction of the non-salient analytical model is 6.5% higher than the prediction of the FE model when the pre fault conditions are rated load at rated speed as shown in Fig. 4-12 and Fig. 4-13. The salient analytical model predicts a 13.5% higher *d*-axis peak fault current compared to the non-linear FE model. While in the previous case (open circuit at rated speed pre fault conditions) the predictions of the non-salient and salient models are very close, this is not the case when there is an initial current excitation present at the moment when the fault occurs. The difference in the peak *d*-axis current predicted by the analytical salient and non-salient models in Fig. 4-13 are due to the L_q/L_d term in the *d*-axis current response in (4.2). However, in the FE model, the saturation caused by the fault current which is significantly higher than the rated current reduces the EMF generated by the PM and this effectively limits the fault current. Hence, the amplitude of the fault current predicted by the analytical model will be higher than the more realistic FE prediction.

Comparing Fig. 4-10 and Fig. 4-11 to Fig. 4-12 and Fig. 4-13, the amplitudes of the fault current predicted by all models are higher in the latter, when the pre fault conditions are rated current at rated speed. The current response in (4.2) and (4.10) shows the contribution of the initial load to the fault current is the dampened current. Thus, when assessing the demagnetization withstand capabilities of the minimum cost machines, the pre fault current will be set to the rated current at 0 current angle. This was chosen over the maximum torque per ampere current angle pre fault condition.

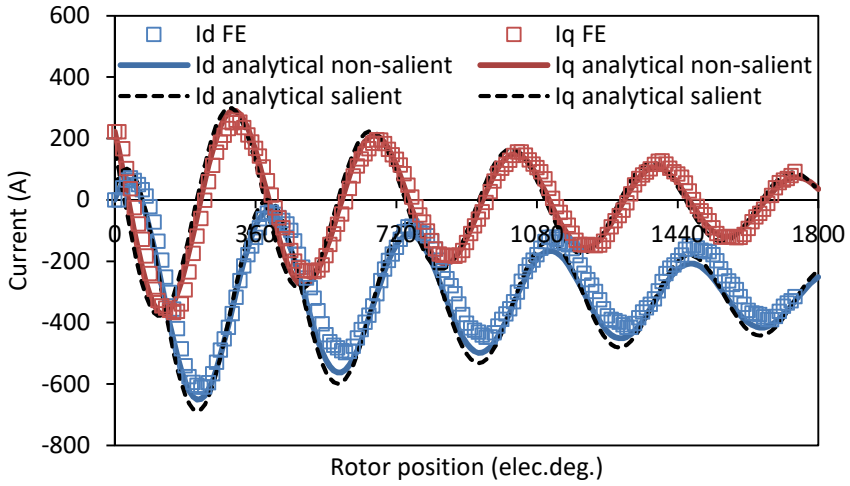

Fig. 4-12 FE and analytical predicted *d*- and *q*-axes currents during three phase to ground short circuit for rated load at rated speed pre fault condition, *Iq*=222A, 16 rpm.

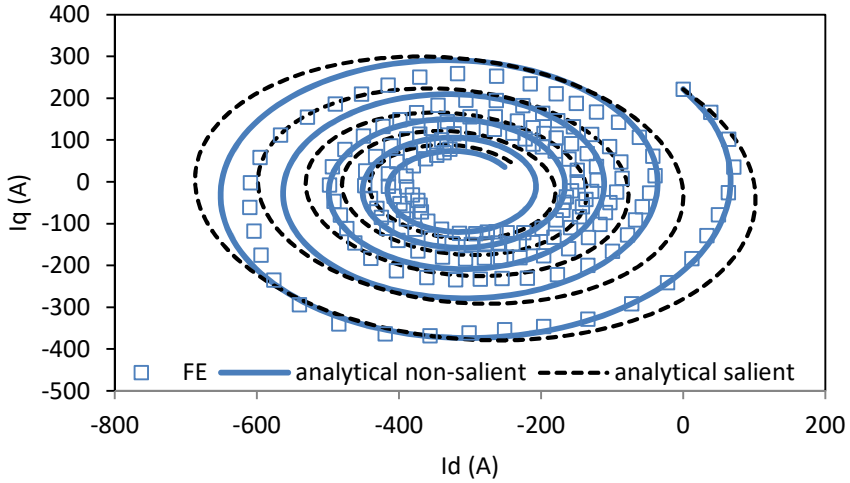

Fig. 4-13 FE and analytical predicted fault currents during three phase to ground short circuit in the *d*-*q* plane for rated load at rated speed pre fault condition, *Iq*=222A, 16 rpm.

4.3 Magnet working point

The following analysis of a magnet working point is done under the assumptions of a linear, non-saturating magnetic circuit with no leakage and no fringing.

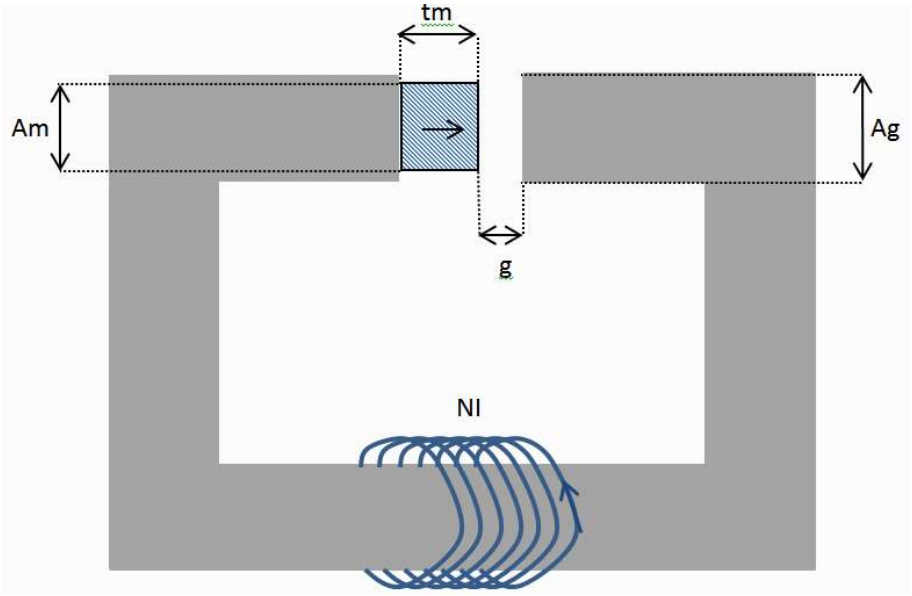

Fig. 4-14 Simple magnetic circuit including PM, air gap and coil.

g	-	air gap length
t_m	-	magnet thickness
A_g	-	air gap area
A_m	-	magnet area
H_g	-	magnetic field strength in air gap
H_m	-	magnetic field strength in PM
B_g	-	air gap flux density
B_r	-	PM remanence flux density
N	-	number of turns per coil
I	-	current amplitude

Linear model of permanent magnet material shown in (4.1):

$$B_m = \mu_0 \mu_r H_m + B_r \tag{4.19}$$

Ampere's law around magnetic circuit:

$$\oint H \, dl = \sum I \tag{4.20}$$

$$H_m t_m + H_g g = -NI \tag{4.21}$$

Gausses law on the magnetic circuit cross sectional area:

$$\oint B\, ds = 0 \tag{4.22}$$

$$B_m A_m = B_g A_g \tag{4.23}$$

The flux density in the PM while subjected to coil magneto-motive force, NI:

$$B_m = -\mu_0 \gamma \left(H_m + \frac{NI}{t_m} \right) \tag{4.24}$$

where:

$$\gamma = \frac{t_m A_g}{g A_m} \tag{4.25}$$

Hence:

$$H_m = -\frac{NI\gamma}{t_m(\gamma + \mu_r)} - \frac{B_r}{\mu_0(\gamma + \mu_r)} \tag{4.26}$$

From (4.19) and (4.24):

$$B_m = -\frac{\mu_0 \mu_r NI\gamma}{t_m(\gamma + \mu_r)} - \frac{B_r \gamma}{\gamma + \mu_r} \tag{4.27}$$

The left-hand side fractions of (4.26) and (4.27) correspond to the H and B-fields induced by the coil. The right-hand side fractions correspond to the open circuit operation point of the PM material. The condition for the magnet to withstand the irreversible demagnetization implies that its working point is not reduced below the knee point. Generally, PM electrical machines are designed so that the working points of the magnets are not reduced below the knee point when subjected to the maximum rated load. However, during a winding fault, the amplitude of the fault current can be significantly higher compared to the rated load current. This is the case of the PM machines designed for DD applications which are characterized by a high magnetic loading (Ψ_{PM}) and a low inductance. This yields a high amplitude fault steady state current and an even higher amplitude transient response fault currents as shown in Section 4.2. For a PM machine, the PM needs to be able to withstand the

demagnetization caused by the fault currents due to a symmetrical converter short circuit to ground. Other winding faults with more severe consequences can be reduced to a symmetrical three phase converter short circuit if the initial fault is detected fast enough.

Fig. 4-15 shows the B-H characteristic curves used for the linear and non-linear PM models. The linear model is used in conjunction with the knee point of the non-linear PM data to assess whether the PM has been subjected to irreversible demagnetization.

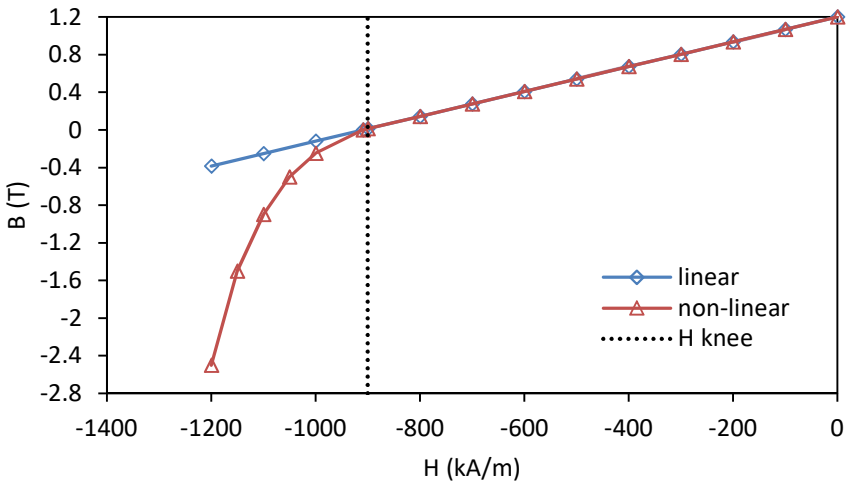

Fig. 4-15 B-H characteristic curve for NdFeB with B_r=1.2T, μ_r=1.05, H_{knee}=900kA/m.

Typically, PM machines equipped with SPM rotors have the ratio $3<\gamma<5$ to maximize the torque per PM material volume. According to (4.26) and (4.27) the typical open circuit magnet working point is between B_m=0.89T, H_m=-236kA/m and B_m=0.99T, H_m=-158kA/m for γ=3 and γ=5, respectively for B_r=1.2T.

4.4 Influence of parameters on fault transient and PM demagnetization

4.4.1 Pre fault load conditions

The fault current response in the *d*-q plane for a SPM machine operating at the same current amplitude but different current angles is plotted in Fig. 4-16. β=0 is the worst case initial condition which yields the maximum amplitude fault current. The analytical model presented in Section 4.2.1 does not account for the influence of pre fault I_d excitation on the fault current response. However, the analytical model can still offer insight on the influence of I_d, i.e. a negative, flux weakening I_d will reduce the amplitude of E, the electromotive force in (4.1), effectively reducing the EMF driving the short circuit current response.

In Fig. 4-16 the steady state current is the same regardless of the pre fault current angle. The steady state fault current is I_d=-Ψ_{PM}/L_d and I_q=0. For pre fault current excitations which are closer to the steady state short circuit current i.e. β=90, the amplitudes of the *d*- and *q*- axis fault transient pulsations are the lowest.

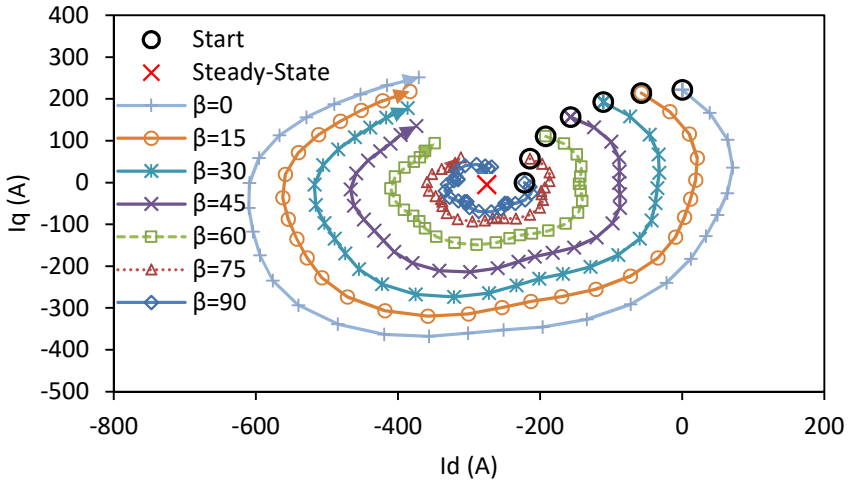

Fig. 4-16 FE predicted fault currents during three phase to ground short circuit in the *d*-*q* plane for the rated current at different current angles and rated speed pre fault condition, *I*=222A, 16 rpm.

Hence, to assess the worst case demagnetization of the optimized machines, the pre fault conditions for all machines will be I_d=0, I_q=I_r, regardless of the maximum torque per ampere current angle.

4.4.2 Machine parameters

4.4.2.1 Chamfered magnet corners

The magnets of an offshore PM machine are usually covered by a non-magnetic retention sleeve which also has the role of protecting the magnetic material from rust and corrosion. There is a requirement to have a gap between adjacent magnet poles where the retention sleeve is connected to the rotor back iron. Nevertheless, even if a non-magnetic retention sleeve is not used, a gap between adjacent magnet poles will still be necessary due to manufacturing constraints.

The presence of a magnet cover influences the rotor design. The first effect is the aforementioned requirement of an inter-magnet gap. The second effect is due to the introduced inter-magnet gap: the working point of the PM in the corner will be marginally lower compared to the rest of the magnet surface as shown in Fig. 4-18. This is because of the removal of the PM corresponding to the inter-magnet gap. The magnet corners are usually chamfered to avoid the localized demagnetization. Another reason to chamfer the PM corner is to minimize the sheer stress the magnet corners exert on the non-magnetic sleeve.

Fig. 4-17 shows the profiles of the rectangular and of the chamfered corner PM. The actual shape of the chamfered PM is described by a cubic Bezier function with the point corresponding to the magnet edge set to 50% of the total magnet height. The value of the other points is 1 or the thickness of the PM.

Fig. 4-17 Rectangular and chamfered corner PM.

The rotor position coresponding to the minimum magnet working point is that when the magnet corner is situated close to the middle of a slot opening as shown in Fig. 4-18 and Fig. 4-19. For this rotor position, the fringing lines are the longest for the elements in the PM corner.

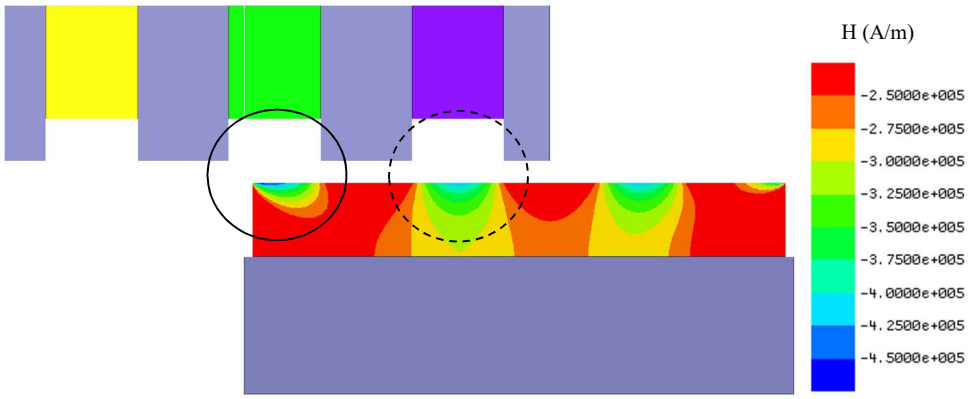

Fig. 4-18 Contour plot of H-field along the magnetization direction in rectangular shape magnet at open circuit.

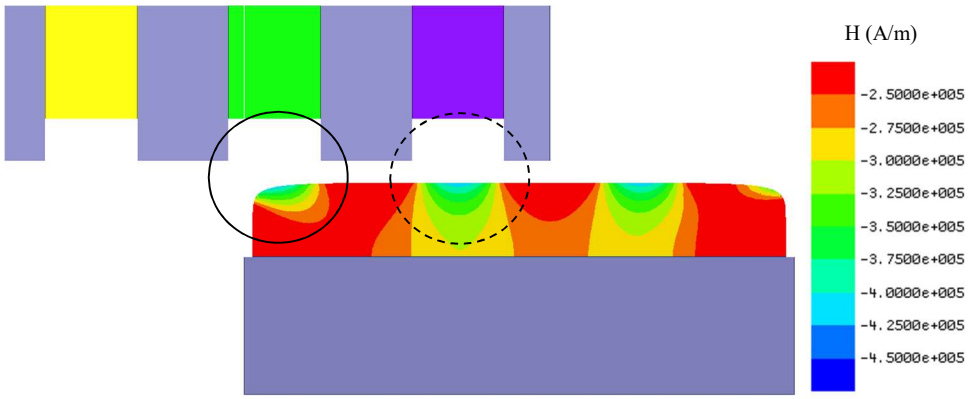

Fig. 4-19 Contour plot of H-field along the magnetization direction in rectangular shape magnet at open circuit.

Fig. 4-20 shows the transient *d*- and *q*-axes current responses of machines equipped with rectangular PM or a chamfered PM. The difference between the peak *d*- and *q*-axes current amplitudes with the two magnets is only ±1A, which is negligible. However, even though the short circuit currents, the average H and B-fields are practically the

same regardless of the magnet chamfering, the minimum magnet working point is significantly lower for the rectangular magnet, both at rated load (for θ<60 elec.deg.) and during the fault transient (for θ>60 elec.deg.) in Fig. 4-21 and in Fig. 4-22. This is due to the lower open circuit magnet working point caused by the inter-magnet gap as explained before. θ is the rotor position in electrical degrees.

Hence, when evaluating the demagnetization withstand capability of a SPM machine the rectangular PM corners are chamfered, if a rotor surface shaping is not already present. For the FE model, the chamfered corners reduce the oscillation of the minimum B and H values caused by localized demagnetization.

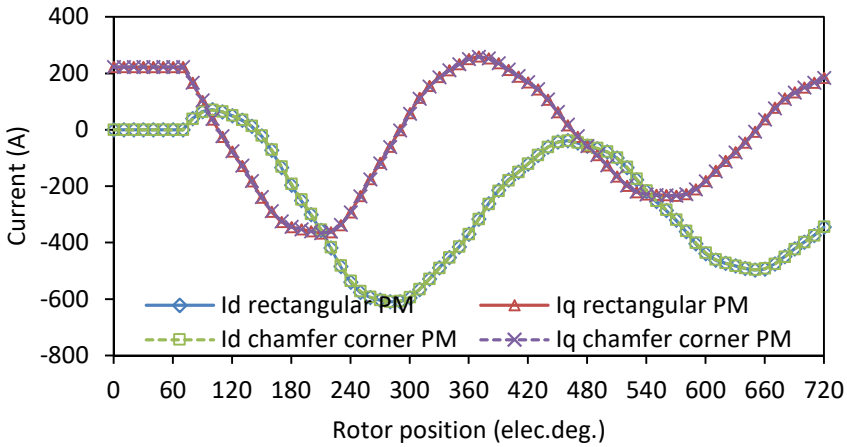

Fig. 4-20 *D*- and *q*-axes currents due to symmetrical three phase to ground short circuit at 60 elec.deg.

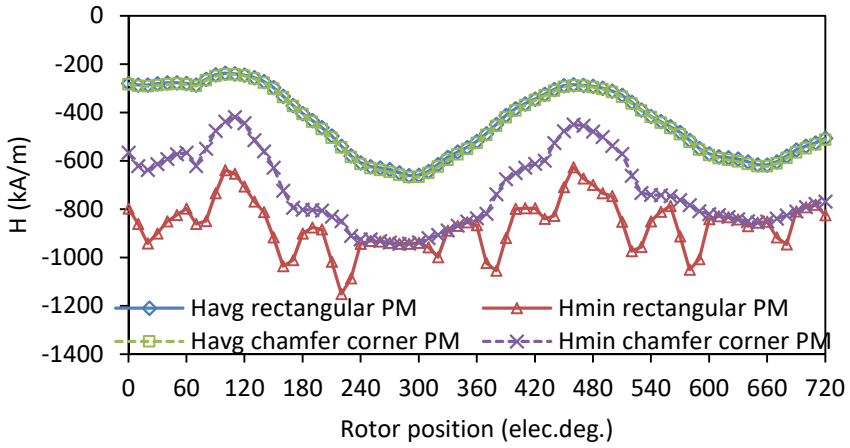

Fig. 4-21 Magnetic field strength in PM due to symmetrical three phase to ground short circuit at 60 elec.deg.

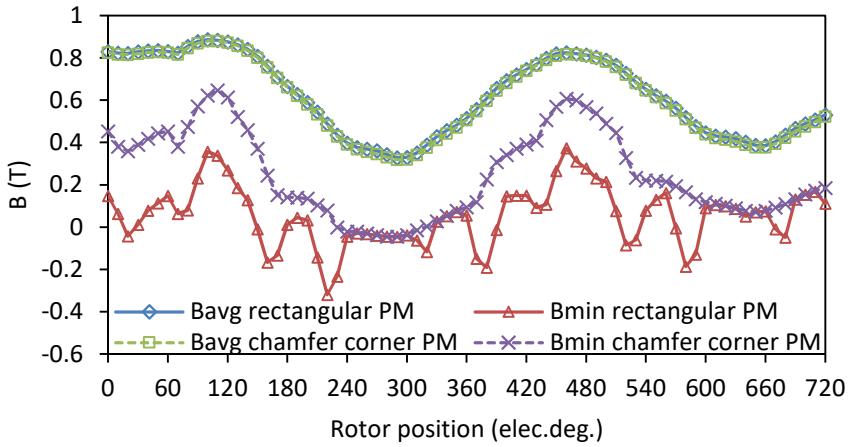

Fig. 4-22 Magnetic flux density in PM due to symmetrical three phase to ground short circuit at 60 elec.deg.

4.4.2.2 PM thickness

The magnet thickness is a key parameters for the demagnetization withstand capabilities of a PM machine. The amplitude of the demagnetizing magnetic field strength due to the armature reaction is inversely proportional to the magnet thickness as shown in the left-hand side fraction in (4.26) from Section 4.3. The ratio γ also increases proportionally to the PM thickness increase. The $\gamma/(\gamma+\mu_r)$ multiplier of the winding magnetic field strength on the left-hand side of (4.26) will increase with γ, however, it is less than 1 $(1-\mu_r/\gamma)$. Due to the increase of γ with the PM thickness, the right-hand side

fraction in (4.26) corresponding to the open circuit operation magnet H-field will decrease.

Hence, the minimum operation point of the PM will increase due to these two effects: operation point of the PM at open circuit will be higher with the thicker PMs; and the demagnetizing MMF which is applied over the PM thickness will be roughly inversely proportional to the PM thickness as in (4.26).

An FE scan of the PM thickness for the minimum cost NdFeB SPM machine was conducted to show its influence on the magnet working point at open circuit, during rated load operation and during a symmetrical three phase to ground short circuit. When the PM thickness is varied, the axial length of the machine is adjusted for constant average output torque while the other parameters are kept constant. The minimum values over one electrical period of the minimum and of the average H-field over the PM area are reported in Fig. 4-23 and in Fig. 4-25, respectively. At open circuit, the amplitudes of the minimum and of the average H-field linearly increase with the normalized PM thickness. This can be explained by the open circuit magnet operating H-field in the fraction on the right-hand side of (4.26) which is inversely proportional to γ when $\gamma >> \mu_r$. For values of the normalized PM thickness between 0.5 and 1.25 the condition $\gamma >> \mu_r$ is not true. This explains the non-linearity of the open circuit magnet H-field for thin magnets.

$$H_m = -\frac{NI\gamma}{t_m(\gamma + \mu_r)} - \frac{B_r}{\mu_0(\gamma + \mu_r)} \tag{4.26}$$

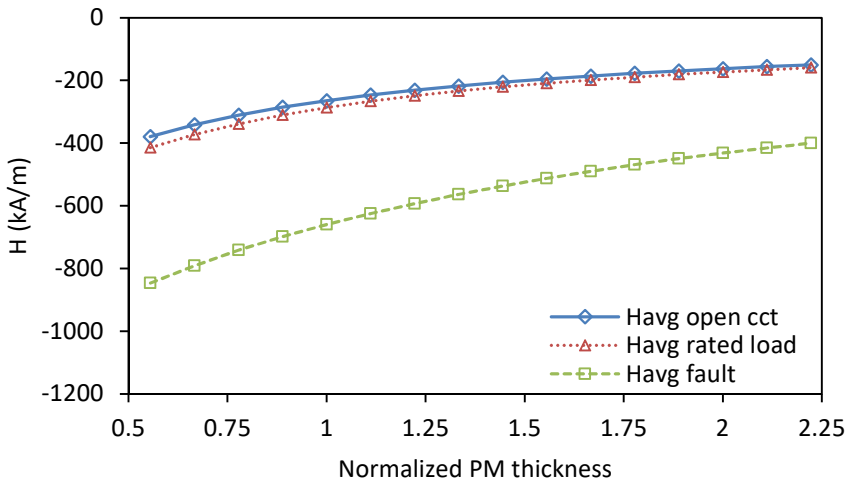

Fig. 4-23 FE predicted minimum average H-field in the magnet vs. PM thickness for different load conditions.

In Fig. 4-24, ΔH_{avg} represents the magnetic field strength in the PM due to the armature reaction. It is the difference between the FE results of the average H-field at the loaded condition and the average H-field at open circuit presented in Fig. 4-23. Overall, the magnetic field strength in the PM due to the winding is expected to decrease with the PM thickness at least at a linear rate as in the saturated case of the ΔH_{avg} fault or faster than linear in the non-saturated case of ΔH_{avg} rated load. The aforementioned saturation refers to the permeability of the main magnetic circuit, especially that of the stator teeth and back-iron during a fault transient. This result is consistent with the left-hand side fraction of (4.26) which predicts the field strength due to the winding is inversely proportional to the PM thickness.

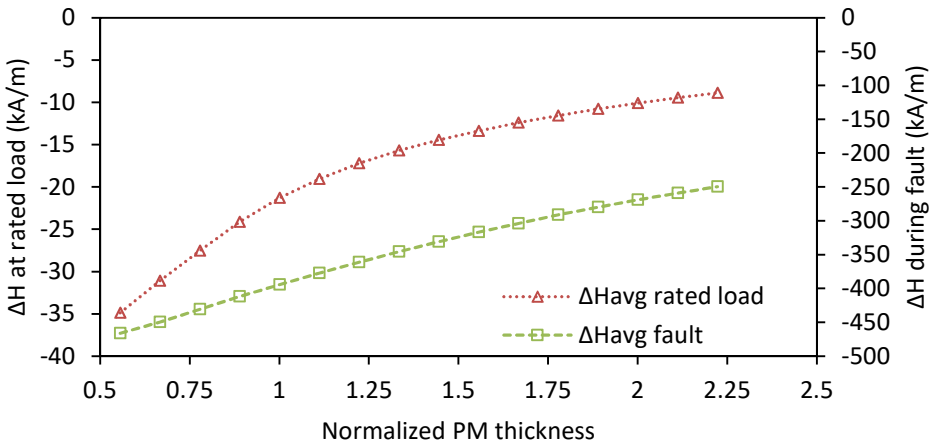

Fig. 4-24 Difference between averages of H-field at load or during fault and open circuit average H-field.

At open circuit, the difference between the minimum average and absolute minimum H-field in the PM is due to the effect of the slotting on the flux paths as shown in Fig. 4-18 and Fig. 4-19. When any load is present, the difference between the minimum average and absolute minimum values of the H-field is caused by both the slotting effect and the *q*-axis component of the armature reaction fields which enhances the flux in half of the PM and the vice versa for the other half. Hence, the minimum H-field during rated operation and during a fault are plotted in Fig. 4-25.

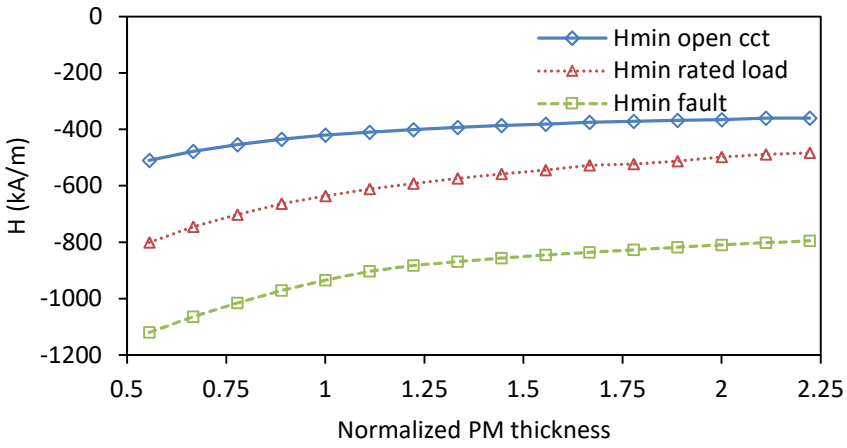

Fig. 4-25 FE predicted absolute minimum H-field in the magnet vs. PM thickness for different load conditions.

According to the analytical model of the fault currents transient presented in Section 4.2.1, the peak amplitudes of the *d*- and *q*-axes fault currents are expected to increase with the PM thickness: the *d*-axis PM flux linkage is expected to increase while the air gap magnetizing part of the inductance will decreases for thicker PMs. Hence in (4.17) and (4.18) Ψ_{PM}/L will increase with the PM thickness. Even though the stator fault current is higher when the PM thickness is increased (Fig. 4-26), the armature reaction demagnetizing field is proportional to $N \cdot I_{fault}/t_m$ as shown in (4.26). As the increase of I_{fault} is lower than the increase of the PM thickness, t_m, the $N \cdot I_{fault}/t_m$ term will decrease with the increase of t_m. Thus, a thicker PM enhances the PM demagnetization withstand capabilities under fault conditions despite the machine also exhibiting higher fault currents.

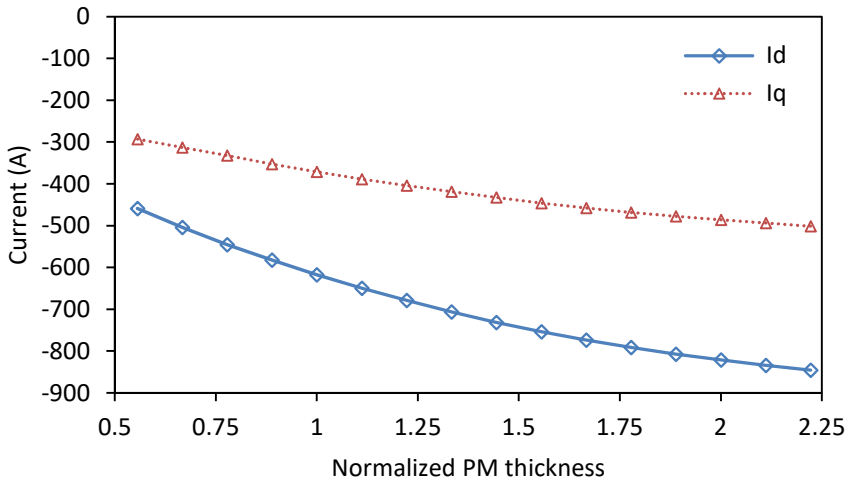

Fig. 4-26 Peak amplitude of *d*- and *q*-axes transient current during symmetrical three phase to ground converter short circuit.

The torque per unit length of the machine increases, and hence, the axial length required for the same average output torque decreases with the increase of the PM thickness. However, when increasing the PM thickness, the total active material cost increases (Fig. 4-27). This is due to the low utilization of the PM (average torque per PM) when $\gamma>3$. The increase of the material cost with the PM thickness in Fig. 4-27 is the same as the one of the optimization SPM population in Chapter 3, Fig. 3-24.

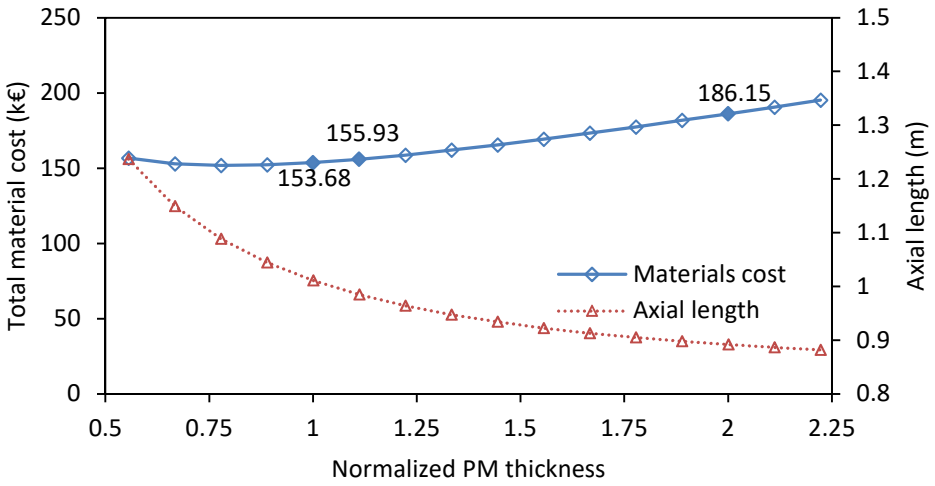

Fig. 4-27 Materials cost and axial length of NdFeB SPM machine with an average torque of 2.4MNm vs normalized PM thickness. Normalized by the PM thickness of the minimum cost t_m=17.5mm.

Generally, increasing the PM thickness by a large margin is not an economically viable method to increase a PM machine demagnetization withstand capabilities. For the NdFeB SPM machine increasing the PM thickness by 11% is sufficient for H_{min}>-900 kA/m during fault as shown in Fig. 4-25. This is in the flat minimum region of the cost vs normalized PM thickness characteristic in Fig. 4-27. Thus, increasing the PM thickness is an economically viable option for reducing the demagnetization in this case, when the required normalized PM thickness is still in the minimum cost region.

4.4.2.3 Number of rotor poles

A more suitable approach to designing a PM machine that can withstand the demagnetization due to a symmetrical three phase converter short circuit at rated speed involves adjusting the number of rotor poles, and hence the number of turns per coil, to reduce the stator MMF. As the number of slots is directly proportional to the number of poles, the number of turns per coil, N, is given by:

$$N = N_{ph}/p \tag{4.28}$$

where N_{ph} is the number of turns per phase, N is the number of turns per coil and p is the number of rotor poles.

For PM machine equipped with an integer slot per pole distributed winding (ISDW), the PM flux linkage is given by:

$$\Psi_{PM} = 2R_g L_{eff} N_{ph} B_g \tag{4.29}$$

where R_g is the radius of the air gap, L_{eff} is the axial length, N_{ph} is the number of turns per phase and B_g is the peak air gap flux density due to the PM. This shows the magnetic loading of an ISDW PM machine is not a function of the number of poles, as is the case for most of the fractional slot concentrated winding (FSCW) machines. ISDW machines with different number of rotor poles should have the same number of turns per phase for equal PM flux linkage (torque/amp constant). Substituting for N, (4.29) in (4.26):

$$H_m = -\frac{N_{ph} I \gamma}{p\, t_m(\gamma + \mu_r)} - \frac{B_r}{\mu_0(\gamma + \mu_r)} \tag{4.30}$$

The average H-field in the magnet at open circuit slightly increases with the number of poles in Fig. 4-28; as the slot-pole number increases, the slot opening is smaller and the Carter factor decreases. Thus, for larger pole numbers the effective air gap length is shorter and the PM working point is marginally higher as in Fig. 4-28.

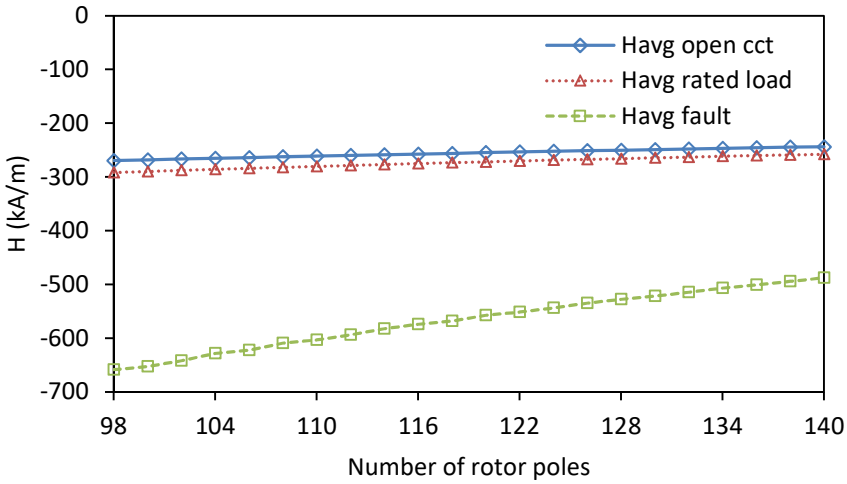

Fig. 4-28 FE predicted minimum average H-field in the magnet vs. number of rotor poles for different load conditions.

As the number of turns per phase is not a function of the number of poles for ISDW machines, the amplitude of the H-field due to the winding, the fraction on the left-hand side in (4.30) is inversely proportional to the number of poles, p.

In Fig. 4-29, ΔH_{avg} represents the magnetic field strength in the PM due to the winding. It is the difference between the FE results of the average H-field at the loaded condition and the average H-field at open circuit presented in Fig. 4-28. The magnetic field strength due to the winding is inversely proportional to the number of rotor poles as shown in (4.30).

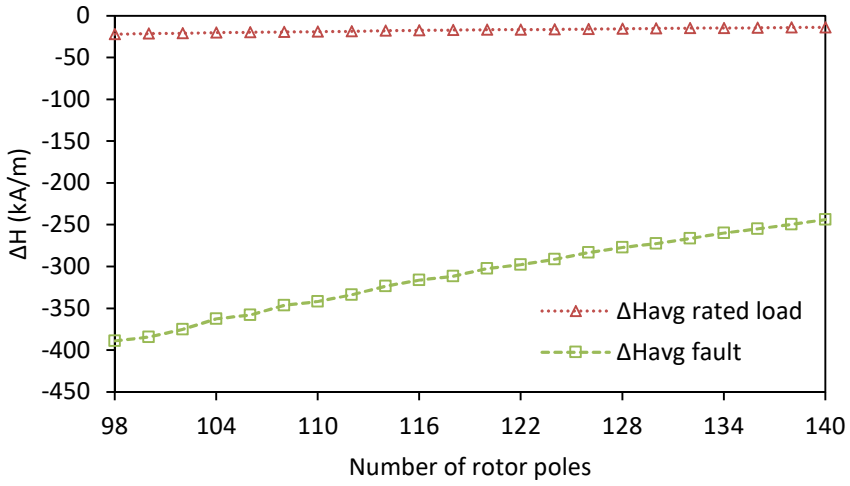

(a)

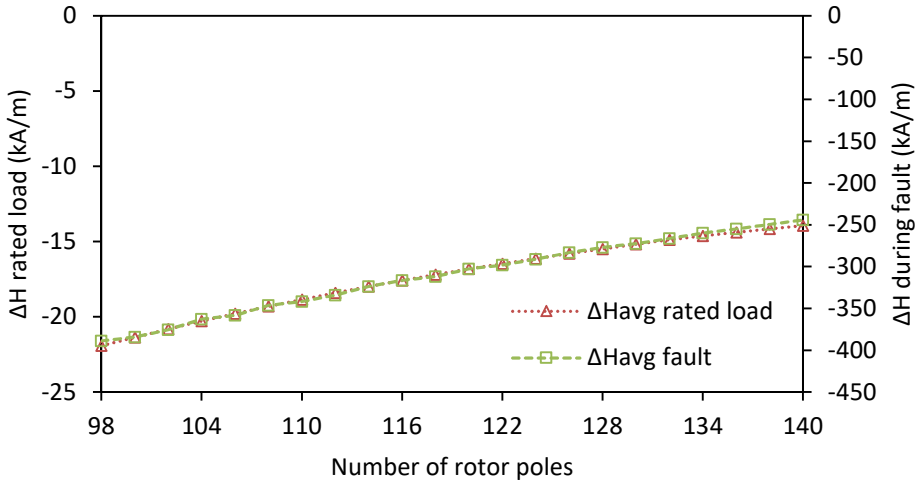

(b)

Fig. 4-29 Difference between averages of H-field at load or during fault and open circuit average H-field plotted on (a) a single Y axis and (b) on two Y axes.

The minimum H-field in the PM versus the number of rotor poles is plotted in Fig. 4-30 for different load conditions. The fault minimum H-field in the PM crosses the -900kA/m knee point close to p=102 for the NdFeB SPM machine. This is close to the optimum rotor pole number for the minimum cost machine, p=98.

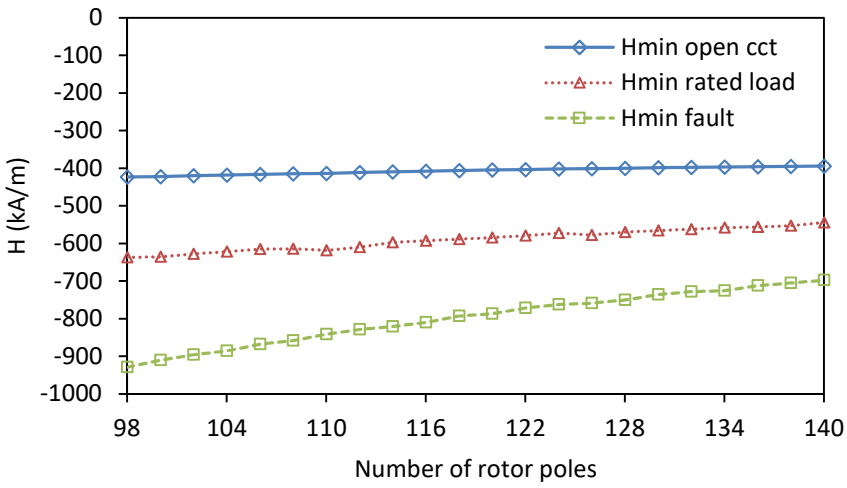

Fig. 4-30 FE predicted absolute minimum H-field in the magnet vs. number of rotor poles for different load conditions.

The peak amplitudes of the *d*- and *q*-axis fault currents from the FE model are plotted in Fig. 4-31. For this range of rotor pole numbers, the amplitude of the peak fault current is constant. This is due to Ψ_{PM} and total average inductance having the same characteristic vs the number of poles: constant and then slightly reducing for large pole numbers. The minimum H-field during fault vs number of pole characteristic is linear in Fig. 4-30, like predicted in (4.30), where the strength of the H-field due to coil is inversely proportional to the number of rotor poles.

The total PM flux linkage, which is the *d*-axis PM flux linkage, Ψ_{PM}, multiplied by the number of rotor pole pairs is the driving force of the short circuit transient. FE results of the average magnetic loading are plotted in Fig. 4-32. The average total flux linkage is mostly constant for $98<p<120$ then it begins to decrease due to the stator flux leakage. As the slot leakage is the dominating part of the inductance, the decrease of the air gap magnetizing inductance with the number of rotor poles will have only a minor effect reducing the total inductance. Hence, only slight variations are expected for Ψ_{PM} and L at this high number of rotor poles and, thus, the peak *d*- and *q*-axes fault currents are constant vs. the number of rotor poles as predicted by (4.17) and (4.18). Increasing the

PM thickness to improve the demagnetization withstand capability yields higher amplitude peak fault currents (Fig. 4-26). When increasing the number of rotor poles, the peak *d*- and *q*-axes fault currents do not increase (Fig. 4-31).

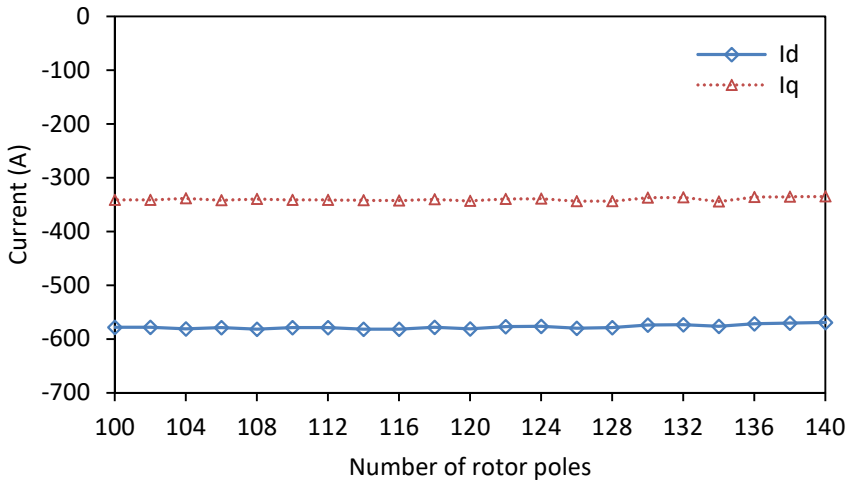

Fig. 4-31 Peak amplitude of *d*- and *q*-axes transient current during symmetrical three phase to ground converter short circuit vs. number of rotor poles.

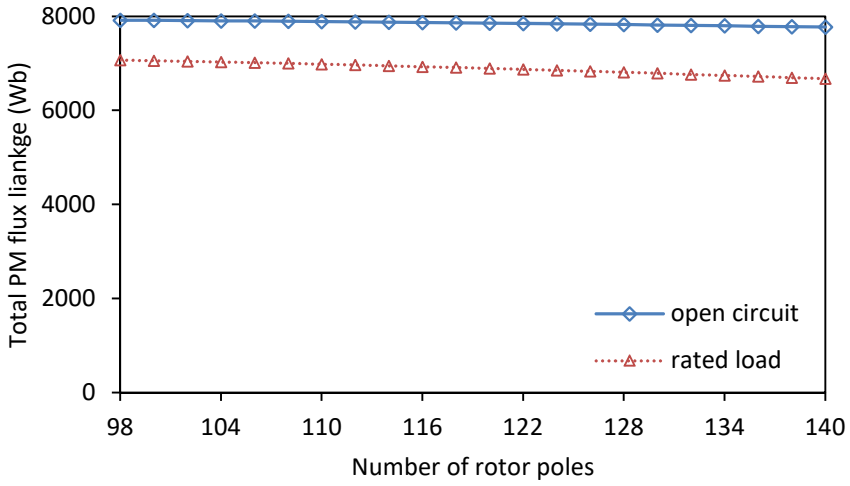

Fig. 4-32 Total magnetic loading, $p \cdot \Psi_{PM}$ vs. number of rotor poles.

The active materials cost of the NdFeB machine versus the number of rotor poles is plotted in Fig. 4-33. For the p=102 machine with the minimum H-field during fault H≈-900kA/m from Fig. 4-30, the active materials are only 0.09k€ (90€) more expensive than the minimum cost machine with p=98. Furthermore, the cost vs number of pole characteristic curve is almost flat over the whole scanned pole range. The small slope on

this curve is due to the increasingly higher leakage at higher pole numbers, which increases the axial length required for equal average torque, and thus, the total material cost.

Compared to the extra material cost due to increasing the PM thickness as shown in Fig. 4-27, the extra material cost due to the higher rotor pole number in Fig. 4-33 is negligible. There are some issues associated with the higher pole number mostly related to the higher frequency that increases the costs of the converters. The iron loss is also expected to increase at a higher rotor pole number and for the same rated speed. However, the iron loss is only a small fraction due to the low rotor speed. The copper loss accounts for most of the total loss in a machine optimized for this type of application. Another issue of the higher pole number is the manufacturing cost which is directly proportional to the number of poles. Nevertheless, for the efficient utilization of the PM material, increasing the number of rotor poles is a better solution than increasing the PM thickness for increasing the demagnetization withstand capabilities during a fault, although it is important to note that operating frequency is also increased.

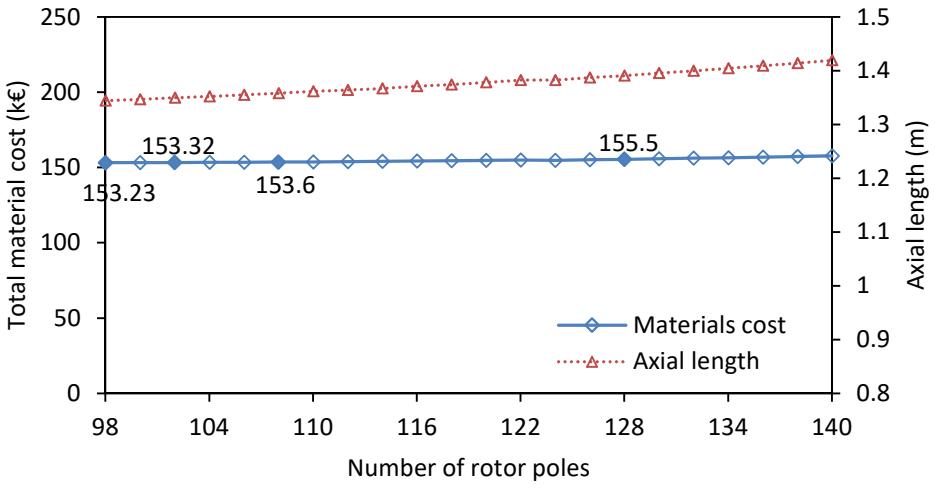

Fig. 4-33 Materials cost and axial length of NdFeB SPM machine with an average torque of 2.4MNm vs number of rotor poles.

4.5 Demagnetization performance of optimized machines

In this section the demagnetization performance of the minimum cost machines from Chapter 3 is reported. FE results of the machines performance during a symmetrical three phase to ground converter short circuit fault transient are presented.

4.5.1 Minimum cost machines

In this section, the demagnetization performance of the minimum cost machines is analyzed using the FE fault transient model. Table 4-2 in section 4.5.1.5 presents a summary of the characteristics of the machines optimized for minimum cost. The active material cost, volume and mass are reported. The parameters included in the optimization and the rated load performance and the demagnetization performance during a symmetrical three phase to ground converter short circuit are also presented.

4.5.1.1 SPM machine with NdFeB magnet

The NdFeB SPM machine *d*- and *q*-axis transient currents during a symmetrical three phase to ground converter short circuit are plotted in Fig. 4-34. The average and minimum H-fields in the PM are plotted in Fig. 4-35. Fig. 4-36 is a contour plot of the PM at the rated load. The *q*-axis excitation enhances the PM field on the right-hand side and vice versa for the left-hand side. Thus, the minimum H-field is located on the left-hand side of the PM, around the surface where the stator slotting effect contributes reducing the open circuit magnet working point. The darkest blue area in Fig. 4-37

corresponds to magnet elements for which the H-field is below the knee point, and thus, are going to be irreversibly demagnetized.

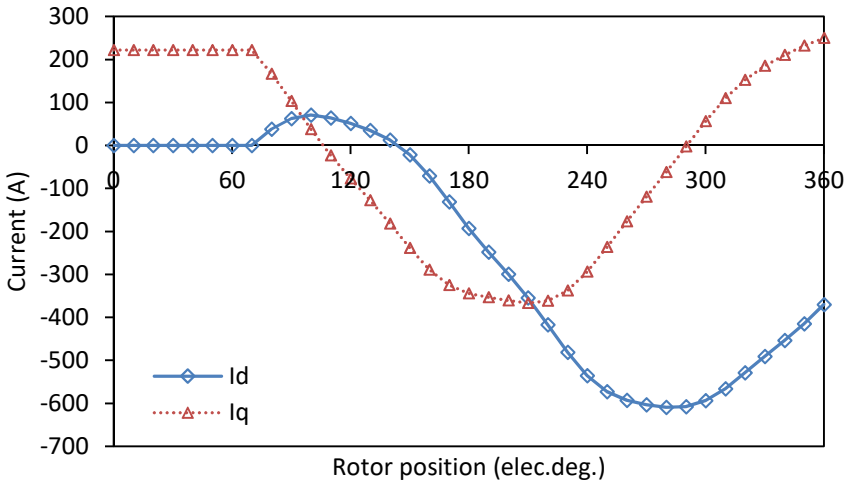

Fig. 4-34 *D*- and *q*-axes currents during a three phase to ground converter short circuit for the minimum cost NdFeB SPM machine.

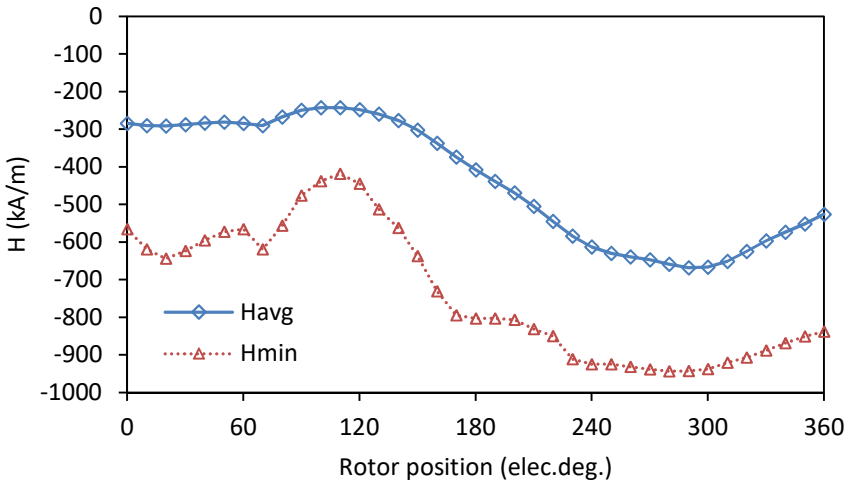

Fig. 4-35 Average and minimum H-fields in the PM before and during a three phase to ground converter short circuit for the minimum cost NdFeB SPM machine.

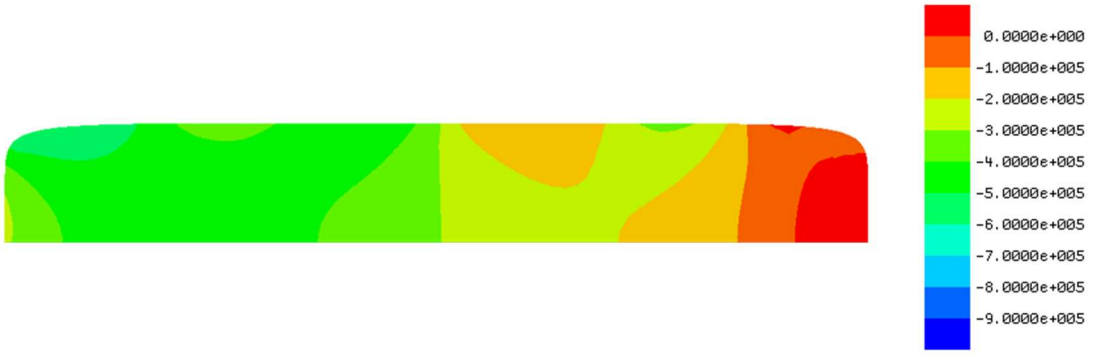

Fig. 4-36 Contour plot of the H-field along the magnetization direction of the PM at rated current operation of the minimum cost NdFeB SPM machine.

Fig. 4-37 Contour plot of the H-field along the magnetization direction of the PM when H_{min} occurs during the fault transient of the minimum cost NdFeB SPM machine.

Due to the slotting effect, the locus of the irreversible demagnetization moves along the PM surface as shown in Fig. 4-38 where the 3rd frame is the one of the absolute minimum H-field also shown in Fig. 4-37. Although it is limited to around 7.5% of the magnet volume (15% of the magnet thickness and 50% of its pitch) as shown in Fig. 4-38, this is unacceptable for the PM. The general criterion for acceptance in DD wind power applications is that the average torque does not decrease by more than 1% after a fault transient. In the case of the minimum cost NdFeB SPM machine, the demagnetization occurs in the center of the PMs pitch, along its surface and the H-field in 60% of the PM volume is decreased to less than -800kA/m.

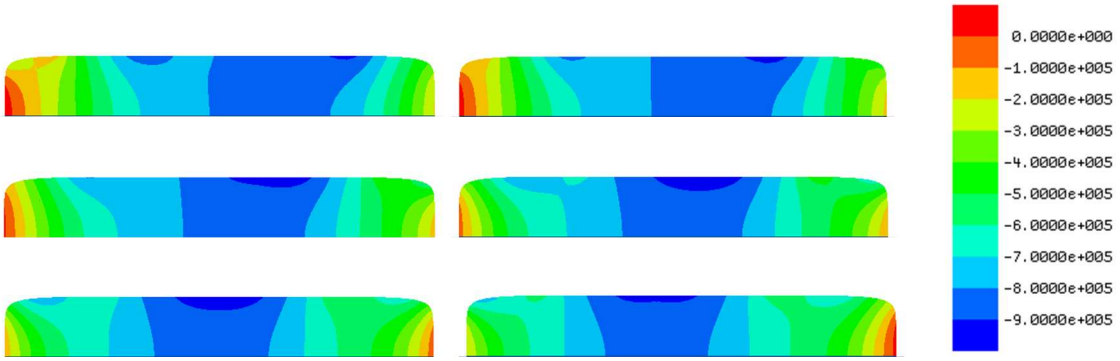

Fig. 4-38 Contour plots of the H-filed along the magnetization direction of the PM with different areas below the knee point during the fault transient of the minimum cost NdFeB SPM machine.

4.5.1.2 IPM machine with NdFeB magnet

The NdFeB IPM machine *d*- and *q*- axis transient currents during a symmetrical three-phase to ground converter short circuit are plotted in Fig. 4-39. The average and minimum H-fields in the PMs are plotted in Fig. 4-40.

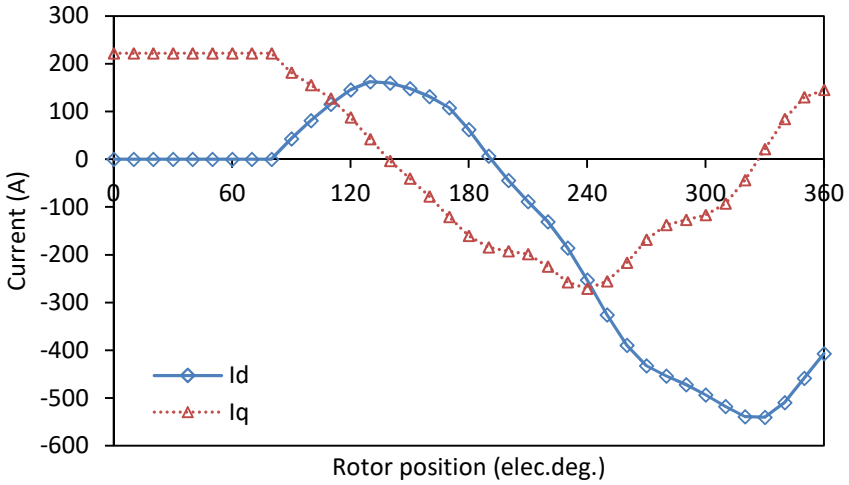

Fig. 4-39 *D*- and *q*-axes currents during a three phase to ground converter short circuit for the minimum cost NdFeB IPM machine.

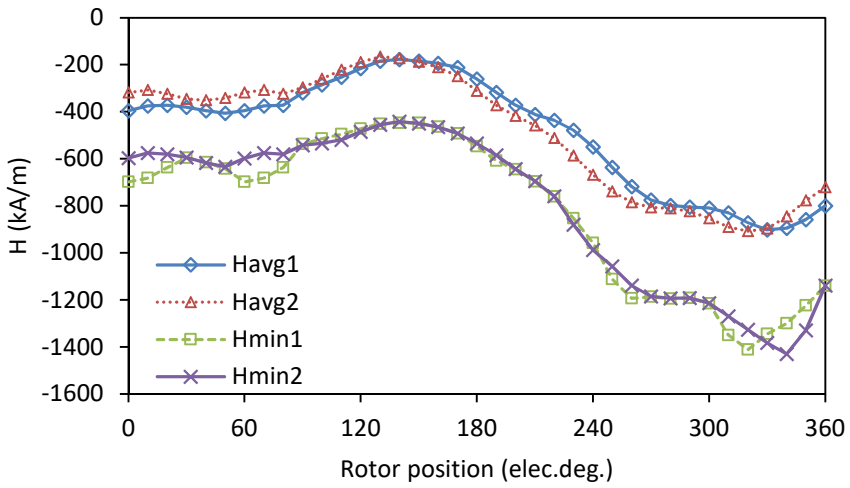

Fig. 4-40 Average and minimum H-fields in the PM before and during a three phase to ground converter short circuit for the minimum cost NdFeB IPM machine.

At rated load, the average and minimum H-fields in the PMs of the minimum cost NdFeB IPM machine are H_{avg}=-406kA/m and H_{min}=-697kA/m, similar to the values of the minimum cost NdFeB SPM machine, H_{avg}=-291kA/m and H_{min}=-643kA/m. The V-shape IPM topology is effective at protecting the PM from the variations of the working point due to the slotting effect (Fig. 4-41). The minimum magnet working point at rated load occurs close to the PM corner. The PM chamfering helps to reduce the oscillation of the FE predicted of H_{min}. The edges of a PM are more vulnerable to irreversible demagnetization because an adjacent PM field is not present on one side of the edge. The air barrier between the rotor bridge and the PM surface is generally used to alleviate the demagnetization of the PM mounted closest to the rotor surface, but was found to only be effective at rated load for the NdFeB IPM.

Most of the PM volume of the NdFeB IPM machine is subjected to irreversible demagnetization during a symmetrical three phase to ground converter short circuit transient as shown in Fig. 4-42. The working point of the PM has been reduced more in the NdFeB IPM machine than in the SPM due to the stronger magnetic field generated by a higher number of turns per coil winding. Alternatively, (4.30) also shows the

magnetic strength of field generated by the winding is inversely proportional to the number of rotor poles which is significantly lower for the IPM.

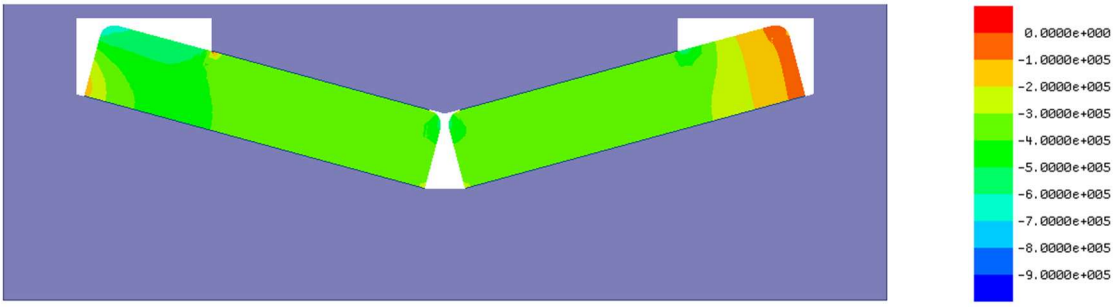

Fig. 4-41 Contour plot of the H-field along the magnetization direction of the PMs at rated current operation of the minimum cost NdFeB IPM machine.

In Fig. 4-42 the air barrier between the PM surface and the rotor bridge is not effective at preventing the irreversible demagnetization due to the high amplitude fault current. In the right-hand side PM the *q*-axis current is enhancing the PM flux. In the left-hand side PM the air barrier only protects the bottom corner of the PM. The fault demagnetization field penetrates the whole magnetic pole of the PMs buried into the V-shape barrier.

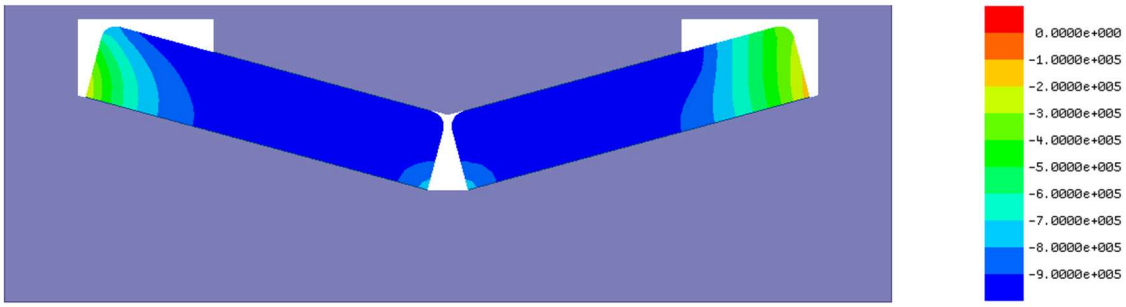

Fig. 4-42 Contour plot of the H-field along the magnetization direction of the PMs when H_{min} occurs during the fault transient of the minimum cost NdFeB IPM machine.

4.5.1.3 SPM machine with ferrite magnet

The ferrite SPM machine *d*- and *q*- axis transient currents during a symmetrical three phase to ground converter short circuit are plotted in Fig. 4-43. The $\omega L/R$ factor governing the amplitude of the current pulsations during the fault transient is lower for the ferrite machines due to the longer effective air gap when thick, ferrite magnets are

used and hence the lower air gap magnetizing inductance. The slot leakage part of the inductance and the resistance are also larger for the axially longer ferrite machines. The average and minimum H-fields in the PMs are plotted in Fig. 4-44. Before the fault occurs at 60 elec.deg., H_{min} in the PM at rated load is below the knee point H_{knee}=-240kA/m for the ferrite SPM machine in Fig. 4-44. This point is not visible in Fig. 4-45 but it is located in the left-hand side chamfered corner of the PM. In this case the magnets of the ferrite SPM machine do not experience any irreversible demagnetization due to the rated load current. Although H_{min} is reduced below the knee point, this only happens in a fraction of a mesh element and is negligible. However, when exposed to the fault currents due to a symmetrical 3-phase to ground converter short circuit occurring at the rated speed, the ferrite SPM magnets experience severe demagnetization as shown in Fig. 4-46 and Fig. 4-47. The dark blue are of the PM will be demagnetized, and most of this will experience magnetic field strengths of over -260kA/m, sufficient for a complete loss of magnetization.

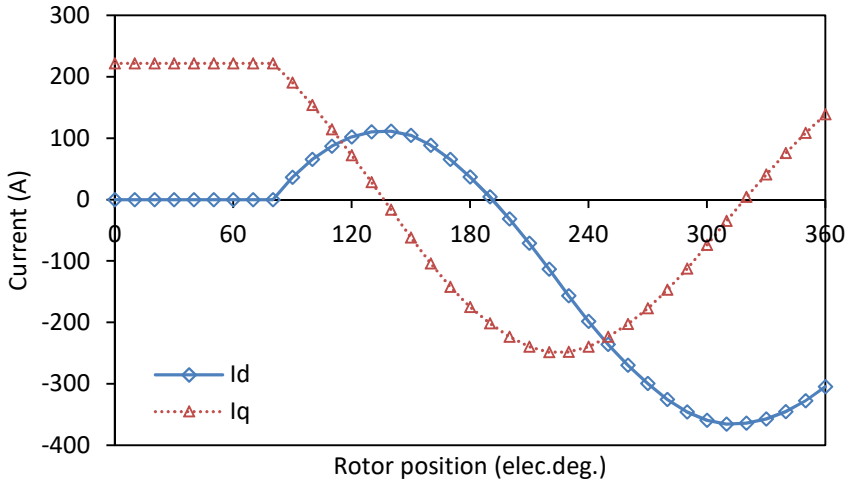

Fig. 4-43 *D*- and *q*-axes currents during a three phase to ground converter short circuit for the minimum cost ferrite SPM machine.

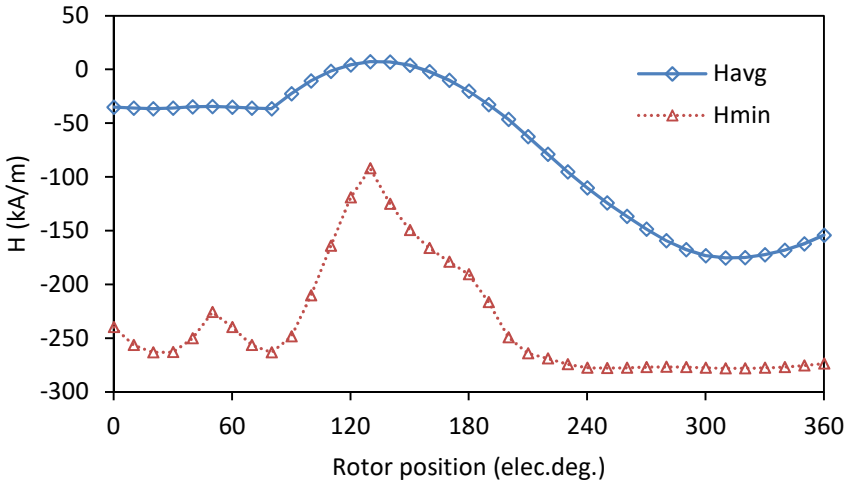

Fig. 4-44 Average and minimum H-fields in the PM before and during a 3-phase to ground converter short circuit for the minimum cost ferrite SPM machine.

Fig. 4-45 Contour plot of the H-field along the magnetization direction of the PM at rated current operation of the minimum cost ferrite SPM machine.

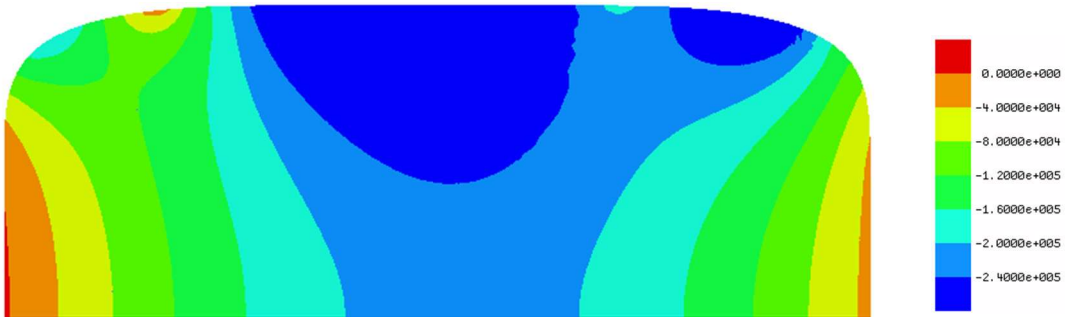

Fig. 4-46 Contour plot of the H-field along the magnetization direction of the PM when H_{min} occurs during the fault transient of the minimum cost ferrite SPM machine.

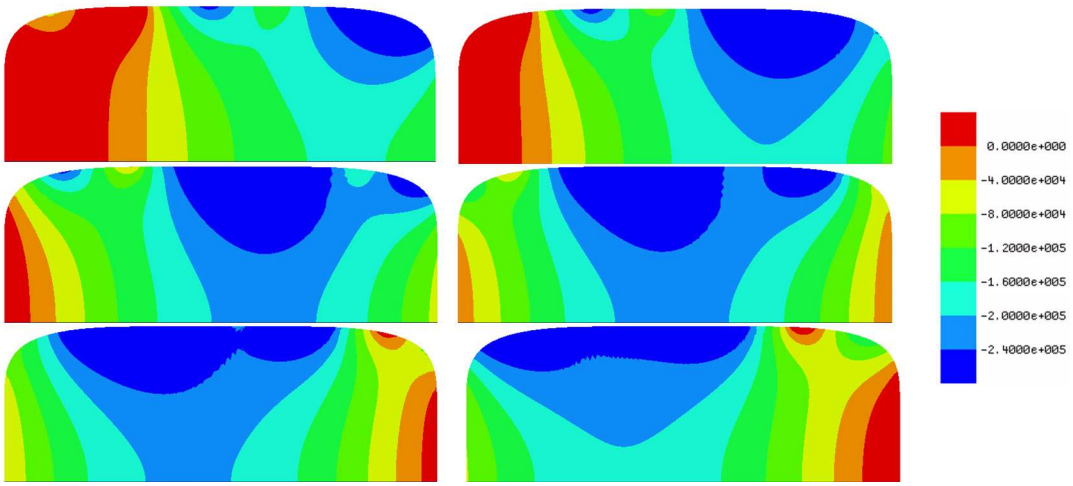

Fig. 4-47 Contour plot of the H-filed along the magnetization direction of the PM with different areas below the knee point during the fault transient of the minimum cost ferrite SPM machine.

4.5.1.4 IPM machine with ferrite magnet

The ferrite IPM machine *d*- and *q*- axis transient currents during a symmetrical three phase to ground converter short circuit are plotted in Fig. 4-48. The average and minimum H-fields in the PMs are plotted in Fig. 4-49. At the rated load, a part close to the chamfered corner of the PM experiences irreversible demagnetization (Fig. 4-50). During the symmetrical 3-phase to ground converter short circuit transient major parts of both PMs are irreversibly demagnetized. The fault magnetic field shifts the average PM working point below H_{avg}=-275kA/m. The demagnetization during the fault is severe; around 60% of the PM volume is expected to completely lose magnetization when operated anywhere close to H_{min}=-820kA/m (Fig. 4-51).

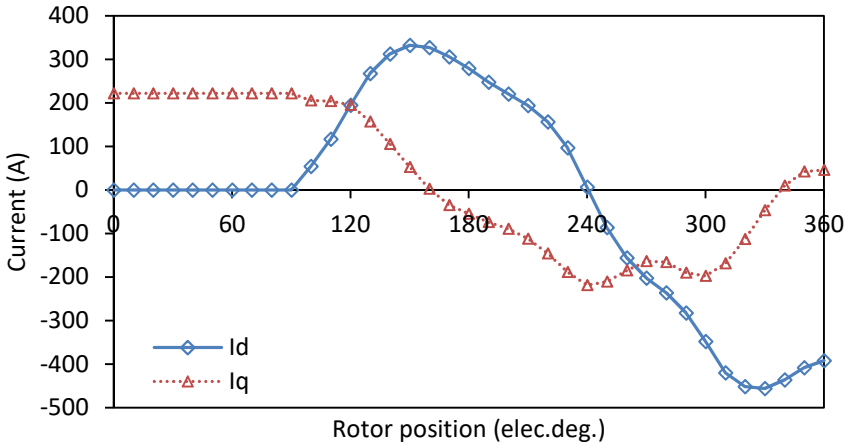

Fig. 4-48 *D*- and *q*-axes currents during a 3-phase to ground converter short circuit for the minimum cost ferrite IPM machine.

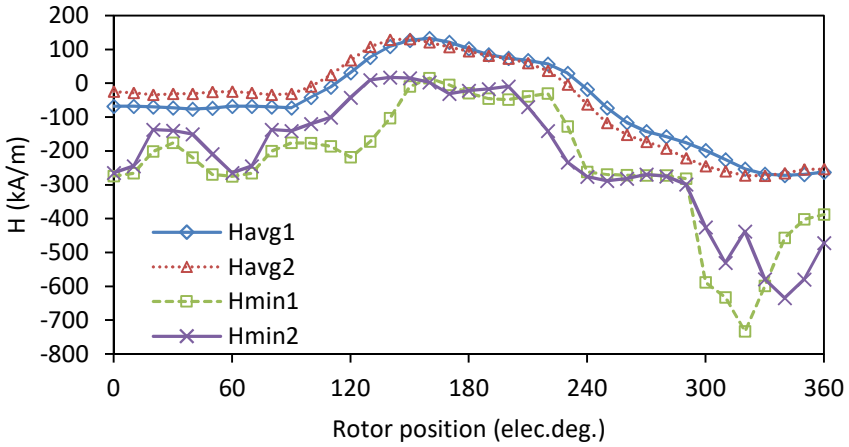

Fig. 4-49 Average and minimum H-fields in the PM before and during a 3-phase to ground converter short circuit for the minimum cost ferrite IPM machine.

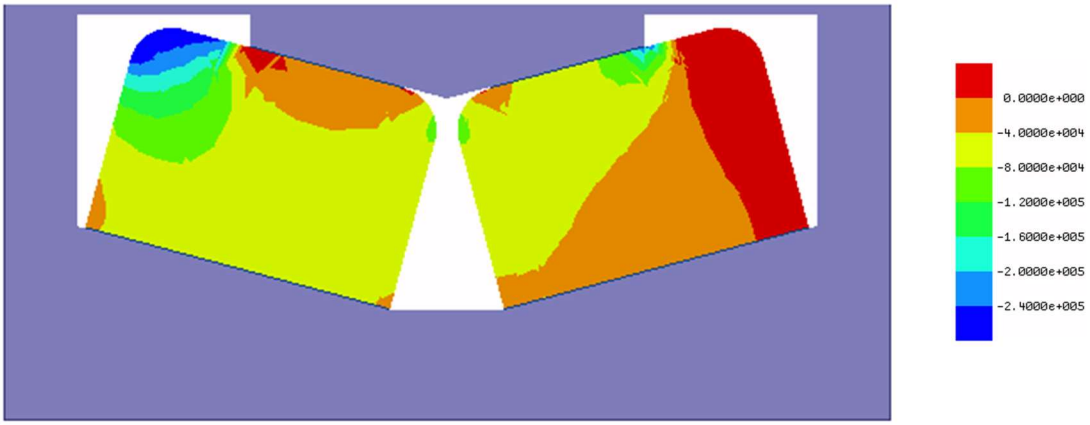

Fig. 4-50 Contour plot of the H-field along the magnetization direction of the PM at rated current operation of the minimum cost ferrite IPM machine.

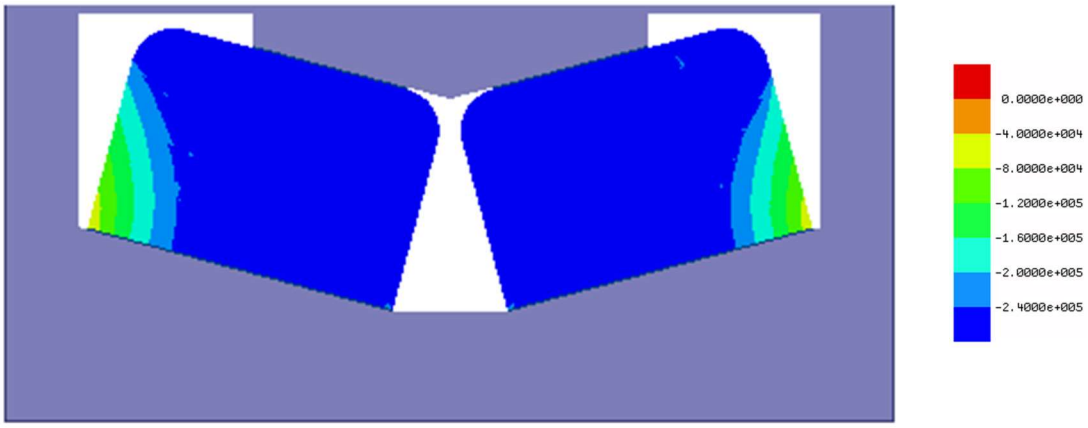

Fig. 4-51 Contour plot of the H-field along the magnetization direction of the PM when H_{min} occurs during the fault transient of the minimum cost ferrite IPM machine.

4.5.1.5 Summary of minimum cost machines

A summary of the minimum cost machines specifications, rated load performance and demagnetization performance is presented in Table 4-2.

Table 4-2 Specifications, optimization parameters, circuit data, rated load performance and demagnetization performance summary of minimum cost machines. Magnetic field strengths in red are below the knee point of the magnet.

	NdFeB B_r=1.2T		**Ferrite B_r=0.4T**	
	SPM	**IPM**	**SPM**	**IPM**
Air gap diameter (m)	4.05			
Axial length (m)	1.344	1.346	2.625	1.73
Active materials cost (k€)	151	158	234.7	167.5
Active material volume (m^3)	3.37	4.52	9.1	7.15
Active material mass (t)	26.9	35.6	66.5	53.6
Optimization parameters				
Number of rotor poles	98	68	72	52
Slot depth (mm)	111.4	114	119.5	119.5
PM/barrier thickness (mm)	17.5	17.5	61.4	60.1
MTPA current angle (elec.deg.)	-12	-36	-1	-45
Circuit data				
Copper loss (kW)	157.6	170	336	221.4
Number of turns per phase	1490	1574	1595	1596
Number of turns per coil	30.4	46.3	44.3	61.4
Rated current amplitude (A)	222			
Rated load performance				
Per pole *d*-axis PM flux linkage	145.3	181.5	198.5	146.7

(Wb)				
Total *d*-axis PM flux linkage (Wb)	7122	6171	7147	3816
Average L_d (H)	0.42	0.9	1.32	1.43
Average L_q (H)	0.49	1.39	1.34	3.05
Power factor at rated load	0.88	0.77	0.56	0.6
Demagnetization performance				
Peak fault I_d (A)	-609	-540	-366	-455
Peak fault I_q (A)	-366	-271	-248	-206
H_{avg} rated load (kA/m)	-292	-407	-36	-76
H_{min} rated load (kA/m)	-644	-698	-263*	**-275**
H_{avg} fault (kA/m)	-668	**-908**	-175	**-270**
H_{min} fault (kA/m)	**-943**	**-1430**	**-278**	**-819**

Note: * mesh extrapolation error, no elements below the knee point, no demagnetization

4.5.2 PM machines with parameters adjusted to withstand demagnetization due to 3-phase to ground short circuit at rated speed

In this section the key machine parameters are adjusted for the PMs to withstand the demagnetization fields due to a symmetrical 3-phase to ground converter short circuit. The influence of the number of rotor poles and of the PM thickness on the material cost and on the demagnetization withstand capability of the NdFeB SPM machine is covered in sections 4.4.2.2 and 4.4.2.3. In summary, the cost of the SPM machines is sensitive to the material cost increase due to thicker magnets. The material cost vs. number of rotor poles characteristic is flat for the SPM machines when p>90. For the IPM machines the influence of magnet thickness and the number of rotor poles is presented in this section.

4.5.2.1 SPM machine with NdFeB magnet

The magnets of the NdFeB SPM machine are only exposed to irreversible demagnetization during the fault. The minimum working point of the magnet at H_{min}=-

943kA/m is only 43kA/m below the knee point. An 11% thicker PM will increase H_{min} over the knee point as in Fig. 4-25. This yields a more expensive machine as shown in Fig. 4-27. Consequently, for the SPM machines it is more cost effective to increase the number of poles as the extra material costs associated with this is marginal as shown in Fig. 4-33. The minimum required pole number for H_{min}>-900kA/m is p=102 as shown in Fig. 4-30. The extra material cost due to the higher number of poles is negligible as shown in Fig. 4-33.

The benchmark 3MW NdFeB SPM machine has a rotor pole number, p=108. As this is close to the FE study minimum cost machine optimum number of rotor poles and because the material cost vs number of rotor poles characteristic curve is flat, the value of the benchmark p=108 will be used for the NdFeB SPM for consistency. Furthermore, a multiple of 12 is preferred for p as this allows the segmentation of the stator into modules of 12 slots and reduces the manufacturing cost of the large OD PM machine.

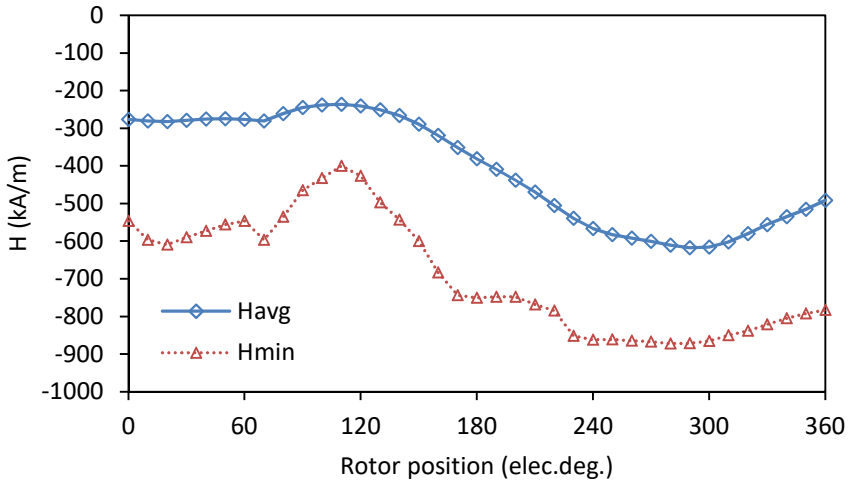

Fig. 4-52 Average and minimum H-fields in the PM before and during a 3-phase to ground converter short circuit for NdFeB SPM machine capable of withstanding demagnetization due to fault.

Fig. 4-53 Contour plot of the H-field along the magnetization direction of the PM at rated current operation of the NdFeB SPM machine capable of withstanding demagnetization due to fault.

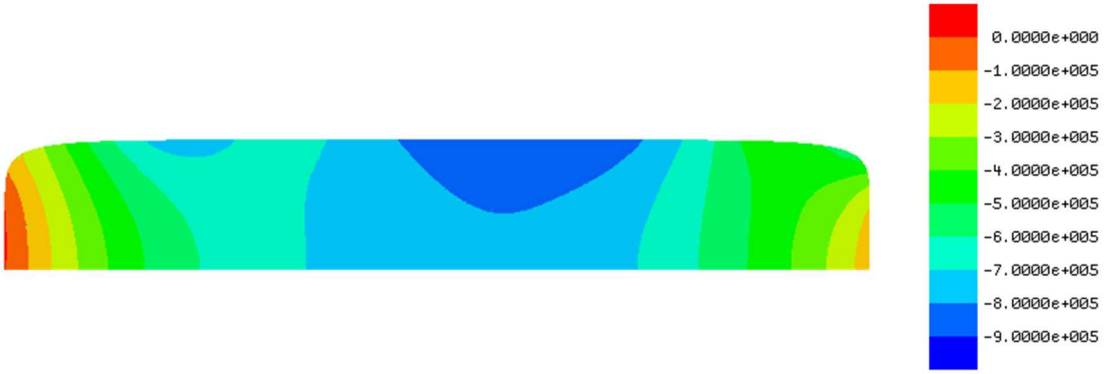

Fig. 4-54 Contour plot of the H-field along the magnetization direction of the PM when H_{min} occurs during the fault transient of the NdFeB SPM machine capable of withstanding demagnetization due to fault.

4.5.2.2 IPM machine with NdFeB magnet

For the NdFeB IPM machine there is a significant increase of the active material cost when either the magnet thickness or the number of rotor poles is increased to eliminate the possibility of irreversible demagnetization. Compared to the SPM machine where the material cost increase due to the higher pole number is marginal, the cost of the IPM significantly changes with the number of rotor poles. This is due to the higher leakage and due to the decrease of reluctance torque for higher rotor pole numbers of the IPM machine. The demagnetization withstand capability of the magnets in the NdFeB IPM can be enhanced by increasing the magnet thickness and the number of rotor poles. Fig.

4-55 shows the minimum average magnetic field strength in the PM during a symmetrical three-phase to ground converted short circuit.

The minimum magnet working point vs number of rotor poles characteristics in Fig. 4-56 is sensitive to the oscillation caused by extrapolating results along the mesh element edges; however, the relationship between the number of poles and the magnet thickness for the machines which are barely capable of withstanding the demagnetization during the fault can be extracted and is shown in Fig. 4-57. This corresponds to the minimum cost machines capable of withstanding the demagnetization during the fault as shown in Fig. 4-58.

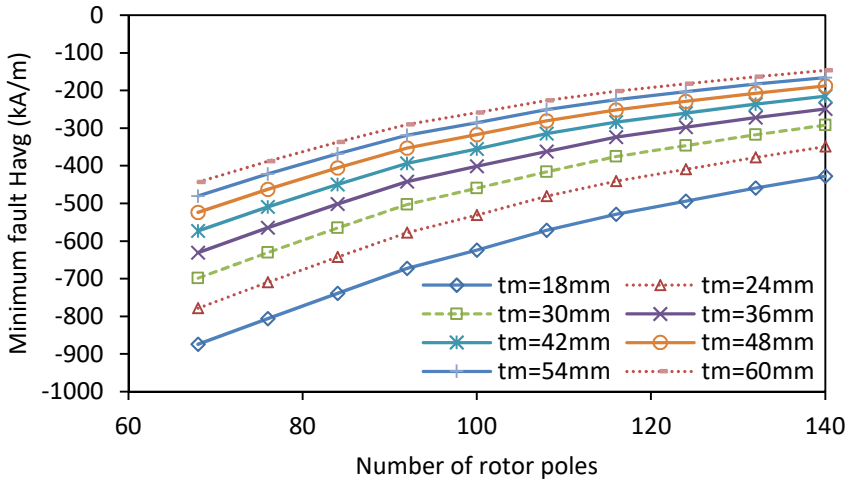

Fig. 4-55 Minimum average H-field in the PM of the NdFeB IPM machine during fault vs. number of rotor poles and magnet thickness.

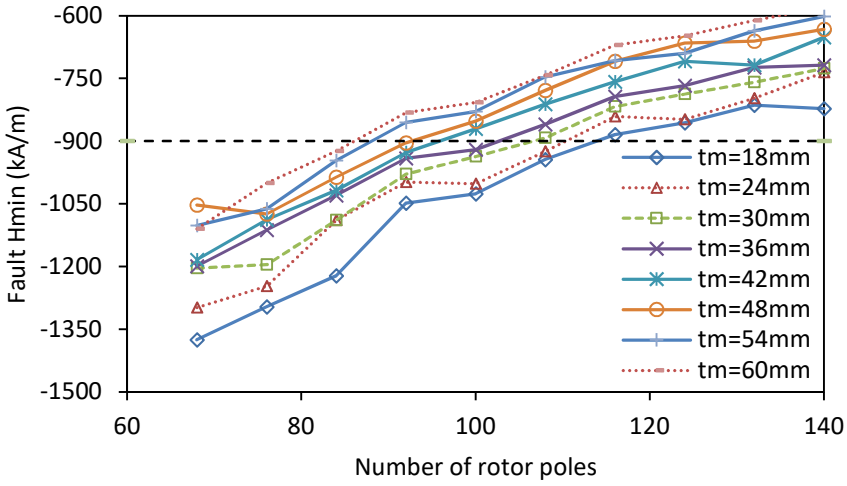

Fig. 4-56 Absolute minimum H-field in the PM of the NdFeB IPM machine during fault vs. number of rotor poles and magnet thickness.

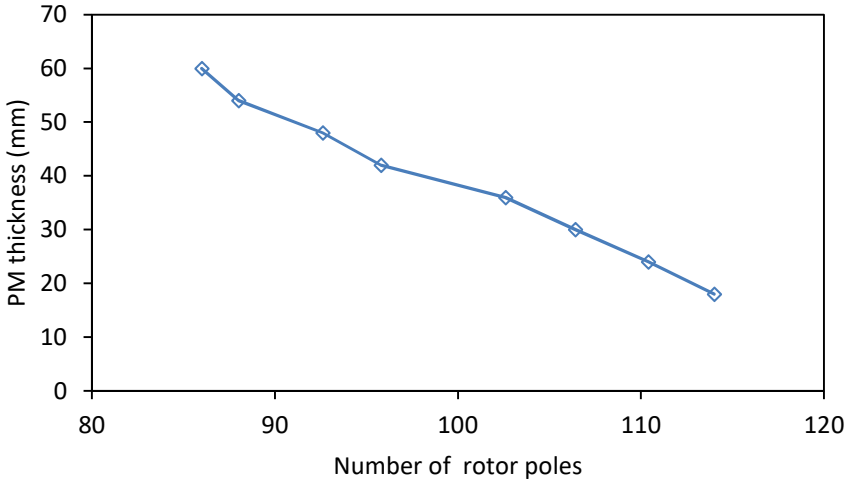

Fig. 4-57 PM thickness required in the NdFeB IPM machines with different number of rotor poles to avoid irreversible demagnetization during fault.

In Fig. 4-58, the increase of material cost associated with increasing the PM thickness is significantly higher than the cost increase caused by the higher rotor pole number. Increasing the number of rotor poles is expected to be the more efficient method to increase the demagnetization withstand capability as it reduces the stator MMF without increasing the amplitude of the fault current as demonstrated in section 4.4 in this chapter. Thus, from Fig. 4-58 the minimum material cost NdFeB IPM machine capable of withstanding the demagnetization during the fault will have the same PM thickness as the minimum cost machine and the number of rotor poles will be increased from

p=68 to p=116. This yields the minimum material cost increase, and thus, it will be regarded as the minimum cost NdFeB IPM machine that can withstand the irreversible demagnetization during the fault.

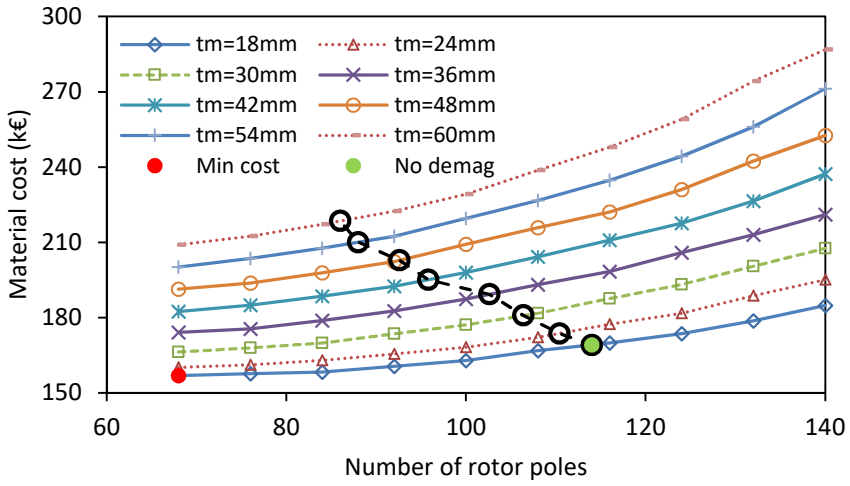

Fig. 4-58 Active material cost of NdFeB IPM machine vs number of rotor poles for different magnet thicknesses. The black dotted line marks the machines exposed to H_{min}=-900 kA/m during the fault (from Fig. 4-56); the machines on the left-hand side of the line experience irreversible demagnetization.

Fig. 4-59 shows the average and minimum H-fields in the magnet before and during the fault transient for the minimum cost NdFeB IPM machine capable of demagnetization withstand. Fig. 4-60 and Fig. 4-61 are contour plots of the H-field in the PM for the rated current operation and at the maximum amplitude demagnetizing field during the fault. The minimum magnet operation points during the fault transient occur near the chamfered corners and at the surface of the PM closest to the air gap. The chamfering and the air barrier between the PM and the rotor bridge contribute to the demagnetization withstand capability of the rotor topology, when the number of turns per coil is reduced at p=116, as shown in Fig. 4-61. In the absolute minimum cost NdFeB IPM machine with p=68 presented in section 4.5.1.2, the number of turns per coil, and thus, the stator MMF is too large for these design details to have a significant contribution.

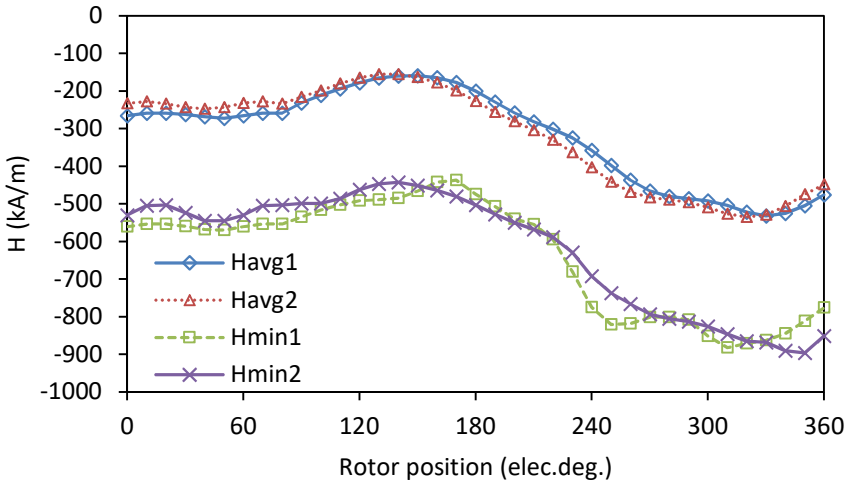

Fig. 4-59 Average and minimum H-fields in the PM before and during a three phase to ground converter short circuit for NdFeB IPM machine capable of withstanding demagnetization due to fault.

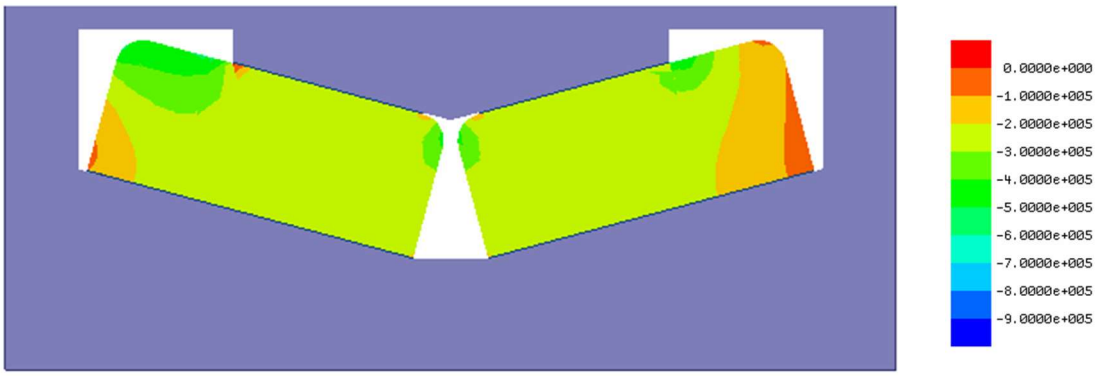

Fig. 4-60 Contour plot of the H-field along the magnetization direction of the PM at rated current operation of the NdFeB IPM machine capable of withstanding demagnetization due to fault.

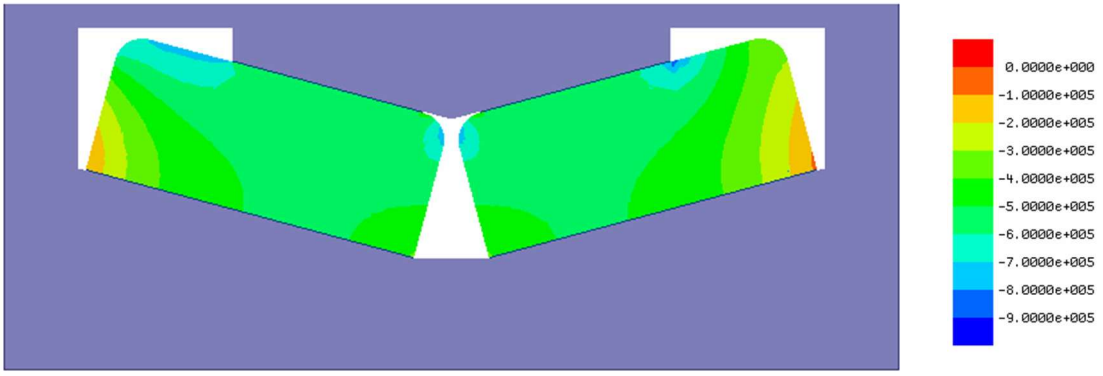

Fig. 4-61 Contour plot of the H-field along the magnetization direction of the PM when H_{min} occurs during the fault transient of the NdFeB IPM machine capable of withstanding demagnetization due to fault.

4.5.2.3 SPM machine with ferrite magnet

In the ferrite PM machines, even though the optimum magnet thickness is significantly higher for the ferrite machines, the lower coercivity of the ferrite material makes it susceptible to demagnetization due to the high current during the fault transient. Fig. 4-62 and Fig. 4-63 show the average and minimum H-fields in the PM during the fault transient for different magnet thicknesses and rotor pole numbers. The process of finding the minimum cost machine with demagnetization withstand capabilities is similar to the one described for the NdFeB IPM machine in section 4.5.2.2.

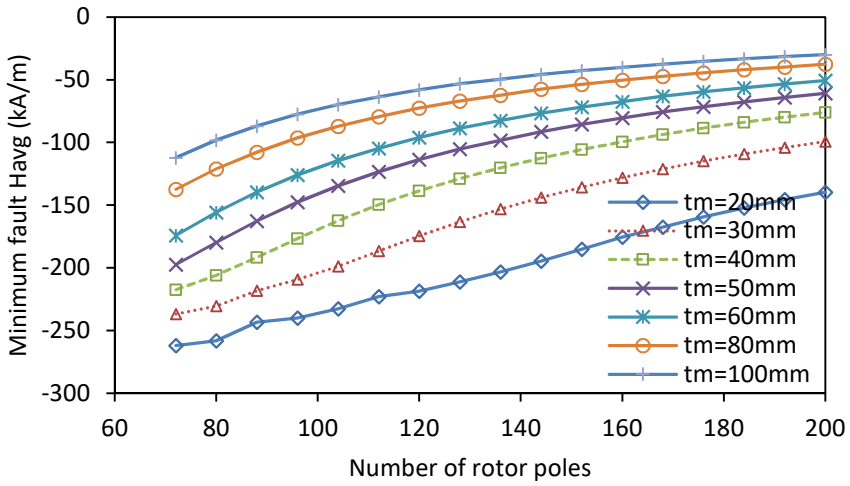

Fig. 4-62 Minimum average H-field in the PM of the ferrite SPM machine during fault vs. number of rotor poles and magnet thickness.

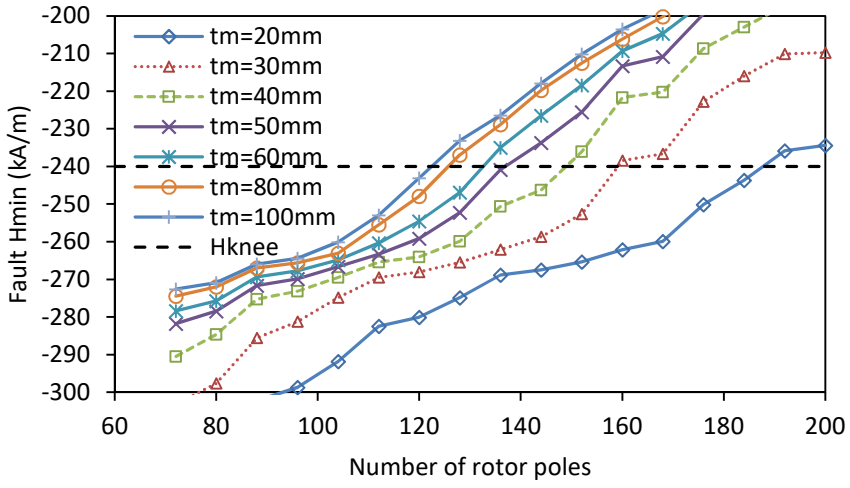

Fig. 4-63 Absolute minimum H-field in the PM of the ferrite SPM machine during fault vs. number of rotor poles and magnet thickness.

In Fig. 4-64 the minimum number of rotor poles for which the machine does not experience irreversible demagnetization during the fault is plotted for different magnet thicknesses. This corresponds to the H_{knee}=-240 kA/m line in Fig. 4-63. The intersect points are used on the total active material cost vs number of rotor poles characteristic in Fig. 4-65. For the FE results in Fig. 4-65, the slot depth is reduced from the optimum at p=72, s_d=114mm, to s_d=100mm, as this is the optimum value for the range of interest (p>100). This is the reason why the minimum cost ferrite SPM machine in Fig. 4-65 is not on the t_m=60mm line, but below. The minimum point corresponds to the absolute minimum cost machine from the previous chapter. For the ferrite SPM machine to have demagnetization withstand capabilities, the number of rotor poles needs to be almost double the optimum value, increasing from p=72 to p=138. This yields a machine with almost half the number of turns per coils, and thus the demagnetizing stator MMF is drastically reduced. Furthermore, due to the significant change of the number of rotor poles, the other key parameters, the magnet thickness and slot depth are slightly reduced. The slot depth was chosen using the material cost vs number of rotor poles characteristic of the ferrite SPM machine from Chapter 3.

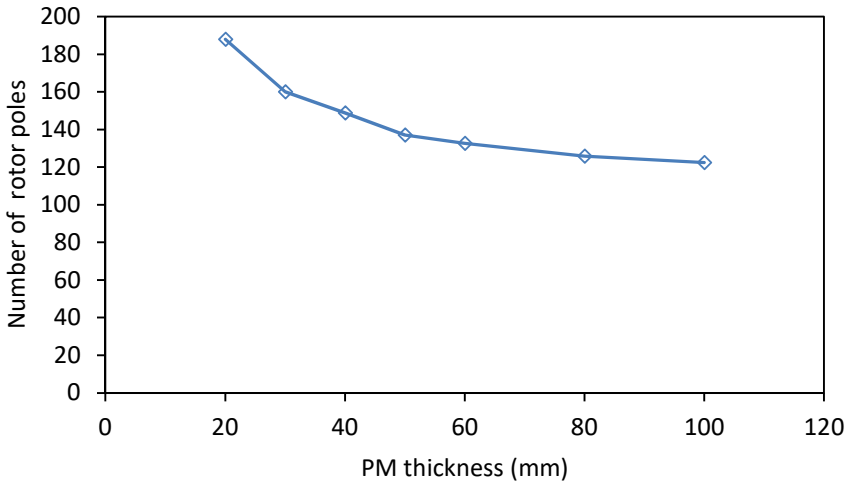

Fig. 4-64 PM thickness required in the ferrite SPM machines with different number of rotor poles to avoid irreversible demagnetization during fault.

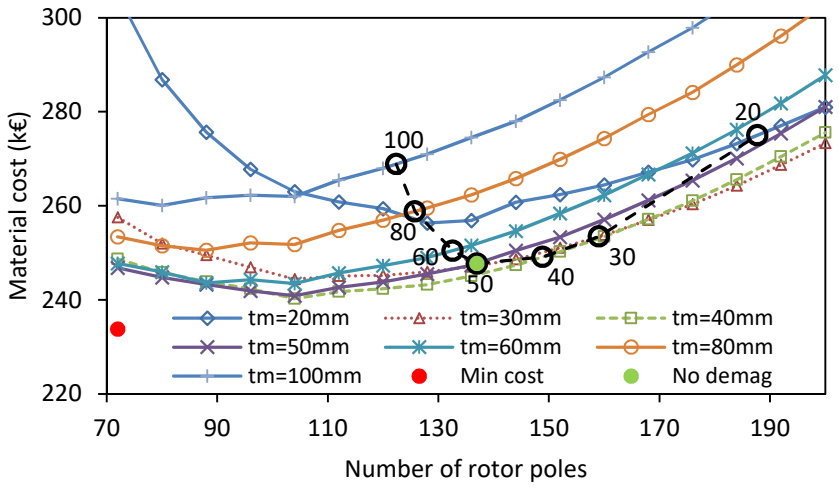

Fig. 4-65 Active material cost of ferrite SPM machine vs number of rotor poles for different magnet thicknesses. The black dotted line marks the machines exposed to H_{min}=-240 kA/m during the fault (from Fig. 4-63); the machines on the left-hand side of the line experience irreversible demagnetization.

In Fig. 4-66 the minimum H-field in the PM does not decrease below the knee point. Fig. 4-67 and Fig. 4-68 show contour plots of the H-field in the PM at rated current and at the moment the absolute minimum H-field occurs during the fault transient.

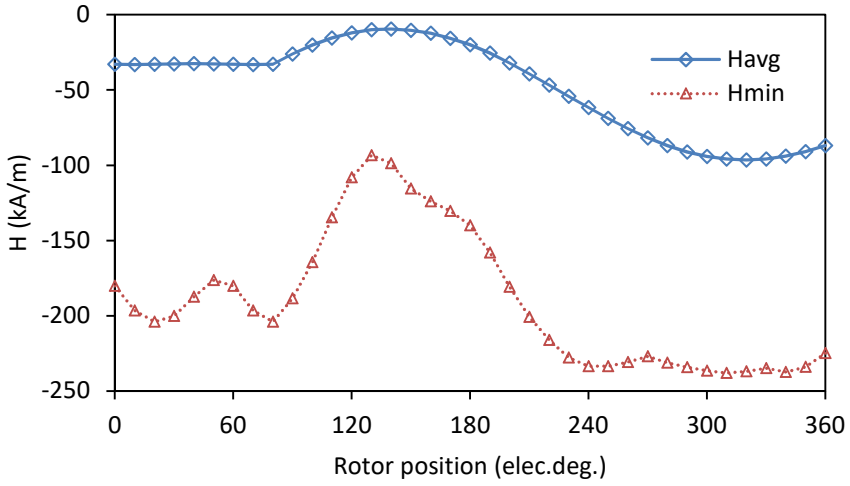

Fig. 4-66 Average and minimum H-fields in the PM before and during a 3-phase to ground converter short circuit for ferrite SPM machine capable of withstanding demagnetization due to fault.

Fig. 4-67 Contour plot of the H-field along the magnetization direction of the PM at rated current operation of the ferrite SPM machine capable of withstanding demagnetization due to fault.

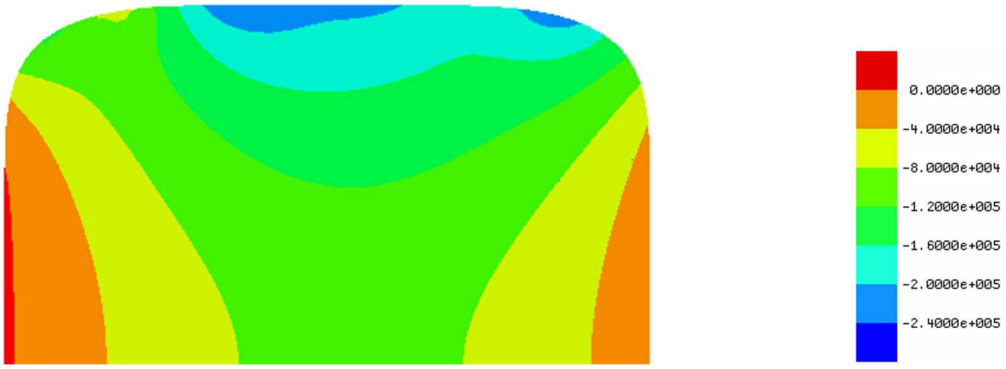

Fig. 4-68 Contour plot of the H-field along the magnetization direction of the PM when H_{min} occurs during the fault transient of the ferrite SPM machine capable of withstanding demagnetization due to fault.

4.5.2.4 IPM machine with ferrite magnet

The average and minimum H-field in the PMs of the ferrite IPM machine during the fault transient are plotted vs. the number of rotor poles for different magnet thicknesses in Fig. 4-69 and Fig. 4-70. The PM thickness vs number of rotor poles curve at which $H_{min}=H_{knee}$ during the fault transient is plotted in Fig. 4-71.

In Fig. 4-72 the material cost of ferrite IPM machines with different PM thicknesses are plotted vs the number of rotor poles. The machines on the right-hand side of the dashed black line have demagnetization withstand capabilities. The minimum cost along this line is at p=116, number of rotor poles, on the t_m=80mm, magnet thickness line. The

number of turns per coil is reduced (by increasing the number of poles) to limit the demagnetization caused by the stator MMF. This has a detrimental effect on the reluctance component of the IPM machine, which is inversely proportional to p. As the minimum cost ferrite IPM machine has the highest reluctance torque of the 4 machines (-45 elec.deg. MTPA current advance angle), it also has the highest material cost increase corresponding to the increase of the number of rotor poles.

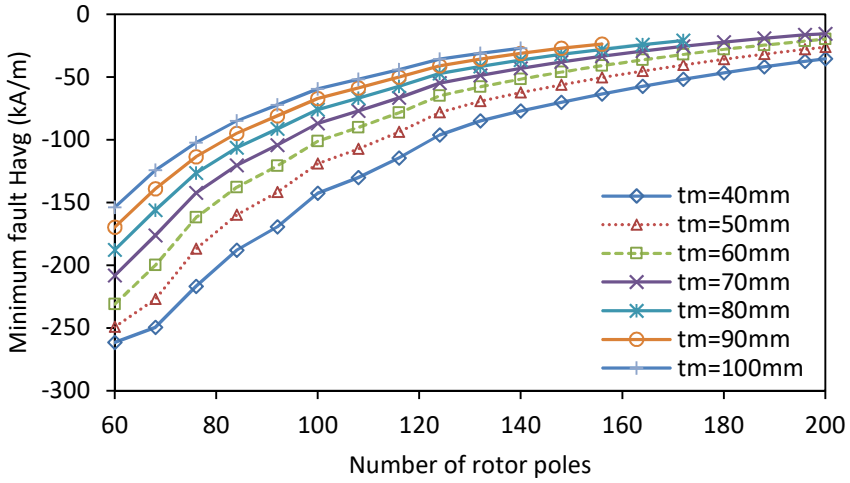

Fig. 4-69 Minimum average H-field in the PM of the ferrite IPM machine during fault vs. number of rotor poles and magnet thickness.

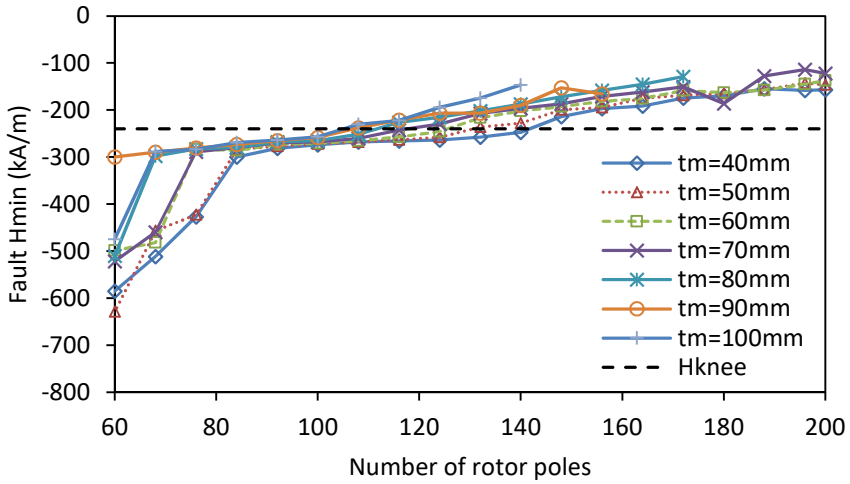

Fig. 4-70 Absolute minimum H-field in the PM of the ferrite IPM machine during fault vs. number of rotor poles and magnet thickness.

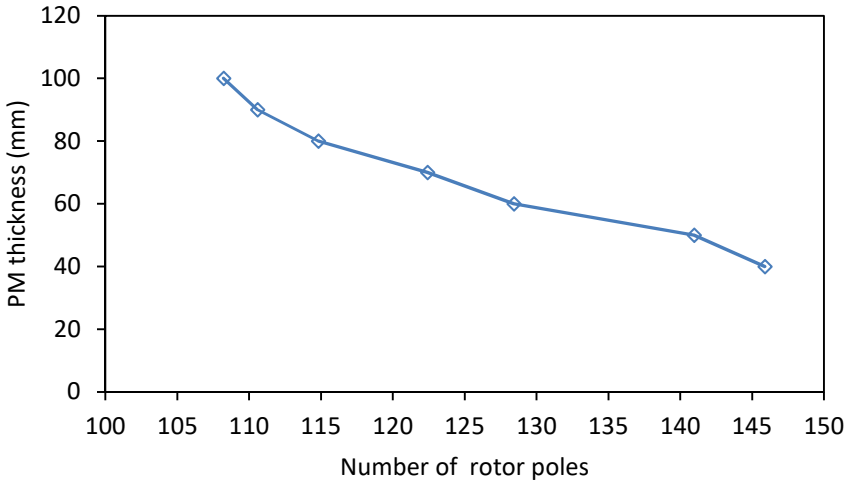

Fig. 4-71 PM thickness required in the ferrite IPM machines with different number of rotor poles to avoid irreversible demagnetization during fault.

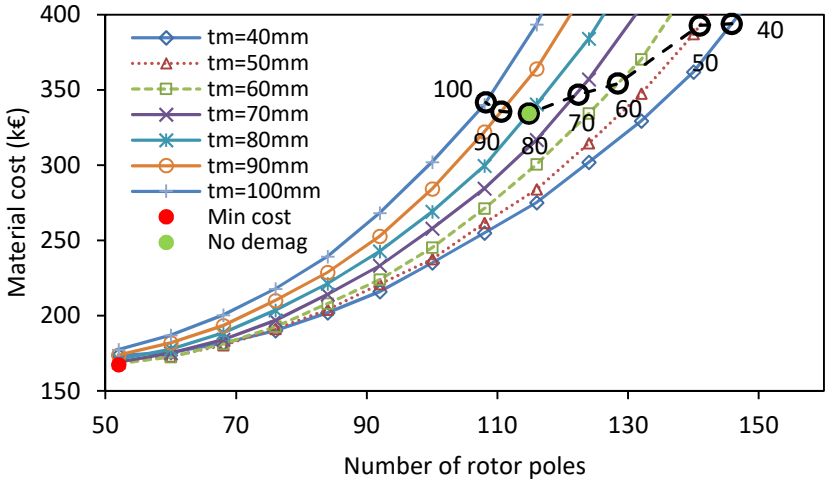

Fig. 4-72 Active material cost of ferrite IPM machine vs number of rotor poles for different magnet thicknesses. The black dotted line marks the machines exposed to H_{min}=-900 kA/m during the fault (from Fig. 4-70); the machines on the left-hand side of the line experience irreversible demagnetization.

Fig. 4-73 shows the average and minimum magnet working points at rated load and during the fault transient of a symmetrical 3-phase to ground converter short circuit at 60 elec.deg. rotor position. Both the average and minimum magnet working points are close to the knee point, H_{knee}=-240kA/m. Due to the low coercivity of the ferrite, it is impractical to design the ferrite IPM machine at the same electrical loading as the NdFeB machines. Despite low number of turns per coil and low stator MMF, the minimum magnet working point is still reduced below the knee point in a small area

close to the rotor surface. This is due to tangential flux flowing along the rotor surface and guided though the high permeability rotor bridges during the fault transient. The high number of rotor poles yields a small pole pitch. When the magnet thickness is comparable to the pole pitch, the space utilization of the traditional V-shape rotor topology is very poor as shown in Fig. 4-74 and Fig. 4-75. For the ferrite IPM machine to have demagnetization withstand capabilities, the number of poles is increased to p=116 and the magnet thickness is increased to t_m=80mm. Although this is the minimum cost ferrite IPM machine with demagnetization withstand capabilities, the material cost has increased by 98% as shown in Fig. 4-72.

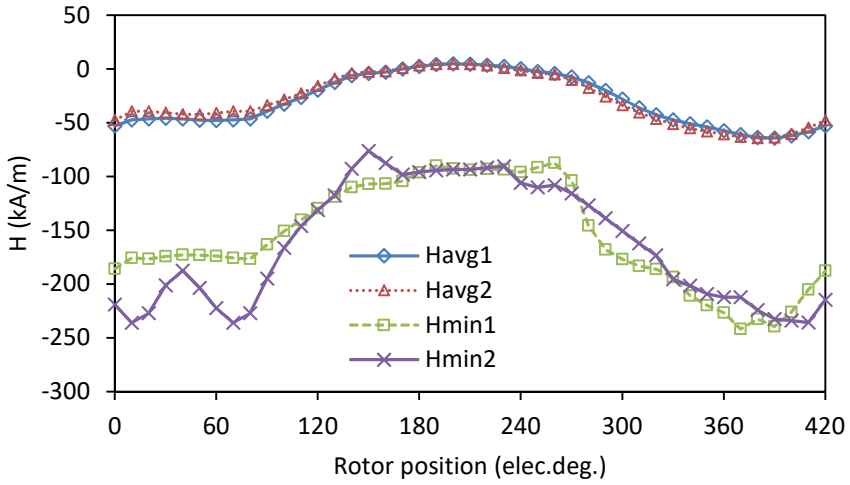

Fig. 4-73 Average and minimum H-fields in the PM before and during a three phase to ground converter short circuit for ferrite IPM machine capable of withstanding demagnetization due to fault.

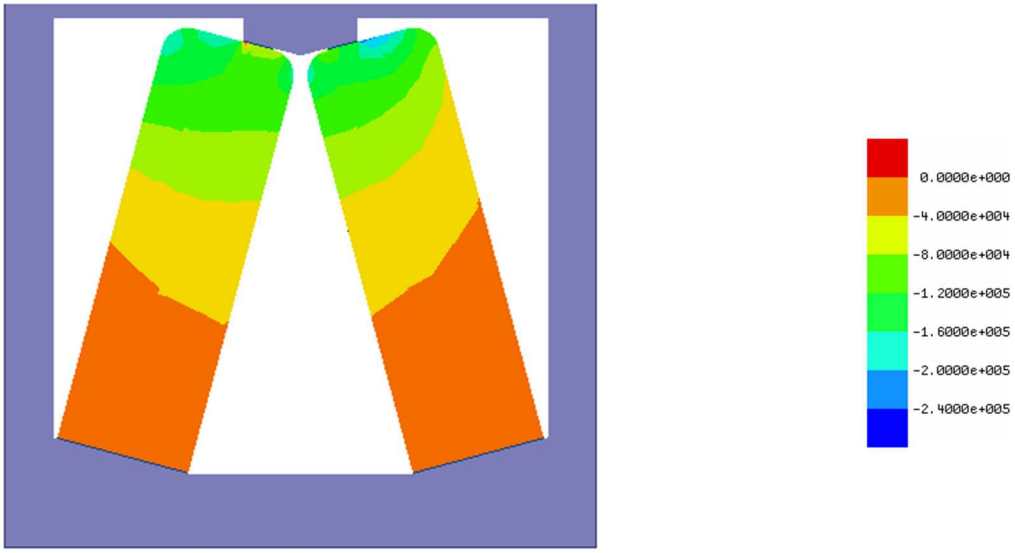

Fig. 4-74 Contour plot of the H-field along the magnetization direction of the PM at rated current operation of the ferrite IPM machine capable of withstanding demagnetization due to fault.

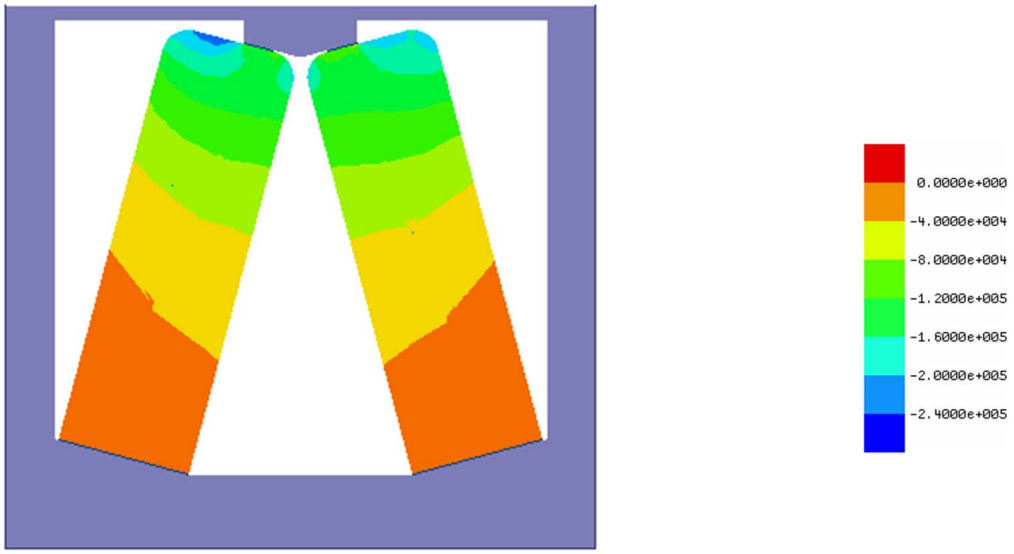

Fig. 4-75 Contour plot of the H-field along the magnetization direction of the PM when H_{min} occurs during the fault transient of the ferrite IPM machine capable of withstanding demagnetization due to fault.

4.5.2.5 Summary of machines capable of magnet demagnetization withstand

Table4-3 Specifications, optimization parameters, circuit data, rated load performance and demagnetization performance summary of minimum cost machines capable of withstanding irreversible demagnetization during fault transient. Magnetic field strengths in red are below the knee point of the magnet.

	NdFeB B_r=1.2T		**Ferrite B_r=0.4T**	
	SPM	**IPM**	**SPM**	**IPM**
Air gap diameter (m)	4.05			
Axial length (m)	1.334	1.59	3.5	4
Active materials cost (k€)	151	170.3	247.3	333.8
Active material volume (m^3)	3.37	4.21	8.89	11.87
Active material mass (t)	26.85	33.5	64.71	89.25
Optimization parameters				
Number of rotor poles	108	116	138	116
Slot depth (mm)	111.4	114	100	119.5
PM/barrier thickness (mm)	17.5	17.5	50	80
MTPA current angle (elec.deg.)	-12	-34	-1	-38
Circuit data				
Copper loss (kW)	159.2	194.6	375	512
Number of turns per phase	1485	1520	1339	1595
Number of turns per coil	27.5	26.2	19.4	27.5
Rated current amplitude (A)	222			
Rated load performance				
Per pole *d*-axis PM flux linkage (Wb)	131.59	110.5	104.2	75.8
Total *d*-axis PM flux linkage (Wb)	7106	6407	7191	4395
Average L_d (H)	0.36	0.6	0.83	1.78
Average L_q (H)	0.49	0.91	0.85	2.37
Power factor at rated load	0.9	0.72	0.51	0.31
Demagnetization performance				
Peak fault I_d (A)	-615	-537	-340	-262
Peak fault I_q (A)	-372	-260	-238	-153
H_{avg} rated load (kA/m)	-282	-273	-33	-53
H_{min} rated load (kA/m)	-609	-569	-204	-236
H_{avg} fault (kA/m)	-618	-535	-97	-64
H_{min} fault (kA/m)	-872	-896	-238	-242

4.5.3 Comparison of PM machines with and without PM capable of withstanding demagnetization

4.5.3.1 Specifications, basic and demagnetization performance

A side-by-side summary of the PM machines without and with magnet demagnetization withstand capabilities is presented in Table 4-4. The most significant difference between these is the higher number of rotor poles of the machines with magnet demagnetization withstand capabilities. The cost of the NdFeB SPM machine does not increase; only a slight adjustment of the number of rotor poles is necessary to decrease the stator MMF and limit the demagnetization during the fault transient. The material cost of the SPM vs number of rotor poles characteristic is flat, there is a negligible cost increase of for the NdFeB SPM machine.

The optimum number of rotor poles for the minimum material cost IPM machine is in the range of p=52 to p=68; for the magnets to not experience irreversible demagnetization, the number of rotor poles is increase to p=116 and p=138. Due to the higher leakage specific for the IPM topology and due to the decrease of reluctance torque with the increase of p, the material cost required for the same average torque increases by 8% for the NdFeB IPM and by 98% for the ferrite IPM. The decrease of the reluctance torque is more severe than the decrease of PM torque due to the extra leakage at the higher number of poles. The ferrite IPM machine without demagnetization withstand capabilities has the highest reluctance torque capability (-45elec.deg. maximum torque per ampere current advance angle). Thus, it has the highest cost increase for the same average torque when the reluctance torque component decreases with the number of rotor poles to enhance the demagnetization withstand capability.

The inductance of the NdFeB SPM machine with magnet demagnetization withstand capabilities is slightly lower owing to the higher number of rotor poles. Hence, its power factor at rated load will be marginally higher. The power factors of all the other machines decrease when they have magnet demagnetization withstand capability. This is mainly because the machines with magnet demagnetization withstand capabilities have lower torque per axial length, longer axial lengths and, hence, higher stator leakage inductances. The power factor issue is the most severe for the ferrite IPM machine with magnet demagnetization withstand capabilities owing to the 4m axial length required for 2.4MNm of average torque.

Table 4-4 Comparison of specifications, parameters, circuit data, rated load performance and demagnetization performance summary of minimum cost machines and machines capable of withstanding irreversible demagnetization during fault transient. Magnetic field strengths in red are below the knee point of the magnet.

	NdFeB B_r=1.2T				Ferrite B_r=0.4T			
	SPM	SPM* w/ dwc	IPM	IPM w/ dwc	SPM	SPM w/ dwc	IPM	IPM w/ dwc
Air gap diameter (m)	4.05							
Axial length (m)	1.344	1.334	1.346	1.59	2.625	3.5	1.73	4
Active materials cost (k€)	151	151 (+0%)	158	170.3 (+8%)	234.7	247.3 (+5%)	167.5	333.8 (+98%)
Active material volume (m3)	3.37	3.37	4.52	4.21	9.1	8.89	7.15	11.87
Active material mass (t)	26.9	26.85	35.6	33.5	66.5	64.71	53.6	89.25
Optimization parameters								
Number of rotor poles	98	108	68	116	72	138	52	116
Slot depth (mm)	111.4	111.4	114	114	119.5	100	119.5	119.5
PM/barrier thickness (mm)	17.5	17.5	17.5	17.5	61.4	50	60.1	80
MTPA current angle (elec.deg.)	-12	-12	-36	-34	-1	-1	-45	-38
Circuit data								
Copper loss (kW)	157.6	159.2	170	194.6	336	375	221.4	512
Number of turns per phase	1490	1485	1574	1519	1595	1339	1596	1595
Number of turns per coil	30.4	27.5	46.3	26.2	44.3	19.4	61.4	27.5
Rated current amplitude (A)	222							
Rated load performance								
Per pole *d*-axis PM flux linkage (Wb)	145.3	131.59	181.5	110.5	198.5	104.2	146.7	75.8
Total *d*-axis PM flux linkage (Wb)	7122	7106	6171	6407	7147	7191	3816	4395
Average L_d (H)	0.42	0.36	0.9	0.6	1.32	0.83	1.43	1.78
Average L_q (H)	0.49	0.49	1.39	0.91	1.34	0.85	3.05	2.37
Power factor at rated load	0.88	0.9	0.77	0.72	0.56	0.51	0.6	0.31
Demagnetization performance								
Peak fault I_d (A)	-609	-615	-540	-537	-366	-340	-455	-262
Peak fault I_q (A)	-366	-372	-271	-260	-248	-238	-206	-153
H_{avg} rated load (kA/m)	-292	-282	-407	-273	-36	-33	-76	-53
H_{min} rated load (kA/m)	-644	-609	-698	-569	-263*	-204	**-275**	-236
H_{avg} fault (kA/m)	-668	-618	**-908**	-535	-175	-97	**-270**	-64
H_{min} fault (kA/m)	**-943**	-872	**-1430**	-896	**-278**	-238	**-819**	**-242**

Note: * w/ dwc – machine with magnet demagnetization withstand capability; its magnets will not be exposed to irreversible demagnetization during symmetrical three phase to ground converter short circuit.

4.5.3.2 Material cost, volume and mass

A breakdown of the active material cost of the machines is shown in Fig. 4-76. The cost of the NdFeB SPM is unchanged. Compared to the minimum cost NdFeB IPM machine, the one with magnet demagnetization withstand capabilities will be 8% more expensive and 17% longer axially. Generally, as the number of rotor poles increases from the value for minimum cost, the trend of the torque per cost is to decrease and the trend of torque per volume and torque per mass is to increase. However, this does not always yields machine with a lower material volume or mass as the axial length is adjusted to compensate for the reduction of the torque per cost. It does, however, yield a lower mass and volume for the NdFeB IPM and a lower mass for the ferrite SPM with magnet demagnetization withstand capabilities as shown in Fig. 4-77 and Fig. 4-78.

The ratio of the copper contribution to the total cost, mass and volume decreases when the number of rotor poles is increased and the thicknesses of the stator and rotor back-irons reduce.

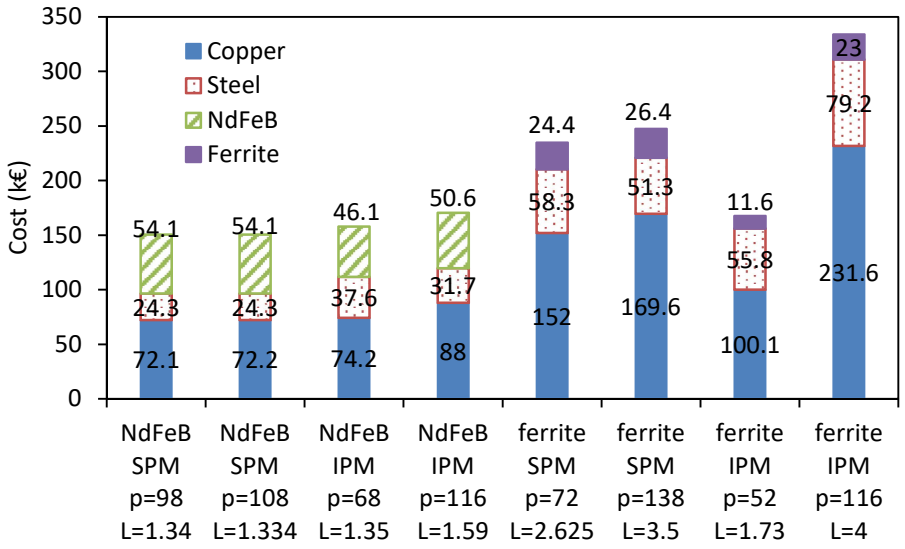

Fig. 4-76 Active material cost breakdown for all machines.

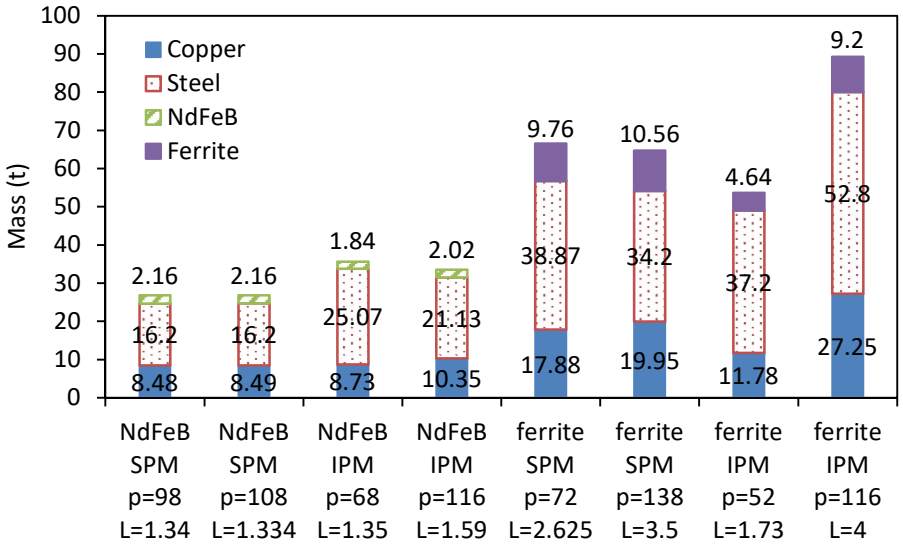

Fig. 4-77 Active material mass breakdown for all machines.

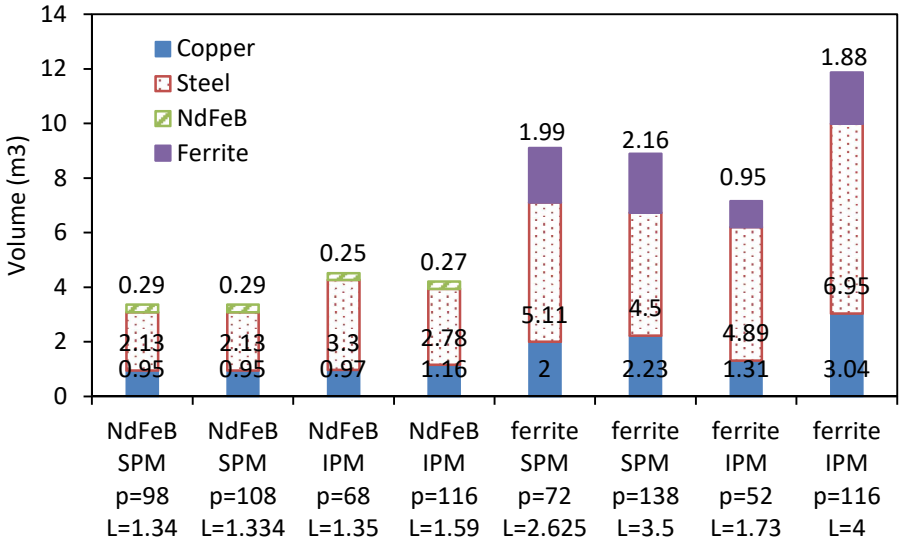

Fig. 4-78 Active material volume breakdown for all machines.

4.5.4 Conclusions

In this chapter, an analytical model and an FE model have been used to predict the fault current in PM machines optimized for DD applications. The influence of the key PM machine parameters on the demagnetization withstand capability was presented.

The demagnetization performance of NdFeB and ferrite, SPM and IPM machines optimized for minimum cost was reported. The machine key parameters have been

adjusted for the PMs to not be subjected to irreversible demagnetization during a symmetrical three-phase to ground converter short circuit. The demagnetization performance and the active material cost, mass and volume of the machines with demagnetization withstand capabilities was presented.

The active material cost of the NdFeB SPM machine has increased only marginally due to its flat material cost vs number of rotor poles characteristic curve. The active material cost has increased by 8% for the NdFeB IPM and by 5% for the ferrite SPM. For the ferrite IPM to have magnet demagnetization withstand capabilities, the rotor pole number is increased to an unfeasible value for the required PM thickness. This is done in order to decrease the number of turns per coil and, thus, the stator demagnetizing MMF during the fault. However, because of the combination of a large pole number and a thick PM, the space utilization is poor in the V-shape ferrite IPM. Thus the cost increase for the ferrite to have magnet demagnetization withstand capabilities is of 98%.

5. Accuracy Validation of Demagnetization Finite Element Solver

5.1 Introduction

One of the drawbacks of high torque/power density PM machines is that the permanent magnet (PM) material is susceptible to irreversible demagnetization when subjected to high strength magnetic fields. For NdFeB, the coercivity is reduced when the PM temperature is increased, further increasing the chance of demagnetization.

Analytical models can predict the average PM working point, but they are usually not used for predicting the minimum local working point of the magnet due to the effect of the stator armature reaction, slotting or complex magnet shapes. Finite element analysis software is used in industry to determine whether the magnet is subjected to irreversible demagnetization during different load or fault conditions.

In this chapter, the accuracy of Cobham Opera Vector Fields demagnetization solver is assessed by the comparison of its results with the experimentally measured demagnetization in a machine with an ISDW stator and 5 identical SPM rotors.

Typical FE results for the decrease in fundamental BEMF and average torque are presented along with contour plots of the flux density in the magnetization direction in the PM. A comparison of the FE results with the demagnetizing current applied at a single rotor position (pulse) and applied at 10 rotor positions over 60 elec.deg. (continuous) is presented.

5.2 Demagnetization solver

5.2.1 Setup

The specifications of the 12slot-4pole ISDW SPM machine with shaped N45h magnets are presented in Table 5-1. The cross section of the machine, modelled in Opera Cobham, is shown in Fig. 5-1, together with equal flux lines and with a contour plot of the flux density at open circuit.

Table 5-1 Specifications of 12s4p SPM.

Parameters	Value
Rated current (A)	0.587
Stator	
Case outer diameter (mm)	110
Lamination outer diameter (mm)	100
Slot bottom diameter (mm)	86.2
Bore diameter (mm)	45
Lamination axial length (mm)	50
Motor axial length (mm)	76.1
Stacking factor (mm)	0.97
Number of slots	12
Tooth width (mm)	5.6
Tip edge thickness (mm)	0.7
Slot opening (mm)	2
Stator winding	
Stator winding connection	Star
Number of phases	3
Coils per phase	2
Turns per coil	125
Wire diameter (mm)	0.57
Packing factor	0.3
Phase resistance (Ohm)	9.2
Winding area (cm^2)	1.1
Air gap length (mm)	0.5
Rotor	
Magnet outer diameter (mm)	44
Magnet inner diameter (mm)	38
Magnet thickness(mm)	3
Axial length (mm)	50
Magnet overhang factor	1
Number of pole pairs	2
Pole-arc to pole-pitch ratio	0.9
Magnet flat arc to magnet pitch ratio	0.2
Magnet edge to magnet mid thickness ratio	0.5
Materials	

Magnet material	N45h
Remanence (T)	1.32
Magnetic relative permeability	1.04
Magnetisation	Parallel
Stator/rotor lamination	Transil1300_16T

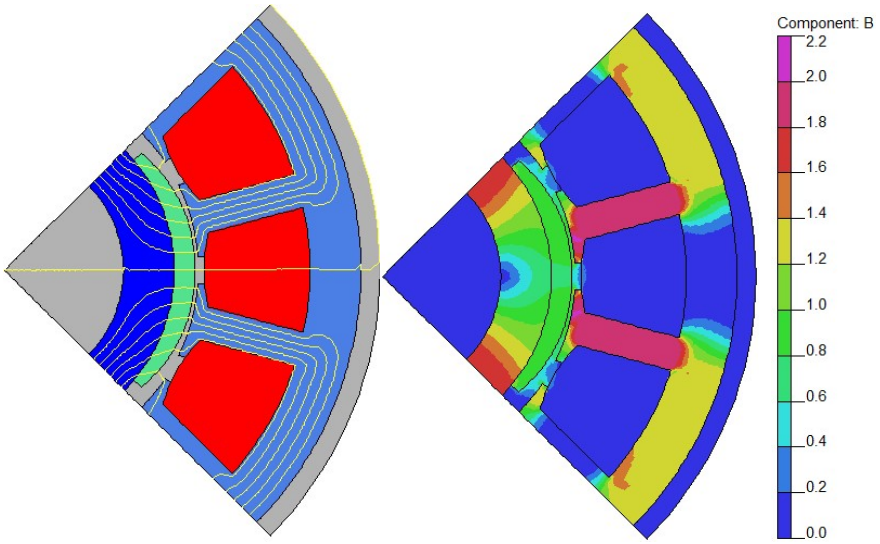

(a) (b)

Fig. 5-1 Cross section of 12 slots-4 poles SPM motor with overlapping winding. (a) Equal potential flux lines. (b) Flux density contour plot at open circuit.

A single time stepping transient FE analysis is used to assess the machine performance before and after the demagnetizing event. The setup as in Fig. 5-2:

- 240 elec.deg. open circuit (original PM magnetization)
- 240 elec.deg. rated current (original PM magnetization)
- 240 elec.deg. demagnetizing I_d
- 240.elec.deg. open circuit (demagnetized PM)
- 240 elec.deg. rated current (demagnetized PM)

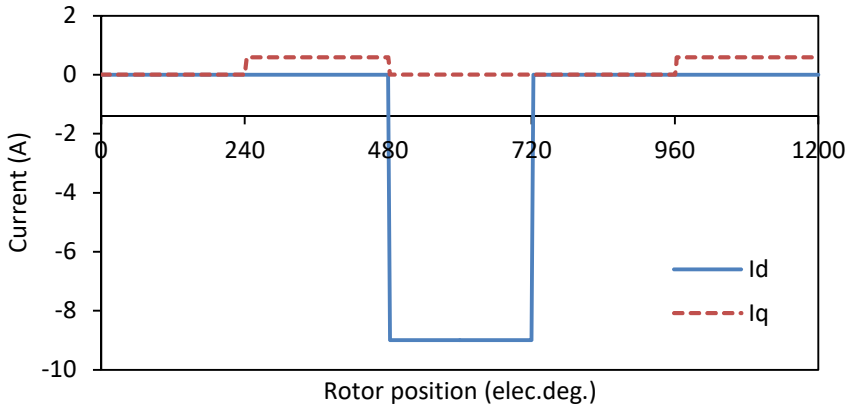

Fig. 5-2 Dq-axis current amplitudes during demagnetization transient (I_d=-9A).

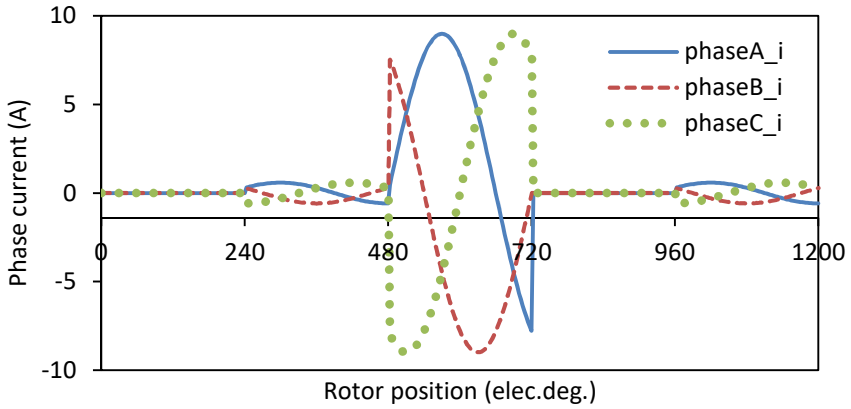

Fig. 5-3 Phase current waveforms during demagnetization transient setup (I_d=-9A).

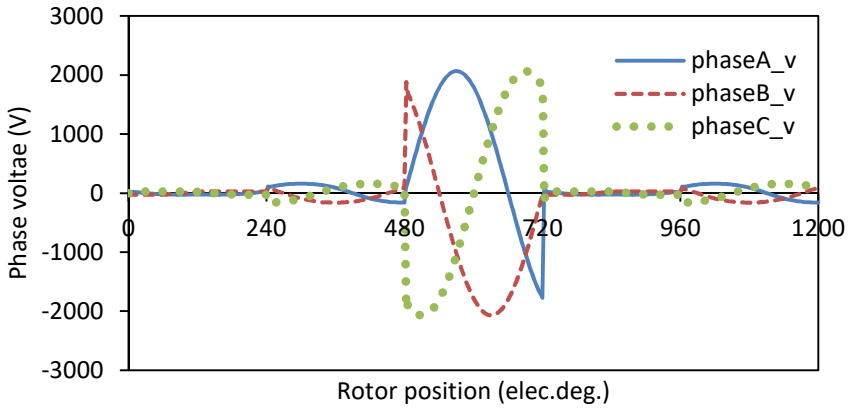

Fig. 5-4 Phase voltage waveforms during demagnetization transient setup (I_d=-9A).

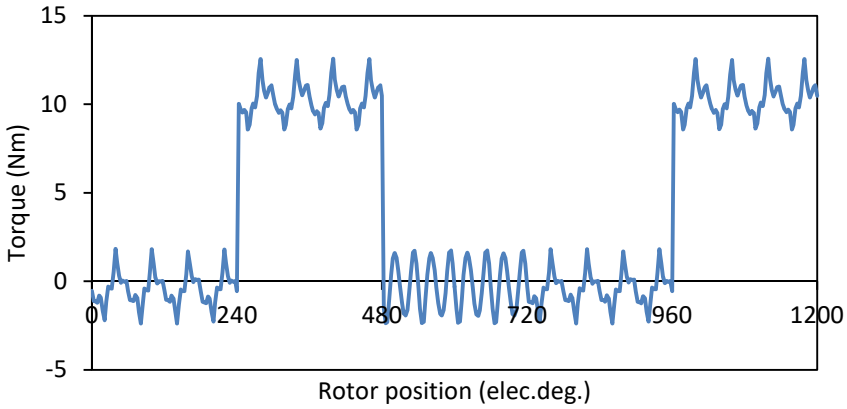

Fig. 5-5 Open circuit and rated load torque waveforms before and after demagnetizing I_d current (I_d=-9A).

The severity of the demagnetization can be quantified by comparing the open circuit and the rated load performance before and after the demagnetization. The average *q*-axis voltage (directly proportional to the back EMF fundamental) is used at open circuit and the average output torque is used at rated load to quantify the demagnetization severity.

There is no irreversible demagnetization in the case of I_{demag}=I_d=-9A from Fig. 5-2 to Fig. 5-5.

5.2.2 Irreversible demagnetization example

An I_{demag}=I_d=30A current, about 50 times the amplitude of the rated current excitation is used to show an example of the irreversible demagnetization, as in Fig. 5-6-Fig. 5-10.

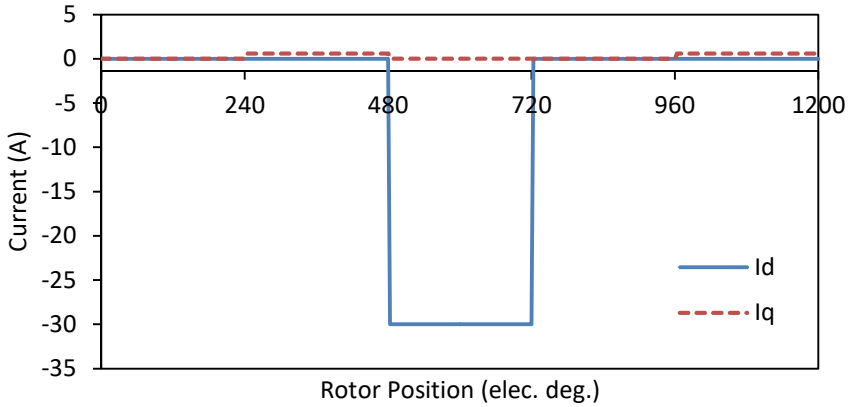

Fig. 5-6 Dq-axis current amplitudes during demagnetization transient (I_d=-30A).

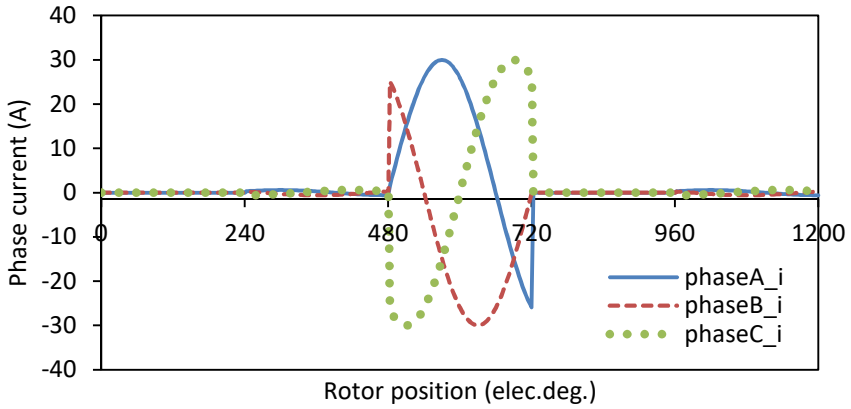

Fig. 5-7 Phase current waveforms during demagnetization transient setup (I_d=-30A).

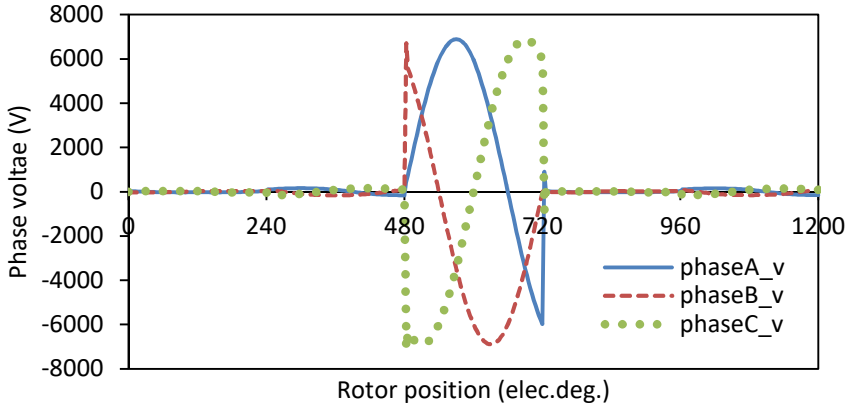

Fig. 5-8 Phase voltage waveforms during demagnetization transient setup (I_d=-30A).

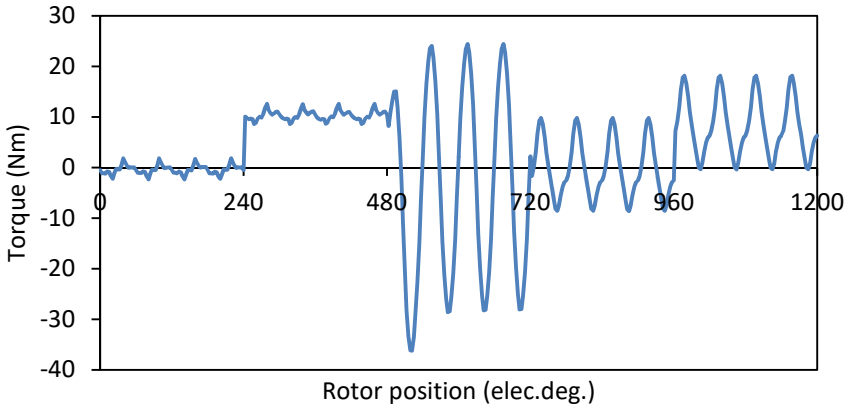

Fig. 5-9 Open circuit and rated load torque waveforms before and after demagnetizing I_d current (I_d=-30A).

Comparing Fig. 5-5 and Fig. 5-9, the most obvious effect of the PM demagnetization is on the cogging torque. In Fig. 5-8, the peak to peak cogging torque and hence the on rated load torque ripple are increased by 5 times, from 4 to 20Nm. This results is as expected and can be justified by considering the sensitivity of the cogging torque to changes in either PM geometries or magnetic properties in machines equipped with integer slot distributed overlapping windings. Thus, when the PM is shaped for the cogging torque minimization, irreversible demagnetization will deteriorate the cogging torque performance.

A demagnetization current I_d=-30A will reduce the open circuit back EMF by 21% and the average rated load torque by 20.4% (10.3 to 8.2 Nm) for this 12-slot-4-pole ISDW SPM machine with N45h grade magnet at 60°C.

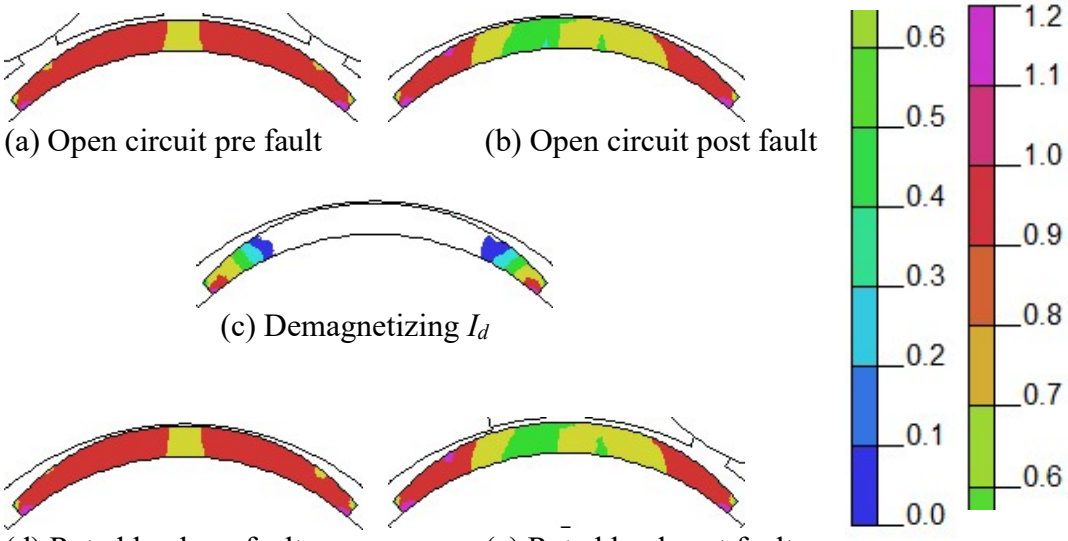

Fig. 5-10 Contour plot of PM flux density pre, during and post fault (I_r=0.58A, I_{demag} =I_d=-30A).

The reductions of the back EMF and the average torque at rated current are plotted in Fig. 5-11 and Fig. 5-12, respectively. The decrease in average torque at the rated current will be directly proportional to the decrease of the magnetic loading in a non-salient SPM machine.

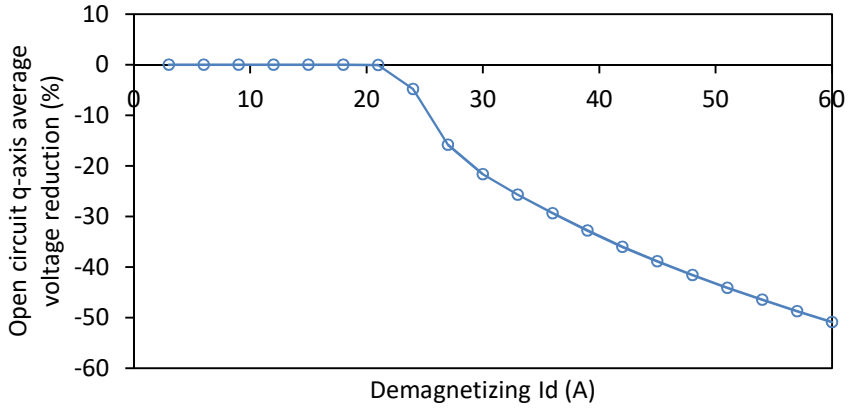

Fig. 5-11 Fundamental back EMF reduction due to demagnetizing I_d.

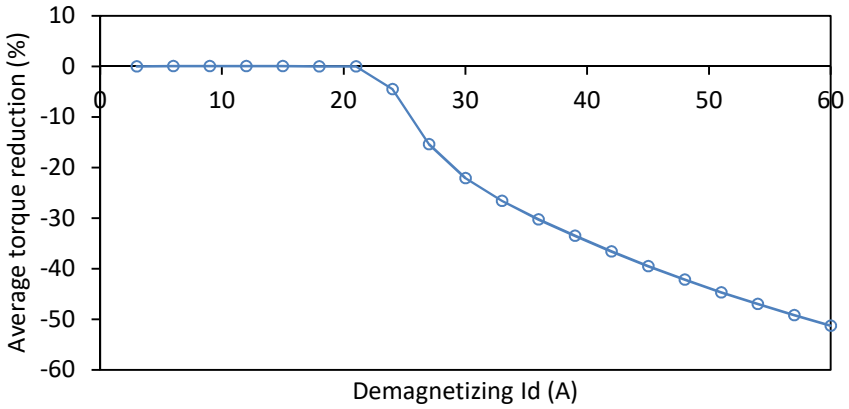

Fig. 5-12 Average torque reduction due to demagnetizing I_d.

5.2.3 Continuous demagnetization vs. pulse demagnetization

The objective is to assess the accuracy of the demagnetization solver. Thus, it is crucial that the FE setup matches the experimental setup. It is impractical to run the demagnetization experiment on a PM machine in operation. The load machine would have to match the braking torque during the demagnetization without a rotational speed decrease.

To reduce the number of factors that can cause errors, a locked rotor demagnetization setup is preferred.

When the demagnetization current is applied continuously for more than 60 elec.deg., the magnet is exposed to the demagnetization field in all positions relative to the stator slots. Fig. 5-13 to Fig. 5-15 are plots of the dq-axis currents vs rotor position for two demagnetization setups: continuous current, a pulse when the PM is aligned to the middle of the slot opening or the tooth. Contour plots of the H-field in the PM at open circuit and at the moment the demagnetization pulse is applied are shown in Fig. 5-16 and Fig. 5-17. Because of the slotting effect, the magnet aligned to the middle of a slot opening yields a more severe demagnetization. Fig. 5-18 is a plot of equal flux lines

across the magnet magnetization direction for the same current at the two rotor positions.

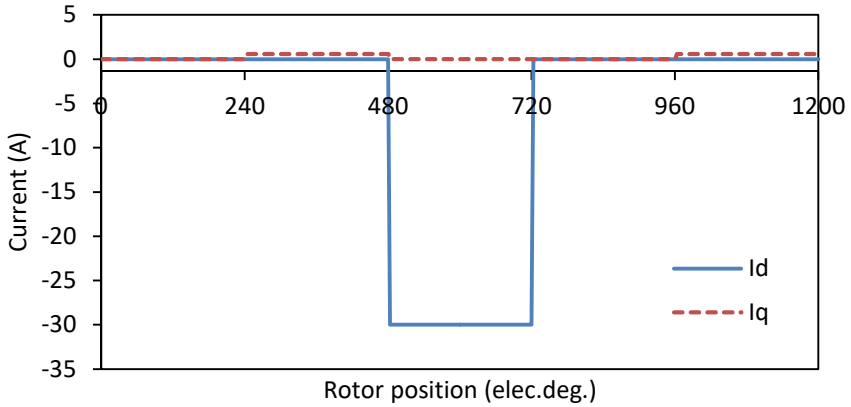

Fig. 5-13 Dq-axis current amplitudes during demagnetization transient (I_d=-30A).

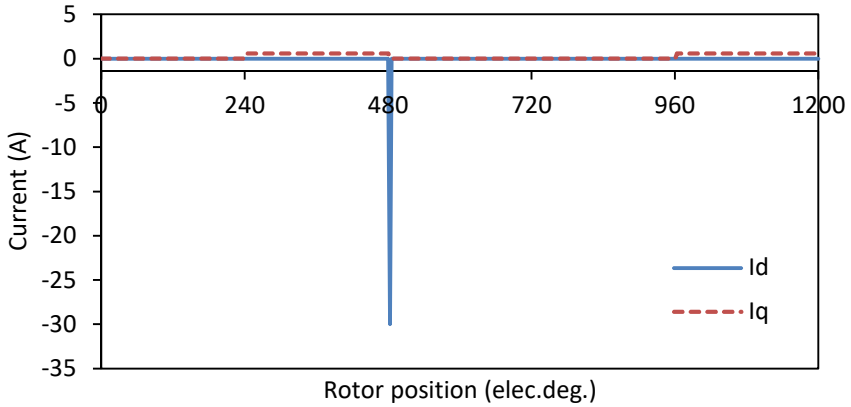

Fig. 5-14 Dq-axis current amplitudes during demagnetization pulse @ 480 elec.deg. when the PM is aligned to slot opening middle (I_d=-30A).

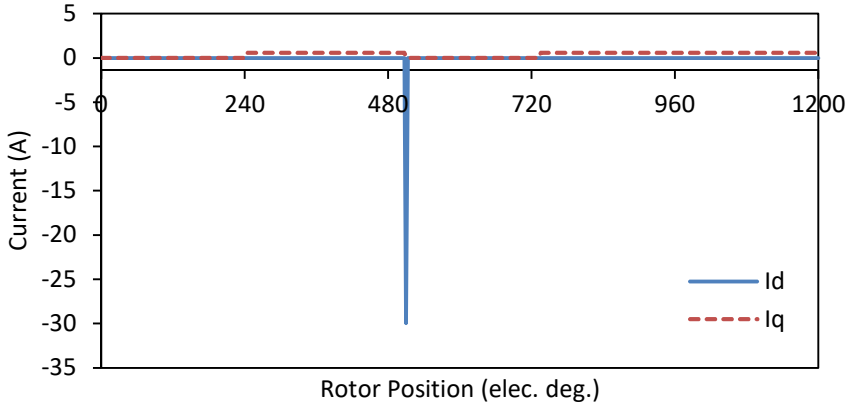

Fig. 5-15 Dq-axis current amplitudes during demagnetization pulse @ 510 elec.deg. when the PM is aligned to tooth middle (I_d=-30A).

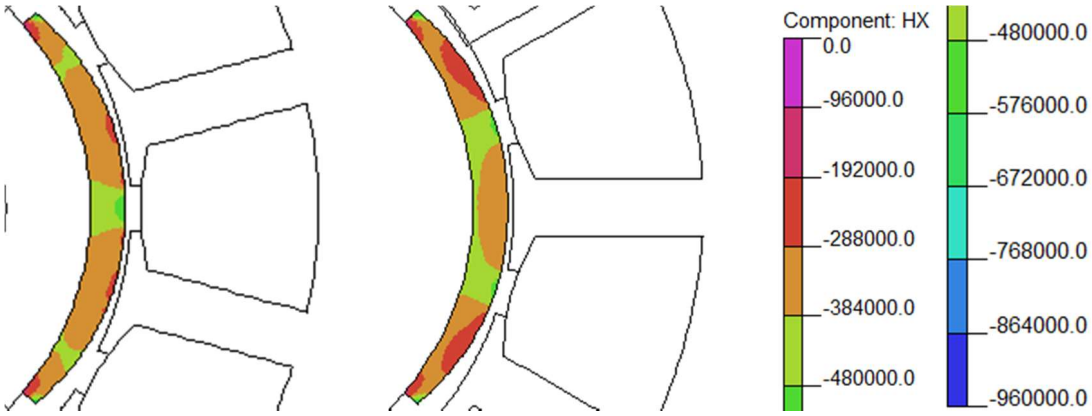

Fig. 5-16 Contour plot of H-field in PM at open circuit for the PM aligned with either slot opening or middle tooth.

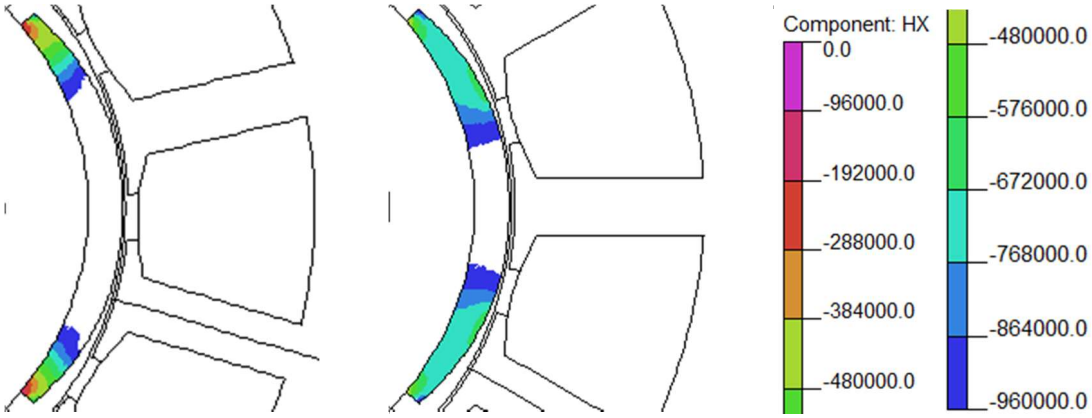

Fig. 5-17 Contour plot of H-field in PM during demagnetizing pulse for the PM aligned with either slot opening or middle tooth (I_d=-30A).

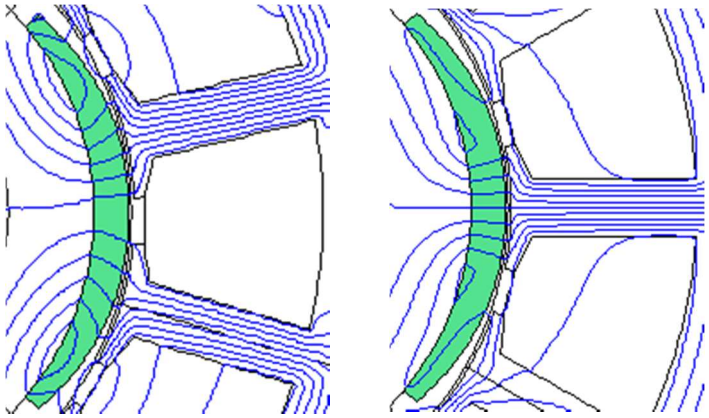

Fig. 5-18 Equal flux lines at demagnetizing pulse for the PM aligned with either slot opening or middle tooth (I_d=-30A).

The reduction of the open circuit q-axis average voltage at the same speed vs the demagnetization current amplitude for the three setups is plotted in Fig. 5-19. Applying the demagnetization for all rotor positions (continuously) yields the most reduction of

the magnetization. Furthermore, if the PM is aligned to the slot opening the demagnetization is more severe than if the PM is aligned to the tooth. The cogging torque is sensitive to the loss in magnetization. In Fig. 5-22, the increase of cogging torque is significantly higher for the pulse current setup with the PM aligned to a tooth. The trend is similar for the rated current peak to peak torque ripple in Fig. 5-23.

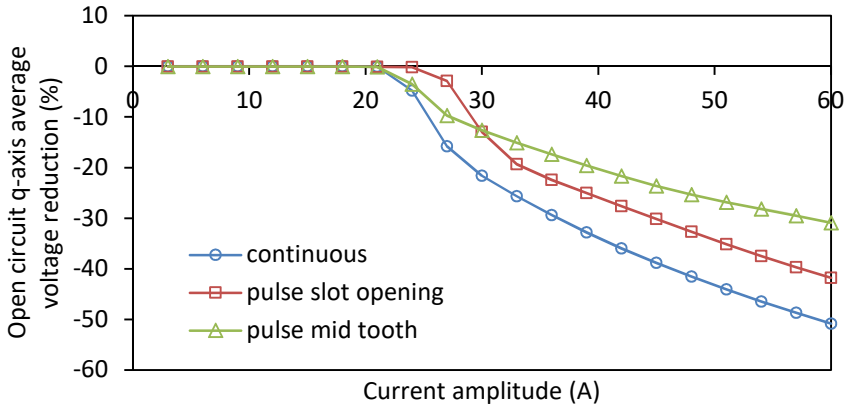

Fig. 5-19 Fundamental back EMF reduction due to demagnetizing Id for locked and rotating rotors.

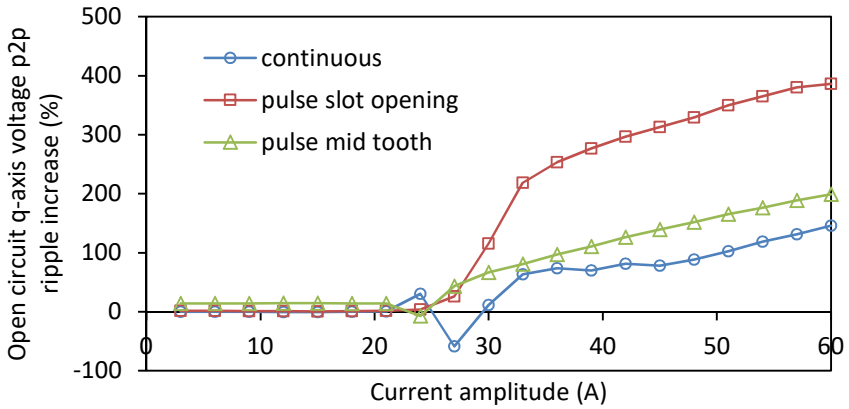

Fig. 5-20 Back EMF THD increase due to demagnetizing Id for locked and rotating rotors.

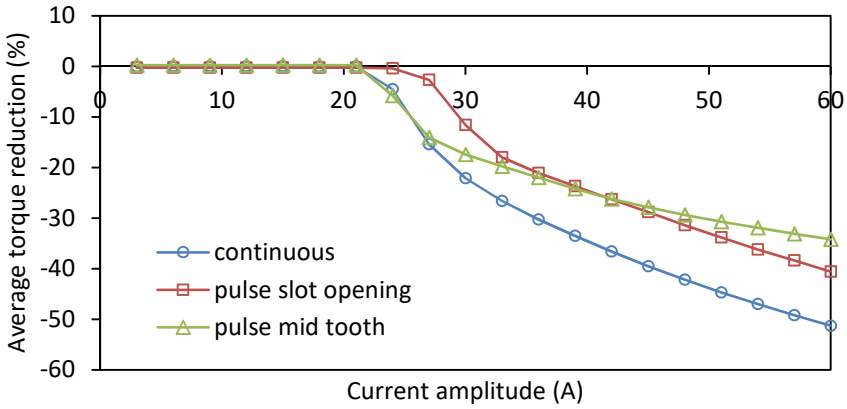

Fig. 5-21 Average torque reduction due to demagnetizing Id for locked and rotating rotors.

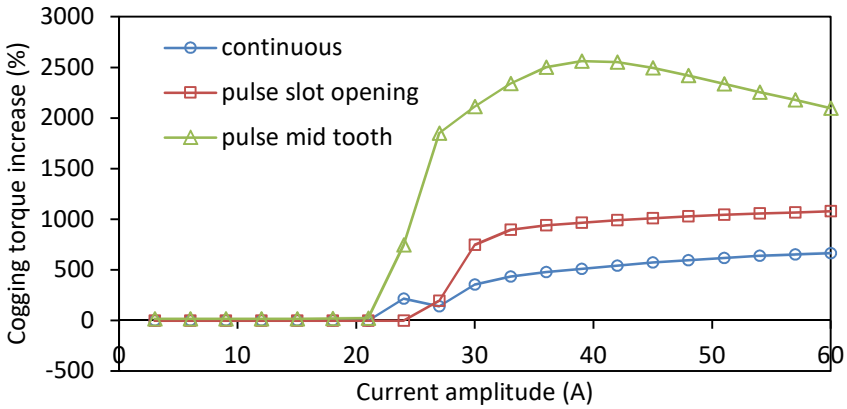

Fig. 5-22 Cogging torque peak to peak ripple increase due to demagnetizing Id for locked and rotating rotors.

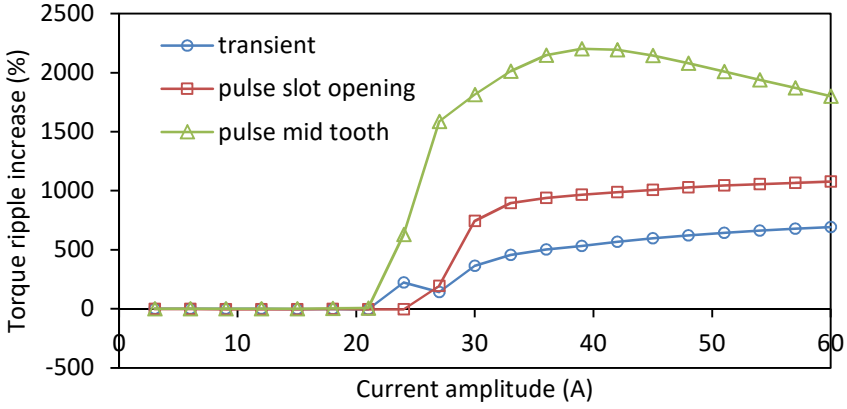

Fig. 5-23 Rated load torque peak to peak ripple increase due to demagnetizing Id for locked and rotating rotors.

5.2.4 PM working points during transient

In this section, the magnet working points at the locations in Fig. 5-24 are presented for three cases, one without any irreversible demagnetization, one where the magnet is demagnetized by a d-axis current and one where a significantly higher amplitude q-axis current is used to cause irreversible demagnetization on one side of the magnet.

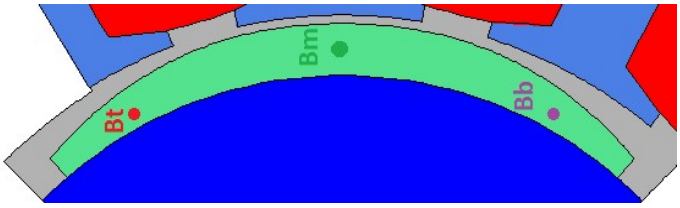

Fig. 5-24 Location of PM points and flux density during demagnetization transient.

5.2.4.1 No demagnetization (Id=-9A)

In Fig. 5-25 the cogging torque and the on load torque ripple before the demagnetizing pulse applied at 480 elec.deg. have identical waveforms after the demagnetizing event. The magnet is not operated below H_{knee} in any of the three points as shown in Fig. 5-25 to Fig. 5-27. The applied demagnetization field is in the d-axis, and hence, the stator generated MMF will be symmetrical to the centre of the magnet, and thus, identical in the points marked by B_t and B_b in Fig. 5-24. For all the points in this case, the magnet working points reduce at the moment of the pulse demagnetizing current, then move back along the same recoil line when the pulse is removed.

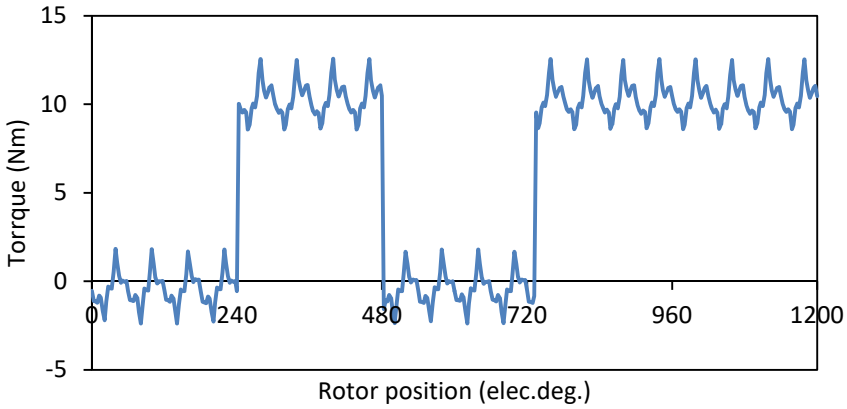

Fig. 5-25 Open circuit and rated load torque waveforms before and after demagnetizing Id current (I_d=-9A).

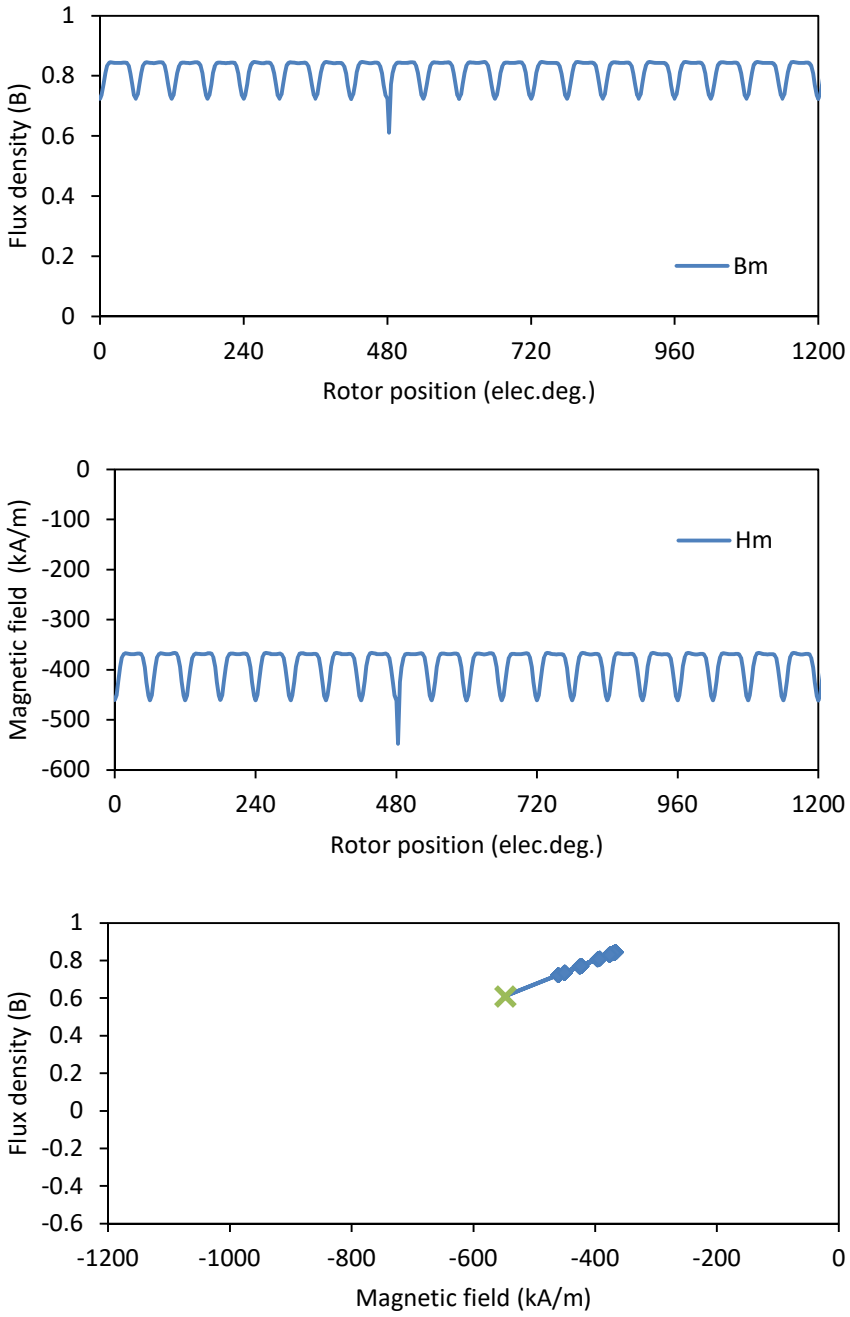

Fig. 5-26 Flux density and magnetic field strength in PM middle point in Fig. 5-24 before and after demagnetizing current (I_d=-9A).

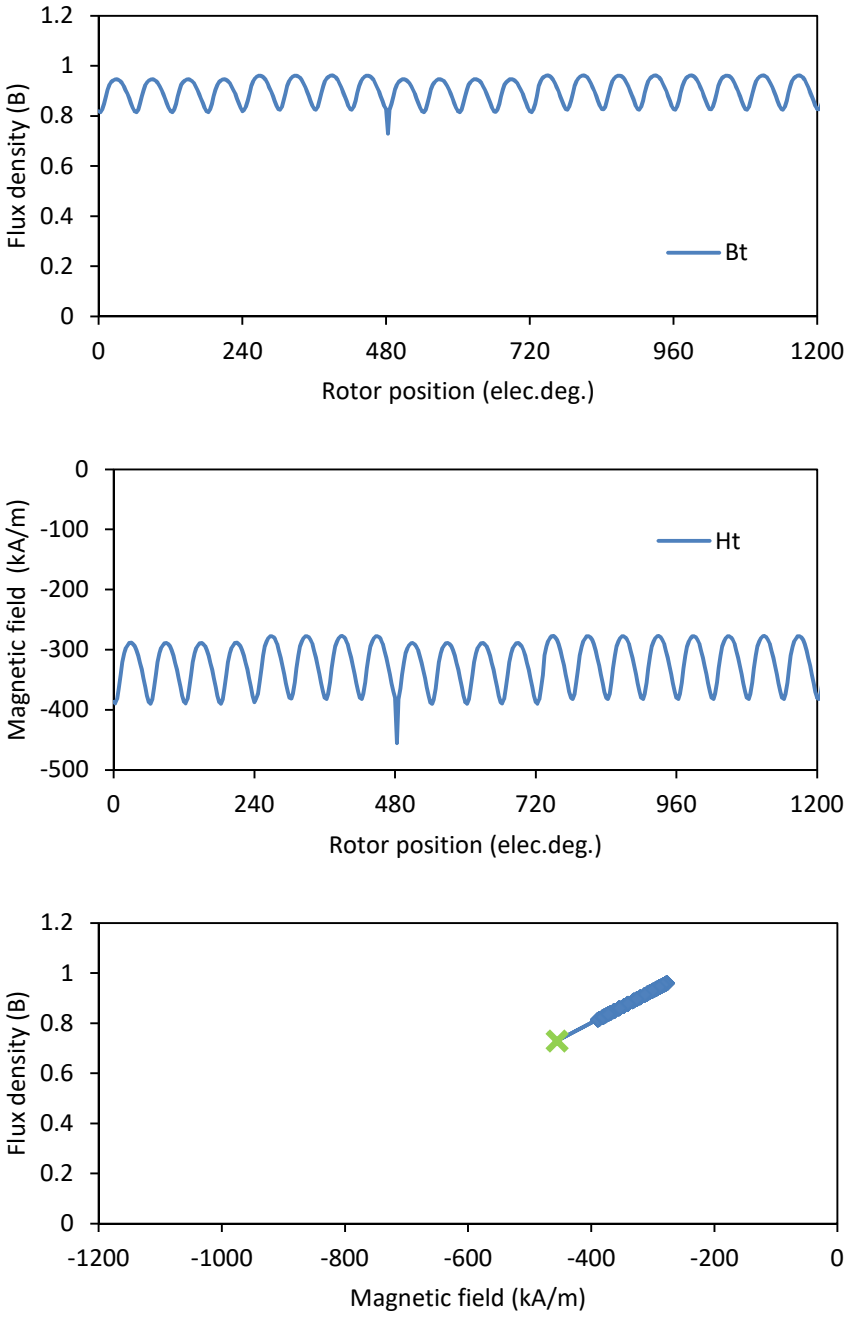

Fig. 5-27 Flux density and magnetic field strength in PM top point in Fig. 5-24 before and after demagnetizing current (I_d=-9A).

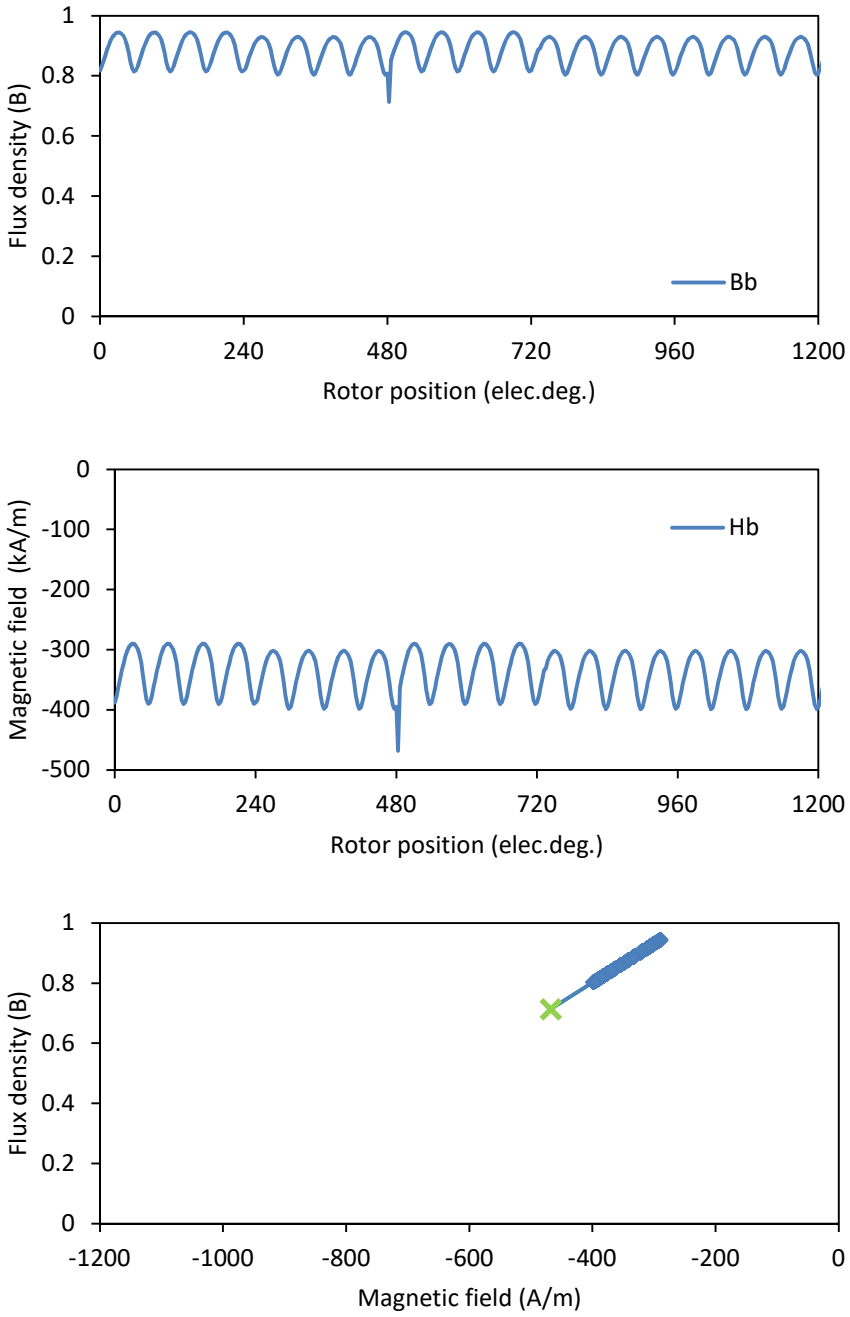

Fig. 5-28 Flux density and magnetic field strength in PM bottom point in Fig. 5-24 before and after demagnetizing current (I_d=-9A).

5.2.4.2 Average torque decrease (Id=-30A)

The average torque decreases by 12% due to the loss of magnetization in this case. The magnet operation point moves below the knee point in the center of the magnet as shown in Fig. 5-30. In the FE software the magnet working point shifts directly to the working point corresponding to the demagnetization field. This behaviour is sufficient to model the magnetization in the element after the external field is removed. The contour plot of the magnetic field strength in the magnetization direction of the PM in Fig. 5-34 shows most of the middle part of PM is operated above the magnetic field safe limit H_{lim}=920kA/m and close to H_{knee}=-960kA/m for the N45h NdFeB at 60°C. The magnetic field safe limit, H_{lim}, is set above the knee point and provides a safety margin used to avoid the loss of magnetization due to the non-linearities of the B-H curve before the knee point.

The maximum demagnetization field in this case for the points marked with B_b ant B_t in Fig. 5-24 is around H=-860kA/m and is not below the knee point. However, because the magnetic circuit will be less saturated after the demagnetization event, the working points in the magnet areas which have not been subjected to irreversible demagnetization will increase as shown in Fig. 5-31 and Fig. 5-32.

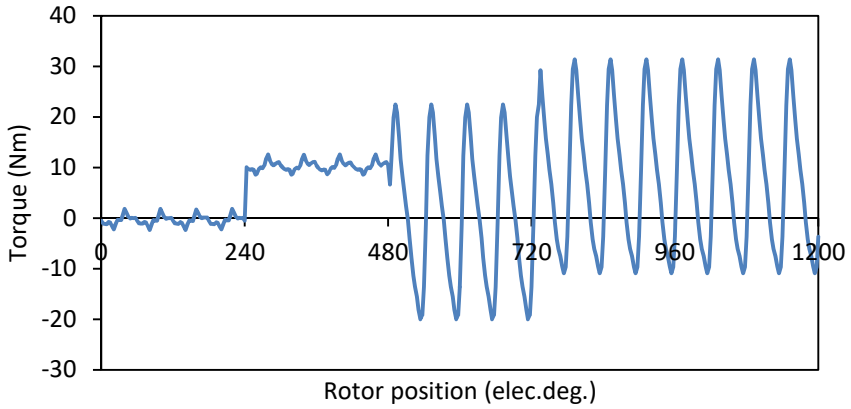

Fig. 5-29 Open circuit and rated load torque waveforms before and after demagnetizing Id current (I_d=-30A).

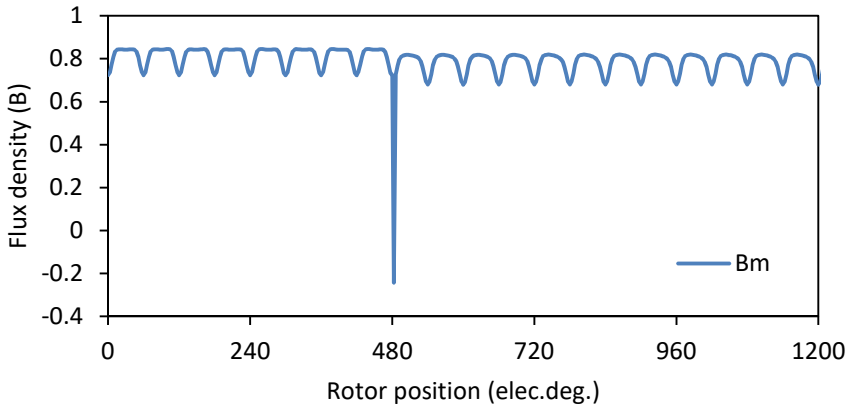

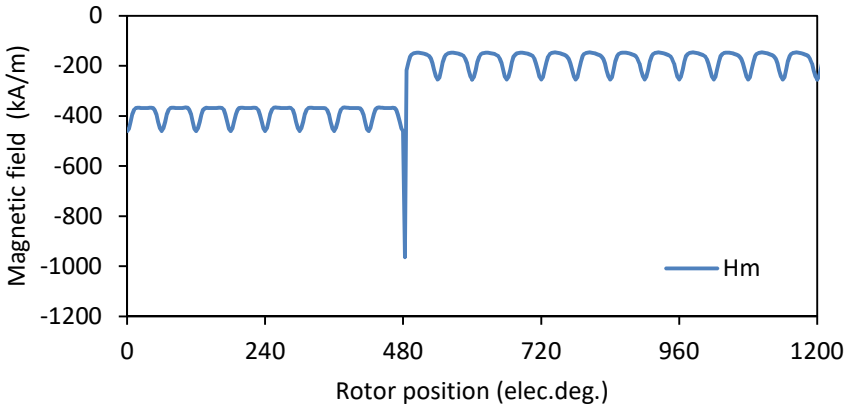

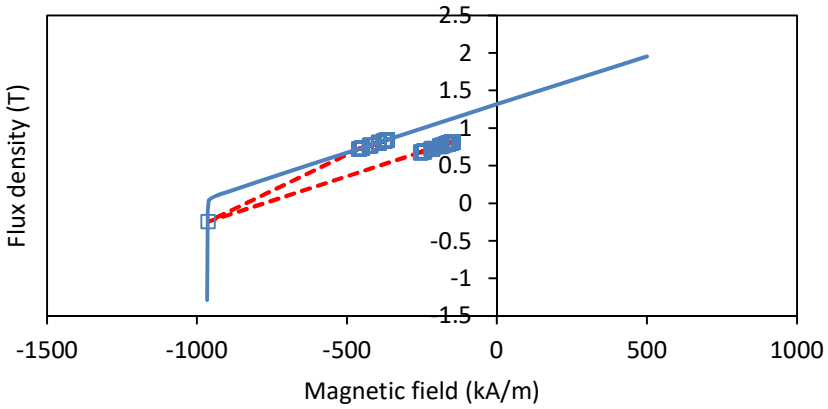

(working point trajectory in finite element simulation)

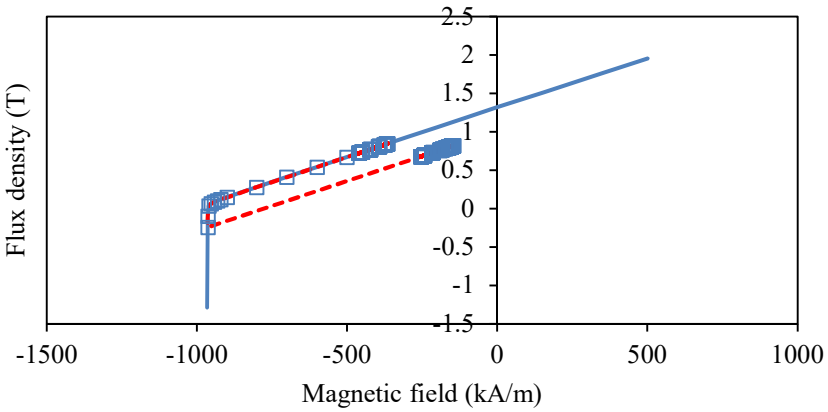

(realistic working point trajectory)

Fig. 5-30 Flux density and magnetic field strength in PM middle point in Fig. 5-24 before and after demagnetizing current (I_d=-30A).

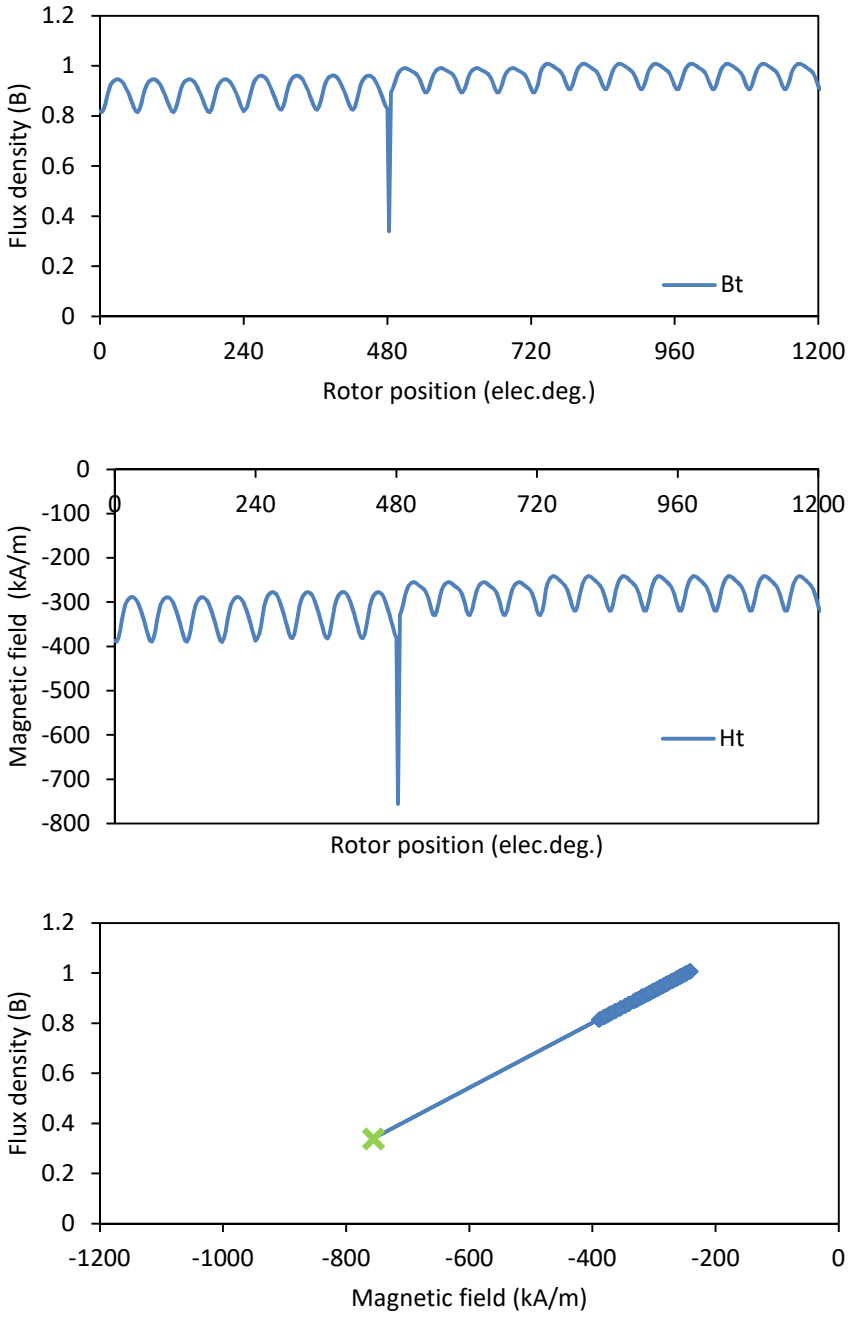

Fig. 5-31 Flux density and magnetic field strength in PM top point in Fig. 5-24 before and after demagnetizing current (I_d=-30A).

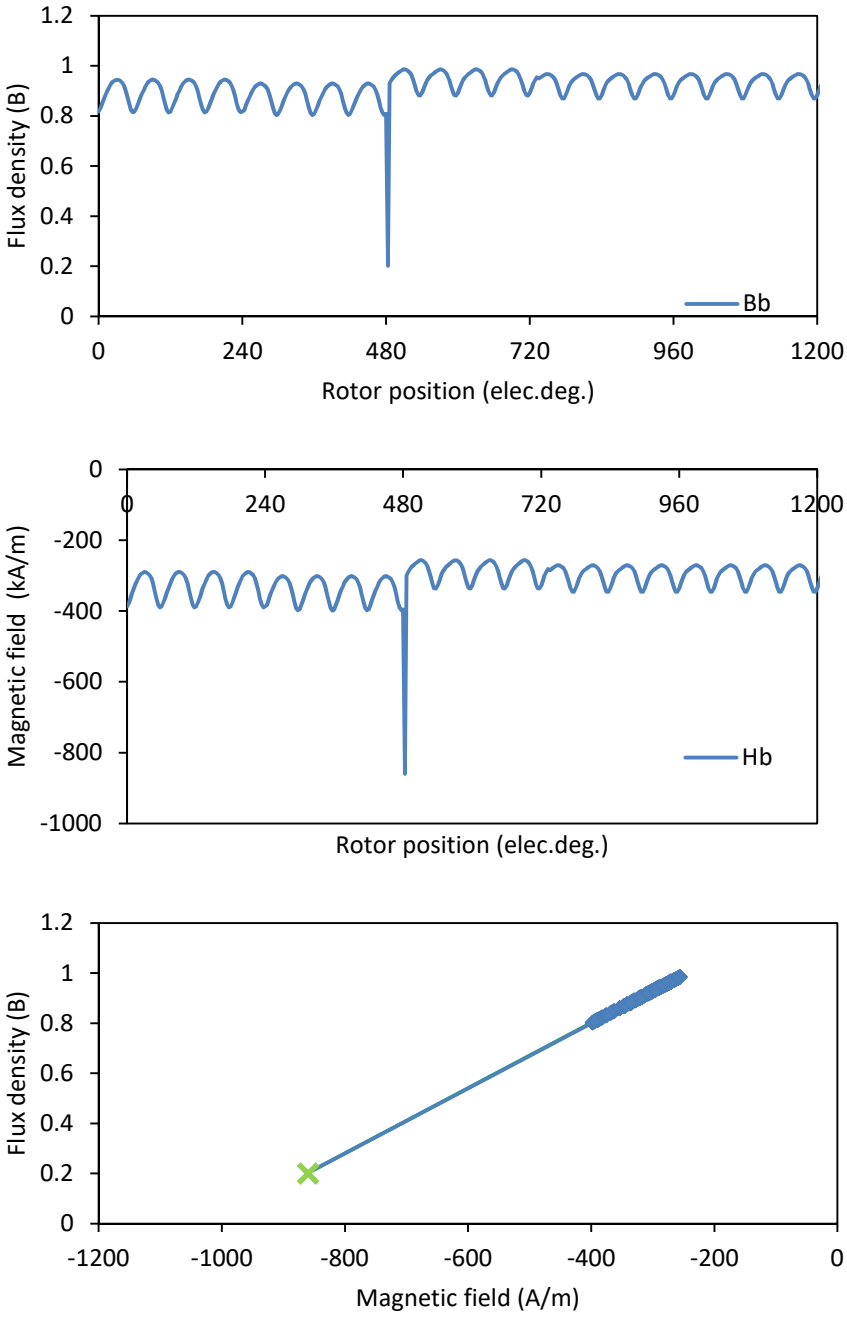

Fig. 5-32 Flux density and magnetic field strength in PM bottom point in Fig. 5-24 before and after demagnetizing Id current (I_d=-30A).

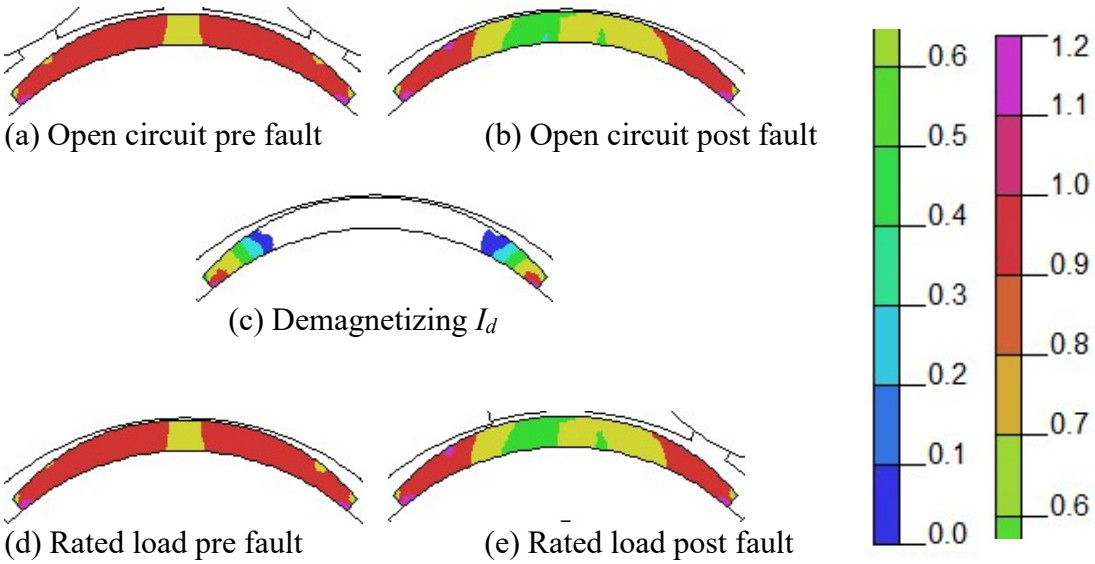

(a) Open circuit pre fault (b) Open circuit post fault

(c) Demagnetizing I_d

(d) Rated load pre fault (e) Rated load post fault

Fig. 5-33 Contour plot of PM flux density pre, during and post fault (I_q=0.58A, I_d=-30A)

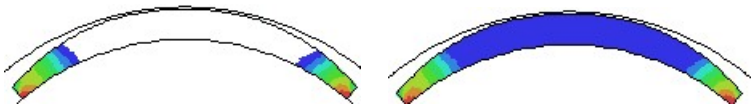

(a) -920 – 0 kA/m (b) -980 – 0 kA/m

Fig. 5-34 Contour plot of magnetic field amplitude in PM due to demagnetizing I_d=-30A.

5.2.4.3 No average torque decrease (Iq=60A)

In the case of a small size PM machine, the number of poles is limited by the spatial constraints. A pole arc will span over 90 mechanical degrees in a 2 rotor pole pair PM machine. The d-axis stator MMF is parallel to magnetization direction of the PM. However, in the case of parallel magnetized PMs, the angle between the PM magnetization direction and the q-axis stator MMF will be roughly 45° for the machine with 2 rotor pole pairs. Thus, a higher amplitude current is required to shift the magnet working point below the knee point. In this case, an I_q=60A current is used. The magnet in the region of the point marked with B_b in Fig. 5-24 experiences a slight loss of magnetization as shown in Fig. 5-38. As with the previous demagnetization case, the

magnet working points in the parts of the PM, which have not been exposed to irreversible demagnetization, will have a higher working point after the demagnetization event due to the less saturated magnetic circuit. In Fig. 5-35, the torques at rated current before and after the demagnetization event have the same average amplitude but different waveforms. In this case, there is no apparent loss of average power capabilities. As the average open circuit q-axis voltage and the average rated current torque are unchanged, the limited loss of the magnetization in one PM sides is compensated by more PM flux from the undamaged magnet areas. This is possible due to the non-linearity of the magnetic circuit and only occurs in the case of a minor loss of a magnetization in a limited area as in Fig. 5-39(c).

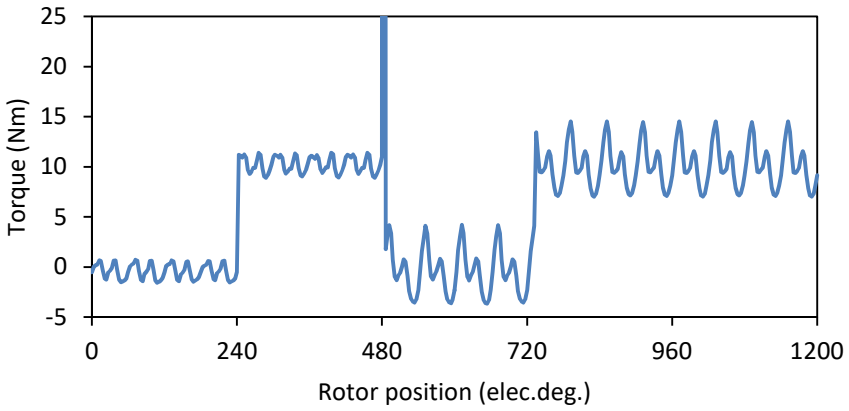

Fig. 5-35 Flux density and magnetic field strength in PM middle point in Fig. 5-24 before and after demagnetizing current (I_q=60A).

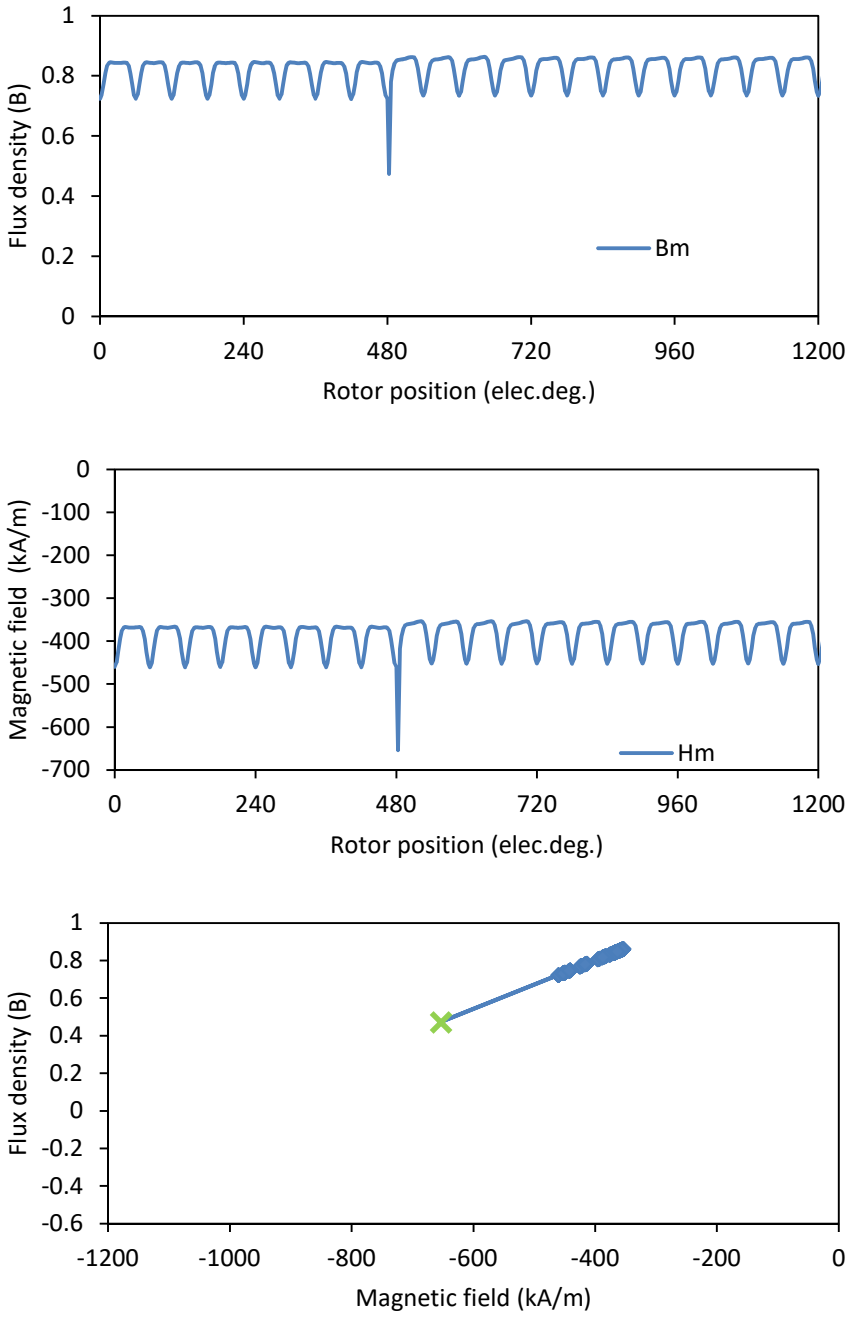

Fig. 5-36 Flux density and magnetic field strength in PM middle point in Fig. 5-24 before and after demagnetizing current (I_q=60A).

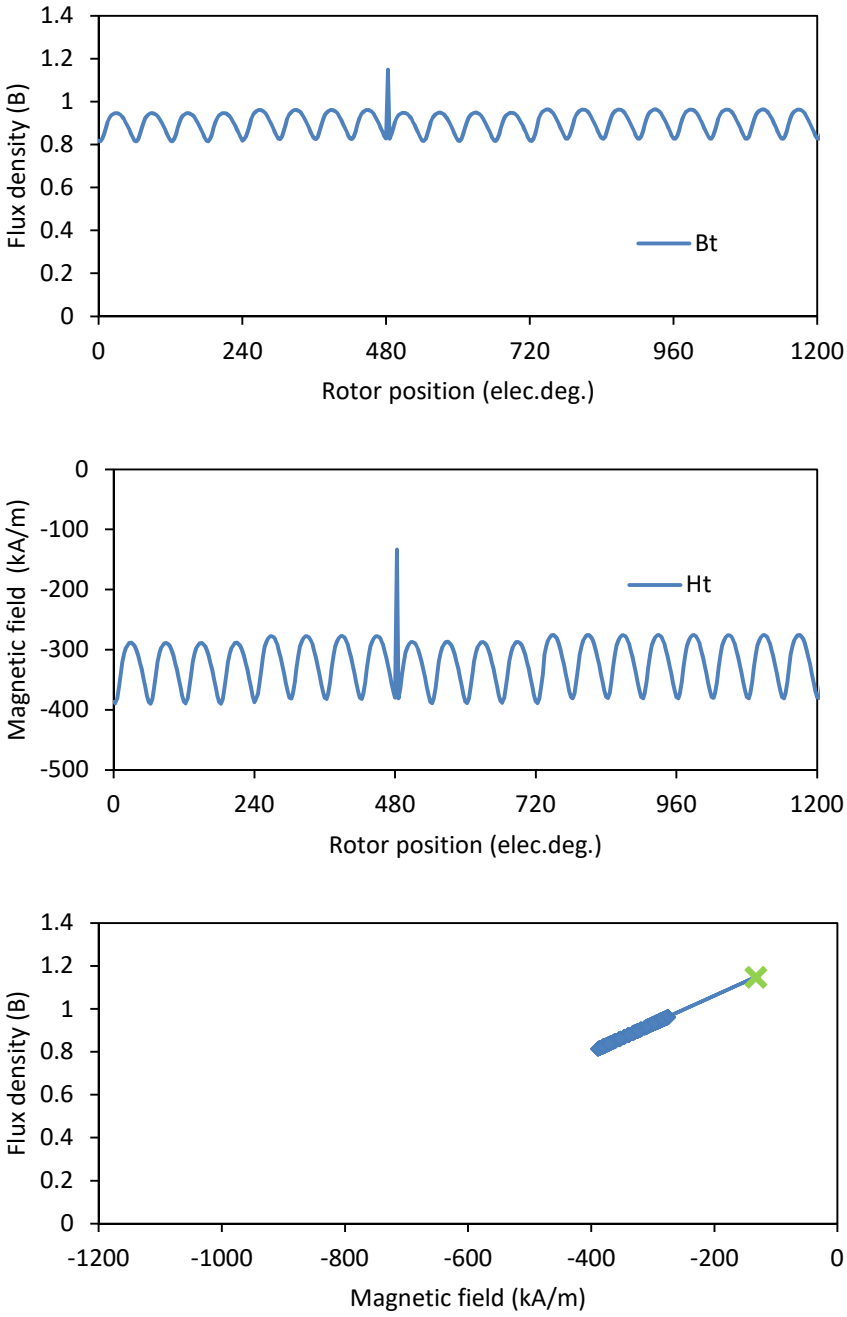

Fig. 5-37 Flux density and magnetic field strength in PM top point in Fig. 5-24 before and after demagnetizing current (I_q=60A).

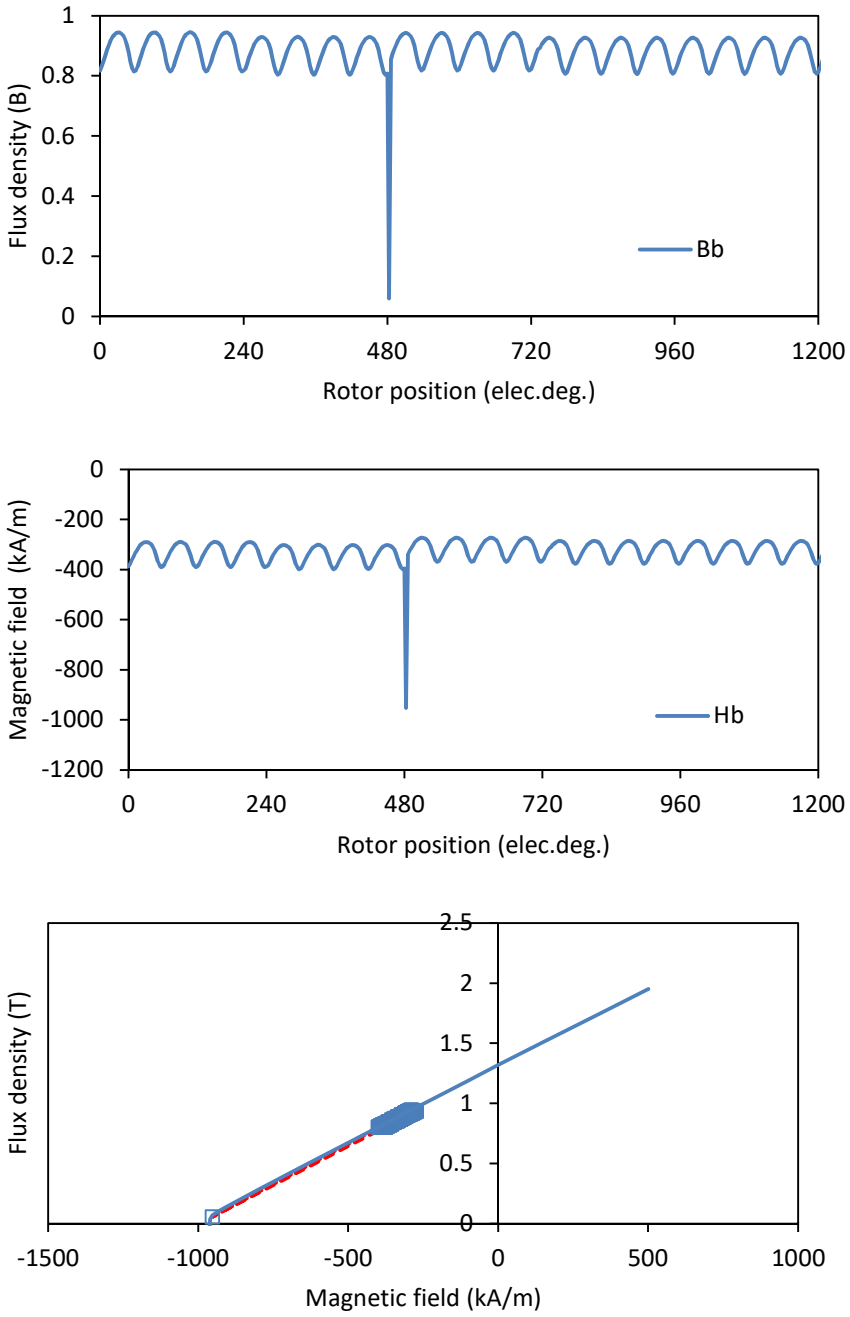

Fig. 5-38 Flux density and magnetic field strength in PM bottom point in Fig. 5-24 before and after demagnetizing current (I_q=60A).

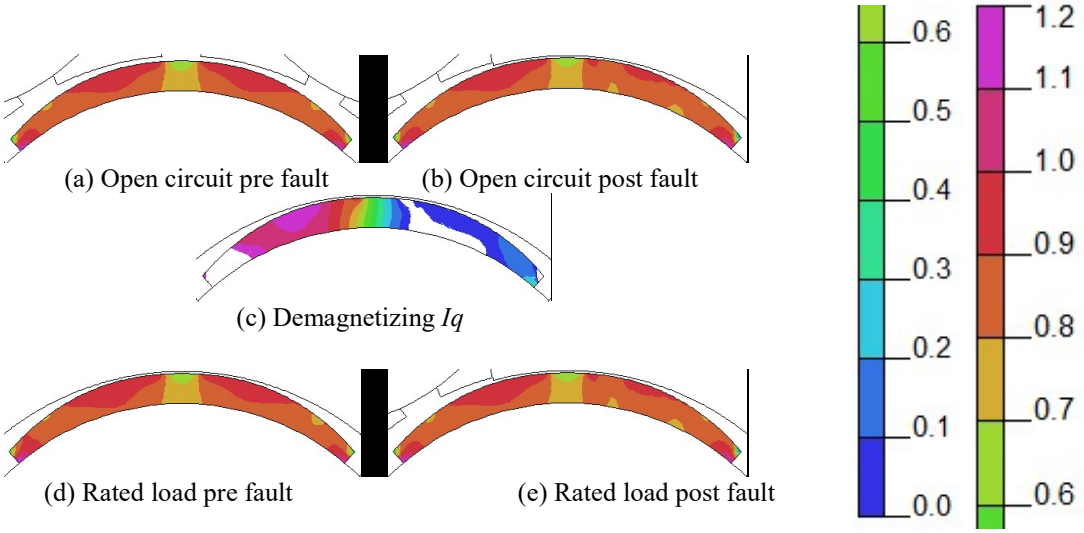

Fig. 5-39 Contour plot of PM flux density pre, during and post fault (Ir=Iq=0.58A, Iq=60A).

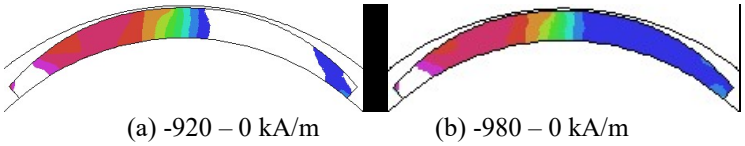

Fig. 5-40 Contour plot of magnetic field amplitude in PM due to demagnetizing Iq=60A.

5.2.5 Comparison of demagnetization with 6 and 12 slot stators

A summary of the comparison of the Cobham Opera demagnetization solver results for the demagnetization in a 12-slot-4-pole ISDW SPM machine and in a 6-slot-4-pole FSCW SPM with all teeth wound is presented in this section. Two magnet temperatures are used, 23°C to model a room temperature experiment and 60°C, a typical operation limit for the N45h magnet grade. The B-H curves at the two temperatures are shown in Fig. 5-41.

The parameters of the 12-slot-4-pole machine are presented in Table 5-2. Fig. 5-42 shows cross sections of one pole of the 12-slot-4-pole machine with equal flux lines and a contour plot of the open circuit flux density. A minimum I_d=24A current amplitude is required at 23°C for any reduction of the average torque (Fig. 5-43).

Table 5-2 Specifications of 12s4p SPM.

Parameters	**Value**
Rated current (A)	0.587
Stator	
Case outer diameter (mm)	110
Lamination outer diameter (mm)	100
Slot bottom diameter (mm)	86.2
Bore diameter (mm)	45
Lamination axial length (mm)	50
Motor axial length (mm)	76.1
Stacking factor (mm)	0.97
Number of slots	12
Tooth width (mm)	5.6
Tip edge thickness (mm)	0.7
Slot opening (mm)	2
Stator winding	
Stator winding connection	Star
Number of phases	3
Coils per phase	2
Turns per coil	125
Wire diameter (mm)	0.57
Packing factor	0.3
Phase resistance (Ohm)	9.2
Winding area (cm^2)	1.1
Air gap length (mm)	0.5
Rotor	
Magnet outer diameter (mm)	44
Magnet inner diameter (mm)	40
Magnet thickness(mm)	2
Axial length (mm)	50
Magnet overhang factor	1
Number of pole pairs	2
Pole-arc to pole-pitch ratio	0.7
Magnet flat arc to magnet pitch ratio	0.2
Magnet edge to magnet mid thickness ratio	1
Materials	
Magnet material	N45
Remanence (T)	1.32
Magnetic relative permeability	1.04
Magnetisation	Parallel
Stator/rotor lamination	Transil1300_16T

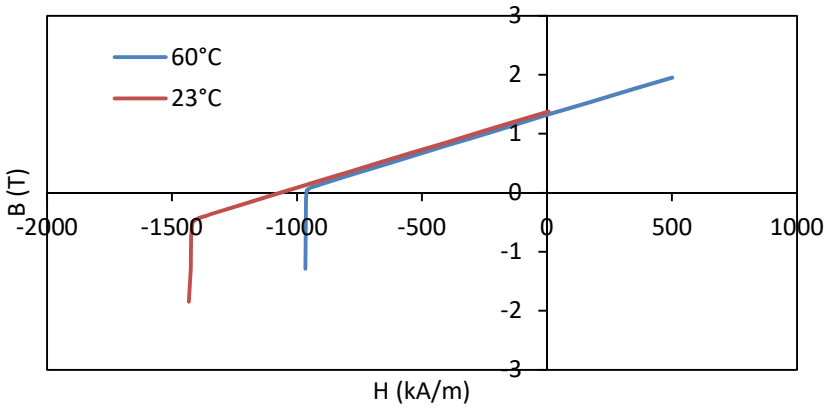

Fig. 5-41 N45H plus B-H curves for 60 and 23°C.

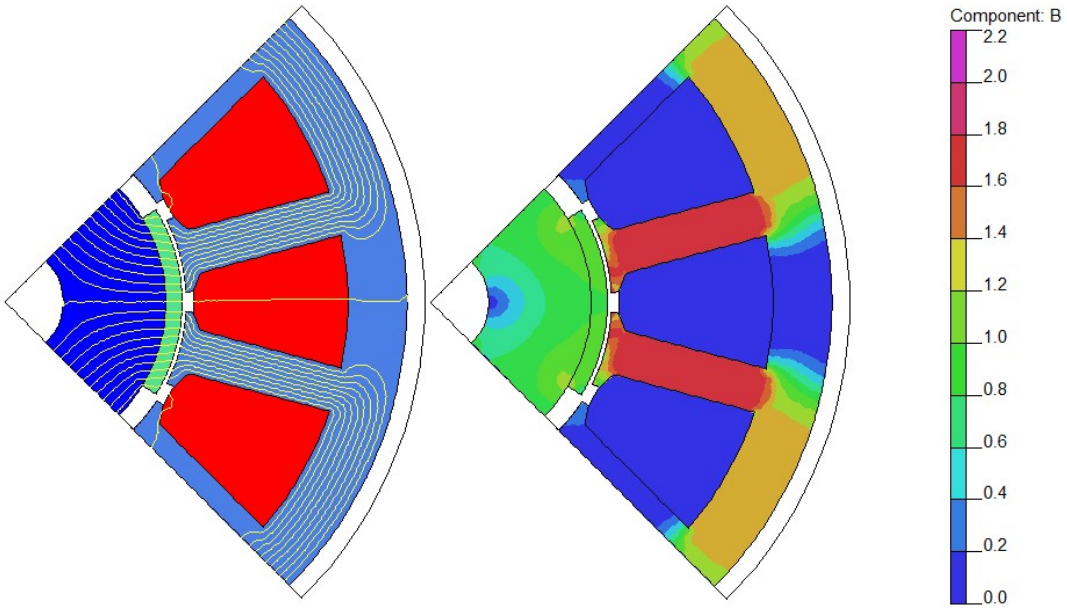

.

(a) (b)

Fig. 5-42 Cross section of 12 slots / 4 poles SPM motor with overlapping winding with (a) equal potential flux lines and (b) flux density contour plot at open circuit.

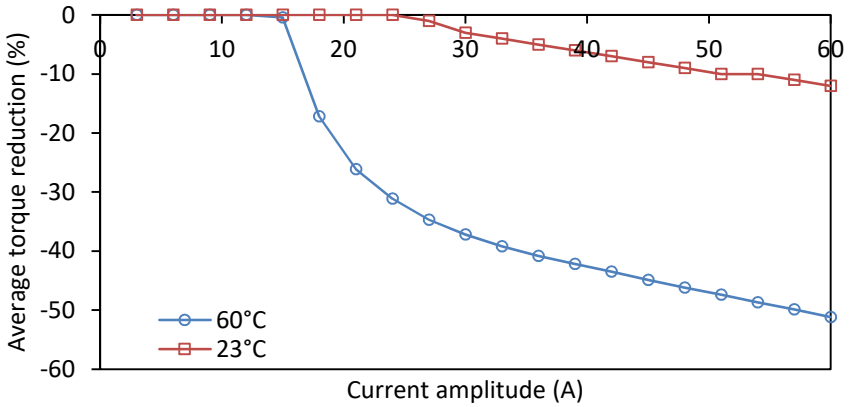

Fig. 5-43 Average torque reduction due to demagnetizing I_d in 12s4p SPM.

The parameters of the 6slot-4pole machine are presented in Table 5-3. Fig. 5-44 shows cross sections of the 6-slot-4-pole machine with equal flux lines and a contour plot of the open circuit flux density. There is no reduction of the average torque at the rated current for 23°C magnet temperature in Fig. 5-45. The demagnetization due to the maximum 60A current at 60°C yields a 26% reduction of the average torque for the 6-slot-4-pole machine. For the 12-slot-4-pole machine the same 26% reduction at 60°C occurs for a current of I_d=21A. For I_d=21A, the 12-slot-4-pole machine does not suffer any loss of magnetization in the 23°C case, which is consistent with the 6-slot-4-pole machine exposed to I_d=60A.

Hence, the 12-slot-4-pole machine will be used in the experiment due to its higher MMF.

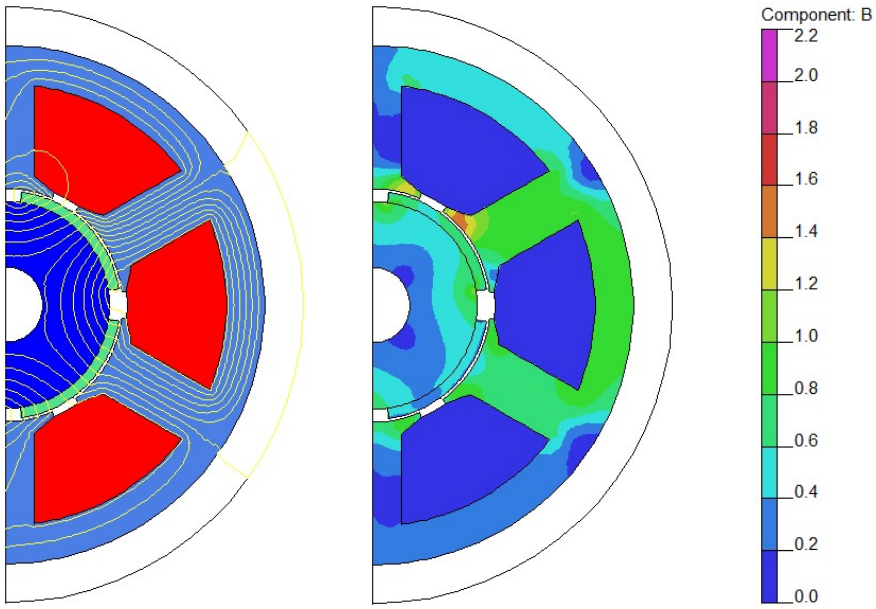

Fig. 5-44 Cross section of 6 slots / 4 poles SPM motor with overlapping winding with (a) equal potential flux lines and (b) flux density contour plot at open circuit.

Table 5-3 Specifications of 6s4p SPM.

Parameters	Value
Rated current (A)	0.587
Stator	
Case outer diameter (mm)	110
Lamination outer diameter (mm)	100
Slot bottom diameter (mm)	86.2
Bore diameter (mm)	45
Lamination axial length (mm)	50
Motor axial length (mm)	76.1
Stacking factor (mm)	0.97
Number of slots	6
Tooth width (mm)	5.6
Tip edge thickness (mm)	0.7
Slot opening (mm)	2
Stator winding	
Stator winding connection	Star
Number of phases	3
Coils per phase	2
Turns per coil	125
Wire diameter (mm)	0.57
Packing factor	0.3
Phase resistance (Ohm)	9.2
Winding area (cm^2)	2.2
Air gap length (mm)	0.5
Rotor	
Magnet outer diameter (mm)	44
Magnet inner diameter (mm)	40
Magnet thickness(mm)	2
Axial length (mm)	50
Magnet overhang factor	1
Number of pole pairs	2
Pole-arc to pole-pitch ratio	0.7
Magnet flat arc to magnet pitch ratio	0.2
Magnet edge to magnet mid thickness ratio	1
Materials	
Magnet material	N45
Remanence (T)	1.32
Magnetic relative permeability	1.04
Magnetisation	Parallel
Stator/rotor lamination	Transil1300_16T

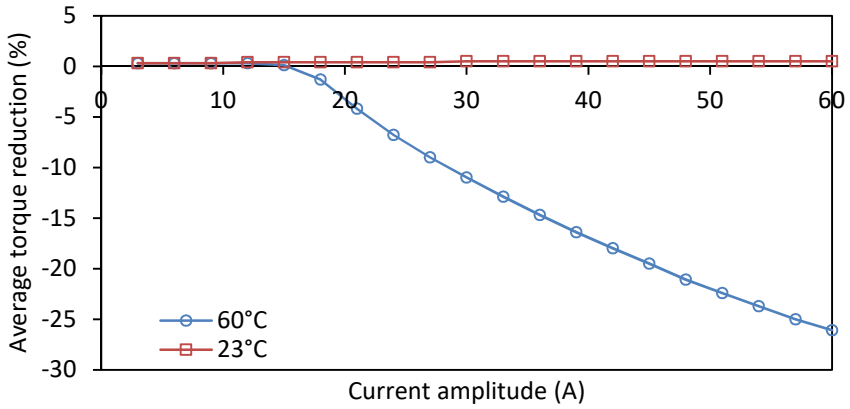

Fig. 5-45 Average torque reduction due to demagnetizing Id in 6s4p SPM.

5.2.6 Comparison of demagnetization in 12-slot-4-pole machine with different grades of NdFeB

The experimental demagnetizing current amplitude should preferably be within the winding amperage. However, I_d=24A required for any irreversible demagnetization of the 12-slot-4-pole machine with N45h magnets at room temperature is more than 10 times the maximum current capacity of the 0.57mm diameter copper windings (I_{max}≈2.1A).

To reduce the demagnetizing current required, the performance of the 12-slot-4-pole machine with lower coercivity NdFeB grades was investigated. Fig. 5-46 and Fig. 5-47 are plots of the current amplitude required for demagnetization of the N45h and the N35 NdFeB magnet grades.

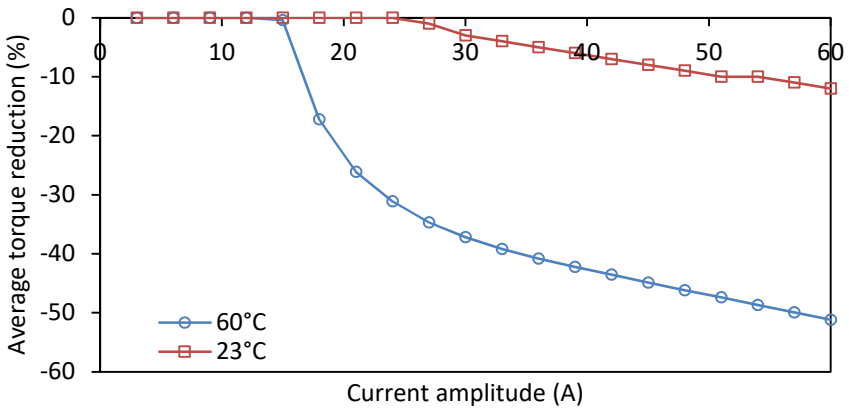

Fig. 5-46 Average torque reduction due to demagnetizing I_d in 12s4p SPM with N45h magnet.

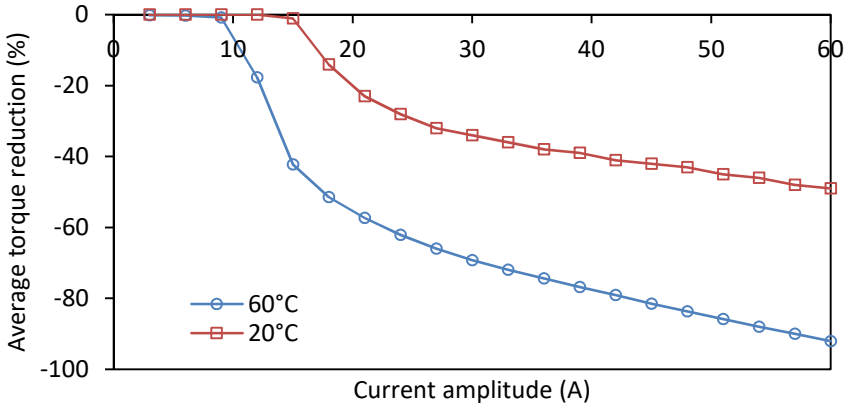

Fig. 5-47 Average torque reduction due to demagnetizing Id in 12s4p SPM with N30 magnet.

However, as neither of the two suppliers had the N30 grade available, the N35 was chosen for this experiment.

A comparison of the torque reduction at room temperature for the 12-slot-4-pole PM machines with the N30 and N35 magnet grades is shown in Fig. 5-48. The d-axis current amplitude for which some demagnetization occurs is roughly the same (~12A), owing to the similar coercivities in Table 5-4.

Table 5-4 N30, N35 and N45h grades NdFeB specifications.

Material	B_r		H_c		H_{ci}		BH_{max}	
	mT	G	kA/m	Oe	kA/m	mT	G	kA/m
N30	1,080	10,800	796	10,000	955	12,000	223	28
N35	1,170	11,700	868	10,900	955	12,000	263	33
N45h	1,320	13,200	875	11,000	955	12,000	342	43

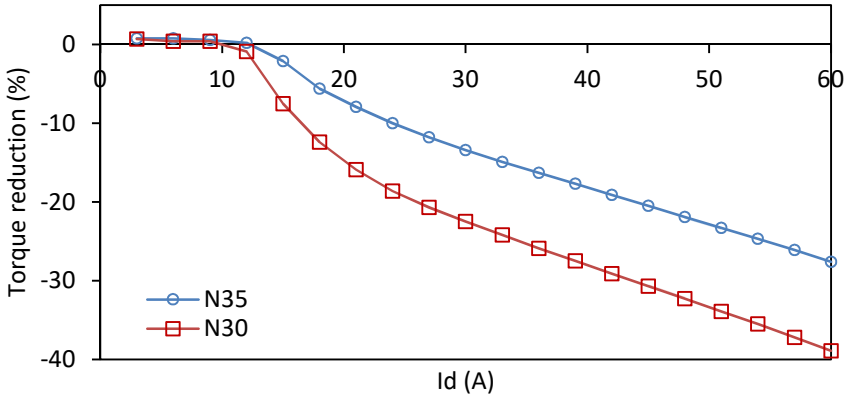

Fig. 5-48 Opera 2D FEA prediction of average torque reduction due to demagnetizing Id in 12s4p SPM with N30 and N35 grade NdFeB.

5.3 Temperature rise in winding

A simple thermal model for the temperature rise of a copper winding due to a high current with a short duration is presented in this section. The assumptions are that the winding is purely resistive (no inductance) and the winding does not exchange heat during the current pulse application.

The temperature rise:

$$\Delta T=Q/C \tag{5.1}$$

where Q is the heat in Joules and C is the heat capacity.

$$Q=I^2 \cdot R \cdot t \tag{5.2}$$

where t is the duration of the high amplitude current.

$$C=m \cdot c \tag{5.3}$$

where m is the mass and c is the specific heat per mass of the material.

$$R=\rho_e \cdot l/A \tag{5.4}$$

where ρ_e is the resistivity of copper, l is the length and A is the cross sectional area of the wire.

$$m= \rho_m \cdot l \cdot A \tag{5.5}$$

where ρ_m is the mass density of copper.

Rearranging for t, the time in which a conductor experiences a temperature rise ΔT due to a current I:

$$\Delta T= I^2 \cdot R \cdot t / m \cdot c \tag{5.6}$$

$$\Delta T= (I^2 \cdot \rho_e \cdot l/A \cdot t) / (\rho_m \cdot l \cdot A \cdot c) \tag{5.7}$$

$$t= (\Delta T \cdot \rho_m \cdot A^2 \cdot c)/ (I^2 \cdot \rho_e) \tag{5.8}$$

The time is independent of the wire length and only a function of its cross sectional area, A, the current, I, the temperature rise ΔT and copper material properties.

The winding in the 12-slot ISDW stator is 0.57mm in diameter, including the insulation which has a typical thickness of less than 0.04mm for these wire sizes. Typical values for copper are: mass density, ρ_m=8960kg/m^3, electrical resistivity, ρ_e=1.68·10^{-8}Ωm and the specific heat, c=385J/kg/K.

Fig. 5-49 is plotted using (5.8). As the time required for a 100K temperature increase is less than 1s for a current I=30A, a microcontroller will be used to time the switching of the demagnetizing current. The resistance of one phase is R=9.2Ω and the inductance is L=50mH, and hence, due to the low inductance, a duration of 200ms is sufficient for the current amplitude to increase to the maximum current in the inductive load.

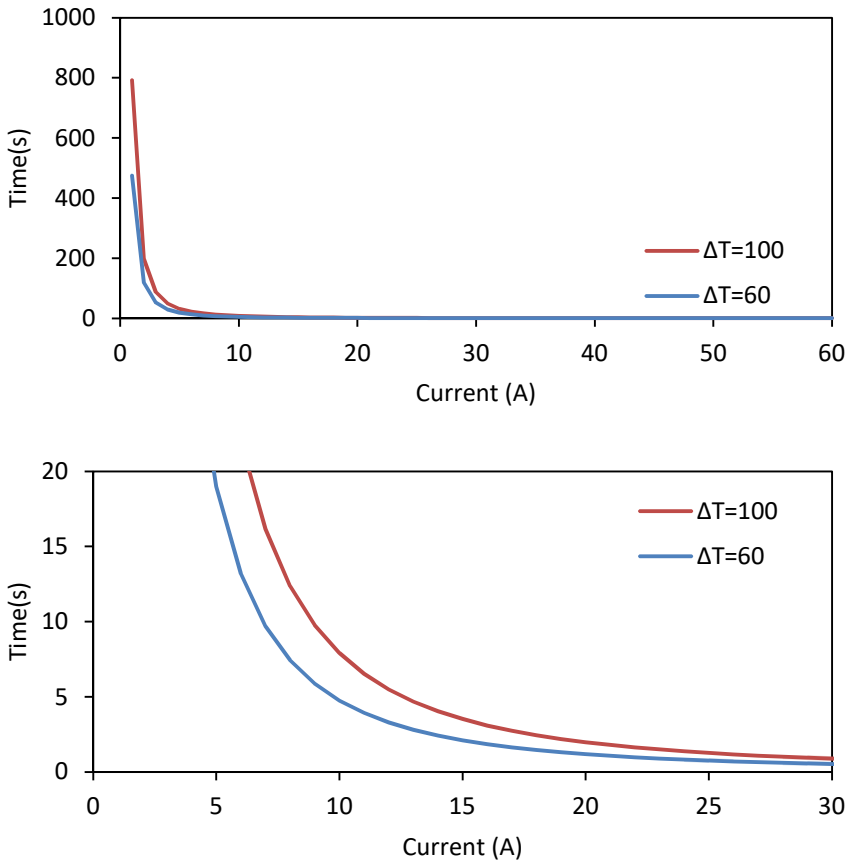

Fig. 5-49 Time required for ΔT temperature increase in conductor.

5.4 Measurements of rotors before demagnetization

5.4.1 Back-EMF

The specification of the stator and manufactured rotors are presented in Table 5-5.

Table 5-5 Specifications of 12s4p SPM machine-stator and 5 manufactured rotors.

Parameters	**Value**
Rated current (A)	0.587
Stator	
Case outer diameter (mm)	110
Lamination outer diameter (mm)	100
Slot bottom diameter (mm)	86.2
Bore diameter (mm)	45
Lamination axial length (mm)	50
Motor axial length (mm)	76.1
Stacking factor (mm)	0.97
Number of slots	12
Tooth width (mm)	5.6
Tip edge thickness (mm)	0.7
Slot opening (mm)	2

Stator winding	
Stator winding connection	Star
Number of phases	3
Coils per phase	2
Turns per coil	125
Wire diameter (mm)	0.57
Packing factor	0.3
Phase resistance (Ohm)	9.2
Winding area (cm^2)	1.1
Air gap length (mm)	0.5
Rotor	
Magnet outer diameter (mm)	44
Magnet inner diameter (mm)	40
Magnet thickness(mm)	2
Axial length (mm)	50
Magnet overhang factor	1
Number of pole pairs	2
Pole-arc to pole-pitch ratio	0.72
Materials	
Magnet material	N35
Remanence (T)	1.17
Magnetic relative permeability	1.04
Magnetisation	Parallel
Stator/rotor lamination	Transil1300_16T

The differences between BEMF harmonics of the measured 12-slot-4-pole machine with the 5 rotors and the 2D FEA prediction are shown in Table 5-6. The waveforms are plotted in Fig. 5-50.

Table 5-6 Percentage difference of amplitude of Back EMF harmonic order to the one predicted by 2D FEA.

	Rotor 1	Rotor 2	Rotor 3	Rotor 4	Rotor 5	2D FEA
1	-9.4	-10.5	-10.2	-9.4	-10.6	0
3	45.1	54.3	44	31.8	28.9	0
5	-19.9	-26.8	-20.9	-16.4	-18.6	0
7	-21.5	-21	-13.2	-10.6	6.7	0

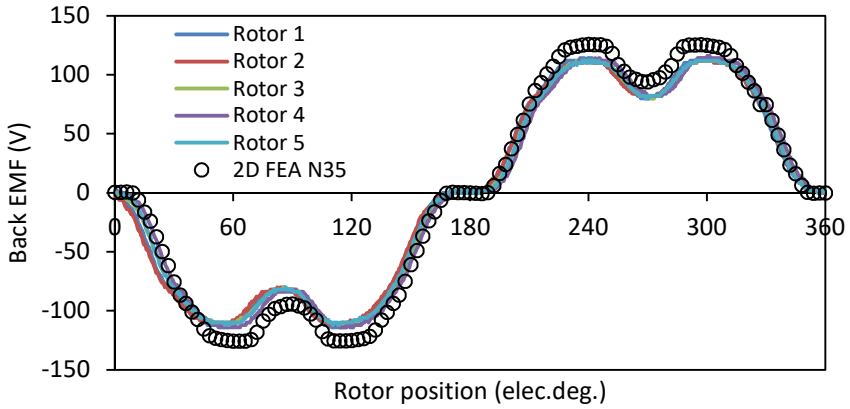

Fig. 5-50 Measured vs. predicted back EMF waveforms at 1153 rpm.

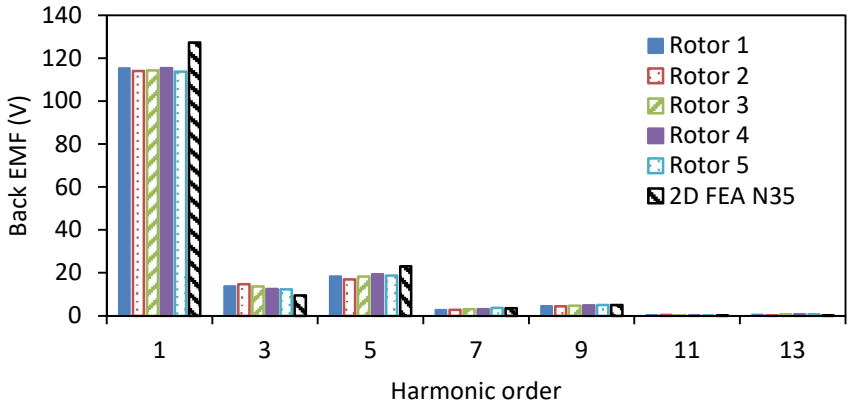

Fig. 5-51 Measured vs. predicted back EMF spectra at 1153 rpm

5.4.2 Cogging torque

The magnet arc width is 23.6mm. All magnets have identical dimensions. The nominal distance between two adjacent magnets is 8.9mm. However, the measured distance between the magnets on the manufactured rotors varies between 8.5 and 9.3mm. Because of these manufacturing tolerances, the measured peak to peak cogging torque is expected to be higher than the FE predicted value.

The peak to peak cogging torque computed by FE is plotted in Fig. 5-52 for different magnet to pole pitch ratios. The measured peak to peak cogging torque for the manufactured rotors is 4 times larger than the results predicted by FE, which will be further investigated in section 6.3.5.

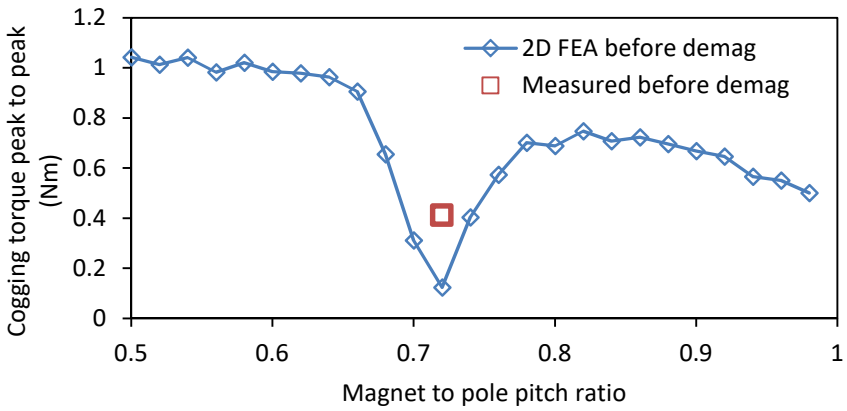

Fig. 5-52 Measured vs. predicted peak to peak cogging torque.

5.4.3 Static torque

For the static torque measurement, two of windings are connected in parallel and in series with the third winding. The measured static torque vs rotor position is compared to the FE predicted result in Fig. 5-53.

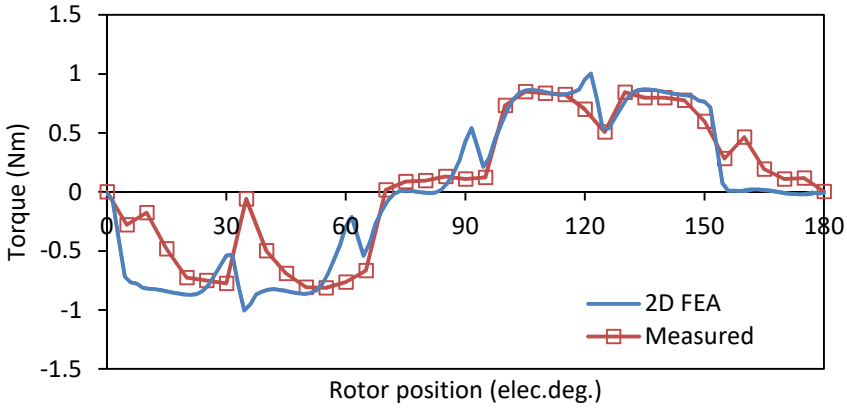

Fig. 5-53 Measured vs. predicted static torque for I=0.55A.

5.4.4 Control circuit timing

The measured control and load voltages vs time for a 3 seconds duration current through a 10Ω load are plotted in Fig. 5-54. The load current vs time is shown in Fig. 5-55. The test was repeated for pulse durations between 0.1s and 5s; all were accurate within 1ms.

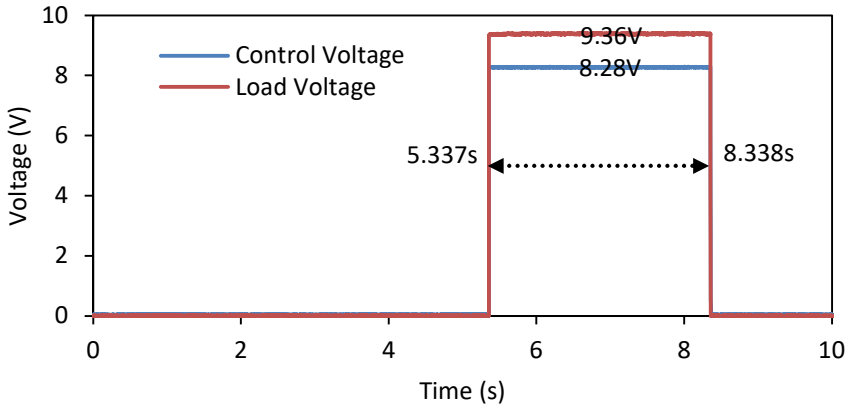

Fig. 5-54 Control voltage and load voltage vs. time (3 seconds pulse, 10Ω load

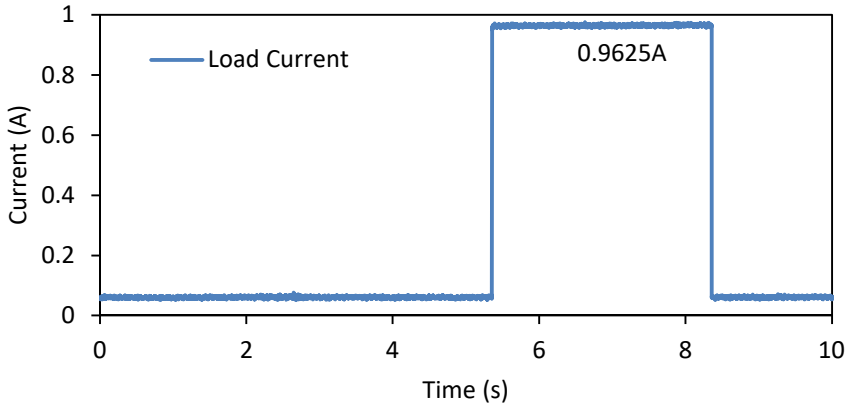

Fig. 5-55 Load current measured using current clamp (3 seconds pulse, 10Ω load).

5.5 Experimental demagnetization

5.5.1 Experimental setup

Two 6kW (360V,17A) power supplies were used for this experiment to provide the high current required for the irreversible demagnetization in this experiment. An IGBT was used to connect the parallel power supplies to the winding terminals as for a static torque test. The IGBT was controlled by a microcontroller (Arduino).

Probes were used to measure the control voltage supplied by the microcontroller and the voltage across the load terminals. A current clamp was also used to measure the load current.

The positive power supply terminals were connected to two of the phases while the other phase was connected to the power supplies common ground though the IGBT like in Fig. 5-56.

5.5.2 Experimental procedure

The experimental procedure has 5 steps:

1. Measure pre demagnetization back EMF.
2. Align the rotor to the positive (flux enhancing) d- axis by supplying the rated current.
3. Mechanically lock the rotor to the positive d-axis and reverse the load connection so that the current supplied will now be in the negative d-axis.
4. Supply the required negative d-axis current.
5. Post demagnetization back EMF measurement.

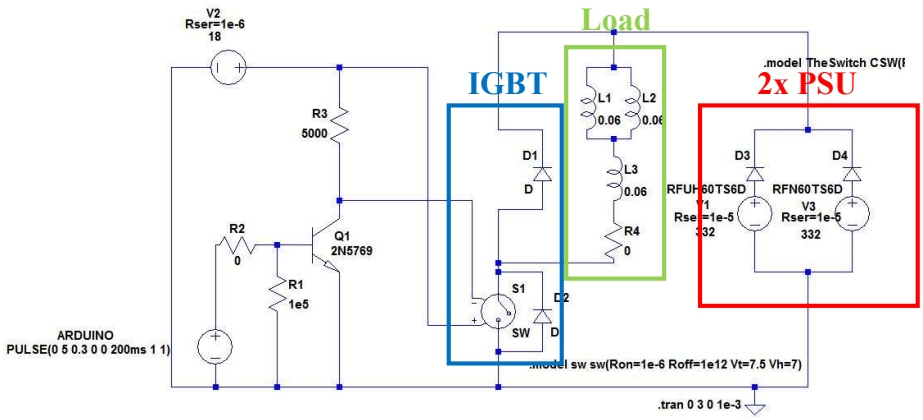

Fig. 5-56 Overview of microcontroller control circuit, motor (load), IGBT and power supplies connections.

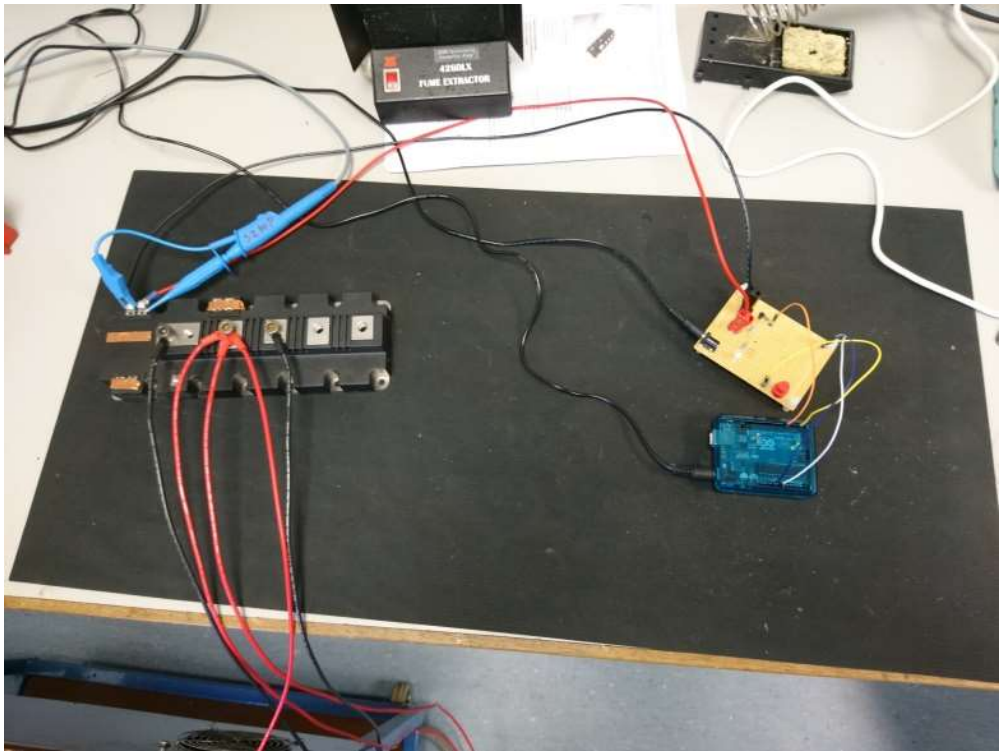

Fig. 5-57 Experimental setup part 1: IGBT and control circuit.


Fig. 5-58 Experimental setup part 2: Lathe, two power supplies and connections.

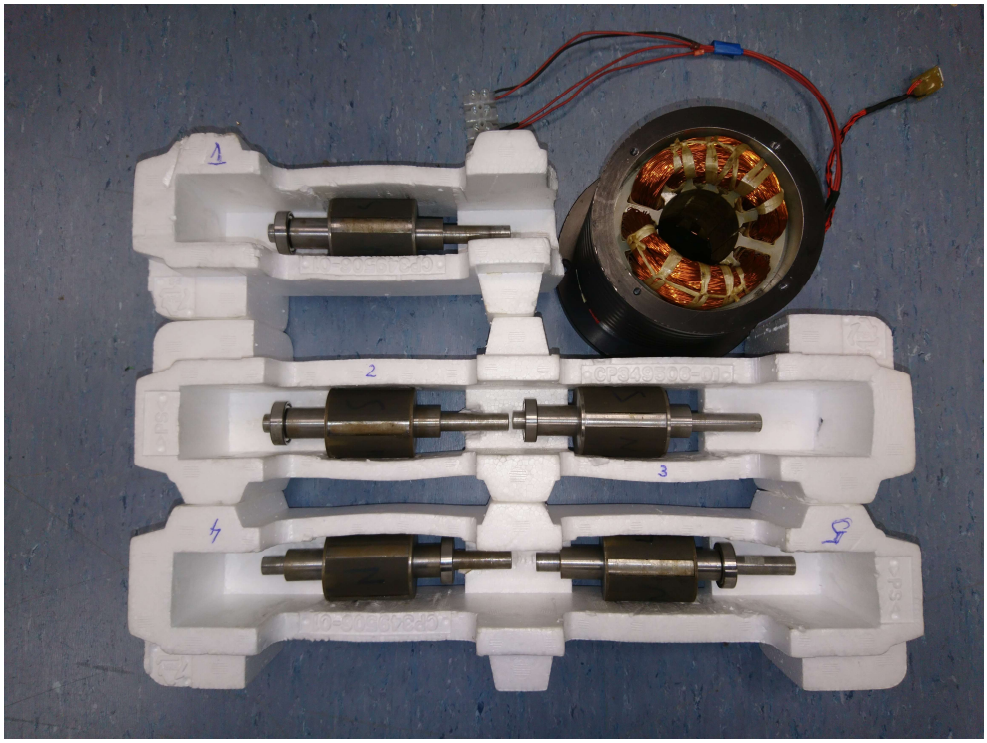

Fig. 5-59 Overlapping winding stator and 5 surface PM rotors.

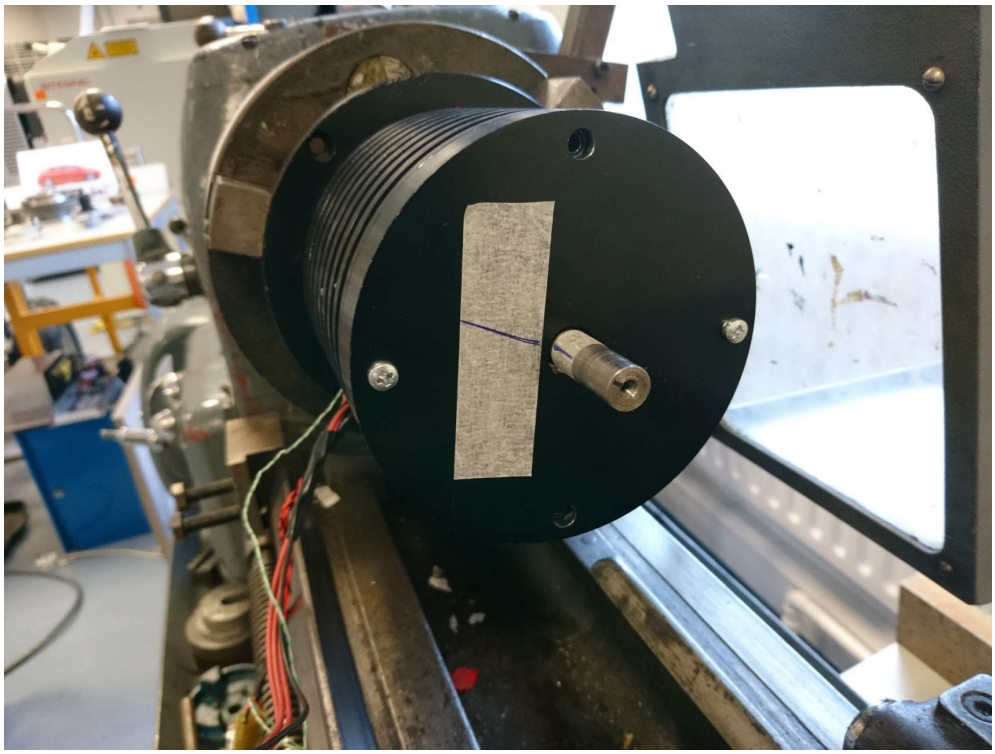
Fig. 5-60 Motor with rotor re-aligned to the positive d-axis by exciting the winding after it has been rotated to a random position.

5.5.3 Results

5.5.3.1 Back-EMF

The microcontroller control voltage and load voltage and current for the I_d=-18A demagnetization case are plotted in Fig. 5-61. The experimentally measured current rise time due to the inductive load was found to be less than 30ms.

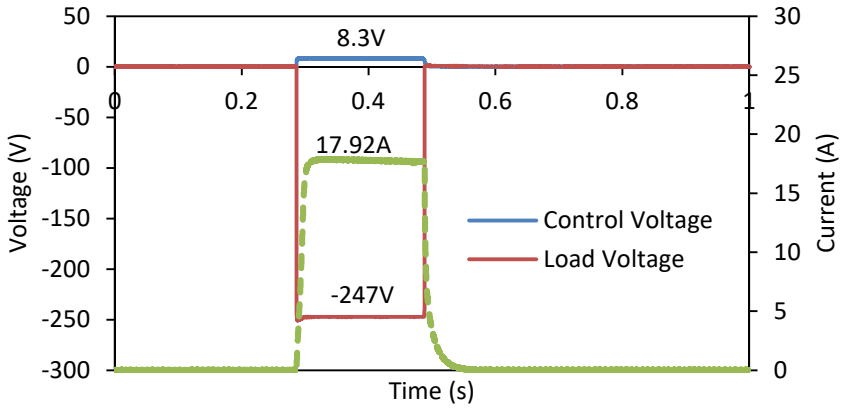

Fig. 5-61 Typical measured IGBT control voltage, voltage across the load terminals and the load current.

Fig. 5-62 shows the FE results and the measured back EMF before and after the demagnetization pulse was applied. By visual inspection of the back EMF waveform the loss in magnetization is obvious. The loss of magnetization was found to increase linearly with the applied current.

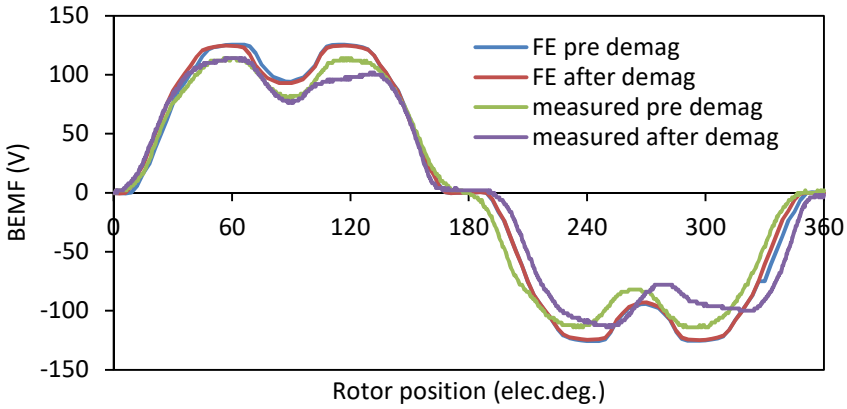

(a) I_d =-12A

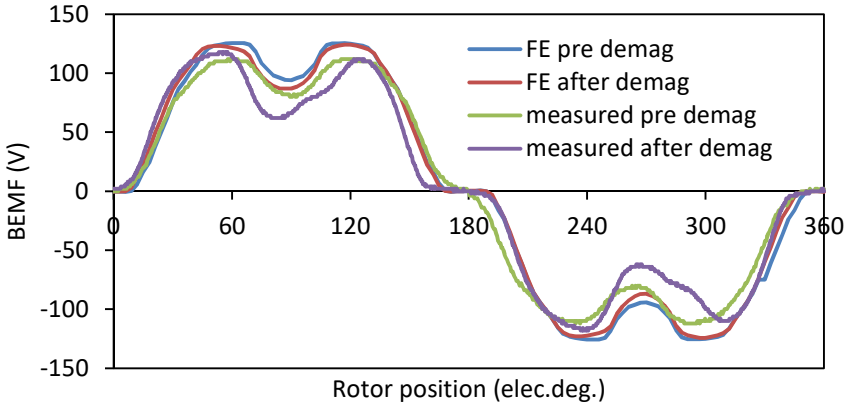

(b) I_d =-15A

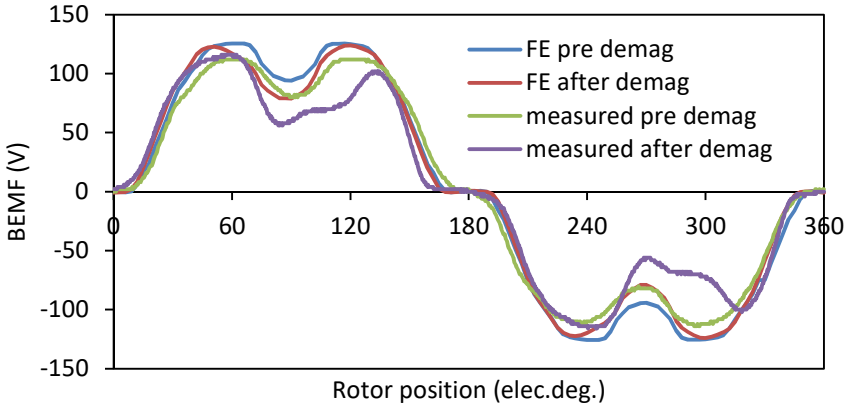

(c) I_d =-18A

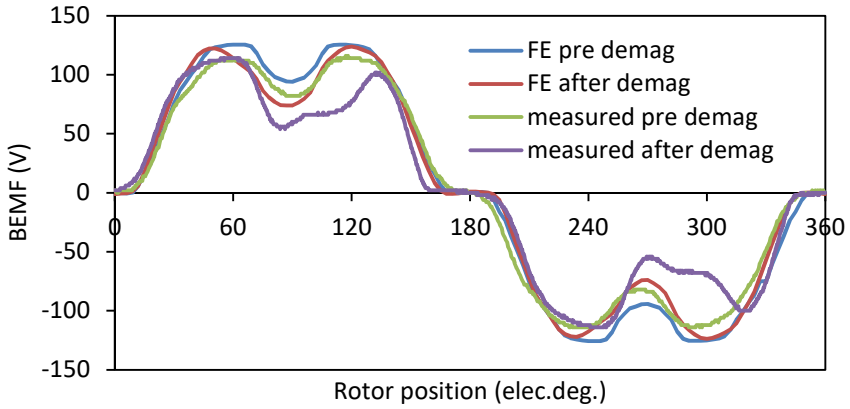

(d) I_d=-21A

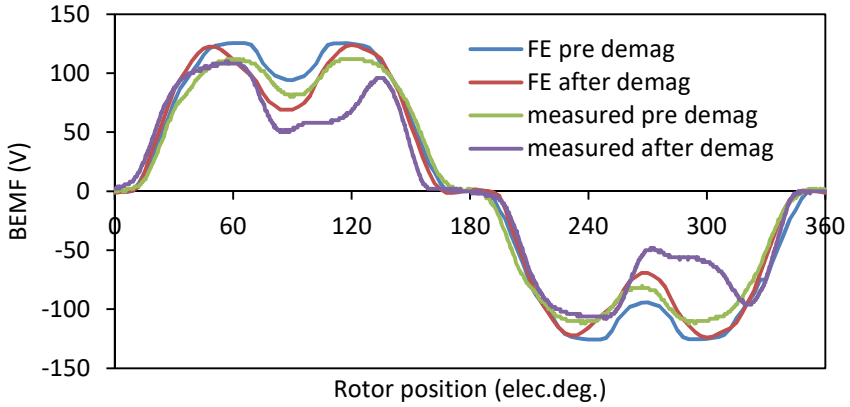

(e) I_d=-24A

Fig. 5-62 Back EMF waveforms before and after demagnetization (1153 rpm).

Fig. 5-63 presents the spectrum of the measured back EMF alongside the 2D FEA prediction. The difference of 8-9% between the measured and predicted results is mainly due to the 3D effects and due to manufacturing tolerances. However, as it will be shown, accurately predicting the open circuit magnet operation region is crucial for the accuracy of the demagnetization toolbox.

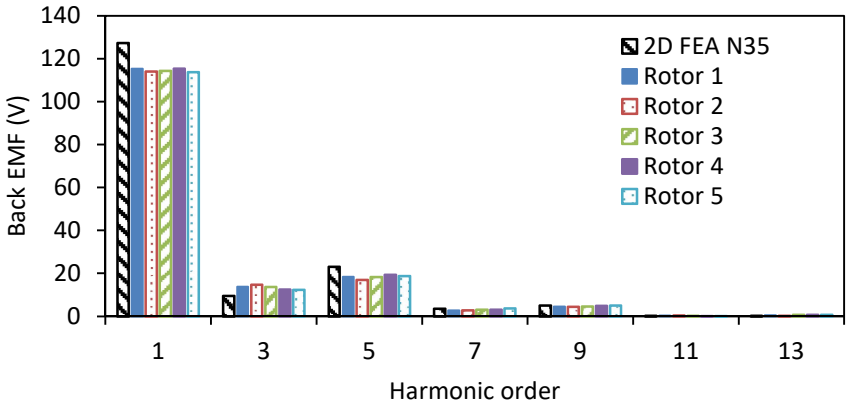

Fig. 5-63 Pre demagnetization measured back EMF spectrum vs. 2D FEA prediction.

In Fig. 5-64 the spectrum of the post demagnetization measured back EMF waveforms from Fig. 5-62 was plotted. A linear reduction of the back EMF fundamental harmonic can be observed. The harmonic content of the back EMF is higher when a rotor was subjected to demagnetization and further increased when higher amplitude demagnetization current was used.

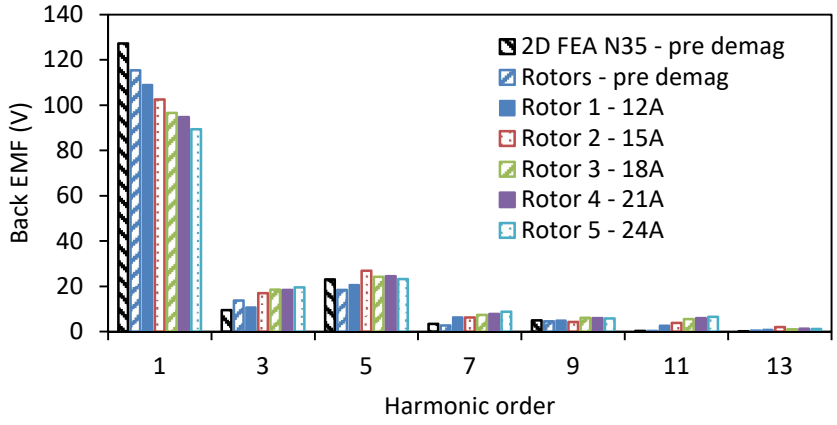

Fig. 5-64 Post demagnetization measured back EMF spectrum.

Fig. 5-65 shows the 2D FEA demagnetization prediction of the N35 at 22°C and the experimentally measured demagnetization at 25-27°C. Only the fundamental back EMF harmonic is used to evaluate the demagnetization percentage.

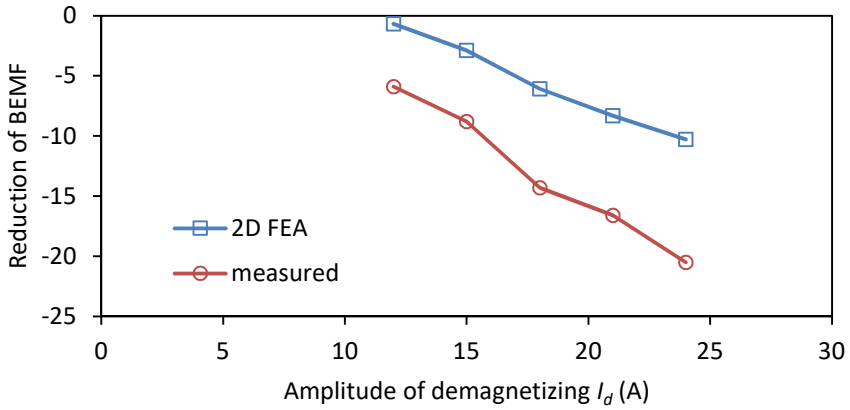

Fig. 5-65 Measured (27°C+) vs. predicted (22°C) reduction of back EMF fundamental due to demagnetizing Id.

Fig. 5-66 shows the effect of shifting the magnet data with temperature. This is done according to the coefficients in Table 5-7. The knee point is more sensitive to the temperature variations compared to B_r. This is also visible in Fig. 5-66.

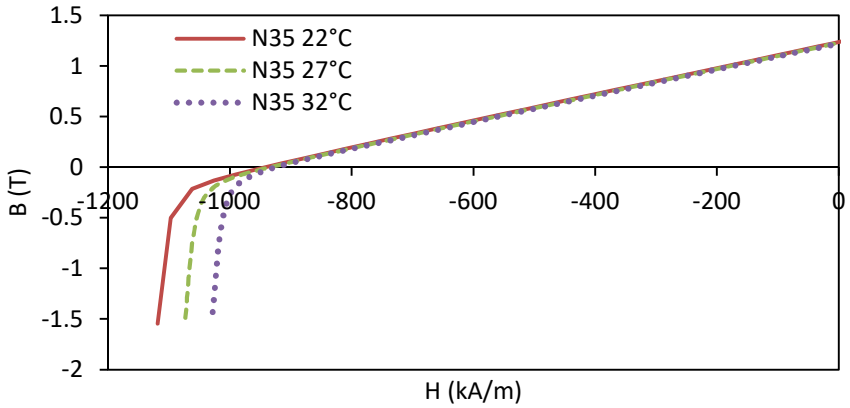

Fig. 5-66 B-H curves N35@22°C (measured), N35 at 27°C and at 32°C (derived from 22°C data).

Table 5-7 Different magnet grades temperature coefficients.

Magnet Type (Suffix)	Reversible temperature coefficient of Induction	Reversible temperature coefficient of Coercivity	Max. Working Temperature
	Br, %/°C (20-100°C)	Hci, %/°C (20-100°C)	
	-0.12	-0.6	80 ºC = 176 ºF *
M	-0.12	-0.58	100ºC = 212 ºF
H	-0.11	-0.58	120ºC = 248 ºF
SH	-0.1	-0.55	150 ºC = 302 ºF
UH	-0.09	-0.52	180 ºC = 356 ºF
EH	-0.085	-0.5	200 ºC = 392 ºF
VH / AH	-0.08	-0.45	230 ºC = 446 ºF
			* 60 ºC for N50 and N52

An FE sensitivity study of the magnet temperature and of the thickness of the magnet was conducted.

In Fig. 5-67 and Fig. 5-68 the measured demagnetization is compared to the 2D FEA predicted demagnetization with the magnet data adjusted to 27°C and 32°C, respectively.

At 27°C, a 20% thinner magnet (1.6mm) will exhibit the same level of demagnetization for the same current as experimentally measured (Fig. 5-67).

At 32°C, a magnet with a 10% lower thickness (1.8mm) would be demagnetized to the same level as the measured rotors (Fig. 5-68).

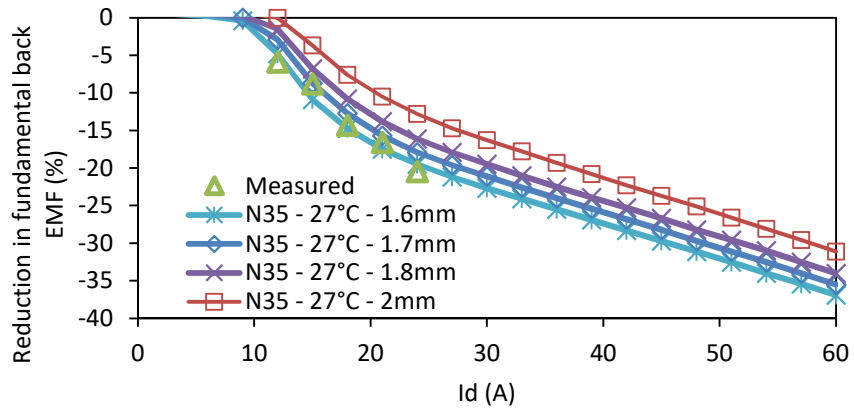

Fig. 5-67 Measured vs. predicted reduction of back EMF fundamental due to demagnetizing I_d (2D FEA magnet data adjusted for +5°C).

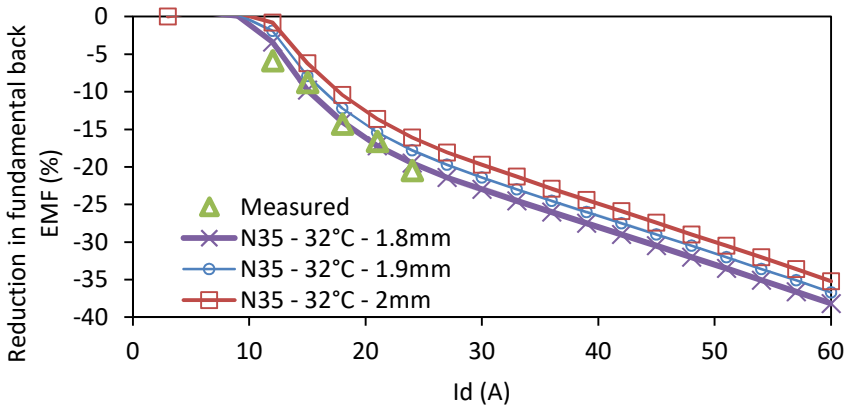

Fig. 5-68 Measured vs. predicted reduction of back EMF fundamental due to demagnetizing Id (2D FEA magnet data adjusted for +10°C).

5.5.3.2 Cogging torque

The measured cogging torque waveforms are presented in Fig. 5-69. The manufacturing tolerances are the main cause for the difference between the predicted and the measured cogging torque before the demagnetization. The distance between two magnets ~8.9mm in the FE model. However, the measured distances varied between 8.6 and 9.3mm, roughly ±0.35mm.

The design with the optimum magnet pole arc for minimum cogging torque will be the most sensitive to manufacturing tolerances.

The manufacturing tolerances are also the reason why the cogging torque does not increase due to the demagnetization. In a machine with an integer number of slots per pole, the force around each magnetic pole is identical and they contribute equally towards the cogging torque. When demagnetized, it was expected that the cogging torque would increase as the magnets would be identically affected. However, the cogging torque did not increase as the forces along each pole were not identical due to the aforementioned magnet misalignment.

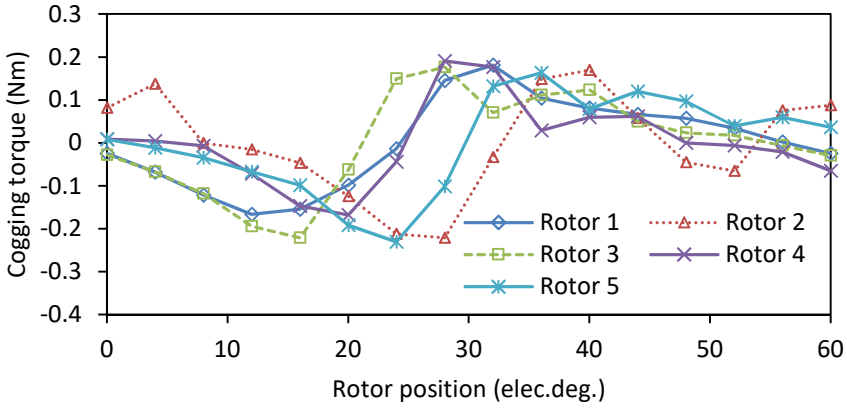

Fig. 5-69 Measured cogging torque waveforms after demagnetization.

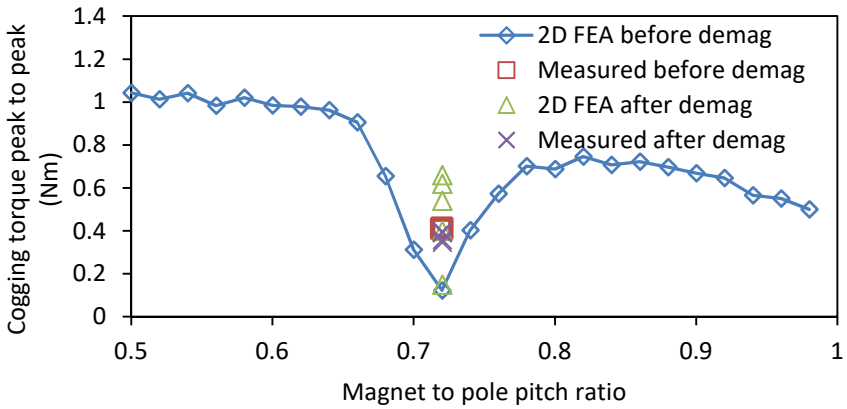

Fig. 5-70 2D FEA predicted and measured peak to peak cogging torques before and after demagnetization.

5.5.3.3 Static torque

The static torque measured after the demagnetization of rotor 5 at I_d=-24A was 22% lower than the one measured before the demagnetization as in Fig. 5-71. This is consistent with the 20% fundamental BEMF reduction measured for this rotor.

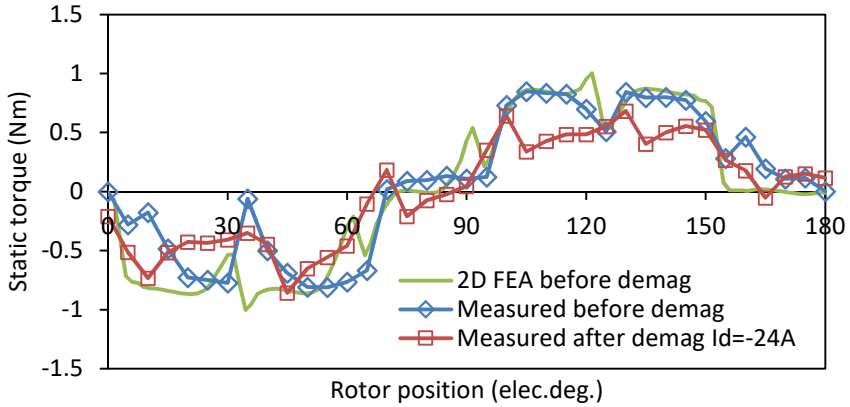

Fig. 5-71 Measured static torque after demagnetization.

5.5.3.4 Discussion

By way of example, the magnet working points of one of the demagnetized rotors are shown in Fig. 5-72. The magnet operation regions corresponding to open circuit (magnet in a magnetic circuit) is marked with red and the loaded magnet region is marked with green in Fig. 5-73.

Fig. 5-73 shows a simplified graphical explanation of how the inaccuracy in the prediction of the open circuit magnet working points will lead to an error in predicting the demagnetization.

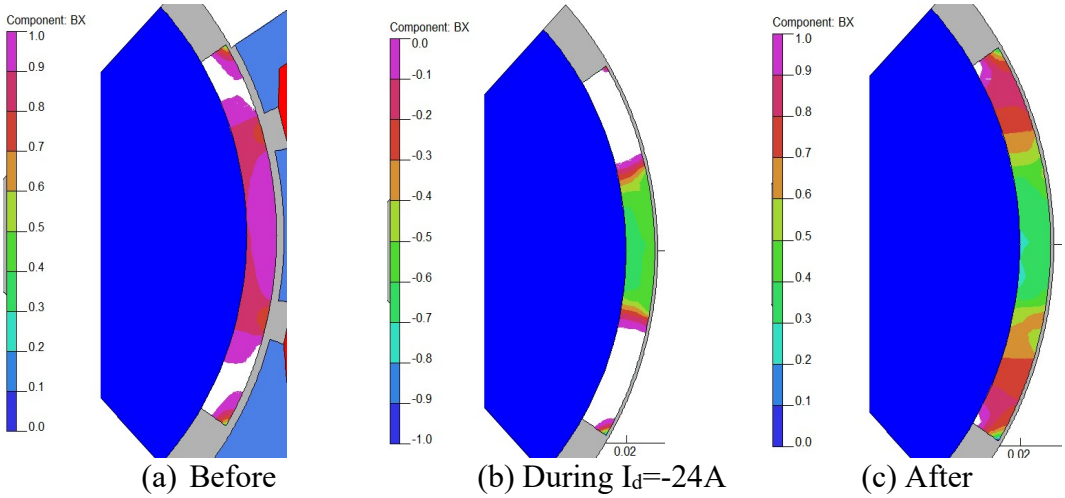

Fig. 5-72 Contour plots of magnet flux density (a) before, (b) during and, (c) after demagnetization. The machine is at open circuit (a) before and (c) after.

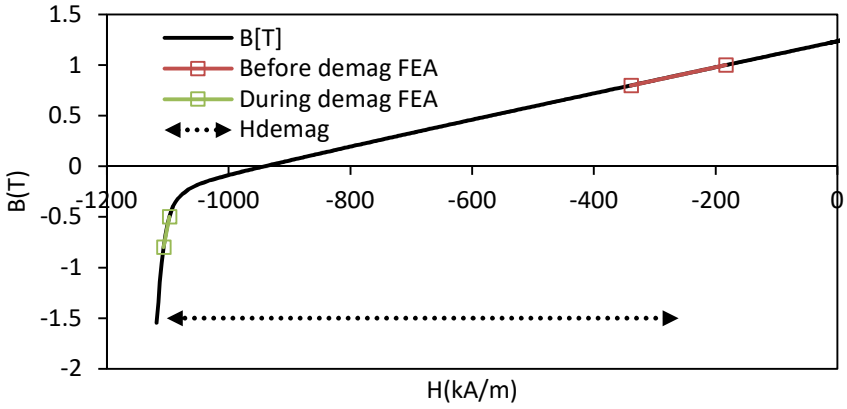

Fig. 5-73 Simplified plot of magnet operation region at open circuit and during demagnetizing Id pulse (Id=-24A - predicted by 2D FEA).

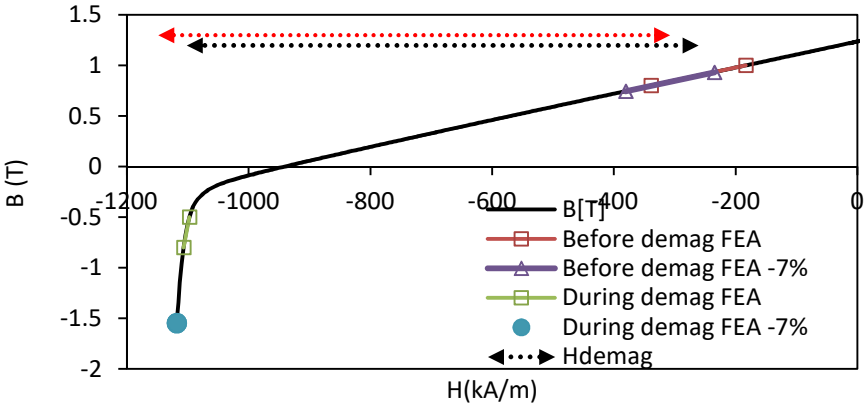

Fig. 5-74 Simplified plot of original and shifted magnet operation region at open circuit and during demagnetizing Id pulse (Id=-24A). The shifted magnet operation regions corresponds to a 7% lower air gap average flux density or a 7% lower fundamental back EMF.

A small shift of the magnet open circuit working points will cause a significant difference in demagnetization as the new loaded magnet operation points will also be shifted. Because the characteristic demagnetization curve is steep after the knee point, one can expect that any error in predicting either the open circuit magnet operation points or the reluctance of the magnetic circuit will make the measured demagnetization deviate from the 2D FEA predicted one.

The current amplitudes for the experiment (Fig. 5-65) were picked when the demagnetization starts occurring, according to the 2D FEA prediction. Thus, the magnet working points will be close to the knee point, around -950kA/m in Fig. 5-75. When moving further down the demagnetization curve, in this steep region, a small change of *H* will correspond to a large loss in magnetization. The lower BEMF and thus lower open circuit magnet working points are the cause of the discrepancy between the predicted and the measured results.

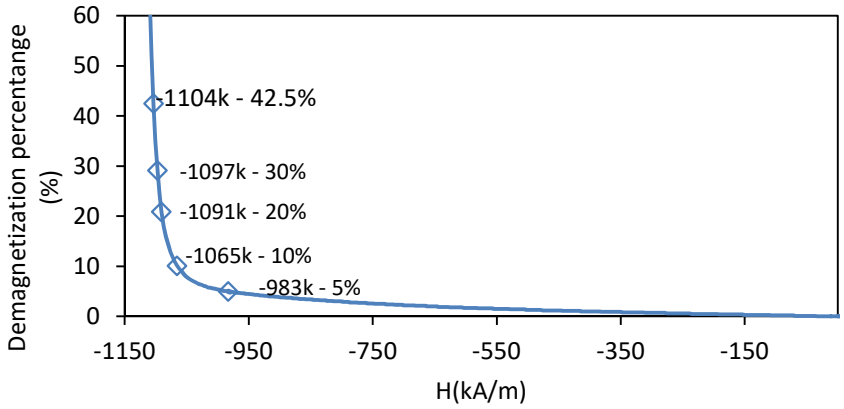

Fig. 5-75 Loss in magnetization vs. demagnetizing field intensity for N35 at 22°C.

Fig. 5-76 shows the B-J-H curve and a more accurate representation of the open circuit and loaded magnet working points from Fig. 5-73. The intersections of the green dotted lines and the B-H curve are the minimum magnet working points at open circuit and under load while the dotted blue lines are for the maximum working points. The solid green lines are parallel and the solid blue lines are also parallel as the reluctance is

equal. The differences in magnetic circuit reluctance makes the magnet working points vary across its length and thickness at both open circuit and under load.

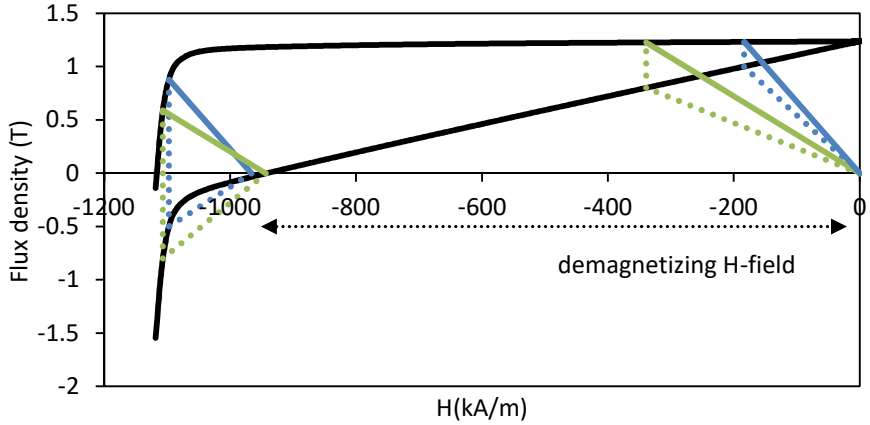

Fig. 5-76 2D FE predicted magnet minimum (green) and maximum (blue) operation points at open circuit and during demagnetization pulse (I_d=-24A).

In Fig. 5-77 the open circuit magnet working points are 7% lower compared to Fig. 5-76, a difference similar to that between the measured BEMF and the 2D FEA predicted BEMF. The applied demagnetizing H-field is the same in both Fig. 5-76 and Fig. 5-77 but in the latter, the magnet reaches lower points along the B-H curve, getting demagnetized to a higher degree. This extra demagnetization is caused by the error in predicting the open circuit magnet operation points.

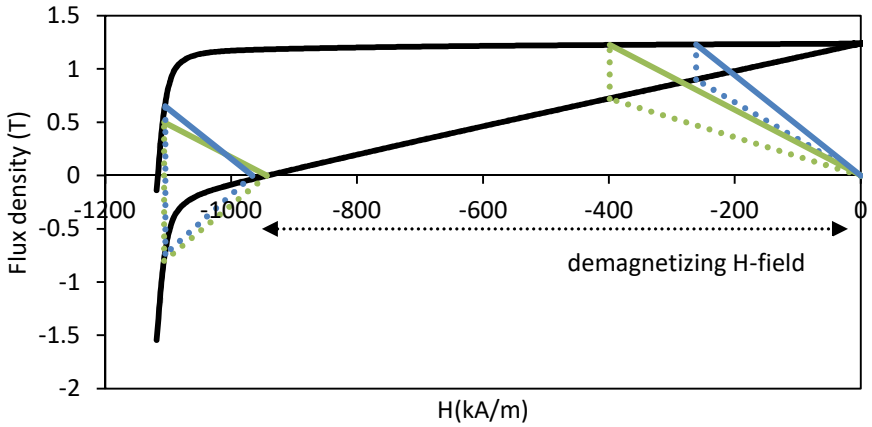

Fig. 5-77 2D FE open circuit minimum (green) and maximum (blue) magnet operation points shifted by -7% and resulting shifted on load magnet operation region.

Fig. 5-78 shows the original and -7% shifted open circuit magnet working points and the under load working points for both cases. This example is based on the I_d=-24A demagnetization current. The open circuit and on load magnet working points were extracted from 2D FEA.

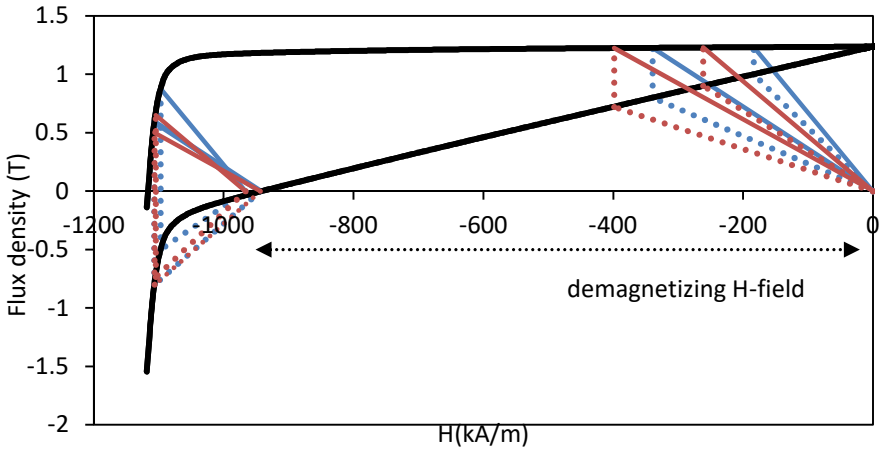

Fig. 5-78 Magnet operation region shift at load due to inaccuracy in predicting the open circuit working point. Open circuit operation points marked with red are shifted by -7% from the blue open circuit operation points predicted using 2D FEA.

There are three possible sources for the error in the open circuit BEMF prediction:

- Magnet temperature
- Magnetic circuit reluctance
- Manufacturing tolerances
- Misalignment of the rotor from the demagnetization position

In general, the BEMF predicted using a 2D analysis will be higher than when including the 3D effects. Fig. 5-79 shows the drawing of the five manufactured solid rotor shafts and back-irons. The ends of the rotor have higher edges to protect the magnet and to ease the manufacturing. However, these rotor lips also increase the rotor PM end effect flux leakage, decreasing the open circuit magnet working point. Furthermore, they also cause some armature reaction fields to cross through them due to their proximity to the

stator (0.5mm distance) compared to the rest of the back-iron (located at 2.5mm distance).

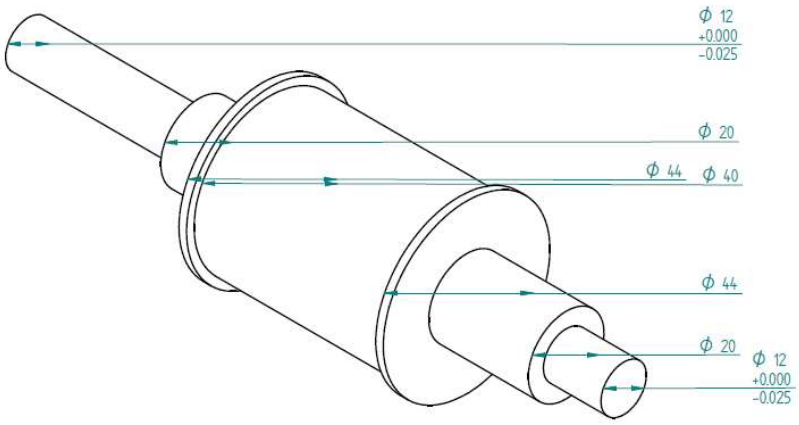

Fig. 5-79 Solid steel rotor shaft and back-iron drawing.

The measured magnet arc width is 23.6mm. All magnets have identical dimensions. The nominal distance between two adjacent magnets is 8.9mm. However, the measured distance between the magnets on the manufactured rotors varies between 8.5 and 9.3mm. These manufacturing tolerances will decrease the average air gap PM flux density, reduce the working point of the magnets and cause a reduction in BEMF compared to the FEA prediction. These tolerances will also cause a significant difference from the predicted cogging torque.

If the rotor position is not perfectly aligned to the middle of a tooth, the demagnetization will be more severe than if it is aligned to the tooth as in the FE simulation (Fig. 5-19). Due to the manufacturing tolerance, especially for the distance between the magnets, and due to the deviation from the d-axis position introduced when mechanically locking the rotor using the lathe, position at which the demagnetizing current was applied is not expected to be that corresponding to the middle of the tooth, for all the 4 magnet poles. In Fig. 5-62, the measured decrease of BEMF is not symmetrical to the 90 and 270 elec.deg. rotor position, suggesting some misalignment exists.

5.6 Conclusions

An SPM rotor was designed and manufactured for the experimental validation of the Cobham Opera Vector Field finite element demagnetization solver accuracy.

Five rotors equipped with N35 grade magnet were designed and manufactured. A microcontroller was used for the timing of the control circuit designed to limit the application time of the demagnetization pulse. Two parallel connected power supplies were required to supply the 24A current. Results for measured and predicted open circuit back EMFs, the peak to peak cogging torques and the average rated current torques were presented.

BEMF, cogging and static torque were measured before and after demagnetization. The results and the discrepancies between the predicted and the measured results are explained.

6. General conclusions

A hybrid FE and analytical method to segregate the PM and reluctance torque components of large data sets of IPM generators with a reduced number of FE simulations is presented. Its results are compared to the results of the conventional partial coupling flux segregation method. The proposed method is used to investigate the influence of the air gap length and the number of rotor poles on the average torque of SPM and V-shaped IPM machines based on the 3kW prototype and the 3MW generator geometries. The average reluctance torque capabilities of the IPM machines decrease when the air gap length or the number of rotor poles are increased from the minimum values in the investigation. The average PM torque of the SPM machines always decreases when the air gap length is increased. Generally, the average reluctance torque of an IPM machine at MTPA operation decreases by 40-80% when the air gap length to air gap diameter ratio increases from 0.02%, the minimum investigated value to 0.1%, the mechanical feasibility limit in large scale electrical machines. Due to the decrease of the reluctance torque, the MTPA current angle moves closer to 0 and the average PM torque increases. Hence, the average PM torque at MTPA of an IPM machine can increase when the air gap length increases, but will decrease monotonically after the average reluctance torque has decreased and the MTPA current angle no longer changes when the air gap length is further increased as in Fig. 2-38, Fig. 2-48 or Fig. 2-58.

NdFeB and ferrite PM electrical machines with SPM and IPM rotors are optimized for a direct drive wind power application. For the minimum material cost designs, the NdFeB IPM machine is found to be 5% more expensive than the NdFeB SPM machine. The minimum material cost ferrite SPM machine using the same current density is found to

be 55% more expensive compared to the NdFeB SPM machine due to the lower air gap flux density, and hence, its longer axial length for the same average torque. The minimum cost ferrite IPM machine is only 11% higher than that of the NdFeB SPM machine due to its reluctance torque capabilities at the low pole number of the minimum cost design.

Analytical and FE models are presented and used to predict the fault current in PM machines optimized for a DD application. The influence of the key PM machine parameters, such as the magnet thickness and the number of rotor poles, on the demagnetization withstand capability is presented.

The demagnetization performance of NdFeB and ferrite, SPM and IPM machines optimized for minimum cost is reported. The machine parameters are adjusted for the PMs to be not subjected to irreversible demagnetization during the fault transient.

The NdFeB SPM machine is found to be the best choice for the direct drive application as it has the lowest material cost for the same average torque. The material cost of the NdFeB IPM machine is 13% higher than that of the NdFeB SPM machine for the machines with demagnetization withstand capabilities. Although the minimum cost ferrite IPM machine seems like a viable alternative, for the ferrite machines to have irreversible demagnetization withstand capabilities, the costs of the ferrite SPM and IPM machines are found to be 64% and 121% higher than those of the cheapest NdFeB SPM machine. The material cost increase for irreversible demagnetization withstand capabilities is 5% for the ferrite SPM machine, and considerably more, 98% for the ferrite IPM machine, due to the increase of flux leakage and the decrease of reluctance torque capabilities when the number of rotor poles is increased. The IPM machines with significant reluctance torque capabilities have a low number of rotor poles and a high number of turns per coil. They are susceptible to irreversible demagnetization during a

fault transient due to the high number of turns per coil. This issue is more severe when low coercivity ferrite magnets are used. Hence, the cost increase for irreversible demagnetization withstand capabilities is higher for the IPM machines and the highest for the ferrite IPM machine.

An experimental investigation on the accuracy of Cobham Opera's Vector Fields demagnetization solver is presented. Experimental locked rotor demagnetization results of the open circuit back-EMF and static torque are compared to the results computed using Vector Fields demagnetization solver for a small size SPM machine. The predictions of the FE solver are found to be consistent with the demagnetization behavior of the investigated NdFeB SPM rotors. The difference between the 2D FE predicted and the experimentally measured results are due to the lower real open circuit magnet operation point, mostly due to the manufacturing tolerances and the 3D effect.

The current technology development trends indicate that the rare earth magnet energy product is increasing. Despite its significantly higher cost, a marginally stronger PM is beneficial as it will reduce the total material cost of an electrical machine and yield a higher torque density. This was demonstrated in this thesis through the NdFeB vs. ferrite machine comparison i.e. the ferrite machines are more expensive and heavier even though the NdFeB is 10 times more expensive and has a remanence only 3 times higher than that of ferrite. Considering the trend of the rare earth materials energy products, it is expected that the difference in material cost between the IPM and the SPM machines designed for the same average torque will increase.

7. Appendix

7.1 Publications

- R. S. Constantin, G. J. Li, and Z. Q. Zhu, “Influence of slot opening and flux gaps on the voltage distortion in SPM machines,” in *Proceedings - 2016 22nd International Conference on Electrical Machines, ICEM 2016*, pp. 796–802, 2016.
- R. S. Constantin, G. J. Li, and Z. Q. Zhu, “Influence of Flux Gaps on the Voltage Distortion in IPM Machines,” – planned publication.

7.2 3kW DD prototype specifications

Table 7-1 Specifications and electromagnetic performance of 3kW DD prototype.

Parameter	Unit	Value
Rotor geometry		
Rotor outer diameter	mm	426.4
Rotor yoke thickness	mm	10
Magnet		N38HT
Magnet height	mm	6
Pole arc to pole pitch ratio		0.97
Flat arc to pole pitch ratio		0.2
Magnet edge height at pole pitch	mm	2.15
Air gap length	mm	2
Pole number		28
Stator geometry		
Stator inner diameter	mm	339.4
Stator outer diameter	mm	390.4
Stator yoke thickness	mm	10
Slot number		84
Slot depth	mm	15.5
Slot width	mm	7.3
Wedge height	mm	1.5
Stator core length	mm	110
Winding data		
Number of turns per phase		420
Resistance DC 20°C	Ω	1.755
Electromagnetic performance data		
Cogging torque (peak-peak)	Nm	1.64
Cogging torque		0.41%
Magnet temperature for load data	°C	60.00
Winding temperature	°C	95.00
Rated speed (mechanical)	rpm	170
Electrical frequency at full load	Hz	39.667
Rated current (RMS)	A	5.83
Current advance angle	Elec.deg.	0
Average rated torque	Nm	195.83
Torque ripple (peak-peak)	Nm	3.03
Torque ripple		0.77%
Input power	W	3486.23
Copper loss	W	231.97
Iron loss	W	59.96
Rated efficiency		91.63%

8. References

[1] H. Polinder, F. F. A. Van Der Pijl, G. J. De Vilder, and P. J. Tavner, "Comparison of direct-drive and geared generator concepts for wind turbines," in *IEEE Transactions on Energy Conversion*, vol. 21, no. 3, pp. 725–733, 2006.

[2] H. Li and Z. Chen, "Design optimization and evaluation of different wind generator systems," in *Proceedings of the 11th International Conference on Electrical Machines and Systems, ICEMS 2008*, pp. 2396–2401, 2008.

[3] H. Li and Z. Chen, "Overview of different wind generator systems and their comparisons," *Renew. Power Gener. IET*, vol. 2, no. 2, pp. 123–138, Jun. 2007.

[4] H. Li, Z. Chen, and H. Polinder, "Optimization of multibrid permanent-magnet wind generator systems," *IEEE Trans. Energy Convers.*, vol. 24, no. 1, pp. 82–92, Mar. 2009.

[5] J. Pyrhonen, J. Nerg, P. Kurronen, J. Puranen, and M. Haavisto, "Permanent magnet technology in wind power generators," in *XIX International Conference on Electrical Machines (ICEM)*, pp. 1–6, 2010.

[6] T. M. Jahns, "The expanding role of PM machines in direct-drive applications," in *2011 International Conference on Electrical Machines and Systems, ICEMS 2011*, pp. 1–6, 2011.

[7] N. Bianchi and S. Bolognani, "Design techniques for reducing the cogging torque in surface-mounted PM motors," *IEEE Trans. Ind. Appl.*, vol. 38, no. 5, pp. 1259–1265, Sep. 2002.

[8] A. M. El-Refaie, Z. Q. Zhu, T. M. Jahns, and D. Howe, "Winding inductances of fractional slot surface-mounted permanent magnet brushless machines," in *Conference Record - IAS Annual Meeting (IEEE Industry Applications Society)*, pp. 1–8, 2008.

[9] J. Cros and P. Viarouge, "Synthesis of high performance PM motors with concentrated windings," *IEEE Int. Electr. Mach. Drives Conf. IEMDC 1999 - Proc.*, vol. 17, no. 2, pp. 725–727, Jun. 1999.

[10] P. Salminen, M. Niemela, J. Pyhonen, and J. Mantere, "Performance analysis of fractional slot wound PM-motors for low speed applications," in *Conference Record of the 2004 IEEE Industry Applications Conference, 2004. 39th IAS Annual Meeting.*, vol. 2, pp. 1032–1037, 2004.

[11] F. Magnussen and C. Sadarangani, "Winding factors and Joule losses of permanent magnet machines with concentrated windings," in *IEMDC 2003 - IEEE International Electric Machines and Drives Conference*, vol. 1, pp. 333–339, 2003.

[12] N. Bianchi and M. Dai Pre, "Use of the star of slots in designing fractional-slot single-layer synchronous motors," *IEE Proc. - Electr. Power Appl.*, vol. 153, no.

3, p. 459, 2006.

[13] A. M. El-Refaie, T. M. Jahns, and D. W. Novotny, “Analysis of surface permanent magnet machines with fractional-slot concentrated windings,” *IEEE Trans. Energy Convers.*, vol. 21, no. 1, pp. 34–43, Mar. 2006.

[14] A. M. EL-Refaie, “Fractional-slot concentrated-windings synchronous permanent magnet machines: Opportunities and challenges,” *IEEE Trans. Ind. Electron.*, vol. 57, no. 1, pp. 107–121, 2010.

[15] Z. Q. Zhu, D. Ishak, D. Howe, and J. Chen, “Unbalanced magnetic forces in permanent-magnet brushless machines with diametrically asymmetric phase windings,” *IEEE Trans. Ind. Appl.*, vol. 43, no. 6, pp. 1544–1553, 2007.

[16] G. Qi, J. T. Chen, Z. Q. Zhu, D. Howe, L. B. Zhou, and C. L. Gu, “Influence of skew and cross-coupling on d- and q-axis inductances and flux-weakening performance of PM brushless AC machines,” *2008 International Conference on Electrical Machines and Systems*, vol. 45, no. 5. pp. 2110–2117, 2008.

[17] T. A. Burress, S. L. Campbell, C. Coomer, C. W. Ayers, A. A. Wereszczak, J. P. Cunningham, L. D. Marlino, L. E. Seiber, and H.-T. Lin, “Evaluation of the 2010 Toyota Prius Hybrid Synergy Drive System,” Oak Ridge, TN (United States), Mar. 2011.

[18] N. A. Bhuiyan and A. Mcdonald, “Optimisation and comparison of generators with different magnet materials for a 6MW offshore direct drive wind turbine,” in *8th IET International Conference on Power Electronics, Machines and Drives (PEMD 2016)*, no. August 2009, pp. 1–6, 2011.

[19] Z. Q. Zhu and D. Howe, “Electrical machines and drives for electric, hybrid, and fuel cell vehicles,” *Proc. IEEE*, vol. 95, no. 4, pp. 746–765, Apr. 2007.

[20] K. T. Chau, C. C. Chan, and C. Liu, “Overview of permanent-magnet brushless drives for electric and hybrid electric vehicles,” *IEEE Trans. Ind. Electron.*, vol. 55, no. 6, pp. 2246–2257, Jun. 2008.

[21] T. M. Jahns, G. B. Kliman, and T. W. Neumann, “Interior Permanent-Magnet Synchronous Motors for Adjustable-Speed Drives,” *IEEE Trans. Ind. Appl.*, vol. IA-22, no. 4, pp. 738–747, Jul. 1986.

[22] T. M. Jahns, “Flux-weakening regime operation of an interior permanent-magnet synchronous motor drive,” *IEEE Trans. Ind. Appl.*, vol. IA-23, no. 4, pp. 681–689, Jul. 1987.

[23] S. Morimoto, M. Sanada, and Y. Takeda, “Wide-Speed Operation of Interior Permanent Magnet Synchronous Motors with High-Performance Current Regulator,” *IEEE Trans. Ind. Appl.*, vol. 30, no. 4, pp. 920–926, 1994.

[24] W. L. Soong and N. Ertugrul, “Field-weakening performance of interior permanent-magnet motors,” *IEEE Trans. Ind. Appl.*, vol. 38, no. 5, pp. 1251–1258, Sep. 2002.

[25] A. M. El-Refaie, T. M. Johns, P. J. McCleer, and J. W. McKeever, “Experimental verification of optimal flux weakening in surface PM machines using concentrated windings,” *Conf. Rec. - IAS Annu. Meet. (IEEE Ind. Appl. Soc.*, vol. 2, no. 3, pp. 1050–1057, May 2005.

[26] A. M. EL-Refaie and T. M. Jahns, “Comparison of synchronous PM machine types for wide constant-power speed range operation,” in *Conference Record - IAS Annual Meeting (IEEE Industry Applications Society)*, vol. 2, pp. 1015–1022, 2005.

[27] A. M. EL-Refaie and T. M. Jahns, “Scalability of surface PM machines with concentrated windings designed to achieve wide speed ranges of constant-power operation,” in *IEEE Transactions on Energy Conversion*, vol. 21, no. 2, pp. 362–369, 2006.

[28] M. Zeraoulia, M. E. H. Benbouzid, and D. Diallo, “Electric motor drive selection issues for HEV propulsion systems: A comparative study,” in *IEEE Transactions on Vehicular Technology*, vol. 55, no. 6, pp. 1756–1764, 2006.

[29] Z. Q. Zhu and C. C. Chan, “Electrical machine topologies and technologies for electric, hybrid, and fuel cell vehicles,” in *2008 IEEE Vehicle Power and Propulsion Conference, VPPC 2008*, pp. 1–6, 2008.

[30] S. H. Han, T. M. Jahns, and Z. Q. Zhu, “Design tradeoffs between stator core loss and torque ripple in IPM machines,” in *IEEE Transactions on Industry Applications*, vol. 46, no. 1, pp. 187–195, 2010.

[31] S. Ooi, S. Morimoto, and M. Sanada, “Performance evaluation of a high power density PMASynRM with ferrite magnets,” in *2011 IEEE Energy Conversion Congress and Exposition*, pp. 4195–4200, 2011.

[32] A. M. El-Refaie, “Motors/generators for traction /propulsion applications: A review,” in *2011 IEEE International Electric Machines and Drives Conference, IEMDC 2011*, pp. 490–497, 2011.

[33] A. Chiba, Y. Takano, M. Takeno, T. Imakawa, N. Hoshi, M. Takemoto, and S. Ogasawara, “Torque density and efficiency improvements of a switched reluctance motor without rare-earth material for hybrid vehicles,” *IEEE Trans. Ind. Appl.*, vol. 47, no. 3, pp. 1240–1246, May 2011.

[34] Z. Zhu, “Fractional slot permanent magnet brushless machines and drives for electric and hybrid propulsion systems,” *COMPEL - Int. J. Comput. Math. Electr. Electron. Eng.*, vol. 30, no. 1, pp. 9–31, Jan. 2011.

[35] Z. Azar, Z. Q. Zhu, and G. Ombach, “Influence of electric loading and magnetic saturation on cogging torque, Back-EMF and torque ripple of PM machines,” *IEEE Trans. Magn.*, vol. 48, no. 10, pp. 2650–2658, Oct. 2012.

[36] M. Barcaro, N. Bianchi, and F. Magnussen, “Permanent-magnet optimization in permanent-magnet-assisted synchronous reluctance motor for a wide constant-power speed range,” *IEEE Trans. Ind. Electron.*, vol. 59, no. 6, pp. 2495–2502, Jun. 2012.

[37] G. Pellegrino, A. Vagati, P. Guglielmi, and B. Boazzo, "Performance comparison between surface-mounted and interior PM motor drives for electric vehicle application," *IEEE Trans. Ind. Electron.*, vol. 59, no. 2, pp. 803–811, Feb. 2012.

[38] P. B. Reddy, A. M. El-Refaie, K. K. Huh, J. K. Tangudu, and T. M. Jahns, "Comparison of interior and surface PM machines equipped with fractional-slot concentrated windings for hybrid traction applications," *IEEE Trans. Energy Convers.*, vol. 27, no. 3, pp. 593–602, Sep. 2012.

[39] A. M. El-Refaie, "Motors/generators for traction/propulsion applications: A review," *IEEE Veh. Technol. Mag.*, vol. 8, no. 1, pp. 90–99, Mar. 2013.

[40] Z. Q. Zhu, W. Q. Chu, and Y. Guan, "Quantitative comparison of electromagnetic performance of electrical machines for HEVsEVs," *CES Trans. Electr. Mach. Syst.*, vol. 1, no. 1, pp. 37–47, Mar. 2017.

[41] B. Boazzo, G. Pellegrino, and A. Vagati, "Multipolar SPM machines for direct drive application: A comprehensive design approach," in *2012 IEEE International Energy Conference and Exhibition, ENERGYCON 2012*, pp. 98–105, 2012.

[42] B. Boazzo, G. Pellegrino, and A. Vagati, "Multipolar SPM machines for direct-drive application: A general design approach," *IEEE Trans. Ind. Appl.*, vol. 50, no. 1, pp. 327–337, Jan. 2014.

[43] J. A. Tapia, J. Pyrhonen, J. Puranen, P. Lindh, and S. Nyman, "Optimal Design of Large Permanent Magnet Synchronous Generators," *IEEE Trans. Magn.*, vol. 49, no. 1, pp. 642–650, Jan. 2013.

[44] X. Zhang and R. Qu, "Pole number selection strategy of low-speed multiple-pole permanent magnet synchronous machines," in *Proceedings of the 2013 IEEE International Electric Machines and Drives Conference, IEMDC 2013*, pp. 1267–1274, 2013.

[45] H. Silaghi and V. Spoială, "PM wind generator topologies," *J. Electr. Electron. Eng.*, vol. 1, no. 1, pp. 125–129, Nov. 2008.

[46] E. Spooner and A. Williamson, "Modular, permanent-magnet wind-turbine generators," in *IAS '96. Conference Record of the 1996 IEEE Industry Applications Conference Thirty-First IAS Annual Meeting*, vol. 1, pp. 497–502, 1996.

[47] F. Luise, A. Tessarolo, S. Pieri, and M. De Martin, "Design for manufacturability of an off-shore direct-drive wind generator," in *2015 10th International Conference on Ecological Vehicles and Renewable Energies, EVER 2015*, pp. 1–6, 2015.

[48] M. Chirca, C. Oprea, P. D. Teodosescu, and S. Breban, "Optimal design of a radial flux spoke-type interior rotor permanent magnet generator for micro-wind turbine applications," in *2016 International Conference on Applied and Theoretical Electricity, ICATE 2016 - Proceedings*, pp. 1–5, 2016.

[49] H. Haraguchi, S. Morimoto, and M. Sanada, “Suitable design of a PMSG for a large-scale wind power generator,” in *2009 IEEE Energy Conversion Congress and Exposition, ECCE 2009*, pp. 2447–2452, 2009.

[50] G. Y. Sizov, P. Zhang, D. M. Ionel, N. A. O. Demerdash, and M. Rosu, “Automated bi-objective design optimization of multi-MW direct-drive PM machines using CE-FEA and differential evolution,” in *IEEE Energy Conversion Congress and Exposition: Energy Conversion Innovation for a Clean Energy Future, ECCE 2011, Proceedings*, pp. 3672–3678, 2011.

[51] S. Eriksson and H. Bernhoff, “Rotor design for PM generators reflecting the unstable neodymium price,” in *Proceedings - 2012 20th International Conference on Electrical Machines, ICEM 2012*, pp. 1419–1423, 2012.

[52] H. Chen, R. Qu, J. Li, and B. Zhao, “Comparison of interior and surface permanent magnet machines with fractional slot concentrated windings for direct-drive wind generators,” in *2014 17th International Conference on Electrical Machines and Systems, ICEMS 2014*, pp. 2612–2617, 2015.

[53] B. C. Mecrow, A. G. Jack, J. A. Haylock, and J. Coles, “Fault-tolerant permanent magnet machine drives,” *IEE Proc. - Electr. Power Appl.*, vol. 143, no. 6, p. 437, 1996.

[54] D. Ede, J.D.; Atallah, K.; Wang, J.B.; Howe, “Modular fault-tolerant permanent magnet brushless machines,” in *International Conference on Power Electronics Machines and Drives*, vol. 2002, pp. 415–420, 2002.

[55] A. J. Mitcham, G. Antonopoulos, and J. J. A. Cullen, “Favourable slot and pole number combinations for fault-tolerant PM machines,” *IEE Proceedings-Electric Power Appl.*, vol. 150, no. 2, pp. 139–145, 2003.

[56] N. Bianchi, S. Bolognani, M. Dai Pré, and G. Grezzani, “Design considerations for fractional-slot winding configurations of synchronous machines,” *IEEE Trans. Ind. Appl.*, vol. 42, no. 4, pp. 997–1006, Jul. 2006.

[57] M. Barcaro, N. Bianchi, and F. Magnussen, “Faulty operations of a PM fractional-slot machine with a dual three-phase winding,” *IEEE Trans. Ind. Electron.*, vol. 58, no. 9, pp. 3825–3832, Sep. 2011.

[58] B. Kötz, M. Schaepman, F. Morsdorf, P. Bowyer, K. Itten, and B. Allgöwer, “Demagnetization Analysis of Permanent Magnets According to Rotor Types of Interior Permanent Magnet Synchronous Motor,” in *Big data security and privacy issues in healthcare*, vol. 4, pp. 2869–2871, 2003.

[59] J. Wang, W. Wang, K. Atallah, and D. Howe, “Demagnetization assessment for three-phase tubular brushless permanent-magnet machines,” *IEEE Trans. Magn.*, vol. 44, no. 9, pp. 2195–2203, Sep. 2008.

[60] S. Ruoho, J. Kolehmainen, J. Ikäheimo, and A. Arkkio, “Demagnetization testing for a mixed-grade dovetail permanent-magnet machine,” *IEEE Trans. Magn.*, vol. 45, no. 9, pp. 3284–3289, Sep. 2009.

[61] T. Hosoi, H. Watanabe, K. Shima, T. Fukami, R. Hanaoka, and S. Takata, “Demagnetization analysis of additional permanent magnets in salient-pole synchronous machines with damper bars under sudden short circuits,” *IEEE Trans. Ind. Electron.*, vol. 59, no. 6, pp. 2448–2456, Jun. 2012.

[62] G. Choi and T. M. Jahns, “Interior permanent magnet synchronous machine rotor demagnetization characteristics under fault conditions,” in *2013 IEEE Energy Conversion Congress and Exposition, ECCE 2013*, pp. 2500–2507, 2013.

[63] P. Guglielmi, B. Boazzo, E. Armando, G. Pellegrino, and A. Vagati, “Permanent-magnet minimization in PM-assisted synchronous reluctance motors for wide speed range,” *IEEE Trans. Ind. Appl.*, vol. 49, no. 1, pp. 31–41, Jan. 2013.

[64] J. D. McFarland and T. M. Jahns, “Investigation of the rotor demagnetization characteristics of interior PM synchronous machines during fault conditions,” *IEEE Trans. Ind. Appl.*, vol. 50, no. 4, pp. 2768–2775, Jul. 2014.

[65] V. I. Patel, J. Wang, and S. S. Nair, “Demagnetization Assessment of Fractional-Slot and Distributed Wound 6-Phase Permanent Magnet Machines,” *IEEE Trans. Magn.*, vol. 51, no. 6, pp. 1–11, Jun. 2015.

[66] G. Choi, Y. Zhang, and T. M. Jahns, “Experimental verification of rotor demagnetization in a fractional-slot concentrated-winding PM synchronous machine under drive fault conditions,” in *ECCE 2016 - IEEE Energy Conversion Congress and Exposition, Proceedings*, pp. 1–8, 2016.

[67] B. A. Welchko, T. M. Jahns, W. L. Soong, and J. M. Nagashima, “IPM synchronous machine drive response to symmetrical and asymmetrical short circuit faults,” *IEEE Trans. Energy Convers.*, vol. 18, no. 2, pp. 291–298, Jun. 2003.

[68] W. Q. Chu and Z. Q. Zhu, “Analytical modeling and investigation of transient response of PM machines with 3-phase short-circuit fault,” in *2011 IEEE International Electric Machines & Drives Conference (IEMDC)*, no. 5, pp. 125–130, 2011.

[69] H. Vu Xuan, H. Polinder, D. Lahaye, and J. A. Ferreira, “Modeling for the design of fractional slot PM machines with concentrated windings protected from demagnetization during three-phase short circuit,” in *2012 IEEE Energy Conversion Congress and Exposition, ECCE 2012*, pp. 1276–1283, 2012.

[70] H. Chen, R. Qu, J. Li, and D. Li, “Demagnetization Performance of a 7 MW Interior Permanent Magnet Wind Generator with Fractional-Slot Concentrated Windings,” *IEEE Trans. Magn.*, vol. 51, no. 11, pp. 1–4, Nov. 2015.

[71] P. Eklund, S. Sjökvist, and S. Eriksson, “Determining demagnetisation risk for two PM wind power generators with different PM material and identical stators,” *IET Electr. Power Appl.*, vol. 10, no. 7, pp. 593–597, Aug. 2016.